A light scattering study of colloid-polymer mixtures.

Angus D. Pirie.

A thesis submitted in fulfilment of the requirements
for the degree of Doctor of Philosophy
to the
University of Edinburgh
1995

Abstract

A detailed light scattering study of non-equilibrium states found in a model colloid-polymer mixture is presented. Conventional light scattering is used to examine the average structure of the phase, over a wide range of wavevectors. For all non-equilibrium samples a 'ring' of scattered radiation is found at small angles, whose temporal evolution is used to investigate aggregation kinetics and the growth of structure. For low concentrations of colloid and just sufficient polymer to induce non-equilibrium behaviour a small angle ring is observed after a initial 'lag time', which remains stationary and brightens rapidly, behaviour reminiscent of classical nucleation. At higher colloid concentrations one finds a continuously collapsing and brightening ring, similar to that found in classical spinodal decomposition. Upon the addition of further polymer the system gels and the small angle ring becomes arrested at a finite wavevector. Direct visual observation of these different regimes is also presented, via video-enhanced microscopy and direct time-lapse video recordings, to complement the light scattering data. The particle dynamics within the aggregates are measured using dynamic light scattering. The results obtained suggest that the onset of non-equilibrium behaviour is caused by the presence of a metastable gas-liquid phase boundary, which can be calculated using a recently-developed mean-field theory.

Declaration

This thesis has been composed by myself and it has not been submitted in any previous application for a degree. The work reported within was executed by me, unless otherwise stated.

December 1995

Acknowledgements

Firstly I would like to thank both my supervisors, Prof. Peter Pusey and Dr. Wilson Poon. Peter for his considerable expertise in light scattering, which he happily passed on to me. Wilson for his boundless enthusiasm and his constructive criticism in proof reading this text. I also note valuable discussions with Henk Lekkerkerker, Bill van Megen, Mike Cates and Bob Gammon. Thanks guys.

I would also like to thank all my friends at Unilever Research, Port Sunlight. Namely Patrick Warren, Moti Lal, Scott Singleton and Mike Ashton, who made my stay at Port Sunlight so enjoyable and fruitful. I would also like to thank Unilever Research for their financial backing and interest in this work.

My 'squidgy' group colleagues must also be thanked for putting up with me during my studies. Oliver Behrend for his drive, energy and Tuesday night drinking (I hope the sheep herding works out), Steve Meeker for his regularly poor bets and ineptitude at video games, Mark Haw for many surreal discussions (all-over-body sandals?), Steve Ilett for his sporting chat, Phil Segre for his golf lessons and finally Dave Grieg and Robert Gray for repeatedly reminding me that I'm a miserable Fifer. The Physics football team must also be remembered for some truly mediocre performances. Remember Alasdair, things can only get better!

Mum, Dad and Iain have been extremely supportive throughout my PhD and their encouragement and backing has been second to none. I hope you understand a little bit of this work! Finally many thanks must go to Lesley. Her inspiration and encouragement has guided me through, what have often been, difficult times. Only through her is any of this possible.

This thesis is dedicated to Lesley, with all my love.

Contents

Abstract i

Declaration ii

Acknowledgements iii

1 Introduction 1

1.1 Research motivation 1

1.2 Colloidal suspensions and interparticle forces 2

1.3 The depletion potential 4

1.4 Thesis summary 6

2 Phase Behaviour 9

2.1 Introduction 9

2.2 Atomic phase behaviour 10

2.2.1 Calculating phase behaviour 11

2.2.2 Nucleation and growth 15

2.2.3 Spinodal decomposition 16

2.2.4 Spinodal decomposition in fluids 21

2.3 The colloid-atom analogy 23

2.4 Colloidal phase behaviour 25

2.4.1 Hard-sphere colloids 25

2.4.2 Colloid-polymer mixtures 26
2.4.3 The interparticle potential range 31
2.5 Experimental colloid-polymer phase behaviour 33
2.5.1 The model experimental system 33
2.5.2 Phase behaviour 34
2.5.3 Temperature dependence 36
2.5.4 Index matching 38
2.6 Concluding remarks 39

3 Light Scattering Theory 40
3.1 Introduction 40
3.1.1 Static Light Scattering - Structure 41
3.1.2 Dynamic Light Scattering - Dynamics 41
3.2 Assumptions 42
3.3 The nature of scattered light 43
3.3.1 The form factor 47
3.3.2 The static structure factor 52
3.4 Theoretical structure factors 53
3.4.1 Hard sphere systems 55
3.4.2 Adhesive hard spheres 57
3.4.3 Square well fluid 58
3.5 Dynamics 60
3.5.1 Dilute suspensions 64
3.5.2 Concentrated suspensions 66
3.5.3 Non-ergodicity 69
3.6 Polydispersity effects 71
3.7 Concluding remarks 73

4 Static structure of the non-equilibrium phase 74

4.1 Introduction 74

4.2 Visual observation 76

4.3 Small angle scattering 80

4.3.1 Experimental setup 80

4.3.2 Equipment tests 82

4.3.3 Results 85

4.3.4 The small angle peak 89

4.3.5 Ring kinetics 91

4.3.6 'Universal' behaviour 100

4.3.7 Fractal geometry 103

4.3.8 Summary 121

4.3.9 Small angle scattering from sediments 125

4.3.10 Small angle scattering in the equilibrium regions 128

4.4 Video-enhanced microscopy 132

4.4.1 Experimental techniques 133

4.4.2 Resolution 134

4.4.3 Phase contrast results 135

4.4.4 DIC results 142

4.5 Observations on larger length scales 145

4.5.1 The structure formation 145

4.5.2 The structural collapse 146

4.6 Large angle scattering 148

4.6.1 Experimental setup 148

4.6.2 Results 149

4.6.3 Discussion 150

4.7 Concluding Remarks 153

5 **Dynamic structure of the non-equilibrium phase** **156**
5.1 Introduction 156
5.2 Experimental setup 156
5.3 Temporal evolution of the single particle dynamics 159
5.4 Short-Time dynamics 165
5.5 Q-dependent dynamics 168
5.6 Long-time dynamics 173
5.7 Concluding remarks 178

6 **Conclusion** **180**
6.1 Thesis summary 180
6.2 Comparison with the study of Allain et al. 181
6.3 Possible future work 184

A **Scattered electric field from a sphere** **186**

B **Scattered electric field from a shell** **187**

C **The relation between $S(Q)$ and $g(r)$** **189**

D **Second Virial coefficients** **191**

E **Structure factor of a doublet** **193**

Bibliography **195**

Publications **205**

Chapter 1

Introduction

'That he should ever have studied science and philosophy was a mistake. These things should be left to the frigid and impersonal investigator for they offer two equally tragic alternatives to the man of feeling and action; dispair if he fail in his quest and terror unutterable and unimaginable if he succeed.'

- **From beyond**, H.P. Lovecraft (1920).

1.1 Research motivation

It has been known since 1938 [1] that the addition of large amounts of non-adsorbing polymer molecules to an otherwise stable colloidal suspension can cause the colloidal particles to phase separate, and at higher polymer concentrations to aggregate and form a 'gel'. These phenomena have subsequently been attributed to depletion zones of polymer coils formed around the colloidal particles, leading to an effective attraction known as the depletion potential [2] - [4].

An understanding of the depletion potential is essential in the manufacture of many commercial products. Typical examples are paint or salad cream, where polymer molecules are added to a colloidal suspension to act as a rheological modifier. There is also much industrial interest concerning the formation of macroscopically connected colloidal structures (*gels*), from previously unconnected suspensions (*sols*). In fact gels appear frequently in every day life, ranging from food products such as yoghurt and cheese to cosmetics and even sewage sludge! [5].

In this thesis I present an experimental study of non-equilibrium aggregation in a model colloid-polymer mixture, primarily using light scattering techniques.

1.2 Colloidal suspensions and interparticle forces

Colloidal suspensions occur in a variety of guises, ranging from solid particles suspended in a liquid through to liquid 'emulsion' droplets dispersed in a continuous phase of a second liquid. The link between all such colloidal systems lies in the mesoscopic length scale that characterises the dispersed phase. This is defined to be of the order of ten nanometers ($1 \times 10^{-8} m$) through to approximately one micron ($1 \times 10^{-6} m$) in size. The spatial scale of these systems is such that they undergo random Brownian motion due to the constant buffeting of the particles by fluid molecules. This characteristic range of length scale coincides with the wavelength of light ($\sim 0.6 \times 10^{-6} m$), and as a result light scattering techniques are widely used to probe colloidal systems and the interactions between them. In this thesis solid colloidal particles, suspended in a fluid continuum, are studied via light scattering techniques and direct observation.

In recent years spherical man-made particles have been produced with extremely peaked size distributions, leading to almost monodispersed suspensions. These particles can also be stabilised so that they approximate 'hard-sphere' behaviour, i.e. they do not interact until they come into contact when the interactions between the particles become highly repulsive. This has led to so called 'model' systems which, due to the uniformity in size and interactions, greatly simplify the interpretation of experimental results.

Colloidal systems are subject to a large variety of interparticle forces which determine the macroscopic, as well as microscopic properties of the colloidal suspension.

For instance, it is well known that two atoms experience an inter-atomic force through their fluctuating dipole moments. By integrating this force over colloidal particles one obtains a short range, attractive interparticle potential, known as the van der Waals interaction [6]. Colloidal particles which are not stabilised will aggregate irreversibly under this potential. To prevent this the particles are frequently charge or sterically stabilised.

Colloidal particles can be charged, and when dispersed in a polar liquid, such as water, counterions dissociate from the surface of the particle but remain in its field of force. An electric double layer is formed, consisting of both counterions and electrolyte ions, which are attracted from the surrounding medium. When two particles approach one another the electric double layers overlap and the particles experience a highly repulsive force which, in the right conditions, can stabilise the particles against aggregation [7]. The resulting interparticle potential, which is simply the addition of the van der Waals attraction and the screened Coulombic interaction is often referred to as the Derjaguin-Landau-Verwey-Overbeek (DLVO) potential.

To prevent aggregation one can also attach flexible polymer 'hairs' or 'brushes' to the surface of neutrally charged colloidal particles, known as steric stabilisation [8]. The size of these hairs is usually adjusted to be far smaller than the particle radius. As two particles approach one another the polymer hairs become compressed which leads to a strong entropic repulsion. Consequently the particles approximate the behaviour of hard spheres.

Another interparticle potential, and the one examined in detail here, is the so called 'depletion' potential due to the addition of another species, for example non-adsorbing polymer molecules (e.g. [9] - [21]), micelles (e.g. [22] - [24]) or other smaller colloidal particles (e.g. [25] - [27]).

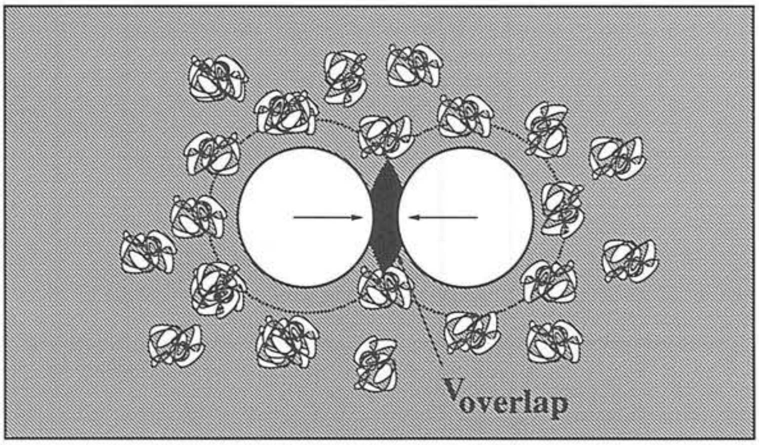

Figure 1.1. The origin of the depletion potential. The dashed lines indicate the depletion zones, the filled-in region represents $V_{overlap}$, the volume of the depletion zones which overlap. Through this depletion mechanism the particles are driven together.

1.3 The depletion potential

The depletion interaction is caused by the formation of a depletion layer of polymer coils around the surface of the colloidal particles (see figure 1.1), as the polymer cannot penetrate the hard-sphere-like colloid. The colloidal particles therefore have a volume surrounding them where the polymer segment concentration is substantially lower than the bulk concentration, which increases the free energy of the system. By overlapping the depletion regions between colloidal particles the system can lower its free energy, which leads to an effective attraction. Alternatively the depletion attraction can be seen to arise, as polymer molecules are excluded from the volume between particles when the separation is less than the radius of gyration of the polymer coils. This leads to an osmotic pressure difference which drives the particles together. Therefore an effective attractive potential between the colloidal particles results.

The original geometrical arguments of Asakura and Oosawa [3], [4], along with subsequent generalisations [2], [28], have determined a theoretical pairwise form for the depletion potential which ignores the internal degrees of freedom of the polymer

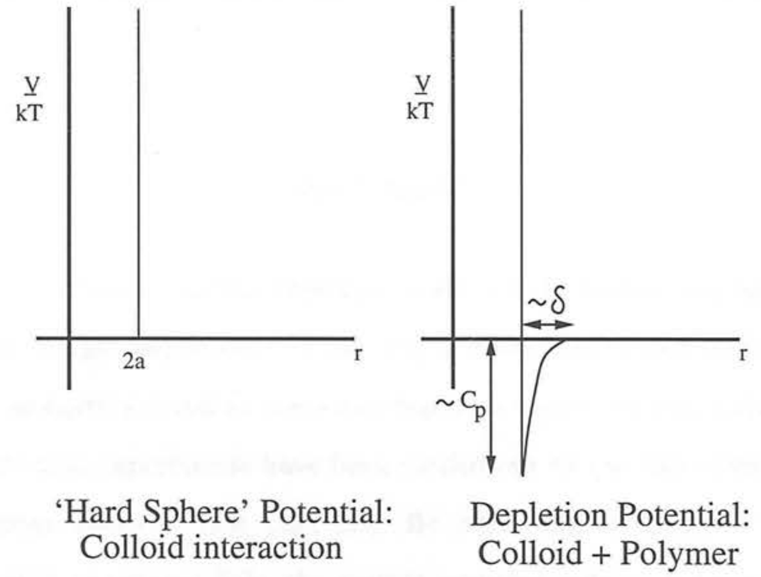

Figure 1.2. A schematic depletion potential, compared with the colloidal hard-sphere interaction.

coils and treats the colloid-polymer interaction as effectively hard-sphere-like[1]. This predicts a potential range assumed to be proportional to the radius of gyration of the polymer molecules and depth dependent upon the polymer concentration,

$$\frac{V(r)}{k_B T} = \begin{cases} \infty & r < 2a \\ -\Pi_{pol} V_{overlap} & 2a < r < 2(a+\delta) \\ 0 & r > 2(a+\delta) \end{cases} \tag{1.1}$$

$$V_{overlap} = \frac{4\pi}{3}(a+\delta)^3 \left\{ 1 - \frac{3}{4}\left(\frac{r}{a+\delta}\right) + \frac{1}{16}\left(\frac{r}{a+\delta}\right)^3 \right\} \tag{1.2}$$

where a is the particle radius, δ the polymer radius of gyration, r the intercentre separation between the colloidal particles and Π_{pol} the polymer osmotic pressure, which

---

[1] Work has also been carried out to calculate realistic depletion potentials, such as accounting for a softness in the repulsive colloidal interaction or polymer-polymer interactions [29] - [31], which will not be covered here.

is proportional to the total number density of polymer coils in the free volume[2] ρ_{pol},

$$\Pi_{pol} = \rho_{pol} k_B T \tag{1.3}$$

$V_{overlap}$ is the volume of the depletion zones which overlap (see figure 1.1). As a consequence simple adjustment of the polymer size and concentration leads to a interparticle potential tunable in range and depth, as shown schematically in figure 1.2.

Light scattering experiments have been carried out to test the validity of the theoretical depletion potential [28], [32], [33]. By measuring the polymer concentration dependence of the scattered light the mutual excluded volume between the polymer molecules and the colloidal particles can be determined. The width of the depletion layer is found to be comparable to the radius of gyration of the polymer coil, as expected. From these measurements the second virial coefficient of the colloidal particles can be obtained. When sufficient amounts of polymer have been added the second virial coefficient becomes negative, indicating an effective attraction between the colloidal particles.

1.4 Thesis summary

This work is primarily concerned with non-equilibrium aggregation in a model colloid-polymer mixture. Non-equilibrium colloidal aggregation is induced when large amounts of a sufficiently small non-adsorbing polymer have been added to an otherwise stable colloidal suspension. The resulting aggregation kinetics are found to be highly sensitive to the polymer and colloid concentrations.

At low concentrations of colloid, in the absence of polymer, one finds fluid equilibrium states which possess short-range order but long-range disorder. Upon the addition

---

[2] i.e. free volume = (total volume) - (volume taken up by the colloidal particles).

of small amounts of a sufficiently small non-adsorbing polymer one still finds the persistence of colloidal fluid states. If the polymer concentration is increased sufficiently the colloidal particles phase separate into coexisting fluid and crystalline phases, a phenomenon which has been verified by both experiment and theory. If even further polymer is added, so that the sample lies far from the fluid-crystal phase boundary, one finds that the colloidal particles undergo non-equilibrium aggregation (see figure 2.13). The onset of colloidal aggregation cannot be explained through equilibrium thermodynamics.

In this study a non-equilibrium region is identified on the equilibrium phase diagram, and is shown to divide into three distinctly different kinetic regimes. At low polymer and colloid concentrations one observes 'nucleation-like' behaviour i.e. the formation of dense discrete (amorphous) droplets of colloidal particles after a finite lag time. Accordingly one observes a delay before the formation of an inter-cluster correlation, characterised by a ring of scattered light at small angles. The discrete clusters then settle under gravity to yield a metastable sediment.

At intermediate colloid and polymer concentrations one observes 'spinodal-like' behaviour i.e. the formation of a dense inter-connected system spanning network, which coarsens rapidly over time. In this case a small angle ring of scattered light forms immediately, which continuously brightens and collapses to smaller angles, indicative of a single rapidly growing characteristic length scale. The time evolution of the scattered ring suggests that the growth is initially diffusion driven, but which rapidly becomes dominated by gravity as the clusters become sufficiently large. As the structure grows the small angle structure factors show dynamic scaling with a scaling exponent of 3. The time-independent scaling function agrees with the Furukawa prediction for classical spinodal decomposition. Dynamic measurements suggest that the particles are relatively free to diffuse, consistent with a lack of structural rigidity. Once the gravity dominated motion has set in the structure rapidly collapses to a metastable sediment.

At large colloid or polymer concentrations one observes 'transient-gelation' i.e. the formation of a rigid, ramified, system-spanning network with a finite life time. The associated small angle ring initially collapses but becomes frozen at a finite wavevector as the system gels. In this case the early stage kinetics follow a diffusion limited cluster aggregation (DLCA). The small angle structure factors scale to an exponent of 1.7 consistent with a DLCA-type mechanism. One can conjecture that the system-spanning structure forms rapidly before gravity can take effect. The subsequent network then has a structural rigidity which prevents a gravity dominated motion. After a finite period of time, roughly coincident with visible gravitational settling, the small angle ring collapses. This can be attributed to a slow particle rearrangement which tends to compactify the local short-ranged structure, observed as slow single particle diffusion when the structure is in its most arrested state. Once the network no longer percolates the now discrete clusters sediment under gravity. One finds that the collapse of these states can be halted by removing the effect of gravity, upon which the structure breaks up into dense discrete droplets, known as a 'percolation to cluster' transition.

Comparison with recent statistical mechanical theory and Ising-like simulation would suggest that the non-equilibrium behaviour is induced by the presence of a metastable gas-liquid boundary. These studies predict quantitatively similar regions of nucleation-like and spinodal-like behaviour to those observed in experiment. One also expects to find frozen percolated states as one goes far from the binodal, consistent with the gel state observed here. Ising-like simulation suggests that the gel state would only span the system for a finite time before breaking up into discrete clusters, consistent with the observed collapse of the gel.

Chapter 2

Phase Behaviour

'The mixture, which was at first of a reddish hue, began, in proportion as the crystals melted, to brighten in colour, to effervesce audibly, and to throw off small fumes of vapour. Suddenly, and at the same moment, the ebullition ceased, and the compound changed to a dark purple, which faded again more slowly to a watery green. My visitor, who had watched these metamorphoses with a keen eye, smiled, set down the glass upon the table and then turned and looked upon me with an air of scrutiny.'

\- **The strange case of Dr. Jekyll and Mr Hyde**, Robert Louis Stevenson (1886).

2.1 Introduction

In this chapter I discuss systems which phase separate, and in particular the phase behaviour of colloid-polymer mixtures. A phase is a homogeneous part of a system with well defined boundaries, across which the overall properties change discontinuously. In equilibrium the phases can either consist of gaseous, liquid or different crystalline forms of matter. Non-equilibrium (metastable) states can also occur such as glasses or gels.

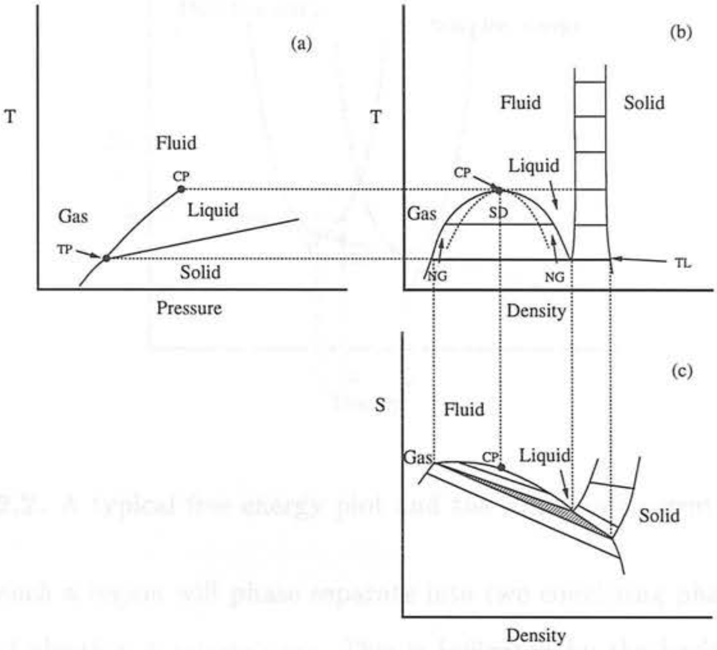

Figure 2.1. Atomic phase behaviour in three different representations.

2.2 Atomic phase behaviour

Figure 2.1 shows a schematic representation of the phase diagram of a simple atomic system, such as argon, in three different representations (after [34]).

As shown the topology of the phase diagram is highly dependent upon the variables used. These can be split into two classes, a *field* variable (one which is the same in all the phases present) or a *density* variable (one which need not have the same value in each of the phases). The first diagram, in the pressure-temperature representation, is a typical field-field phase diagram in which one finds single phase areas and lines along which one finds coexisting phases. These lines meet at the well known triple point (TP) of coexisting gas, liquid and solid. There is also a critical point (CP) beyond which one can no longer distinguish between a liquid and a gas.

The second diagram, in the temperature-density representation, is a typical field-density phase diagram. One now finds coexistence areas, rather than lines, so that a

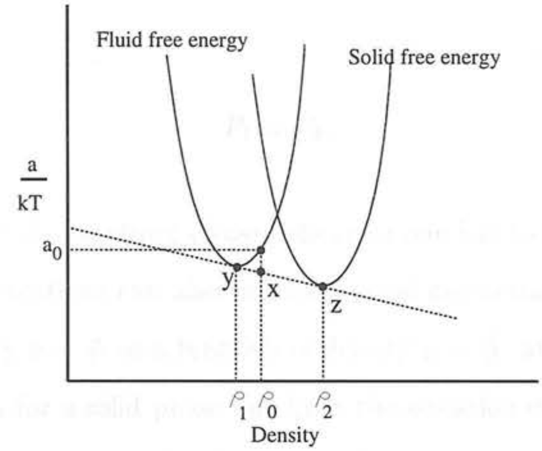

Figure 2.2. A typical free energy plot and the common tangent method.

system within such a region will phase separate into two coexisting phases of different densities, but of identical temperatures. This is indicated by the horizontal tie lines. Accordingly a triple line now emerges, rather than a triple point.

Finally in a specific entropy against density diagram [35], a density-density representation, one finds that the triple line expands to a triple area, so that a system within this region will phase separate into coexisting gas, liquid and solid with properties given by the apexes of the triangle i.e. phases of different specific entropies and densities. In the two-phase regions one now finds tielines which are slanted.

2.2.1 Calculating phase behaviour

When a system phase separates, into say phases 1 and 2, two conditions must be satisfied by the coexisting phases; They must have equal chemical potentials,

$$\mu_1 = \mu_2, \tag{2.1}$$

and equal pressures,

$$P_1 = P_2. \tag{2.2}$$

Therefore to calculate the resulting phase behaviour one has to solve two equations in two unknowns. The solutions can also be constructed geometrically. If one calculates the free energy density $a = \frac{A}{V}$ as a function of density $\rho = \frac{N}{V}$, at a single temperature, firstly for a fluid then for a solid phase one finds the situation depicted in figure 2.2.

If one starts with a state of density ρ_0 and free energy density a_0, one can then ask what the free energy of the whole system would be if it phase separated into states labelled ρ_1 and ρ_2. Through mass conservation,

$$\rho_0 V_0 = \rho_1 V_1 + \rho_2 V_2 \tag{2.3}$$

or equivalently,

$$\frac{\rho_1 - \rho_0}{\rho_1 - \rho_2}(a_1 - a_2) = (1 - \frac{V_1}{V_0})(a_1 - a_2) \tag{2.4}$$

Now consider the resulting free energy of the whole system,

$$aV_0 = a_1 V_1 + a_2 V_2 \tag{2.5}$$

or by rearranging,

$$a_1 - a = (a_1 - a_2)(1 - \frac{V_1}{V_0}) \tag{2.6}$$

Therefore by combining equations (2.4) and (2.6) one finds,

$$a = a_1 + (a_2 - a_1)\frac{\rho_1 - \rho_0}{\rho_1 - \rho_2} \tag{2.7}$$

and the resulting free energy density a is given by the point X in figure 2.2[1]. A system of density $\rho_1 < \rho_0 < \rho_2$ can therefore maximally lower its free energy by phase separating into states ρ_1 and ρ_2.

By constructing a common tangent between the two free energy curves, one can readily obtain the composition of these final phases. Both equations (2.1) and (2.2) are satisfied, as by constructing a common tangent we firstly satisfy equation (2.1),

$$\begin{aligned} \mu &= \left[\frac{\partial A}{\partial N}\right]_{V_0} && (2.8)\\ &= V\left[\frac{\partial a}{\partial N}\right]_{V_0} + a\left[\frac{\partial V}{\partial N}\right]_{V_0} && (2.9)\\ &= \left[\frac{\partial a}{\partial \rho}\right]_{V_0} && (2.10) \end{aligned}$$

i.e. equal slopes are equivalent to equal chemical potentials, and secondly we also satisfy equation (2.2) as,

$$-P = \left[\frac{\partial A}{\partial V}\right]_N \tag{2.11}$$

---

[1] Equation (2.7) simply implies equal slopes from point Y to X, and Y to Z

$$= \quad a + V\left[\frac{\partial a}{\partial V}\right]_N \tag{2.12}$$

$$= \quad a + V\left[\frac{\partial a}{\partial \rho}\right]_N\left[\frac{\partial \rho}{\partial V}\right]_N \tag{2.13}$$

$$= \quad a - V\frac{N}{V^2}\left[\frac{\partial a}{\partial \rho}\right]_N \tag{2.14}$$

$$= \quad a - \rho\left[\frac{\partial a}{\partial \rho}\right]_N \tag{2.15}$$

i.e. equal intercepts are equivalent to equal pressures. Therefore by repeating this process for a number of different temperatures one can calculate the full phase behaviour.

Free energy plots can also be used to infer whether a particular homogeneous state in a coexistence region will be metastable or unstable i.e. whether the system is stable or unstable to small scale density fluctuations. Figure 2.3(a) shows a free energy density with a characteristic double minimum. Consider a homogeneous state of density ρ_0 and free energy density a_0. This state can maximally lower its free energy by decomposing into two states labeled ρ_g and ρ_l, given by the common tangent method. Around ρ_0 any small fluctuations in composition will lead to an increase in the systems free energy (c.f. figure 2.2) and the metastable state will be stable to any small density fluctuations i.e. the system must overcome a free energy barrier to phase separate.

Consider now a second state of density ρ_1 and free energy density a_1 which is within the region of negative curvature (figure 2.3(b)). Now any small density fluctuations act to decrease the overall free energy of the system (c.f. figure 2.2) and as such the system can be described as unstable. Consequently any small density fluctuations will grow spontaneously. The locus of points where the second derivative of the free energy density is negative, and which defines the region of unstable states, is known as the 'Spinodal' [36].

Also indicated in the atomic phase diagram, figure 2.1(b) the field-density representation, are two regions within the gas liquid region which define regions where the metastable fluid is either stable or unstable to small density fluctuations. These

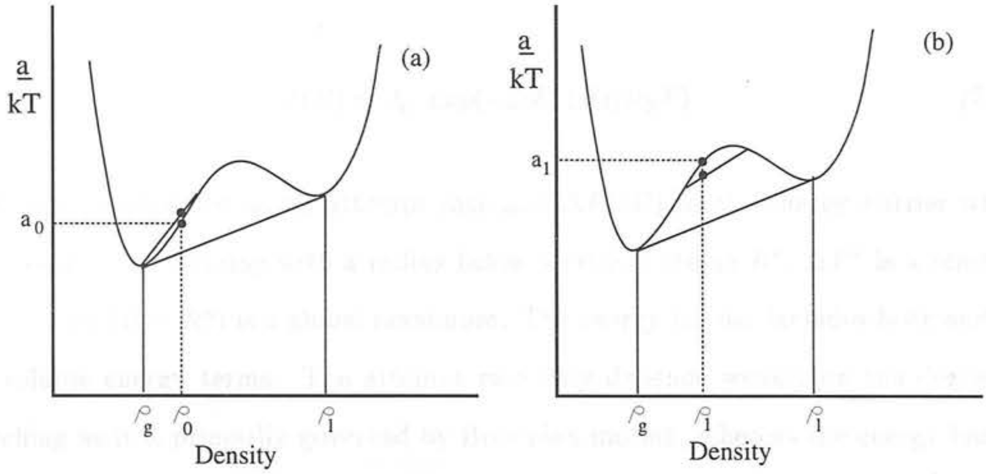

Figure 2.3. Stable and unstable states.

regions define different mechanisms toward phase separation. When a system phase separates, it does so by either *nucleation and growth* or *spinodal decomposition*, the regions indicated by NG and SD respectively.

2.2.2 Nucleation and growth

When a system is quenched into a thermodynamically metastable state, the system will phase separate by *nucleation and growth.* Nucleation is a process which is associated with metastability and the presence of an energy barrier which must be overcome before a droplet of the new phase can develop. In *homogeneous* nucleation a local thermal fluctuation which produces droplets that exceed a critical size continue to grow, whereas droplets smaller than this do not develop as the cost in surface energy is too great. The growth of a droplet is inhibited by the cost in surface energy yet is compensated by a gain in volume energy. It is the conflict between these two terms which drives the system to nucleate.

In the simplest form of nucleation theory [37], [38], the nucleation rate J at which droplets form (per unit time) is given by the Arrhenius formula,

$$J(R) = J_0 \ exp(-\Delta F^*(R)/k_B T) \tag{2.16}$$

J_0 can be regarded as an attempt rate and $\Delta F^*(R)$ as the energy barrier which prevents droplets forming with a radius below a critical radius R^*. ΔF^* is a function of R and $\Delta F(R = R^*)$ is a global maximum. The energy barrier includes both surface and volume energy terms. The attempt rate only depends weakly on the degree of quenching as it is primarily governed by Brownian motion, whereas the energy barrier is highly sensitive to the quench depth. Consequently the nucleation rate is extremely dependent upon the region of the phase diagram examined.

2.2.3 Spinodal decomposition

In contrast to phase separation by nucleation, one can quench a system into a thermodynamically unstable state which phase separates by a mechanism known as *spinodal decomposition* (SD). SD is said to occur when $\Delta F^* = 0$ i.e when there is no barrier to nucleation. As such the system can be regarded as unstable as any small fluctuations will initially grow unhindered. One can regard the growth of small fluctuations as the system having a negative diffusion coefficient. i.e. particles will tend to diffuse *against* concentration gradients.

The original linear (Cahn) theory of SD [36] depends on the concentration fluctuations following a simple diffusion equation,

$$\frac{\partial c(\mathbf{r},t)}{\partial t} = D\nabla^2 c(\mathbf{r},t) \tag{2.17}$$

One must also assume a phenomenological behaviour to the particle flux $\mathbf{J}(\mathbf{r},t)$, expressed in terms of a chemical potential gradient $\vec{\nabla}\mu(c(\mathbf{r},t))$ which drives the system to phase separate. The particle flux must be an odd function, so that it reverses its direction upon reversal of the coordinate system, and therefore to lowest order one can assume,

$$\mathbf{J} = -M\vec{\nabla}\mu(c(\mathbf{r},t)) \tag{2.18}$$

M represents a transport coefficient or mobility. For a homogeneous system one can assume a Landau form for the free energy. To take into account inhomogeneities one can then introduce a phenomenological second term so that the chemical potential can be written,

$$\begin{aligned}
\mu &= \frac{\partial F}{\partial c} && (2.19)\\
&= \frac{\partial}{\partial c}(f_l - \frac{1}{2}K(\nabla c)^2) && (2.20)\\
&= \frac{\partial f_l}{\partial c} - K\nabla^2 c && (2.21)
\end{aligned}$$

where f_l is the homogeneous free energy density in a polynomial (Landau) form and K is known as the gradient energy coefficient. The second term essentially takes into account the effect of inhomogeneities, its form arising as the free energy must be symmetrical under a reversal of the coordinate system and $(\nabla c)^2$ is the first non-trivial term of this kind.

Assuming the continuity equation (i.e. conservation of mass),

$$\frac{\partial c}{\partial t} = -\vec{\nabla}.\mathbf{J} \tag{2.22}$$

one can then use this set of equations to derive the temporal behaviour of concentration fluctuations.

$$\begin{aligned}
\frac{\partial c}{\partial t} &= -\vec{\nabla}.(-M\vec{\nabla}\mu) && (2.23)\\
&= M\vec{\nabla}.(\vec{\nabla}(\frac{\partial f_l}{\partial c} - K(\nabla^2 c))) && (2.24)\\
&= M\vec{\nabla}.(\frac{\partial^2 f_l}{\partial c^2}\vec{\nabla}c - K\vec{\nabla}(\nabla^2 c)) && (2.25)\\
&= (\frac{\partial^2 f_l}{\partial c^2} - K\nabla^2)M(\nabla^2 c) && (2.26)
\end{aligned}$$

Equation (2.24) assumes that the transport coefficient M is concentration independent. One can now define a new variable $u(\mathbf{r},t)$ which simply represents fluctuations about some mean concentration c_0 i.e.,

$$c(\mathbf{r},t) = c_0 + u(\mathbf{r},t) \qquad (2.27)$$

This linear approximation renders equation (2.26) soluble by taking the Fourier transform,

$$\begin{aligned}
\frac{\partial \hat{u}}{\partial t} &= (\frac{\partial^2 f_l}{\partial c_0^2} + KQ^2)(-MQ^2)\hat{u} && (2.28)\\
&= \omega(Q)Q^2\hat{u} && (2.29)
\end{aligned}$$

where,

$$\omega(Q) = -M(\frac{\partial^2 f_l}{\partial c_0^2} + KQ^2) \qquad (2.30)$$

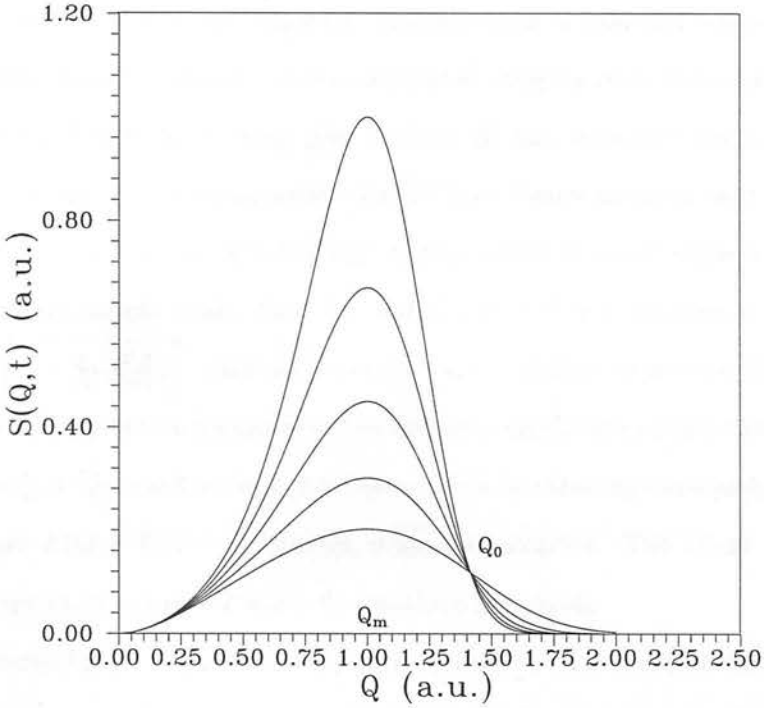

Figure 2.4. Time evolution of the static structure factor from linear Cahn theory.

and the solution to equation (2.29) is,

$$\hat{u}(\mathbf{Q}, t) = \hat{u}(\mathbf{Q}, t = 0) \ \ exp(\omega(Q)Q^2 t) \tag{2.31}$$

$\hat{u}$ represents the Fourier transform of u,

$$\hat{u}(\mathbf{Q}, t) = \int (c(\mathbf{r}, t) - c_0) e^{i\mathbf{Q}.\mathbf{r}} d^3 r \tag{2.32}$$

and Q the scattering wavevector. Consider the case where $KQ^2 << \frac{\partial^2 f_l}{\partial c_0^2}$. If an initial state has a concentration c_0 such that $\frac{\partial^2 f_l}{\partial c_0^2} > 0$ then the amplitude of any fluctuation will decrease over time as $\omega(Q) < 0$. Such a system is said to be stable. If

$\frac{\partial^2 f_l}{\partial c_0^2} < 0$ then density fluctuations become unstable as $\omega(Q) > 0$ i.e. the macroscopic diffusion coefficient becomes negative, and one finds a spinodal region, when $\frac{\partial^2 f_l}{\partial c_0^2} < 0$. Accordingly spinodal regions can be calculated directly from free energy diagrams.

In terms of light scattering (see chapter 3) the structure factor can be written $S(Q,t) = \langle|\hat{u}(\mathbf{Q},t)|^2\rangle$. Consequently linear Cahn theory predicts that a stationary ring of scattered radiation (i.e. at a fixed Q) will be found at small angles i.e. corresponding to a dominant length scale, that for which $\omega(Q)Q^2$ is a maximum i.e. $Q = Q_m = \left[\frac{Q_0}{\sqrt{2}}\right] = \left[\sqrt{-\frac{1}{2K}(\frac{\partial^2 f_l}{\partial c_0^2})}\right]$ with an intensity which grows exponentially in time (as in figure 2.4). $\omega(Q)$ can be regarded as the diffusion coefficient of this characteristic length scale. For $Q > Q_0$ small wavelength fluctuations become exponentially suppressed, and at all times $S(Q = 0, t) = 0$ through mass conservation. The linear approach applies only to very early stage SD when fluctuations are small.

Experimentally a non-stationary ring is seen in spinodally decomposing systems, which moves to smaller angles as the intensity grows algebraically. The disparity arises as non-linear terms have been excluded from the above treatment. Also omitted is a spontaneous thermal fluctuation term (which is entirely responsible for nucleation) and a contribution from the effect of fluid flow. Advances have been made though in non-linear theories, especially that of Langer, Bar-on and Miller (LBM) [39] although many others have proved unsatisfactory. The LBM model predicts a ring which decreases in radius over time, yet this model can still only describe early stage SD as it assumes the growth of a single characteristic length scale. In late stage there will exist at least two length scales, the correlation length and the typical cluster or domain size [40]. Despite the limitations of linear Cahn theory a stationary, exponentially growing ring has been observed in the very early stages of spinodal decomposition in a number of systems [41].

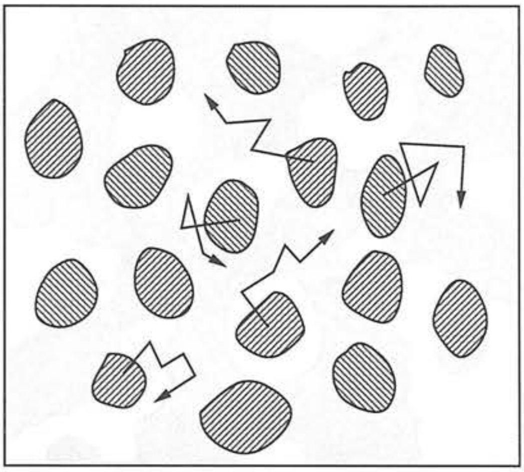

Figure 2.5. Early stage spinodal decomposition.

2.2.4 Spinodal decomposition in fluids

Cluster formation in fluids is speeded up by diffusion, when compared with cluster growth in solids. Assuming a system to be deeply quenched, so that the resulting structure has a cluster size L roughly equal to the intercluster spacing (see figure 2.5) (an approximation which is valid for short time scales) one can write,

$$t_L \sim \frac{L^2}{D} \tag{2.33}$$

where t_L is roughly the time taken for a cluster to diffuse its own diameter. Assuming a Stoke's law type diffusion $D \sim \frac{1}{L}$ one expects the cluster size to grow as,

$$L \sim t^{\frac{1}{3}} \tag{2.34}$$

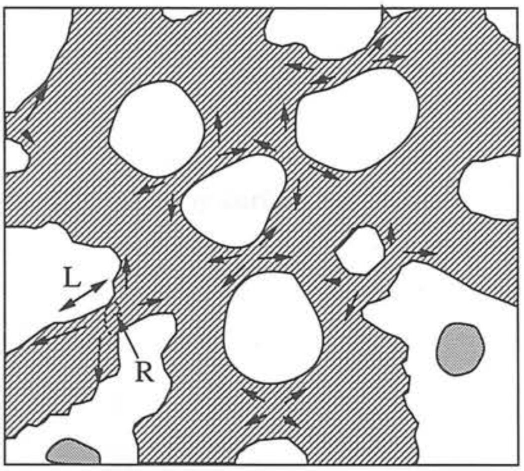

Figure 2.6. Late stage spinodal decomposition.

It is somewhat surprising that such a simple argument has been verified by several experiments [42] and simulation [43], [44]. The above derivation is similar to that of Binder and Stauffer [45], and is also consistent with the evaporation-condensation mechanism proposed by Lifshitz and Sloyozov [46]. Further progress is possible if one accounts for flow-induced coupling between fluctuations (i.e. hydrodynamics) which will not be discussed here further (see for instance the work of Kawasaki and Ohta [47]).

In the late stages of SD in fluids one expects surface tension to play a role [48]. Within a well defined, percolating structure there will exist regions of fluctuating density (see figure 2.6). As the system tries to reduce its interfacial free energy the structure will become pinched at weak points which squeezes fluid along the structure. Such a system can be modelled as tubular regions of space (of radius R) with fluctuations which are assumed to have a wavelength L ($L > R$). This process can be modelled as Poiseuille flow, of velocity v, along a tube,

$$v = \frac{\Delta p}{4\eta L} R^2 \tag{2.35}$$

with a pressure gradient induced by surface tension σ,

$$\frac{\sigma}{R} \sim \Delta p \tag{2.36}$$

One can approximate a spinodally decomposing system to have only a single characteristic length scale L, (not valid for very late stage SD) and one finds,

$$L \sim \frac{\sigma}{\eta} t \tag{2.37}$$

Therefore in fluid systems undergoing spinodal decomposition one expects to see a cross-over from an initial growth rate $L \sim t^{\frac{1}{3}}$ to a late stage growth $L \sim t^1$, which has been observed frequently [49], [50].

2.3 The colloid-atom analogy

So far I have only considered the phase behaviour and phase separation kinetics of atomic systems. In this section I discuss the similarities and differences between colloidal and atomic systems and argue that under appropriate conditions, these are analogous and in particular that the ideas presented in the previous section are applicable to colloidal systems.

In any theoretical calculation of the phase behaviour of colloidal systems one regards the liquid suspension as a continuum with well defined properties. Within this framework one can then define a potential of mean force, which represents the total interaction energy between all the colloidal particles [51]. The potential of mean force is usually approximated as a sum of pair potentials, which represent a well defined particle interaction. Then the thermodynamic properties of a suspension of colloidal particles is identical to an ensemble of atoms with an inter-atomic potential of the same form. Using well established, 'text-book', statistical mechanics, originally devised for simple atomic systems, one can then obtain properties directly from details of the interparticle potential, such as the equation of state or macroscopic phase behaviour. For an excellent discussion of the 'course grained' approach to the statistical mechanics of colloidal suspensions see van Megen and Snook [52].

An appealing attribute of colloidal suspensions is the ability to manipulate the particle interaction. For example it has been predicted that the interparticle potential range greatly affects the topology of the phase diagram. An interesting property of the colloid-polymer system is that adjusting the polymer molecular weight, and subsequently its radius of gyration, determines the depletion potential range. A model colloid-polymer mixture is therefore ideal for testing theoretical predictions which are impossible to examine in atomic systems. Colloidal interparticle potentials also tend to be short ranged and often highly attractive e.g. the secondary minimum in the DLVO potential or a depletion induced attraction. Apparently a sufficiently attractive, short ranged potential, in the right conditions, can lead to the formation of metastable, non-equilibrium interconnected structures such as gels. Aggregated states have not been seen in atomic systems as the inter-atomic potential tends to be shallow and long ranged.

One significant difference between atomic and colloidal systems is that the dynamics of colloidal suspensions and atoms are fundamentally different. Atoms move ballistically, governed by Newton's laws, whereas colloidal suspensions diffuse under Brownian motion. Atoms can therefore be modelled using Liouville's equation whereas colloidal suspensions are governed by the Smoluchowski equation [53]. As the colloidal particles are suspended in a fluid continuum they experience the effect of hydrodynamics which couples particle motion. Colloidal particles are also approximately 5000 times greater in size and a typical colloidal particle will take approximately one tenth second to diffuse a distance comparable to its own diameter, whereas a typical atom takes only one pico second. Therefore once quenched into an unstable state, a typical atomic system can crystallise in pico seconds whereas colloidal suspensions take minutes to hours to phase separate. As the thermodynamics of collections of colloids and collections of atoms are equivalent one could well conjecture that these systems would show similar phase kinetics. Evidence for this is emerging, such as the observation of spinodal type rings in colloidal systems quenched into unstable states [54] - [56], and such behaviour will be examined in detail here. As a consequence 'model' colloidal suspensions are ideal in determining the kinetics of phase transitions, as the short time scales associated with atomic phase separation are experimentally inaccessible.

2.4 Colloidal phase behaviour

2.4.1 Hard-sphere colloids

The phase behaviour of hard-sphere like suspensions has been studied extensively in experiment, simulation and theory [34], [53]. The hard sphere 'phase diagram'[2] is shown in figure 2.7. As the suspension is purely of a hard-sphere-like nature temperature has no effect on the resulting phase behaviour. If one considers the Helmholtz free energy of hard spheres then the temperature can be factored out, which leads to phase boundaries parallel to the temperature axis [34]. Conventionally the phase behaviour is expressed in terms of the colloid volume fraction ϕ, which is defined as,

$$\phi = \frac{N_C \frac{4}{3}\pi a^3}{V} \tag{2.38}$$

---

[2] As the percentage of crystal is not a thermodynamic variable, one cannot call this a true phase diagram.

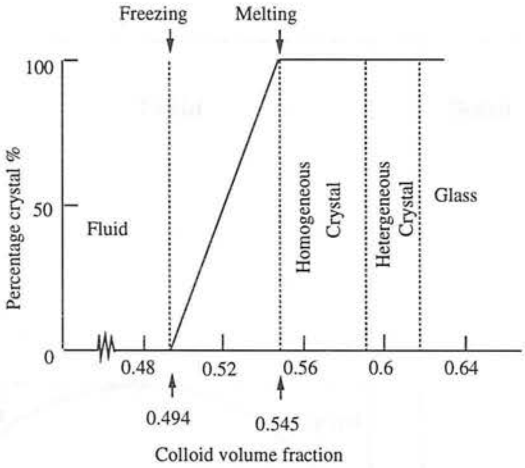

Figure 2.7. Hard sphere 'phase diagram'.

where N_C is the total number of particles, V the total volume of the sample and a the colloid radius.

For low volume fractions of spheres ($\phi < 0.494$) colloidal fluid states are formed exhibiting short range order, but long range disorder. As the volume fraction is increased phase separation into colloid rich and colloid poor phases is observed ($0.494 < \phi < 0.545$), the colloid rich phase possessing long range crystalline order. At still higher concentrations ($0.545 < \phi \lesssim 0.58$) fully crystalline states are observed, whereas for the highest volume fractions ($\phi \gtrsim 0.58$) amorphous, metastable states (colloidal glasses) are observed.

2.4.2 Colloid-polymer mixtures

A strong interparticle attraction is known to cause otherwise stable suspensions to phase separate. Figure 2.8 shows the phase diagram of a colloid-polymer mixture for a large polymer to colloid size ratio, $\xi = 0.5$, in the $\mu_p - \phi$ representation. μ_p is the chemical potential of the polymer solution in the mixture and is simply proportional to the depletion potential depth. Therefore the phase diagram is in a field-density

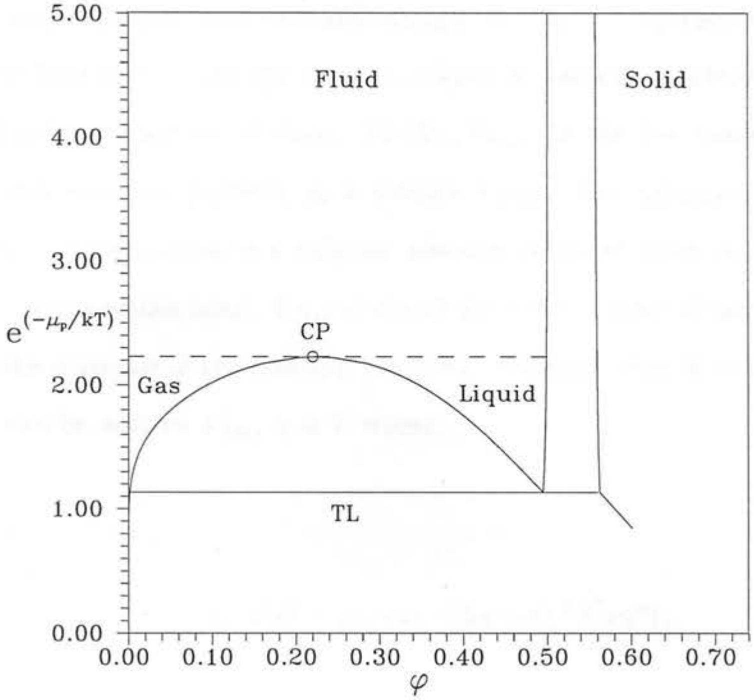

Figure 2.8. Colloid-polymer phase diagram for $\xi > 0.33$, calculated using a code written by P.B. Warren. The dashed line defines the gas and liquid regions.

representation. The size ratio $\xi = \frac{\delta}{a}$ where δ is the polymer radius of gyration. Note that the similarity to an atomic system is striking (c.f. figure 2.1(b)). One would expect to find similar regions of nucleation and spinodal decomposition, within the gas-liquid coexistence region, to that of the atomic phase diagram.

To predict the phase behaviour of colloid-polymer mixtures one can adopt a mean-field approach. The above phase behaviour was calculated using the recent theory of Lekkerkerker et al. [57], and relies on a decoupling of the system's free energy into a sum of two terms,

$$F = F_C(N_C, V) + F_P(N_P, V_{free}) \tag{2.39}$$

As colloidal suspensions are, to a good approximation, constant volume systems [58] F is accordingly a Helmholtz free energy. $F_C(N_C, V)$ represents the free energy of a colloidal fluid of N_C hard spheres in a volume V and can be obtained by integrating the hard sphere equation of state. $F_P(N_P, V_{free})$ is the free energy of an ideal gas of N_P point polymer particles in a volume V_{free}. The assumption of ideality is a reasonable approximation to a polymer solution at the Θ point (i.e. when the second virial coefficient equals zero). V_{free} is simply the total volume of the system taking into account the presence of the colloidal particles. Through work in scaled particle theory [59] this can be written $V_{free} = \alpha\, V$ where,

$$\alpha = (1-\phi)exp(-(A\gamma + b\gamma^2 + c\gamma^3)) \tag{2.40}$$

$\gamma = \frac{\phi}{(1-\phi)}$, $A = 3\xi + 3\xi^2 + \xi^3$, $B = \frac{9}{2}\xi^2 + 3\xi^3$ and $C = 3\xi^3$. The colloid-polymer interaction is contained solely in the dependence of α on ϕ. Such hard sphere colloid-colloid, ideal polymer-polymer and effectively hard sphere colloid-polymer interactions is known as a 'non-additive' hard sphere model. Accordingly the osmotic pressure of the polymer solution of N_P particles is that of an ideal gas confined to a volume $\alpha\, V$,

$$\Pi_p = n_p^* k_B T \neq n_p k_B T, \tag{2.41}$$

where $n_p = \frac{N_P}{V}$ is the number density of polymer coils in the total volume and n_p^* the number density in the free volume $n_p^* = \frac{N_P}{V_{free}}$. n_p^* can also be regarded as the polymer concentration in an infinite reservoir of polymer coils in osmotic equilibrium with the sample [59]. Consequently the polymer chemical potential can be expressed, by direct integration of the polymer free energy, in terms of the reservoir polymer concentration,

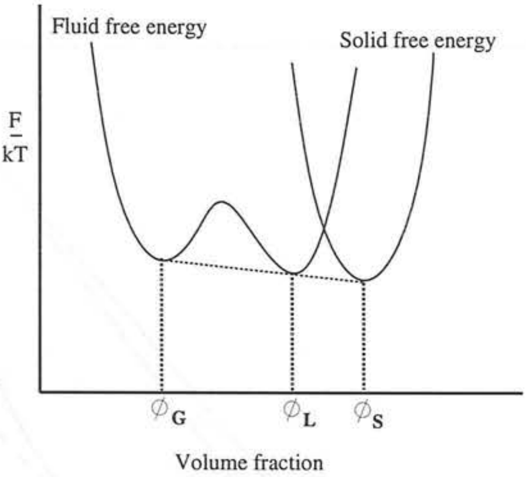

Figure 2.9. A free energy profile for $\xi > 0.33$ at a fixed μ_p, which leads to three phase coexistence.

$$\frac{\mu_p}{k_B T} = log(n_p^* \lambda_p^3) + const. \tag{2.42}$$

where λ_p is the de Broglie (thermal) wavelength of the polymer [57]. As a colloid-polymer mixture will phase separate into two phases with equal μ_p then these phases will also have equal n_p^*.

One can then obtain the phase behaviour of colloid-polymer mixtures directly from the total free energy of the system F, now taken as a function of μ_p (or n_p^*), $F = F(\phi, \mu_p)$. Calculation of a colloidal fluid free energy and that of a colloidal FCC crystal both perturbed by the presence of the polymer can lead to the situation depicted in figure 2.9. Using μ_p as a parameter and equating the colloid chemical potentials and pressures (in the presence of polymer) one can readily calculate the volume fractions of colloid that the system will phase separate into, both of which will have polymer chemical potential μ_p (or n_p^*). As discussed one can use the common tangent method to obtain the equilibrium phase volume fractions (see figure 2.9). Once this process is

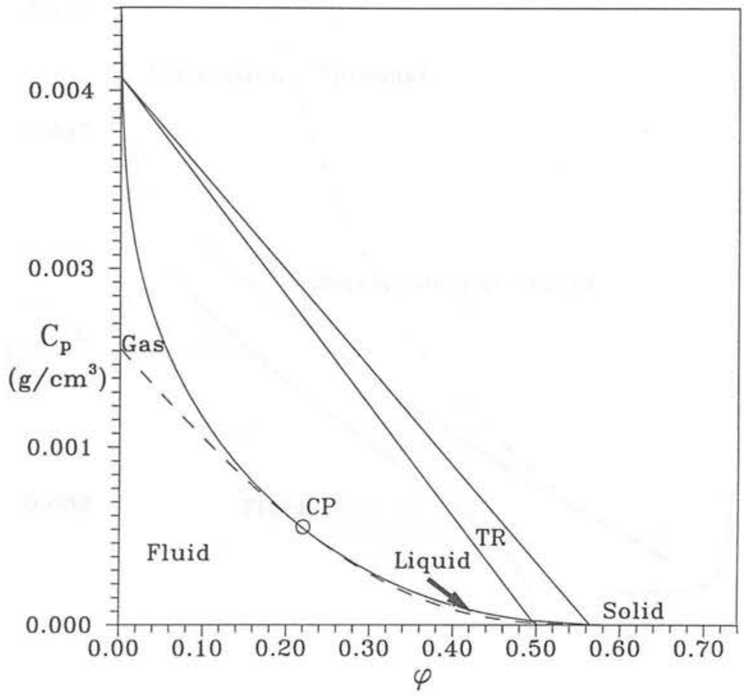

Figure 2.10. Colloid-polymer phase diagram for $\xi > 0.33$ in the C_p representation, calculated using a code written by P.B. Warren. TR ≡ triple region, CP ≡ crtical point and the dashed line defines the gas and liquid regions.

repeated for successive values of μ_p, one can build up a complete phase diagram.

The representation of the colloid-polymer phase behaviour in figure 2.8 is somewhat unusual, certainly to an experimentalist, and the conventional representation is shown in figure 2.10. The coordinate axes in this representation are C_p, the concentration of polymer in the whole system and ϕ the colloid volume fraction. C_p is simply

$$C_p = \alpha \left(\frac{M_w}{N_A}\right) n_p^* = \alpha \left(\frac{M_w}{N_A}\right) exp\left(\frac{\mu_p}{k_B T}\right) \tag{2.43}$$

where M_w is the polymer molecular weight and N_A Avagadro's constant. As shown one finds a segregation (or partition) of polymer in the coexisting phases. Most strikingly the triple line in figure 2.8 expands to a triple region in the C_p representation

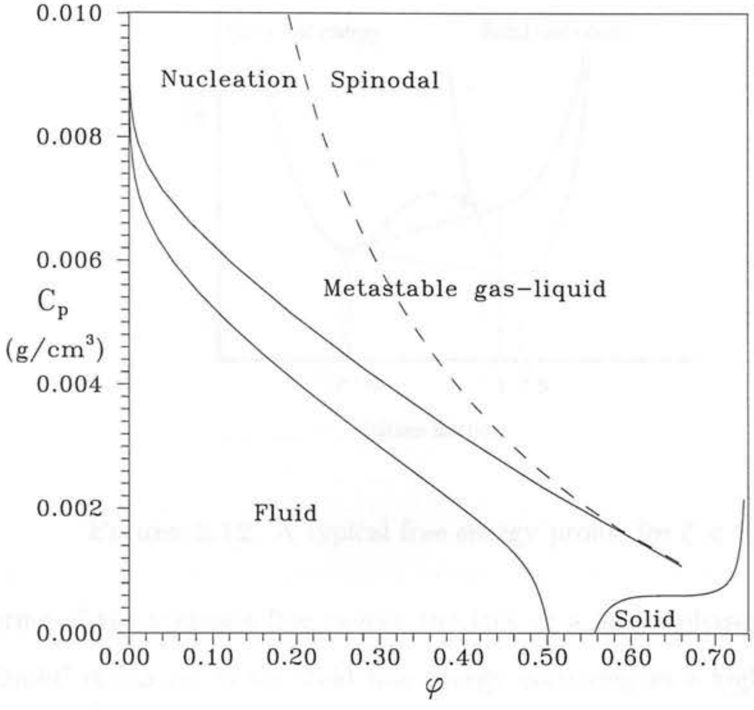

Figure 2.11. Colloid-polymer phase behaviour, $\xi < 0.33$, calculated using a code written by P.B. Warren.

(i.e. a sample within the triple region will phase separate into coexisting colloidal gas, liquid and crystal phases, of composition given by the apexes of the three phase triangle). Note that in the absence of polymer, $C_p = 0$, one regains the hard sphere phase behaviour of figure 2.7.

2.4.3 The interparticle potential range

The phase behaviour of colloid-polymer mixtures is found to be strongly dependent upon the size ratio ξ, and accordingly the depletion potential range. For small size ratios one no longer finds a liquid phase, as shown in figure 2.11 in the C_p representation. Through much theoretical and experimental effort it has been shown that the interparticle potential range must be $\gtrsim \frac{1}{3}$ that of the particle radius to obtain a liquid phase [17], [21], [57], [60] - [62].

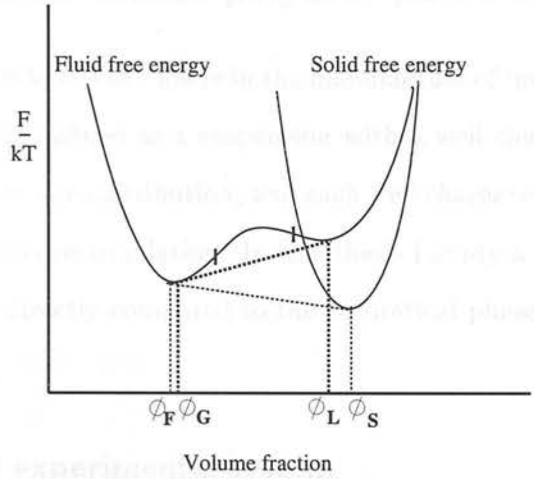

Figure 2.12. A typical free energy profile for $\xi < 0.33$.

In terms of the system's free energy the lack of a liquid phase can be attributed to the 'liquid' minimum in the fluid free energy occurring at a higher value than the minimum in the solid free energy, found at high polymer concentrations. This behaviour is depicted in figure 2.12. Therefore the only stable states one finds are fluid, crystal and fluid-crystal coexistence. Construction of a common tangent about the double minimum in the fluid branch of the free energy gives a metastable gas-liquid binodal in figure 2.11. One can also construct the mean field spinodal from the region within the double minimum where $\frac{\partial^2 f}{\partial \phi^2} < 0$ i.e. the region of negative curvature.

For even smaller size ratios $\xi < 0.05$ one finds a double minimum in the solid free energy [60] and hence the possibility of a solid-solid phase transition [63]. This interesting possibility is outwith the scope of this work and will not be discussed further (See Tejero et al. [60], [64] for discussions on the interplay between potential range and subsequent phase behaviour).

2.5 Experimental colloid-polymer phase behaviour

Recently huge advances have been made in the manufacture of 'model' colloidal systems [53]. A model system is defined as a suspension with a well characterised interaction, composition and narrow size distribution, and such well characterised systems facilitate any comparison to theory or simulation. In this thesis I study a model colloid-polymer mixture which can be directly compared to the theoretical phase predictions of section 2.4.

2.5.1 The model experimental system

The model system which is investigated here, consists of sterically stabilised polymethylmethacrylate (PMMA) spheres of average radius $a \sim 238nm$ and polydispersity $\sigma \sim 0.05$, where σ is defined as the standard deviation of the particle size distribution, divided by its mean. This model system has been shown to approximate the behaviour of hard spheres in the absence of free polymer [65]. The non-adsorbing polymer used was random coil polystyrene of molecular weight $M_w = 370,000$ ($\frac{M_w}{M_n} = 1.04$) and radius of gyration $\delta \sim 17nm$. Therefore the polymer to colloid size ratio $\xi \sim 0.071$, and as a consequence three phase coexistence was never observed in this set of experiments, yet the size ratio is large enough to avoid the possibility of a solid-solid phase transition. The colloidal particles and polymer are dispersed in either pure cis-decalin or in a mixture of cis-decalin and tetralin, which are both known to be good solvents for polystyrene [66]. For light scattering experiments the tetralin to cis-decalin volume ratio is adjusted to approximately 0.30, so that the mixed solvent refractive index approximately matches that of the colloidal particles ($n_p \sim 1.50$). Subsequently in any light scattering study the probability of scattering will be small and the first Born approximation can be assumed. Consequently multiple scattering effects will be negligible.

In either solvent the colloid volume fraction is calculated by assuming the accepted literature densities of PMMA and cis-decalin and then scaling the observed phase behaviour so that it coincides with the hard sphere model at freezing. For samples which contain polymer, concentrated colloid and polymer solutions of known concentrations were mixed and then diluted to the required overall concentration. All subsequent phase behaviour was then determined by visual observation.

2.5.2 Phase behaviour

For the case where the background solvent is cis-decalin the phase behaviour has been studied extensively [16], [17], [21]. Indeed one finds a size ratio dependence consistent with that described in sections 2.3 and 2.4, although a quantitative agreement is lacking. For the case studied here $\xi \sim 0.07$ the resulting phase behaviour is shown in figure 2.13 (c.f. figure 2.11).

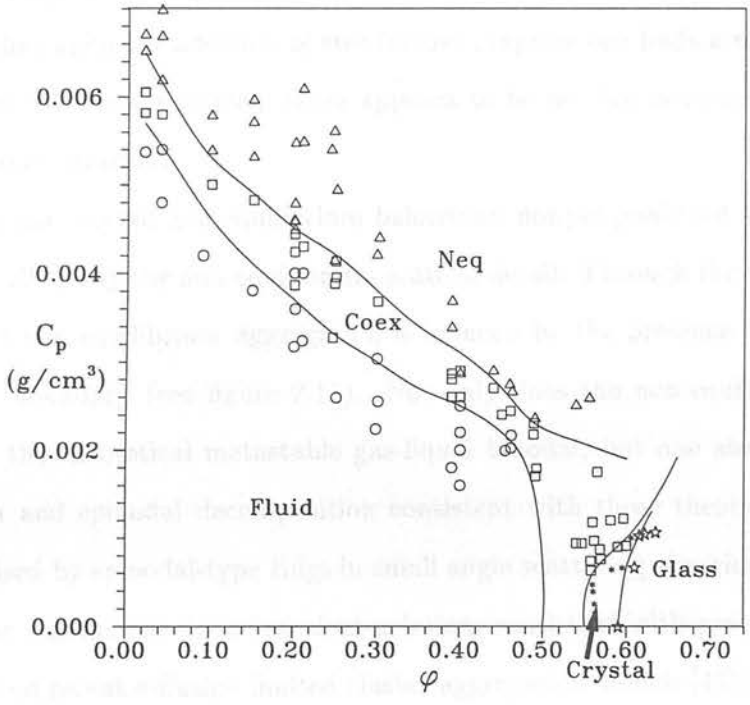

Figure 2.13. Experimental phase behaviour $\xi \sim 0.07$. Coex ≡ fluid-crystal coexistence and Neq ≡ Non-equilibrium region.

In the absence of polymer ($C_p = 0$) one finds good quantitative agreement between the observed colloidal phase behaviour and that of the hard sphere system (figure 2.7), at all volume fractions. Upon the addition of polymer the fluid-crystal coexistence region expands as predicted by theory. If still further polymer is added then crystallisation becomes suppressed as the depletion potential becomes sufficient to cause the colloidal particles to undergo non-equilibrium aggregation, shown by the region 'Neq' in figure 2.13. Visually the aggregated state shows no sign of irridescence, the system sediments over time, indicating a collapse of the structure, and proceeds to form a metastable sediment. The non-equilibrium boundary is found to be reproducible, and as yet there appears to be no evidence of a non-equilibrium region if the depletion potential range is sufficiently large to form a three phase region in the phase diagram. Colloid-polymer non-equilibrium aggregates have been observed frequently in experiment [9] - [18], but have yet to be predicted by theory. Some authors have previously reported that upon the addition of still further polymer one finds a re-stabilised single phase fluid [67]. In our system there appears to be no sign of re-stabilisation at any polymer concentration.

Due to unexpected non-equilibrium behaviour, not yet predicted by current theory, this work will study the non-equilibrium state in detail. Through this study it has been found that non-equilibrium aggregation is induced by the presence of the metastable gas-liquid boundary (see figure 2.11). Not only does the non-equilibrium line coincide with the theoretical metastable gas-liquid binodal, but one also finds regions of nucleation and spinodal decomposition consistent with those theoretically predicted, characterised by spinodal-type rings in small angle scattering experiments [18]. Underlying these regions one finds transient gelation, consistent with previous observations [55], [56] and recent diffusion limited cluster aggregation models [43], [44], which shows the persistence of an arrested structure. The collapse of these states is found to be directly comparable to recent Ising-like simulation of phase separation in systems with a short range potential [68], [69] in which one observes an initial system-spanning structure which disintegrates into discrete clusters. Such a 'percolation to cluster' transition has been observed as the gel structure disintegrates into dense discrete droplets in the absence of gravity.

2.5.3 Temperature dependence

In hard sphere systems temperature has no effect on the overall phase characteristics. Temperature can play a role in colloid-polymer mixtures as the polymer is sensitive to small changes in the ambient temperature.

To examine the effect of temperature, although not the main topic of this thesis, samples were prepared with a colloidal volume fraction $\phi \simeq 0.2$ and polymer concentration so that they spanned the fluid, fluid-crystal coexistence, and non-equilibrium regions at room temperature. After being mixed homogeneously by gentle tumbling the samples were then inserted in a temperature bath which could be controlled to an accuracy of $\pm\ 0.1^oC$. The phase characteristics were then determined by visual observation. A section of the resulting phase diagram is plotted in figure 2.14.

As can be seen, the main effect of increasing the temperature is to decrease the amount of polymer needed to cause fluid-crystal phase separation. This can be attributed to two factors;

- The polymer coils will expand with increasing temperature, leading to an increase in δ and subsequently the range of the depletion potential.
- The polymer solution net osmotic pressure Π_{pol} will increase due to an increased contribution to the second virial coefficient as the temperature diverges from the Θ point (in this system $T_\Theta \simeq 12.5^oC$). The potential depth is proportional to the polymer osmotic pressure and leads to an increased interparticle attraction.

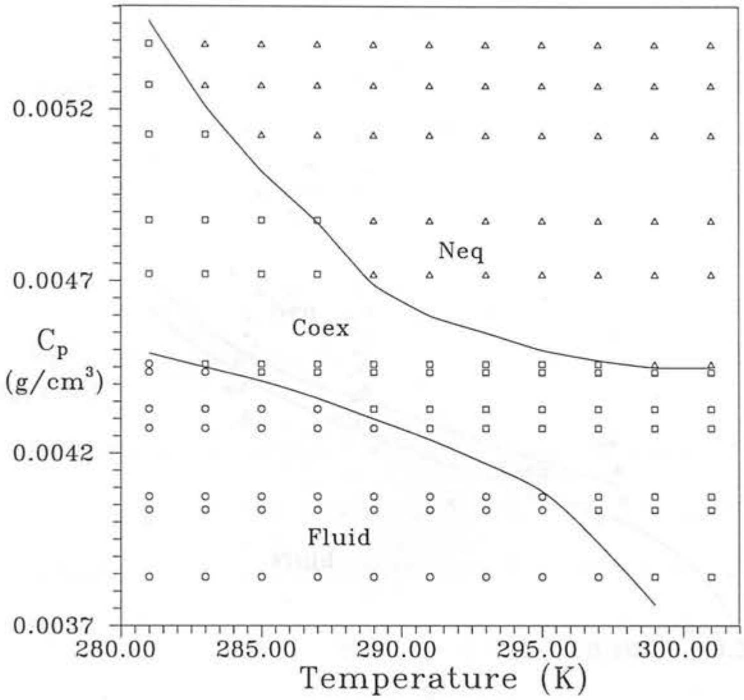

Figure 2.14. Experimental temperature dependent phase behaviour $\xi \sim 0.07$. Coex $\equiv$ fluid-crystal coexistence and Neq $\equiv$ non-equilibrium region.

Indeed non-ideality[3] of the polymer solution must be taken into account if one is to understand such behaviour fully. Recently Warren et al. [70] analysed the effect of a non-ideal polymer solution on a hard sphere colloidal suspension, and find qualitatively similar behaviour. They introduce the non-ideality through a detailed calculation of the second virial coefficient of the polymer solution. Applying a non-ideal approach to the theory of Lekkerkerker et al. [57] they find that upon increasing the temperature, the fluid boundary lowers in a similar fashion to that seen here. Interestingly they find that the metastable gas-liquid phase boundary follows the behaviour of the non-equilibrium boundary yet the absolute magnitude differs by 20%.

---

[3] To describe non-ideal gases one represents the equation of state as power series density expansion $PV = RT(1 + \frac{B_2}{V} + \frac{B_3}{V} + ...)$ where B_2, B_3 are known as the second, third, etc. virial coefficients.

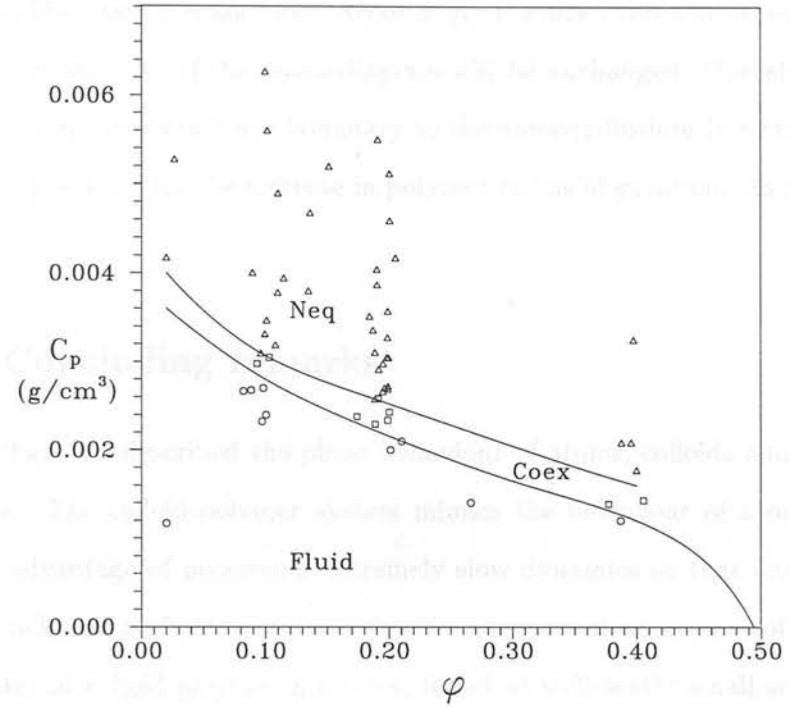

Figure 2.15. The index matched phase diagram. Coex ≡ fluid-crystal coexistence and Neq ≡ non-equilibrium region.

2.5.4 Index matching

To study colloidal suspensions further and in more detail one can utilise the power of light scattering techniques. Sample index matching is essential for any light scattering study as multiple scattering must be suppressed to compare with theoretical predictions. Upon the addition of tetralin, to a colloid-polymer mixture in cis-decalin, the coexistence phase boundary lowers considerably as shown in figure 2.15. This can be attributed to an increase in δ, as tetralin has a lower Θ point than cis-decalin, driving the polymer solution away from ideality. An estimate of the size increase can be obtained by comparing the experimental phase boundaries to the theory of Lekkerkerker et al. [57][4]. The radius increases from approximately 17nm to 23nm, an increase of

---

[4] Comparison cannot be made to the work of Warren et al. [70], as their theory relies on small deviations from ideality.

35%. Such a comparison must only be approximate as the theoretical approach assumes an ideal polymer solution. Accordingly the size ratio will become $\xi \sim 0.09$, but as such the topology of the phase diagram will be unchanged. One also finds that the distance from the coexistence boundary to the non-equilibrium line also decreases, but not in proportion with the increase in polymer radius of gyration. As yet this is poorly understood.

2.6 Concluding remarks

In this chapter I described the phase behaviour of atoms, colloids and colloid-polymer mixtures. The colloid-polymer system mimics the behaviour of atomic systems, yet has the advantage of possessing extremely slow dynamics so that one can readily examine the kinetics of phase separation. The unexpected occurrence of non-equilibrium aggregates in colloid-polymer mixtures, found at sufficiently small size ratios, is now investigated over the next few chapters. The methods used include conventional light scattering, dynamic light scattering, video enhanced microscopy and direct visual observation. Light scattering is an invaluable tool to the experimentalist and the next chapter lays down the theoretical background to such techniques.

Chapter 3

Light Scattering Theory

'In this house I chanced to find a volume of his works. I opened it with apathy; the theory which he attempts to demonstrate, and the wonderful facts which he relates, soon changed this feeling to enthusiasm. A new light seemed to dawn upon my mind; and bounding with joy, I communicated my discovery to my father. My father looked carelessly at the title page of my book, and said, 'Ah! My dear Victor, do not waste your time with this; it is but trash.'

- **Frankenstein**, Mary Shelley (1818).

3.1 Introduction

As discussed, light scattering is widely used to determine the structure and dynamics of colloidal suspensions, and will be used here to study colloid-polymer mixtures. When laser light is incident upon a colloidal particle, the electric field of the light induces an oscillating dipole. This dipole then radiates secondary radiation, and the particle is said to 'scatter' the incident light. The techniques used to monitor this scattered radiation fall into two main categories: those studying the average structural properties (static light scattering) and those studying dynamic properties (dynamic light scattering).

3.1.1 Static Light Scattering - Structure

The simplest form of static light scattering relies on the decoupling of the scattered radiation into two components, one dependent upon the single particle scattering and the other upon the collective, interparticle scattering. These are referred to as the form and structure factors respectively. Thus from two independent measurements of the angular dependence of the total scattered radiation from a concentrated dispersion and from a dilute suspension in identical experimental conditions, the structure factor of the system can be determined. From the scattering wavevector Q ($Q = \frac{4\pi n_p}{\lambda} sin\frac{\theta}{2}$, where θ is the scattering angle, n_p is the particle refractive index and λ the wavelength of the incoming radiation), the length scale probed can be inferred (approximately $\left(\frac{2\pi}{Q}\right)$) and as a consequence static light scattering is used to determine the structure of colloidal suspensions on length scales from single to many particles. Static light scattering is analogous to x-ray and neutron scattering from molecular fluids and has been widely used to determine the equilibrium structure of colloidal suspensions at large wavevectors [53] i.e. the structure of suspensions on the length scale of single to a few particle diameters. Recently however in aggregation and nucleation experiments, where clusters of many tens of particles occur, small angle static light scattering (angle of $0 - 10^o$ usually) has been used to study large scale structure [54] - [56], [71]. Time-resolved measurements at low angles can be used to study the mechanisms by which the particles aggregate and the fractal (or self similar) structure of these systems.

3.1.2 Dynamic Light Scattering - Dynamics

In Dynamic light scattering (DLS) (often referred to as Quasi-elastic light scattering (QELS) or Photon correlation spectroscopy (PCS)) one studies the temporal fluctuations of the scattered radiation to determine dynamic information on different length scales. As the colloidal particles undergo random thermal motion the scattered radiation forms a fluctuating 'speckle' pattern, each speckle representing a single Fourier component of a density fluctuation on the length scale $\left(\frac{2\pi}{Q}\right)$. Through the use of a photon correlator, these fluctuations can be monitored and the time-dependent intensity correlation function can be calculated [72]. In the low density, non-interacting limit, this function decays as a single exponential with a time constant directly related to the diffusion coefficient of the particles. As a consequence this technique is often used to obtain average particle radii, through the use of the Stokes-Einstein diffusion equation. For systems at high concentration, or involving significant interparticle forces, diffusion becomes highly dependent upon interactions, and interpretation of experimental data becomes problematic as the suspension represents a complex many body system. The intermediate scattering function no longer decays as a single exponential and the effective short time diffusion coefficient, that over which the system has hardly changed its configuration, becomes highly Q-dependent [73] analogous to De Gennes narrowing in molecular fluids [74]. Particle motion becomes coupled through hydrodynamic and direct interparticle interactions resulting in a reduction in the diffusion throughout the system.

The well established technique of DLS has been used widely over the years, to study a multitude of systems ranging from such diverse subjects as cataracts in the human eye to synthetic detergent systems [75].

3.2 Assumptions

To extract physical information from the light scattered by colloidal particles, one must first theoretically predict the scattering properties of colloidal suspensions. Although the theory presented here represents the least complex interpretation of the theory of light scattering, certain assumptions must first be made to make this problem soluble. These necessary assumptions are summarised here, alongside the experimental criteria which fulfil them.

- The particles only scatter the incident light weakly i.e. the probability of scattering is small, so that the first Born approximation is valid. As a consequence only singularly scattered light is assumed to reach the detector. Experimentally the Born criterion is met by adjusting the refractive index of the suspension solvent, to approximately that of the colloidal particles. Index matching suppresses multiple scattering, although it leads to problems concerning sample preparation.

- The detector is assumed to be situated in the far field i.e. one assumes Fraunhofer rather than Fresnel diffraction.

- The particles are assumed spherical and identical in size (i.e. monodispersity), composition (i.e. identical refractive index profiles) and interaction (e.g. hard spheres). The identical particle condition is achieved by the adoption of model systems which have a small polydispersity and are of well characterised composition e.g. PMMA spheres are used in this study with a polydispersity $\sigma \sim 0.05$. Suspensions with a small polydispersity such as this can be regarded as a single-size system, yet one must keep in mind that even small polydispersities can prove to yield significant effects in light scattering measurements [53]. The PMMA particles have been sterically stabilised by the addition of a polymer brush to the surface of the colloidal particles. As discussed in the introduction steric stabilisation leads to a hard-sphere like interaction between the colloidal particles.

- A final assumption is that the particulate system is orientationally symmetric.

3.3 The nature of scattered light

Figure 3.1 depicts a typical scattering event, from a spherical colloidal particle. By applying the first Born approximation (i.e. only single scattering) one obtains an expression for the electric field amplitude $dE(\mathbf{r_s})$ scattered from a small volume element

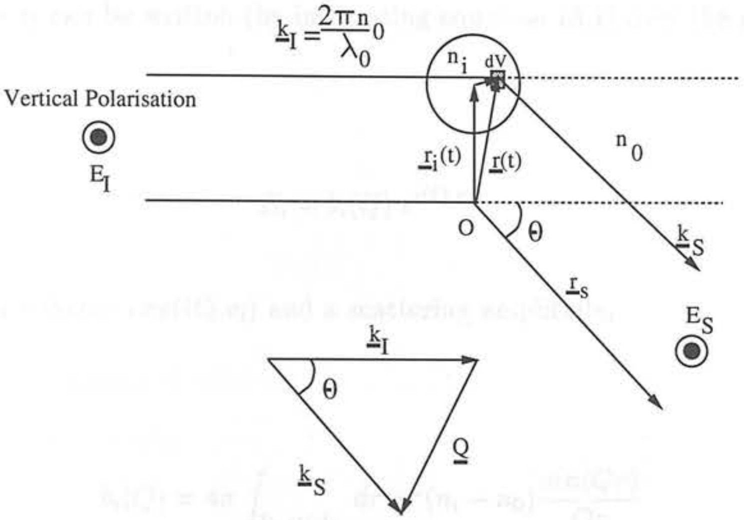

Figure 3.1. The assumed scattering geometry.

dV of refractive index n_i at a position $\mathbf{r}$ from the origin [34],

$$dE(\mathbf{r_s}) \propto E_I \frac{e^{i(\mathbf{k_s}.\mathbf{r_s}-\omega t)}}{r_s} \frac{1}{\lambda^2}(n_i - n_0)e^{i\mathbf{Q}.\mathbf{r}} \; dV \tag{3.1}$$

Here r_s is the distance between the sample and the detector. $\mathbf{Q}$ represents the scattering wavevector and is the difference between the incident wavevector $\mathbf{k_I}$ and the final wavevector $\mathbf{k_S}$,

$$|\mathbf{Q}| \equiv \frac{4\pi n_i}{\lambda_0} sin\left(\frac{\theta}{2}\right) \tag{3.2}$$

and n_i and n_0 are the refractive indices of the particle and background fluid respectively. λ_0, E_0 and ω are the wavelength, amplitude and angular frequency of the incident radiation and θ the scattering angle.

Therefore the angularly dependent electric field scattered from a particle i, with a centre of mass $\mathbf{r_i}$ can be written (by integrating equation (3.1) over the particle),

$$E_i = b_i(Q)\ e^{i(\mathbf{Q}.\mathbf{r_i})} \tag{3.3}$$

with a phase factor $exp(i\mathbf{Q}.\mathbf{r_i})$ and a scattering amplitude,

$$b_i(Q) = 4\pi \int_{Particle_i} dr\ \ r^2(n_i - n_0)\frac{sin(Qr)}{Qr} \tag{3.4}$$

Therefore for a collection, or ensemble, of particles the resulting electric field of the scattered light is simply a summation of the electric field amplitudes of all the scattering events multiplied by a phase factor due the different path lengths taken by the scattered light,

$$E(Q,t) = \sum_{i=1}^{N} b_i(Q)\ e^{i(\mathbf{Q}.\mathbf{r}_i(t))} \tag{3.5}$$

$\mathbf{r}_i(t)$ now represents the time dependent center of mass of particle i, which changes continuously as the particle undergoes Brownian motion. The resulting intensity can be written as,

$$I(Q,t) = |E(Q,t)|^2 \tag{3.6}$$

The scattered field takes on the form of a random diffraction pattern, often referred to as a 'speckle pattern', which consists of dark and bright regions of light. Each speckle, of intensity $|E(Q,t)|^2$, constitutes a single Fourier component of a density fluctuation of length scale $\left(\frac{2\pi}{Q}\right)$. The intensity averaged over a large number of speckles, $\langle I(Q)\rangle$ is then,

$$\langle I(Q)\rangle = b^2(Q)\sum_{i=1}^{N}\sum_{j=1}^{N}\langle e^{(i\mathbf{Q}.(\mathbf{r}_i-\mathbf{r}_j))}\rangle \tag{3.7}$$

where monodispersity is assumed ($b_i(Q) = b_j(Q) = b(Q)$). Alternatively this can be written in a more succinct form,

$$\langle I(Q)\rangle = N(b(0))^2P(Q)S(Q) \tag{3.8}$$

where $P(Q)$ represents the 'form factor' i.e. the contribution to the detected light from single particle scattering which is independent of the particle configuration,

$$P(Q) = \left(\frac{b(Q)}{b(0)}\right)^2 \tag{3.9}$$

and $S(Q)$ is known as the 'structure factor' i.e. the contribution to the scattered light from collective scattering which depends on the overall spatial configuration within the ensemble,

$$S(Q) = \frac{1}{N}\sum_{i=1}^{N}\sum_{j=1}^{N}\langle e^{(i\mathbf{Q}.(\mathbf{r}_i-\mathbf{r}_j))}\rangle \tag{3.10}$$

Therefore the scattered light can be decoupled into two distinct contributions, providing a simple method for extracting structural information.

Experimentally a measurement of the total scattered intensity from a concentrated colloidal suspension and the scattered intensity from a dilute solution in identical experimental conditions (temperature, wavelength, index match condition, etc) yields a measure of the structure factor. Practically this is achieved by first measuring the total intensity scattered by a concentrated suspension. Then by centrifuging the sample for a number of hours, until a dense compact sediment is formed, and redispersing a few particles into the supernatant the single particle form factor is then measured (to within an arbitrary multiplicative constant) in identical experimental conditions. This method has been applied to numerous experimental systems, notable examples of which include hard sphere colloidal fluids, crystals and glass samples [53].

3.3.1 The form factor

The form factor, the single particle contribution to the scattered light, is fundamental to light scattering experiments and its basic properties are summarised here. For identical spherical particles of radius a and refractive index n the scattered electric field can be calculated, using equations (3.4) and (3.5) (see appendix A)[1],

$$E(Q) = V_{sphere}\frac{3}{(Qa)^3}(n - n_0)(sin(Qa) - (Qa)cos(Qa)) \tag{3.11}$$

The resulting scattered intensity, $I = |E(Q)|^2$, is simply the Fourier transform of a sphere of radius a. In the studies carried out here the particles are not of uniform refractive index and equation (3.11) does not apply. Due to steric stabilisation, to ensure hard-sphere-like interactions, the particles can be represented as a core-shell system with a core of different refractive index than that of the shell (n_c and n_s respectively). A core-shell particle modifies the single particle form factor considerably

---

[1] This expression ignores the exponential phase factor, which plays no role in the resulting form factor.

when the background fluid has a refractive index near the index of either core or shell. In this case the total electric field E_T is simply a summation of the contributions from the core scattering E_C and shell scattering E_S where,

$$E_C(Q) = V_{core}\frac{3}{(Qa)^3}(n_c - n_0)(sin(Qa) - (Qa)cos(Qa)) \tag{3.12}$$

and in the thin shell limit (shell thickness $\Delta << a$, see Appendix B),

$$E_S(Q) = V_{shell}(n_s - n_0)\frac{sin(Qa)}{Qa} \tag{3.13}$$

The resulting form factor,

$$P(Q) = |E_T|^2 = |E_C + E_S|^2 \tag{3.14}$$

becomes highly sensitive to the solvent refractive index n_0 and through simple adjustment the form factor can be manipulated so that the first minimum can be situated over a wide range of Qa.

When n_0 is less than that of the core and shell both the core and shell scatter positively and the first zero in the total electric field (first minimum in the form factor) occurs at a high wavevector, as can be seen in figure 3.2(a). As n_0 is increased so that it lies between the indices of core and shell (assuming a core of higher refractive index), then the core scatters negatively (as $n_0 > n_c$) whereas the shell still scatters positively. As can be seen, from figure 3.2(b), the scattered electric field from the shell decays faster than that from the core, and the first zero occurs at a lower wavevector. As n_0 is increased sufficiently the first zero becomes coincident with the origin, as

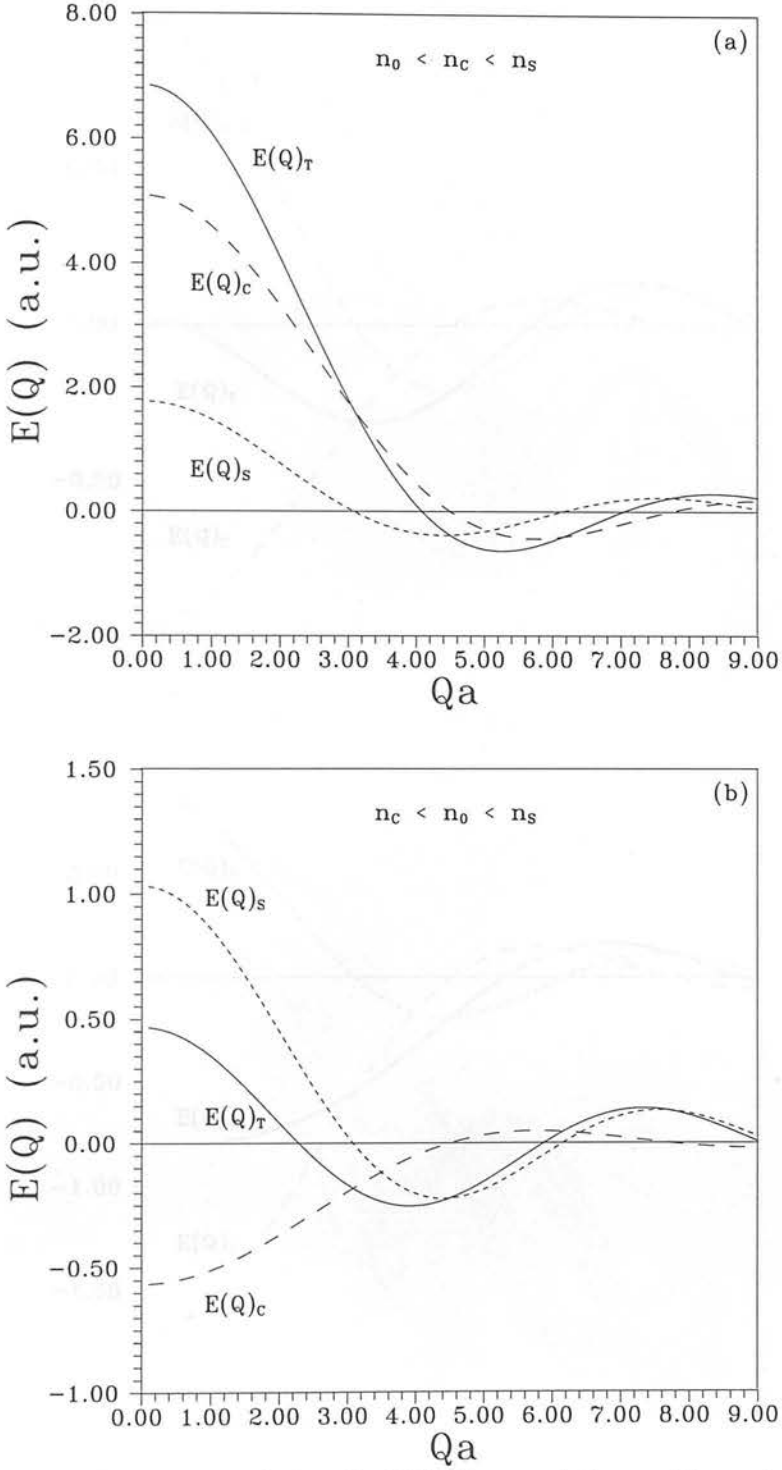

Figure 3.2. The scattered electric fields from solutions with an increasing solvent refractive index.

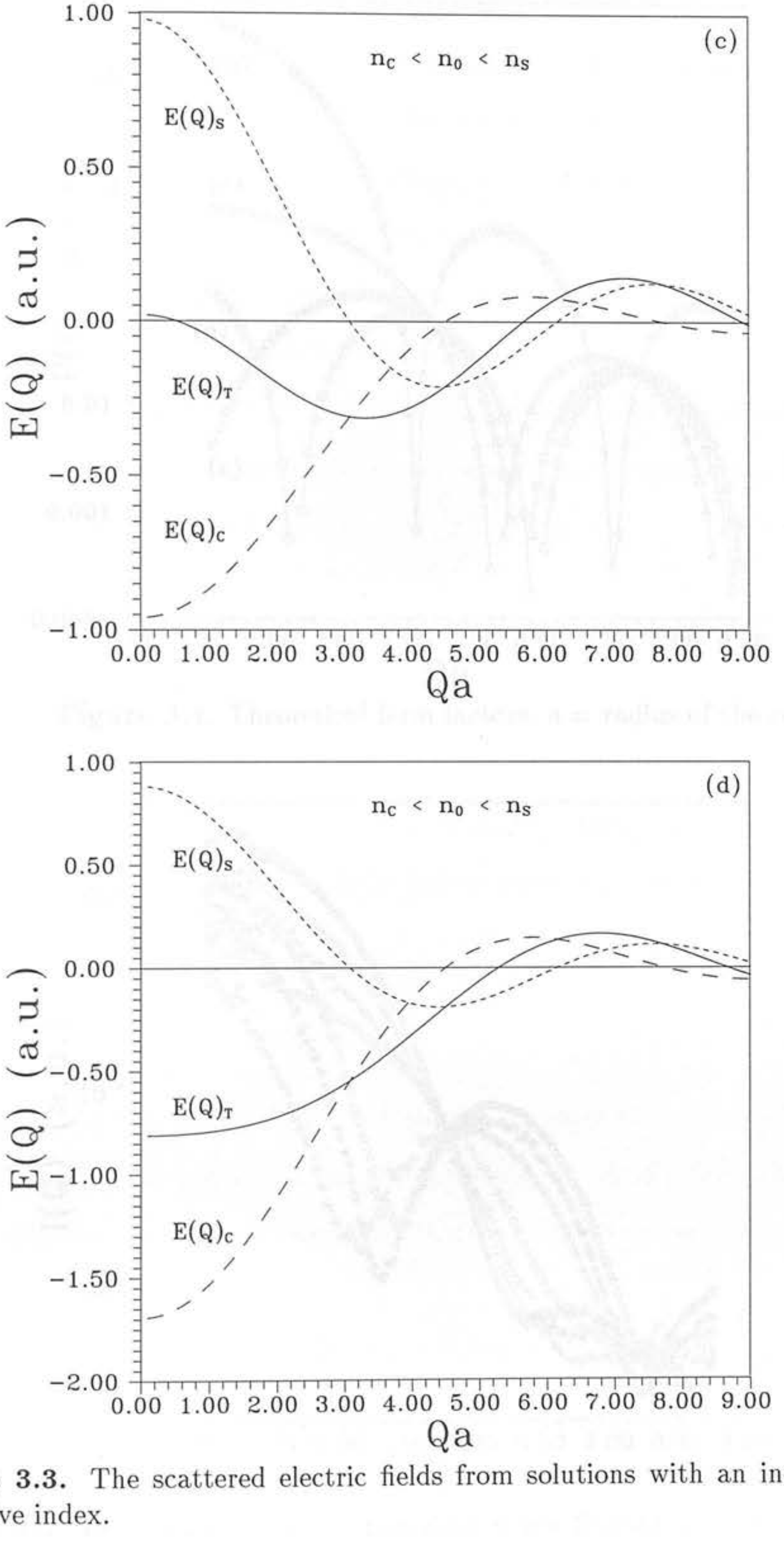

Figure 3.3. The scattered electric fields from solutions with an increasing solvent refractive index.

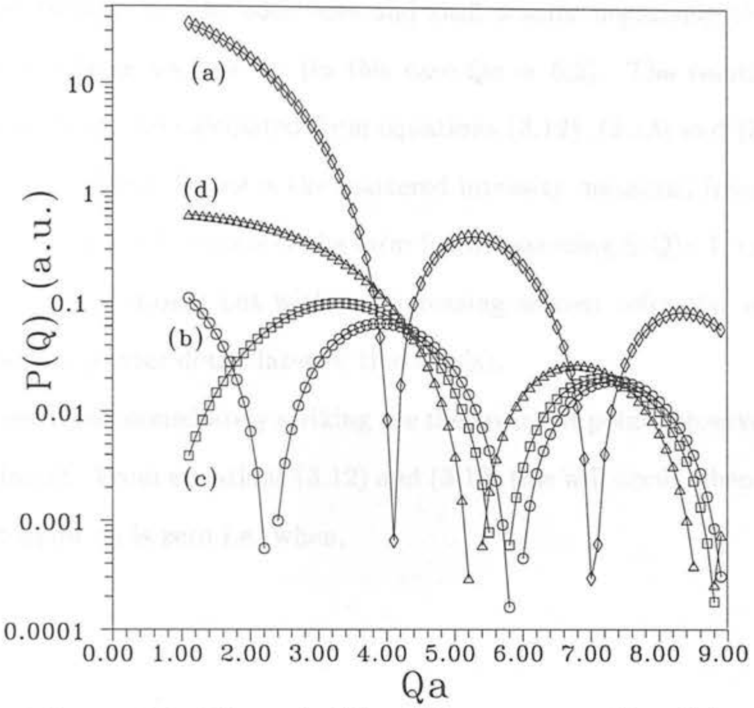

Figure 3.4. Theoretical form factors. a = radius of the core.

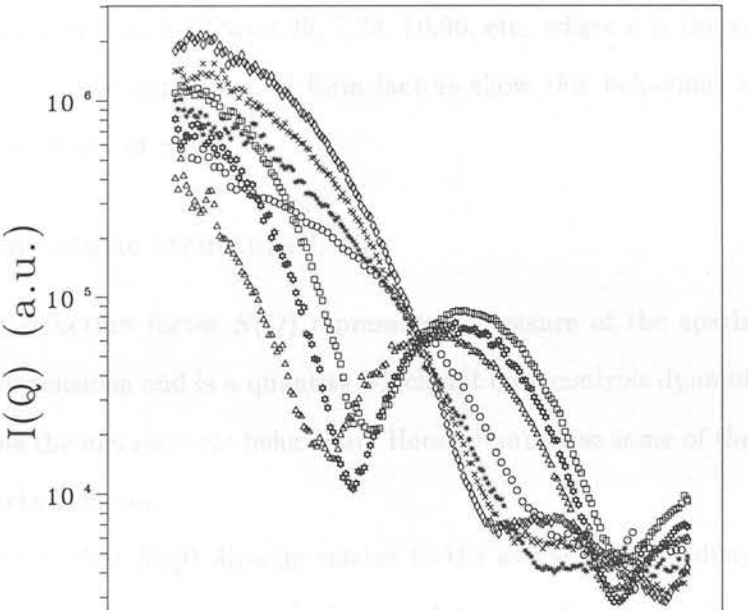

Figure 3.5. Experimental form factors from dilute PMMA solutions. $a \simeq$ radius of the core.

shown in figure 3.3(c), and the previously secondary zero becomes the first. When n_0 is increased further so that both core and shell scatter negatively then the first zero again lies at a large wavevector (in this case $Qa = 5.2$). The resulting form factors are shown in figure 3.4 calculated from equations (3.12), (3.13) and (3.14) for the four cases described above. Below is the scattered intensity measured from a dilute sample of PMMA (i.e. this will represent the form factor assuming S(Q)=1, i.e. in the absence of structural correlations) but with an increasing solvent refractive index (which will be discussed in greater detail later in this thesis).

What becomes immediately striking are the invariant points observed in both theory and experiment. From equations (3.12) and (3.13) this will occur when the contribution dependent upon n_0 is zero i.e. when,

$$Qa = tan(Qa) \tag{3.15}$$

solutions of which are Qa=4.49, 7.73, 10.90, etc. where a is the radius of the core. As can be seen the experimental form factors show this behaviour extremely well to within an accuracy of ±5%.

3.3.2 The static structure factor

The static structure factor $S(Q)$ represents a measure of the spatial correlations in colloidal suspensions and is a quantity which not only controls dynamic properties, but also governs the macroscopic behaviour. Here I summarise some of the basic properties of the structure factor.

The reason that $S(Q)$ directly relates to the average spatial distribution within a colloidal suspension is due to its intimate relation to the equilibrium pair distribution function $g(r)$. $\left(g(r)\frac{4\Pi r^2 N}{V}dr\right)$ is the number of particles which lie within a spherical shell of radius r, thickness dr, given that there is a particle situated at the origin $r = 0$.

N is the total number of particles and V the total volume. It can be shown that equation (3.10) can be expressed as (see Appendix C),

$$S(Q) = 1 + \rho \int d^3r \; e^{i\mathbf{Q}.\mathbf{r}} (g(r) - 1) \tag{3.16}$$

or equivalently

$$S(Q) = 1 + \rho \, h(Q) \tag{3.17}$$

where $h(Q)$ is known as the total pair correlation function and is simply the Fourier transform of $(g(r) - 1)$ i.e. $S(Q)$ essentially represents the contribution of pair correlation effects within a system. For a dilute suspension, one with a lack of structural correlations, $g(r) = 1$ and from equation (3.16) $S(Q) = 1$. With increasing density, or interaction, the dispersion will become structured and oscillations are observed in $g(r)$, due to the particles sitting at preferred distances apart, leading to a highly Q-dependent structure factor.

3.4 Theoretical structure factors

Structure factors for a collection of spherical particles, in thermal equilibrium, can be approximated analytically through the Percus-Yevick (PY) closure to the Ornstein-Zernike (OZ) integral equation [76]. OZ realised that the link between a spatially varying, static, external field and the subsequent response from the system, could be expressed in terms of a property known as the direct correlation function $C(r)$. $C(r)$ essentially represents a measure of the short-ranged correlations in the system. Assuming a homogeneous and isotropic system the OZ integral equation relates the total pair correlation function $h(r_{12})$ between particles 1 and 2, which is simply the Fourier transform of $h(Q)$, to not only direct correlations between particles $C(r_{12})$, but also due to the indirect correlations propagated via an increasing number of intermediate particles. The OZ equation can be expressed as,

$$h(r_{12}) = C(r_{12}) + \rho \int dr_3\, C(r_{13})h(r_{32}) \tag{3.18}$$

where ρ is the number density of the system and $\int dr_3$ is the integral over all third particles. $h(r_{32})$ is simply the total pair correlation between particles 2 and 3,

$$h(r_{32}) = C(r_{32}) + \rho \int dr_4\, C(r_{34})h(r_{42}) \tag{3.19}$$

and therefore,

$$h(r_{12}) = C(r_{12}) + \rho \int dr_3\, C(r_{13})C(r_{32}) + \rho^2 \int\int dr_3 dr_4\, C(r_{13})C(r_{34})h(r_{42}) \tag{3.20}$$

ad infinitum. As shown the OZ equation leads to an infinite series of integral equations representing direct correlations, indirect via one other, indirect via two others, etc. Introducing a 'closure' equation one obtains a closed relation between $h(r)$ and $C(r)$ which leads to an analytical expression for $S(Q)$ e.g. the PY approximation which relates the direct correlation function to the pair correlation function,

$$C(r) = \left(1 - e^{V(r)/k_BT}\right) g(r) \tag{3.21}$$

where $V(r)$ is the interparticle potential.

Solutions to the OZ integral equation have been solved for three notable interparticle potentials; the hard sphere fluid, the adhesive hard sphere fluid and the hard sphere square well fluid.

3.4.1 Hard sphere systems

Hard spheres are defined to have an interparticle potential,

$$\frac{V(r)}{k_B T} = \begin{cases} \infty & r < 2a \\ 0 & r > 2a \end{cases} \tag{3.22}$$

i.e. the spheres become infinitely repulsive upon contact. The paradigmatic hard sphere structure factor, in the PY limit, can be calculated analytically [76] and is shown for varying volume fractions ϕ in figure 3.6.

The PY solution for simple hard sphere fluids has features common to all equilibrium structure factors. The first peak in $S(Q)$ is commonly known as the first diffraction maximum and one might expect the length scale this represents to coincide with the interparticle spacing. Physically the main peak occurs as the colloidal particles stay, on average, at a preferred distance apart, due to the particles being caged in by the presence of all the others. Although this does indeed represent the effect of interparticle correlations no obvious direct connection exists [77]. The asymptotic value of $S(Q)$ at large Q equals unity and is indicative of the lack of pair correlations at short wavelengths. In the other extreme of small Q it is well known for a system in equilibrium,

$$\lim_{Q \to 0} S(Q) \propto \chi_T \tag{3.23}$$

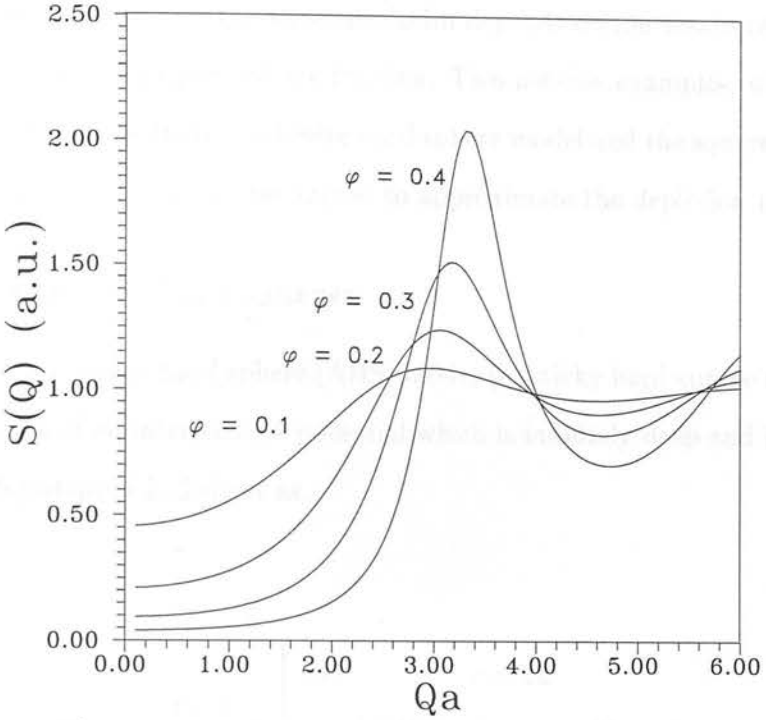

Figure 3.6. Hard sphere structure factors in the PY limit.

χ_T represents the isothermal compressibility of the system i.e. Measurements at low Q probe long wavelength fluctuations which govern the response of a system to an externally applied field.

As is evident from figure 3.6, the effect of increasing the fluid density is to effectively increase the magnitude of the pair correlations, as shown by the increase in the main peak of $S(Q)$. As the fluid becomes increasingly structured, the preferred particle separation concomitantly decreases. Accordingly the peak in $S(Q)$ moves to larger Q values. Physically the increased short scale structure and decrease in the interparticle spacing are due to a greater caging-in of the particles as the density increases.

The hard sphere structure factor, in the PY limit, is known to be valid for low densities differing by less than 5% compared to computer simulations and experiment [76]. At higher volume fractions differences are observed, but can be improved through the semiempirical Verlet-Weis correction to the effective volume fraction [78], which will not be discussed here further.

One can also ask how the structure factor depends on the details of the interparticle potential rather than just volume fraction. Two notable examples, which will be used in this work, are the Baxter adhesive hard sphere model and the square well fluid which, in the right conditions, can be argued to approximate the depletion potential.

3.4.2 Adhesive hard spheres

The Baxter adhesive hard sphere (AHS) model (or sticky hard sphere model) [79] is the limiting case of an interparticle potential which is infinitely deep and infinitely narrow. The AHS potential is defined as,

$$\frac{V(r)}{k_B T} = \begin{cases} \infty & r < 2a \\ -ln(\frac{(a+\delta)}{12\tau_B \delta}) & 2a < r < 2(a+\delta) \\ 0 & r > 2(a+\delta) \end{cases} \tag{3.24}$$

where the limit $\delta \to 0$ is assumed in any subsequent discussion. The parameter τ_B is known as the stickiness parameter and essentially governs the number of dimers in the system. In the limit of τ_B tending to infinity the above AHS potential reduces to that of the hard sphere system. AHS structure factors have been solved analytically, in the PY limit [79], and are often used to analyse experimental systems which are subject to a short ranged potential. Arguably the most appropriate experimental systems are solutions which are reduced in temperature such that the background fluid no longer represents a good solvent for the stabilising hair of the colloidal particles. Subsequently the particles aggregate under an extremely short ranged attraction [80], [81]. The AHS structure factor in the PY approximation is shown in figure 3.7 for a colloidal fluid of volume fraction $\phi = 0.2$, but with a decreasing stickiness parameter τ_B.

As can be seen from figure 3.7 the effect of increasing the number of dimers in the

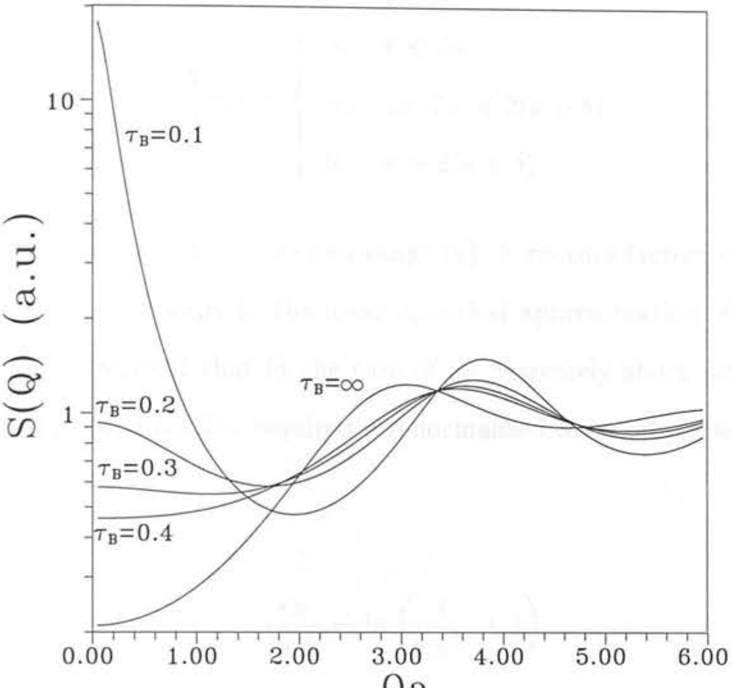

Figure 3.7. PY structure factors for the AHS model, $\phi = 0.2$.

suspension decreases the interparticle spacing and increases the pair correlations, in a similar fashion to the effect of increasing fluid density. On the other hand unlike the hard sphere model, the increasing number of dimers leads to a large increase in S(0) i.e. the isothermal compressibility χ_T increases dramatically as the number of dimers increases.

3.4.3 Square well fluid

The square well potential (SW) has been frequently used to model colloidal suspensions [82], [83]. Recently, for example, Bibette et al. [82] compared their emulsion systems subject to a depletion potential, induced by the addition of micelles, to an appropriate square well fluid. The SW interparticle potential is defined as

$$\frac{V(r)}{k_BT} = \begin{cases} \infty & r < 2a \\ -\epsilon & 2a < r < 2(a+\delta) \\ 0 & r > 2(a+\delta) \end{cases} \tag{3.25}$$

and is one of variable depth (ϵ) and range (δ). Structure factors of the SW system have been solved analytically in the mean spherical approximation [84]. Subsequently Huang et al. [83] realised that in the case of an extremely short range potential the mean spherical approximation required a renormalised microscopic well depth,

$$\frac{\epsilon_R}{k_BT} = ln\left(\frac{\epsilon}{k_BT} + 1\right) \tag{3.26}$$

The modified potential depth arises through a virial expansion of the interparticle attraction. Any future reference to this model assumes a renormalised well depth. The SW fluid reduces to that of the HS fluid in the limit $\delta \to 0, \epsilon \to 0$. The SW system also approximates the adhesive hard sphere model in the deep, narrow limit $\epsilon \to \infty, \delta \to 0$. The effect of increasing the SW potential depth, in the case of a short range potential, is analogous to increasing the number of dimers in the AHS model.

It can be argued that either of these models would approximate the strong and short ranged depletion potential found in colloid-polymer mixtures i.e. in the appropriate conditions both these models represent a deep and narrow interparticle potential. Both the AHS and SW models will be used to analyse the experimental results presented in this thesis.

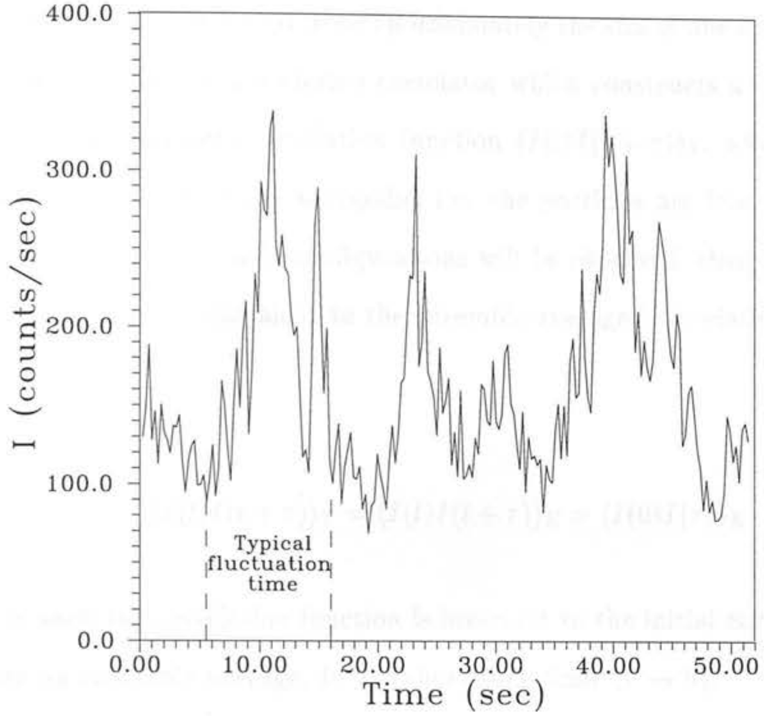

Figure 3.8. Intensity fluctuations in the far field.

3.5 Dynamics

Light scattering can also be used to measure the dynamics of colloidal suspensions, through the technique of dynamic light scattering (DLS). For a review of this subject refer to Pusey [53], Berne and Pecora [72] and Pecora [85], which all give comprehensive discussions of this method. Here I briefly summarise the technique to identify the quantities measured and their relation to the properties of the system.

As described in section 3.3 the scattered radiation field, from an ensemble of particles, takes on the form of a 'speckle' pattern. As the particles undergo Brownian motion the speckle pattern fluctuates, as the conditions for constructive and destructive interference in the far field change. Figure 3.8 shows a typical example of such temporal intensity fluctuations. An individual speckle intensity is given by equations (3.5) and (3.6).

To monitor the speckle fluctuations a detector is placed in the far field with a sensitive area which is adjusted to be approximately the size of one speckle. The output from the detector is fed to a photon correlator which constructs a quantity known as the time average intensity correlation function $\langle I(t)I(t+\tau)\rangle_T$, where $\langle\rangle_T$ represents a time average. If the system is ergodic, i.e. the particles are free to diffuse, so that given enough time all particle configurations will be observed, then the time averaged correlation function is equivalent to the ensemble averaged correlation function,

$$\langle I(t)I(t+\tau)\rangle_T = \langle I(t)I(t+\tau)\rangle_E = \langle I(0)I(\tau)\rangle_E \tag{3.27}$$

and as such the correlation function is invariant to the initial correlation time. $\langle\rangle_E$ represents an ensemble average. In the short time limit ($\tau \rightarrow 0$),

$$\lim_{\tau\rightarrow 0}\langle I(0)I(\tau)\rangle = \langle I^2\rangle \tag{3.28}$$

and in the long time limit ($\tau \rightarrow \infty$),

$$\lim_{\tau\rightarrow\infty}\langle I(0)I(\tau)\rangle = \langle I\rangle^2 \tag{3.29}$$

as the intensities $I(0)$ and $I(\tau)$ are no longer correlated in any way. Consequently the intensity correlation function takes on the general form shown in figure 3.9, which assumes the Schwarz inequality i.e. $\langle I^2\rangle$ is always greater than or equal to $\langle I\rangle^2$. Also indicated on figure 3.9 is the time taken for the intensity correlation function to decay to $\left(\frac{1}{e}\right)$ of its initial value, known as the structural relaxation time τ_R. In the high-Q

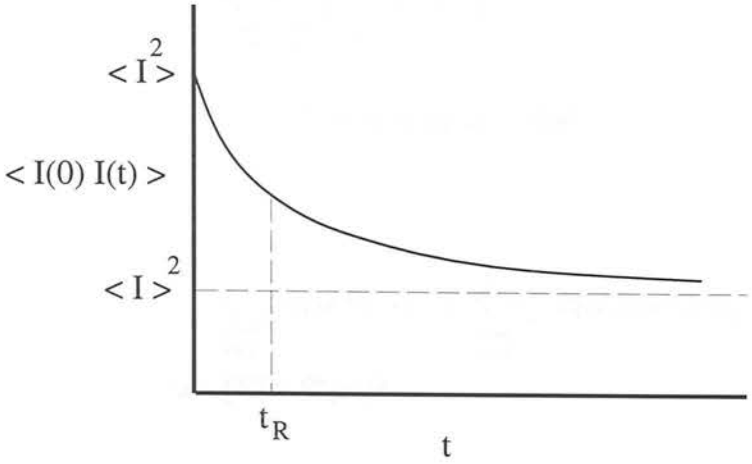

Figure 3.9. A schematic intensity correlation function.

limit (yet less than $Q \to \infty$) this corresponds to the time taken for a particle to diffuse a distance comparable to its own diameter.

As reviewed in section 3.3 the time dependent ensemble averaged intensity can be written (ignoring time independent prefactors),

$$\langle I(Q,t)\rangle = \sum_{i=1}^{N}\sum_{j=1}^{N}\langle e^{i\mathbf{Q}.(\mathbf{r}_i(t)-\mathbf{r}_j(t))}\rangle \tag{3.30}$$

Assuming independent particles and full ergodicity (as in a dilute suspension without structural correlations) all the cross terms in equation (3.30) can be ignored and only two contributions exist to the intensity correlation function, one $(i=j) \neq (k=l)$ such that,

$$\langle I(0)I(\tau)\rangle \;=\; \sum_{i=1}^{N}\sum_{j=1}^{N}\sum_{k=1}^{N}\sum_{l=1}^{N}\langle e^{i\mathbf{Q}.(\mathbf{r}_i(0)-\mathbf{r}_j(0)+\mathbf{r}_k(\tau)-\mathbf{r}_l(\tau))}\rangle \tag{3.31}$$

$$= \sum_{i=1}^{N}\sum_{k=1}^{N}\langle 1\rangle = N^2 = \langle I\rangle^2 \qquad (3.32)$$

(using equation (3.30)), and $(i = l) \neq (j = k)$ such that,

$$\begin{aligned} \langle I(0)I(\tau)\rangle &= \sum_{i=1}^{N}\langle e^{i\mathbf{Q}.(\mathbf{r}_i(0)-\mathbf{r}_i(\tau))}\rangle . \sum_{j=1}^{N}\langle e^{-i\mathbf{Q}.(\mathbf{r}_j(0)-\mathbf{r}_j(\tau))}\rangle && (3.33) \\ &= \langle E(0)E^*(\tau)\rangle^2 && (3.34) \end{aligned}$$

when compared to equation (3.5).

Therefore the intensity correlation function can be expressed in the ergodic limit,

$$\langle I(0)I(\tau)\rangle = \langle I\rangle^2 + \langle E(0)E^*(\tau)\rangle^2 \qquad (3.35)$$

or which can be normalised by $\langle I\rangle^2$,

$$g^{(2)}(Q,\tau) = 1 + (g^{(1)}(Q,\tau))^2 \qquad (3.36)$$

where

$$g^{(2)}(Q,\tau) = \frac{\langle I(0)I(\tau)\rangle}{\langle I\rangle^2} \qquad (3.37)$$

is known as the normalised intensity correlation function and

$$g^{(1)}(Q,\tau) = \frac{\langle E(0)E^{*}(\tau)\rangle}{\langle I\rangle} \tag{3.38}$$

is the well known normalised field correlation function, often referred to as the intermediate scattering function $f(Q,\tau)$ i.e. From the measured time averaged intensity correlation function, one can readily construct the quantity of interest, the intermediate scattering function. In practice [53],

$$g^{(2)}(Q,\tau) = 1 + (\beta\, g^{(1)}(Q,\tau))^2 \tag{3.39}$$

where β is an experimental constant determined largely by the ratio of the detector pin hole to coherence area. The field correlation function decays from an initial value $g^{(1)}(Q,0) = \frac{\langle E(0)E^{*}(0)\rangle}{\langle I\rangle} = 1$ to $g^{(1)}(Q,\infty) = 0$. Therefore the intensity correlation function decays from $g^{(2)}(Q,0) = 1 + \beta^2$ to a final value $g^{(2)}(Q,\infty) = 1$ i.e. figure 3.9 once normalised by $\langle I\rangle^2$. Conventionally the detector aperture is adjusted so that $\beta \sim 1$ i.e. only one coherence area (speckle) is measured, and therefore $g^{(2)}(Q,0) \sim 2$.

3.5.1 Dilute suspensions

DLS has frequently been used to study the dynamics of dilute suspensions of particles. By ignoring the effects of density and particle interaction the 'zero concentration' properties of the solution can be measured. From measurements in the dilute limit one can obtain the free diffusion coefficient and consequently the particle radius. Theoretically the dynamics of dilute suspensions are well understood and are summarised here.

In the case of non-interacting monodispersed particles one can readily calculate the intermediate scattering function from equation (3.38). Without structural correlations (i.e. no cross terms) $g^{(1)}(Q,\tau)$ simply reduces to,

$$\begin{aligned} g^{(1)}(Q,\tau) &= \frac{\langle E(0)E^{*}(\tau)\rangle}{\langle I\rangle} && (3.40)\\ &= \frac{N\langle e^{(i\mathbf{Q}.(\mathbf{r}(0)-\mathbf{r}(\tau)))}\rangle}{\langle I\rangle} && (3.41)\\ &= \langle e^{(i\mathbf{Q}.(\mathbf{r}(0)-\mathbf{r}(\tau)))}\rangle && (3.42)\end{aligned}$$

The displacement $\Delta\mathbf{r} = (\mathbf{r}(\tau) - \mathbf{r}(0))$ of a free Brownian particle in time τ can be shown to be a Gaussian variable of mean square value,

$$\langle \Delta\mathbf{r}^2\rangle = 6D_0\tau \tag{3.43}$$

where D_0 represents the free particle diffusion coefficient of a particle of radius a which directly relates to the particle radius through the Stokes-Einstein expression,

$$D_0 = \frac{k_B T}{6\pi\eta a} \tag{3.44}$$

η is the shear viscosity of the suspension medium (where one assumes stick boundary conditions). The intermediate scattering function then reduces to,

$$\begin{aligned} g^{(1)}(Q,\tau) &= \langle e^{i\mathbf{Q}.(\mathbf{r}(0)-\mathbf{r}(\tau))}\rangle && (3.45)\\ &= \int e^{-i\mathbf{Q}.\Delta\mathbf{r}} P(\Delta\mathbf{r})\ d^3\Delta\mathbf{r} && (3.46)\end{aligned}$$

where $P(\Delta\mathbf{r})\ d^3\Delta\mathbf{r}$ is the probability that a particle will suffer a displacement in the neighbourhood of $d^3\Delta\mathbf{r}$ of the point $\Delta\mathbf{r}$ in time t. Assuming, as above, a Gaussian distribution,

$$g^{(1)}(Q,\tau) = \left(\frac{3}{2\pi\langle\Delta r^2\rangle}\right)^{\frac{3}{2}} \int e^{-i\mathbf{Q}.\Delta\mathbf{r}} e^{-\frac{3(\Delta r)^2}{2\langle\Delta r^2\rangle}} \, d^3\Delta\mathbf{r} \tag{3.47}$$

$$= e^{-\frac{Q^2}{6}\langle\Delta r^2\rangle} \tag{3.48}$$

$$= e^{-D_0 Q^2 \tau} \tag{3.49}$$

Therefore from a single measurement of the time averaged intensity correlation function, from a dilute solution, the free particle diffusion coefficient can be obtained. As a consequence DLS is often used to characterise particle radii.

3.5.2 Concentrated suspensions

Concentrated colloidal solutions provide a complex many-body problem which remains a challenging field for both experiment and theory [73]. For systems at high concentration ($\phi \geq 0.05$) or of strong particle interaction the field correlation function no longer decays as a single exponential. The origin of such complex relaxations is due to the coupling of particle motions through their interactions. The coupling arises from the direct interparticle potential and the indirect hydrodynamic force propagated through the suspension medium. The time scale associated with direct interparticle interactions τ_I can be regarded as approximately the duration of a particle collision $\sim 10^{-4}s$. On the other hand the characteristic hydrodynamic time τ_H, which corresponds to the time taken for the fluid to reach a steady state, is far shorter $\tau_H \sim \frac{\rho a^2}{\eta} \sim 10^{-7}s$ and can be regarded as instantaneous with respect to correlation experiments.

The short time limit of the field correlation function is determined by dynamics which take place on a time scale much less than τ_I. In the absence of hydrodynamics it can be shown that [73],

$$D_{eff}(Q) = \frac{D_0}{S(Q)} \tag{3.50}$$

where $D_{eff}(Q)$ represents the effective short time diffusion coefficient over which the particle configuration has hardly changed. As is evident the effective diffusion coefficient becomes highly sensitive to the nature of the static structure factor in concentrated suspensions. This phenomenon is analogous to de Gennes narrowing in simple atomic fluids, i.e. the slowing down of concentration fluctuations near the peak in the structure factor [74]. $D_{eff}(Q)$ is obtained experimentally by measuring the first cumulant of the intermediate scattering function,

$$D_{eff}(Q) = -\frac{1}{Q^2} \lim_{\tau \to 0} \frac{\partial}{\partial \tau} ln(g^{(1)}(Q, \tau)) \tag{3.51}$$

In the case of a dilute suspension where the field correlation function decays as a single exponential, as in equation (3.49), the effective diffusion coefficient becomes equal to the free diffusion coefficient $D_{eff}(Q) = D_0$.

As has been alluded to previously the effect of hydrodynamics can be regarded as instantaneous in terms of light scattering and subsequently affects the intermediate scattering function throughout its decay. For hydrodynamically interacting particles one can write,

$$D_{eff}(Q) = D_0 \frac{H(Q)}{S(Q)} \tag{3.52}$$

by analogy with equation (3.50). $H(Q)$ is known as the hydrodynamic factor and can be regarded as an effective mobility.

Theoretical calculations of full interparticle hydrodynamics is an extremely complex many-body problem. Beenaker and Mazur [86], [87] calculated an approximate $H(Q)$ including full many-body hydrodynamics. With their method it was possible to reduce the problem to solving a hierarchy of linear algebraic equations, which described the decay of hydrodynamically coupled density fluctuations. The full Q-dependent hydrodynamic factor is known to be valid for $\phi \leq 0.3$. Experimental measurement of the Q-dependent effective diffusion coefficient and the static structure factor leads directly to the hydrodynamic factor.

The effective diffusion coefficient has a Q-dependence which can be interpreted in terms of its limits. In the high-Q regime ($S(Q) \sim 1$) the length scales probed are approximately that of a single particles and the effective diffusion coefficient reduces to the short time self diffusion coefficient,

$$\lim_{Q \to \infty} D_{eff}(Q) = D_s = D_0 H(Q \to \infty) \tag{3.53}$$

i.e. high-Q measurements probe the motion of single particles perturbed by the presence of all the other particles. In the high-Q limit the intermediate scattering function reduces to the self function and can be written,

$$g_s^{(1)}(Q, \tau) = \langle e^{iQ.\Delta x(\tau)} \rangle \tag{3.54}$$

where $\Delta x(\tau)$ is a single cartesian component of the particle displacement in time τ (c.f. equation(3.42)). The self approximation is most likely to hold for times less than τ_I in the free Brownian limit [73]. Consequently the self intermediate scattering function, by analogy with equation (3.49), is

$$g_s^{(1)}(Q,\tau) = e^{-\frac{Q^2}{2}\langle \Delta x^2(\tau)\rangle} \tag{3.55}$$

i.e. in the high-Q limit one can directly obtain the mean squared particle displacement from the measured field correlation function.

As in the static case the $Q \to 0$ limit measures the behaviour of the system on large length scales. $D_{eff}(0)$ can be regarded as the diffusion coefficient which describes the decay of density fluctuations of macroscopic extent. Appropriately,

$$\lim_{Q\to 0} D_{eff}(Q) = D_c = D_0 \frac{H(0)}{S(0)} \tag{3.56}$$

where D_c is referred to as the collective diffusion coefficient. As $S(0)$ represents the systems compressibility, $H(0)$ describes a macroscopic mobility.

3.5.3 Non-ergodicity

In highly concentrated systems, or suspensions with a strong interparticle potential, the particle motion can become retarded. The system can then exhibit frozen-in density fluctuations. The particles no longer probe the whole of phase space and as a consequence the speckle pattern retains partial memory. Each speckle fluctuates about a static mean value which varies from speckle to speckle. Such a phenomenon is known as non-ergodicity [88].

The consequences for DLS are considerable as the time average intensity correlation function is no longer equivalent to the ensemble-averaged function i.e. the measured time average intensity correlation function varies from speckle to speckle. Equation (3.31) no longer holds and if one requires the field correlation function it must be constructed rather than inferred from a single measure of the time averaged intensity correlation function. The method which is conceptually easiest, is to construct the ensemble average manually. As in the definition of an ensemble average one can measure the intensity correlation function over a infinitely large number of individual speckles (in practice a large finite number) to derive the ensemble average. Such a measurement is trivial if tedious. Recently however several novel methods have been suggested to obtain the ensemble average through a minimum of measurements.

- **Improved manual case**

Rather than measuring many independent speckles one can adopt an enlarged scattering volume and an enlarged detection slit. By adjusting these parameters, up to ten speckles can be measured at once. A measurement such as this probes ten independent Fourier components of a density fluctuation of length scale $\left(\frac{2\pi}{Q}\right)$. Measurements of a number of spatially different scattering volumes leads to the ensemble average, but the number of measurements required is down by a factor of ten, compared with the method described above. Recently van Megen and Pusey [89] used this procedure to study colloidal glasses.

- **Translational case**

A method which is a direct way of measuring the ensemble average from a single DLS experiment is to simply translate the sample to obtain data from a number of spatially varying configurations i.e. sample numerous independent speckles throughout a single measurement. The procedure depends on adjusting the translational (or rotational) time to be far greater than the longest decay time in the fluctuating part of the correlation function. This method has been shown to measure the full ensemble average in an experimental study of polymer gels [90].

- **Scanning case**

Recently a method has been proposed which through a single DLS measurement yields the full ensemble average, but does not rely on measuring the time dependence of a number of speckles. It can be shown that, for a detector set to observe a single coherence area, the field correlation function can be expressed as [88],

$$g^{(1)}(Q,\tau) = 1 + \frac{\langle I(Q)\rangle_T}{\langle I(Q)\rangle_E}\left(\sqrt{1 + g_T^{(2)}(Q,\tau) - g_T^{(2)}(Q,0)} - 1\right) \tag{3.57}$$

where $\langle I(Q)\rangle_T$ represents the time-averaged intensity of the speckle being studied and $\langle I(Q)\rangle_E$ is the average intensity over a number of speckles e.g. by first scanning the sample through a laser beam. $g_T^{(2)}(Q,\tau)$ is simply the time averaged intensity correlation function of the speckle being studied. Note that if this treatment is carried out for an ergodic system i.e.,

$$\langle I(Q)\rangle_T = \langle I(Q)\rangle_E,\ g_T^{(2)}(Q,0) \sim 2 \tag{3.58}$$

then equation (3.57) reduces to equation (3.36). The scanning method has been used to study polymer gels and colloidal glasses although in marginally non-ergodic systems, e.g. weakly flocculated suspensions, this treatment is questionable. The problem arises as the speckle fluctuations may sit on a slowly varying, non-static, background.

3.6 Polydispersity effects

The effects of polydispersity, although not explicitly treated here, can be large. In terms of the static structure factor the effect of polydispersity is to nulify the decoupling approximation of equation (3.8). In essence this arises through a correlation between the scattering amplitudes $b_i(Q), b_j(Q)$ and the exponential factor in the structure factor $exp(i\mathbf{Q}.(\mathbf{r}_i - \mathbf{r}_j))$, as they both depend strongly on the individual particle radii a_i, a_j. One can still measure the total intensity from a concentrated polydisperse

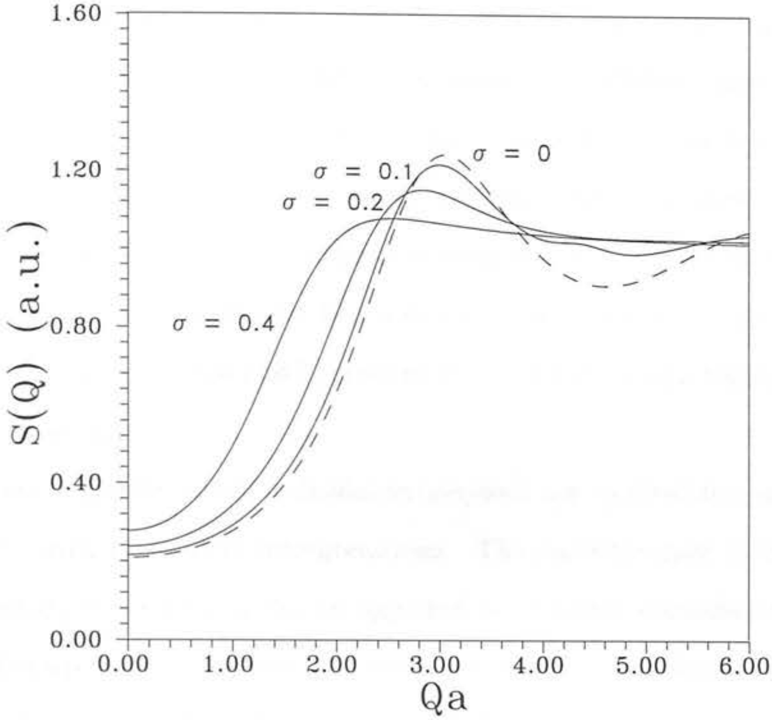

Figure 3.10. The effect of polydispersity on the hard sphere structure factor, $\phi = 0.2$, calculated using a code provided by T.T. Chui.

suspension and from a dilute polydisperse suspension to yield a measured structure factor, but as yet few theoretical polydisperse structure factors have been calculated and little structural information can be inferred. For hard sphere suspensions the effect of polydispersity on the structure factor is striking, as shown in figure 3.10 [91][2].

The main peak in $S(Q)$ moves to smaller wavevectors and pair correlations decrease sharply as the polydispersity is increased. The polydispersity effectively 'washes out' the information available from the structure factor as the scattered intensities from particles of different sizes interfere destructively. Even small polydispersities can alter the measured structure factor considerably, and for a polydispersity $\sigma \sim 0.05$ the deviation between that and the mondispersed case is of the order of 2% at the first diffraction maximum.

---

[2] To calculate these structure factors the particle size distribution is assumed to follow a Schulz distribution.

For dilute polydisperse suspensions one can still measure an average free diffusion coefficient over the particle size distribution. The correlation function associated with this tends to be non-single exponential as particles of different sizes possess different relaxation times. In such a situation where the dominant particle size has a form factor minimum within the limits of the experimental setup then DLS can be used to directly provide a measure of the polydispersity [92]. In concentrated suspensions the effective diffusion coefficient becomes extremely complicated as the free diffusion coefficient, structure factor and hydrodynamic factor all become highly dependent upon the polydispersity.

As a consequence 'model' colloidal suspensions are required to compare experimental results with theoretical interpretations. The particles used in this study have a polydispersity $\sigma \sim 0.05$ and can be regarded as relatively monodisperse, although one must still keep in mind the fact that even such small polydispersities as these can lead to effects in the behaviour of the scattered light.

3.7 Concluding remarks

Light scattering has been used extensively to study the structure and dynamics of colloidal suspensions. In this chapter I have covered the basic quantities which are measured in a light scattering experiment, be it static or dynamic, and shown how these measurements relate to the physical properties of the system.

In this thesis I will use both the techniques of static and dynamic light scattering to examine the colloid-polymer non-equilibrium state. The particles used in this study are relatively monodisperse ($\sigma \sim 0.05$) and of well characterised hard-sphere-like interaction, so that the theory discussed in this chapter can be used as a guide to the experimental results presented.

Chapter 4

Static structure of the non-equilibrium phase

4.1 Introduction

In this chapter I examine structure formation kinetics in the non-equilibrium region of the phase diagram (see figure 4.1). To study the static structure one can use conventional light scattering over a wide range of wavevectors - the structure probed is inversely proportional to the wavevector at which the scattering is studied. To complement the information obtained by this method one can also use microscopy and direct visual observation. Although these remove the theoretical interpretations implicit in determining structure from light scattering data, one can be misled as microscopy can be dominated by local defects. In fact it is frequently necessary to compare information from both direct observation and scattering to uniquely determine the structure.

To explore a sufficiently large section of the non-equilibrium region index-matched samples were prepared of volume fractions $\phi \sim 0.02, 0.1, 0.2$ and 0.4. These varied in polymer concentration, from just sufficient added polymer to induce non-equilibrium behaviour to large amounts of polymer so that the samples were 'quenched' deeply into the non-equilibrium region. These samples are summarised in table 4.1 (c.f. figure 4.1).

	ϕ	C_P
1	0.026	5.28e-3
2	0.020	8.21e-3
3	0.021	9.62e-3
4	0.020	12.00e-3

	ϕ	C_P
5	0.100	3.32e-3
6	0.092	4.01e-3
7	0.109	4.87e-3
8	0.101	5.60e-3
9	0.100	6.27e-3

	ϕ	C_P
10	0.196	2.71e-3
11	0.198	3.05e-3
12	0.184	3.52e-3

	ϕ	C_P
13	0.400	1.78e-3
14	0.388	2.09e-3
15	0.398	3.25e-3

Table 4.1. Non-equilibrium samples of varying volume fraction.

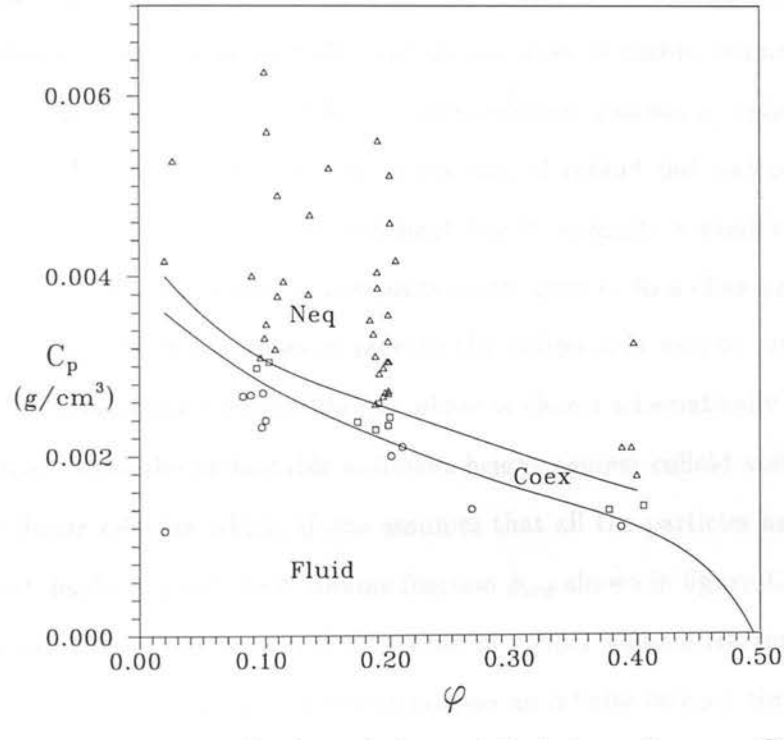

Figure 4.1. The previously shown index matched phase diagram. Coex ≡ fluid-crystal coexistence and Neq ≡ non-equilibrium region.

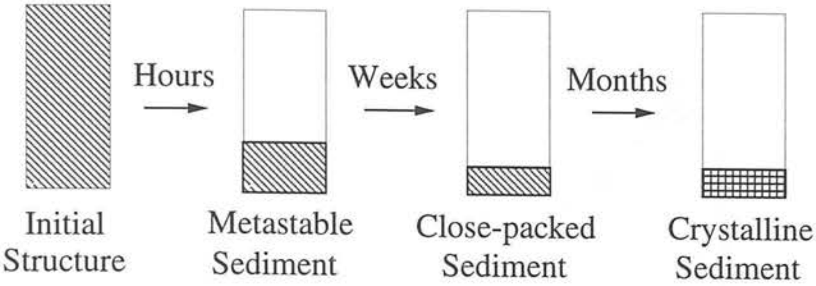

Figure 4.2. Evolution of the non-equilibrium phase over a number of months.

4.2 Visual observation

Once sufficient polymer has been added to an otherwise stable colloidal suspension the sample separates into coexisting crystal and fluid phases. If further polymer is added then crystallisation becomes suppressed and over time the sample separates into a colloid-rich sediment and a clear supernatant. At large colloid and polymer concentrations one observes a latency time before the onset of visible sedimentation. Once the structure has collapsed one finds that the sediment reaches a *metastable* state which is dependent upon the initial volume fraction of colloid but *independent* of polymer concentration. Surprisingly the sediment height suggests a ramified structure which slowly, over a matter of weeks, compacts under gravity to a close-packed volume fraction $\phi \sim 0.64$. After a number of months the sediment is seen to crystallise fully. The time evolution of the non-equilibrium phase is shown schematically in figure 4.2. Figure 4.3(a) shows the metastable sediment height against colloid volume fraction. One finds a linear relation which, if one assumes that all the particles are contained in the sediment, leads to a sediment volume fraction ϕ_{sed} shown in figure 4.3(b). Interestingly it suggests that a non-equilibrium sample of colloid volume fraction $\phi \geq 0.48$ would not sediment i.e. the structure would possess an infinite latency time.

The time dependence of the sediment heights are shown in figures 4.4(a), 4.4(b) and 4.5 for volume fractions $\phi \sim 0.02, 0.1$ and 0.4 respectively. The exact nature of

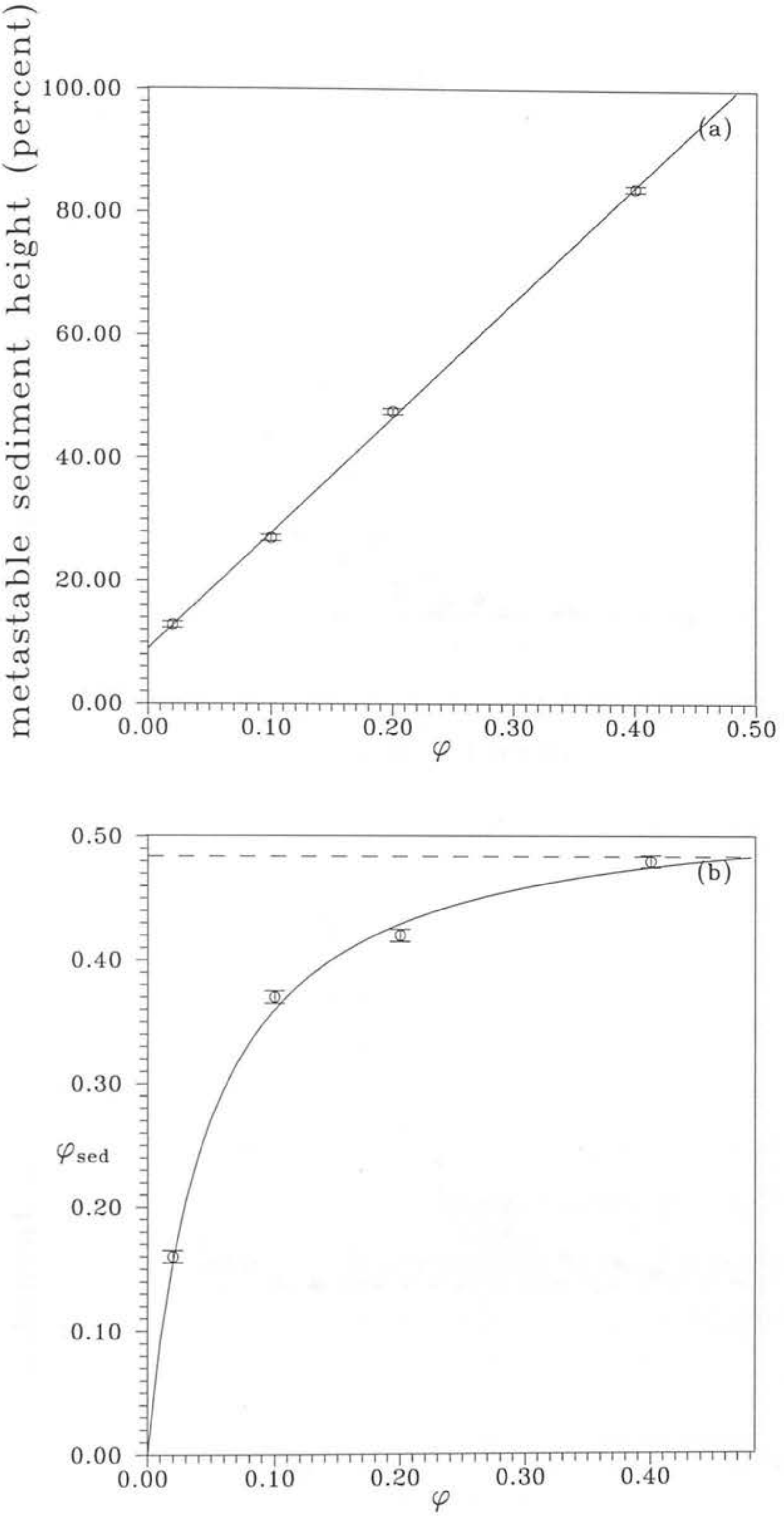

Figure 4.3. (a) Metastable sediment height against colloid volume fraction. (b) Volume fraction of the metastable sediment against colloid volume fraction.

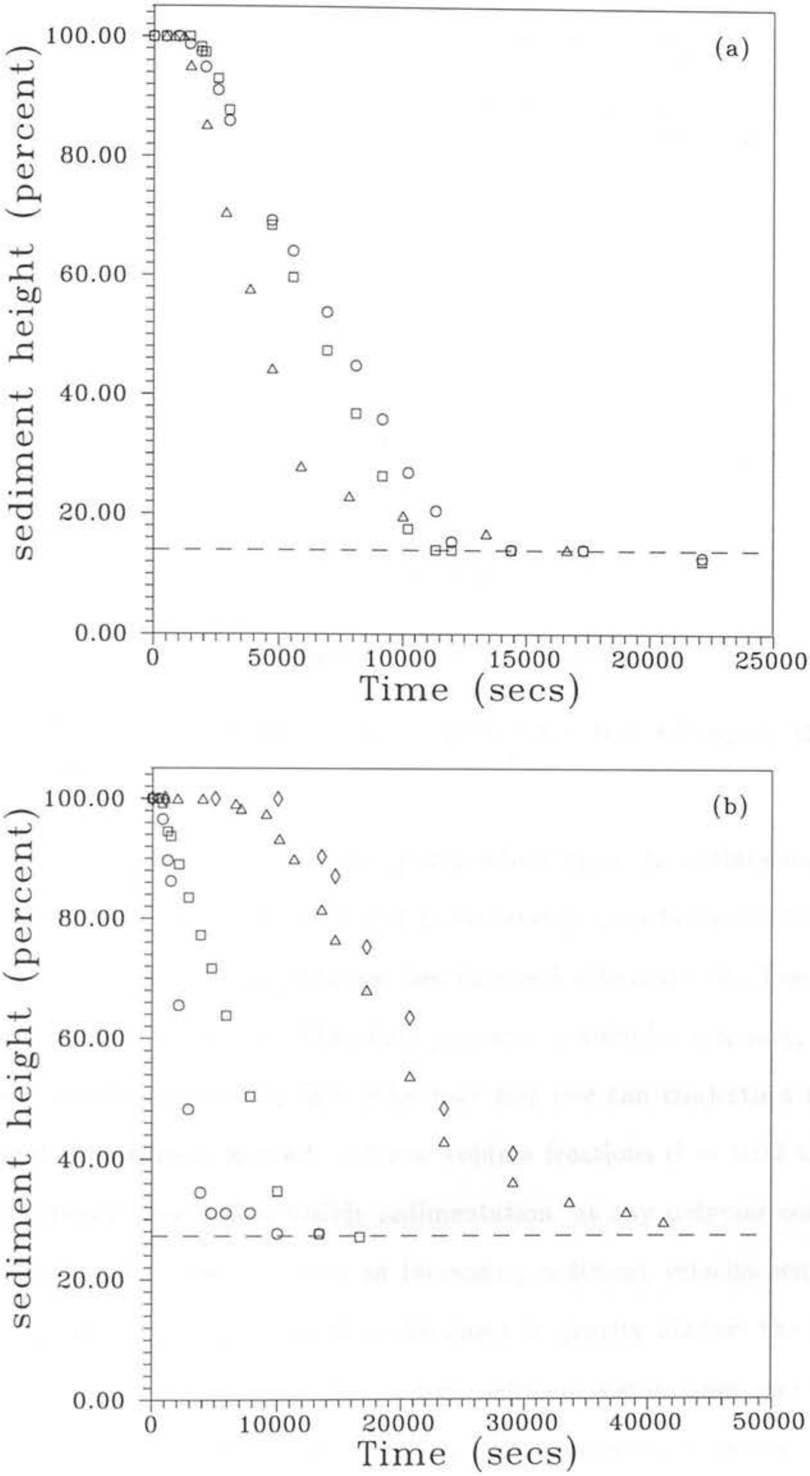

Figure 4.4. (a) Sediment height against time for $\phi = 0.02$. Circles $\equiv$ 2, Squares $\equiv$ 3 and Triangles $\equiv$ 4. (b) Sediment height against time for $\phi = 0.1$. Circles $\equiv$ 5, Squares $\equiv$ 6, Triangles $\equiv$ 7 and Diamonds $\equiv$ 9. Note the reversal of trend with polymer concentration.

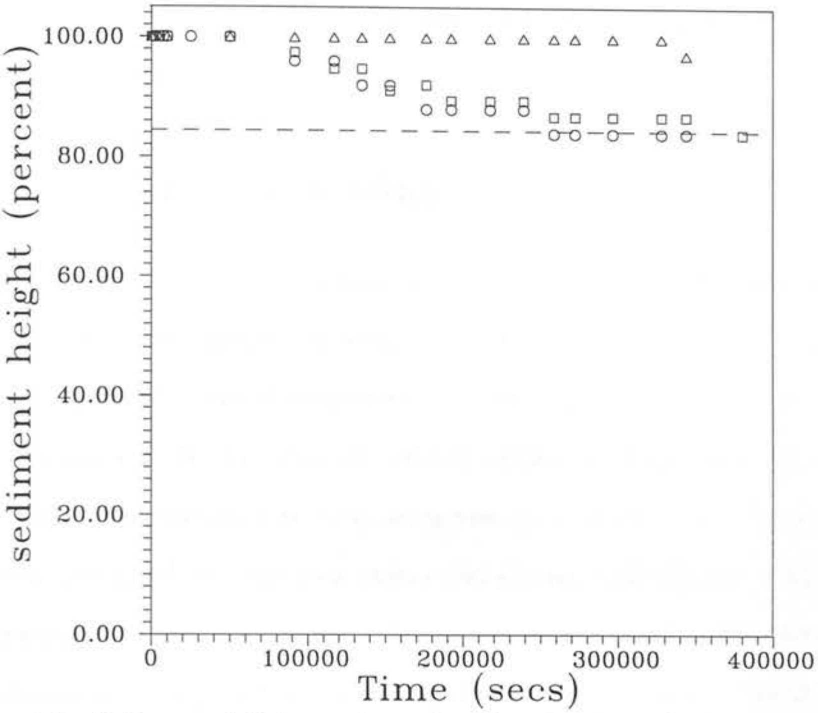

Figure 4.5. Sediment height against time for $\phi = 0.4$. Circles ≡ 13, Squares ≡ 14 and Triangles ≡ 15.

the sedimentation is found to be highly dependent upon the initial colloid volume fraction. For large volume fractions, $\phi \geq 0.1$, the latency time before visible sedimentation increases with polymer concentration (see figures 4.4(b) and 4.5). The sediment velocity concomitantly decreases. The slight increase in solution viscosity, with additional polymer, cannot account for this behaviour and one can conjecture that an increasingly rigid structure is formed. At low volume fractions $\phi \sim 0.02$ there appears to be little latency time before visible sedimentation, at any polymer concentration (see figure 4.4(a)). One also observes an increasing sediment velocity with polymer concentration. One can conjecture that the effect of gravity hinders the formation of an interconnected structure, i.e. the clusters sediment before they can percolate, then larger clusters will be formed as the interparticle potential is increased, and will sediment faster than those formed at low polymer concentrations. Allain et al. [93] in a recent study of salt-induced aggregates find an increasing latency time and decreasing sediment velocity as the colloid volume fraction is increased, consistent with that shown in figures 4.4 and 4.5.

4.3 Small angle scattering

A ring in the small angle scattering is observed for all non-equilibrium samples studied, which brightens and collapses to smaller angles over time [18]. The ring eventually fills in to leave peaked forward scattering. These rings indicate the formation of large scale structures with characteristic length scales far larger than individual particle radii. This phenomenon has been observed in a variety of colloidal systems which have been quenched into unstable states and appear qualitatively similar to spinodally decomposing systems (i.e. when a thermodynamically unstable system undergoes a spontaneous phase separation (see Chapter 2, section 2.2.3)). Small angle rings are also observed in diffusion limited cluster aggregation (DLCA) at high density [43], [44]. The DLCA model is a process in which one has an ensemble of monomers which undergo random diffusion. When monomers collide they form irreversible clusters. The resulting clusters diffuse and aggregate until all that remains is a single system spanning gel. The similarities between this model and the colloid-polymer non-equilibrium phase will be discussed later.

4.3.1 Experimental setup

To measure the intensity at small angles (approximately 0 - 10^0), a new apparatus was built as shown in figure 4.6. It comprises a focused laser beam incident upon a sample which scatters light from large scale density fluctuations onto a thin white screen, in the forward direction. The scattered radiation is then monitored by a CCD camera, positioned behind the screen. The signal is recorded onto video cassette and stored for future analysis. Throughout this procedure the incident beam is monitored,

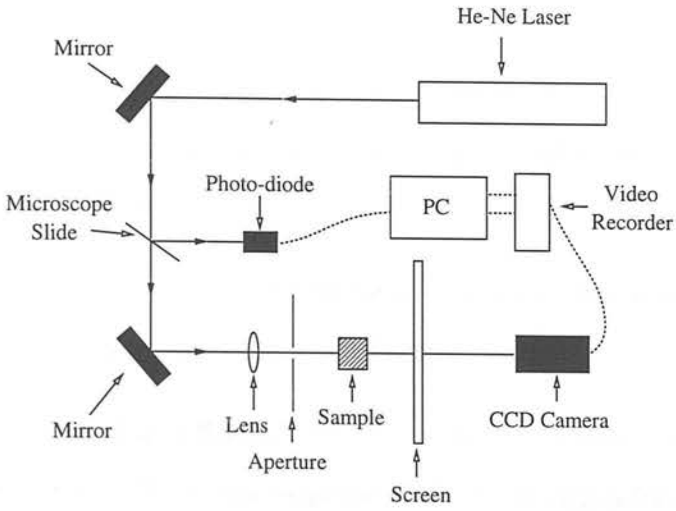

Figure 4.6. Small angle scattering apparatus.

using a photo diode, to ensure that any laser intensity fluctuations are accounted for. To analyse the scattered radiation the video recorder is attached to a PC with an 8 bit digitiser board (256 different grey scale levels), which stores single images and using external software the angular dependence of the scattered light can be calculated. The program essentially takes the image and integrates the measured pixel values from the centre outward, in annuli of set widths (usually 0.2^0 steps). The signal processing procedure takes into account refraction and reflection at the cell-air interface, the polarisation dependence of the light as it strikes the screen and subtracts contributions from external light sources. The angular dependence from an image without the sample in place is subtracted from all the subsequent data sets.

When light is shone through a non-equilibrium sample the transmitted intensity decreases, due to a time dependent turbidity i.e. multiple scattering increases as clusters form. At most an 18% loss in transmission was observed from the most turbid non-equilibrium samples over the time scale of a typical experiment. Accordingly multiple scattering effects will remain small in these experiments, and can be neglected in any further analysis of the scattering patterns.

recent study of salt-induced aggregates find an increasing latency time and decreasing sediment velocity as the colloid volume fraction is increased, consistent with that shown in figures 4.4 and 4.5.

4.3 Small angle scattering

A ring in the small angle scattering is observed for all non-equilibrium samples studied, which brightens and collapses to smaller angles over time [18]. The ring eventually fills in to leave peaked forward scattering. These rings indicate the formation of large scale structures with characteristic length scales far larger than individual particle radii. This phenomenon has been observed in a variety of colloidal systems which have been quenched into unstable states and appear qualitatively similar to spinodally decomposing systems (i.e. when a thermodynamically unstable system undergoes a spontaneous phase separation (see Chapter 2, section 2.2.3)). Small angle rings are also observed in diffusion limited cluster aggregation (DLCA) at high density [43], [44]. The DLCA model is a process in which one has an ensemble of monomers which undergo random diffusion. When monomers collide they form irreversible clusters. The resulting clusters diffuse and aggregate until all that remains is a single system spanning gel. The similarities between this model and the colloid-polymer non-equilibrium phase will be discussed later.

4.3.1 Experimental setup

To measure the intensity at small angles (approximately 0 - 10^0), a new apparatus was built as shown in figure 4.6. It comprises a focused laser beam incident upon a sample which scatters light from large scale density fluctuations onto a thin white screen, in the forward direction. The scattered radiation is then monitored by a CCD camera, positioned behind the screen. The signal is recorded onto video cassette and stored for future analysis. Throughout this procedure the incident beam is monitored,

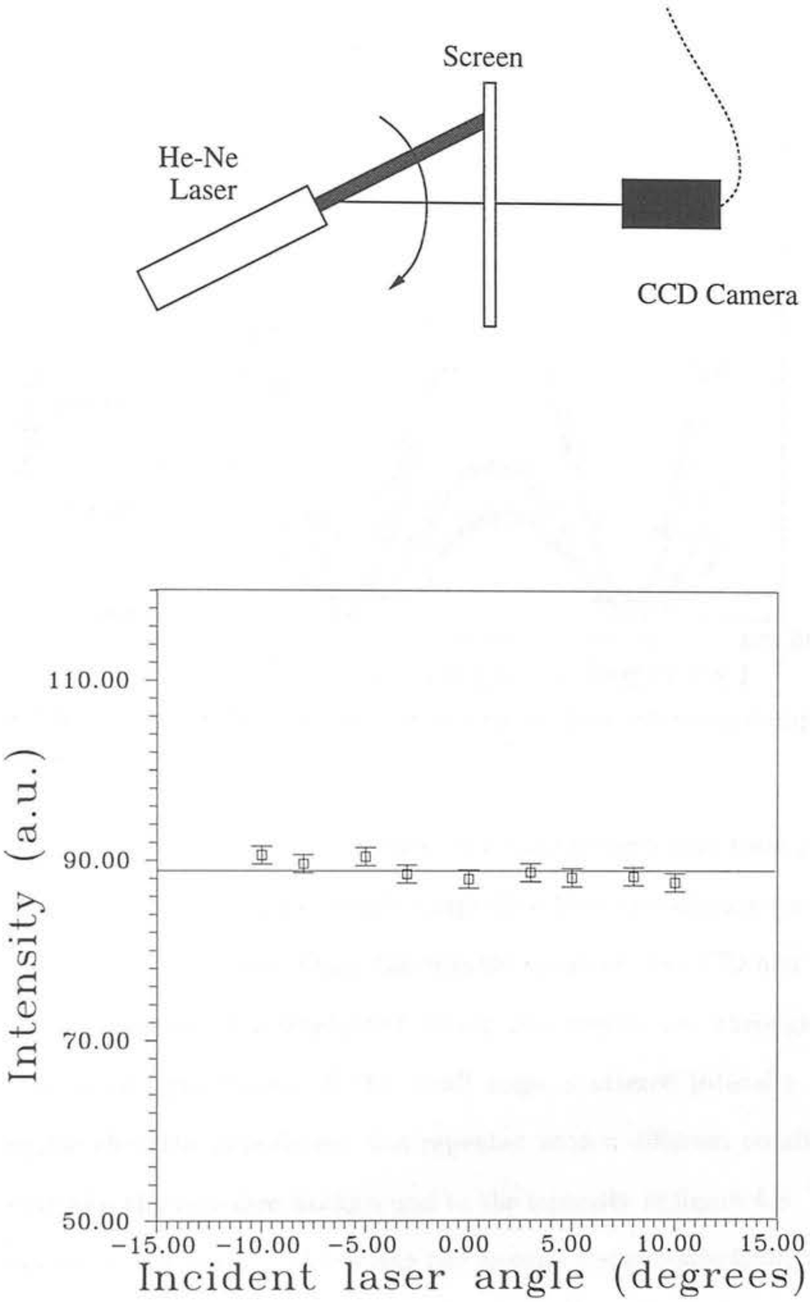

Figure 4.7. Detected intensity vs incident angle of laser: experimental setup and results. Note that within error the $cos(\theta)$ correction to the illuminated area is negligible over such a small angular range.

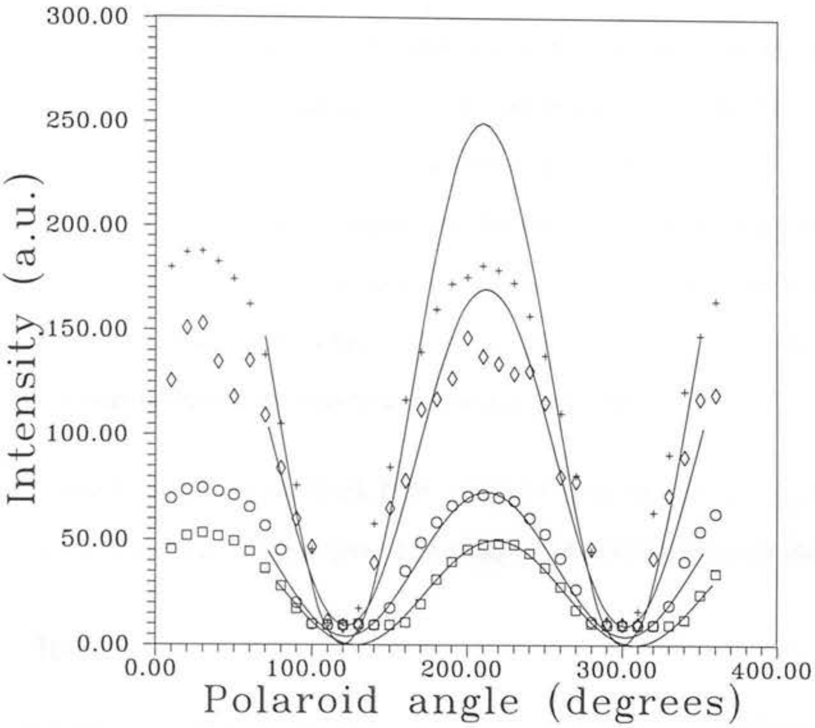

Figure 4.8. Crossed polaroids with increasing incident intensity, compared to a $cos^2(\theta)$ dependence (solid line).

scattered from a circular aperture. By conducting these tests it was found that the camera had a small dynamic range (less than two decades) and was unreliable at very low intensities. Once the reliable range of the CCD had been determined all experiments were conducted within this regime i.e. through the addition or removal of light filters. If the small angle scattered intensity fell outwith this regime then the experiment was repeated with a different combination of filters. Note also the non-zero background to the intensity in figure 4.8. This background was accounted for by subtracting the angular dependence from an image without the sample in place from all the subsequent data sets.

- To test the analysis code, circles were drawn on a sheet of paper, and the camera was positioned so that the circles subtended known angles in the image. The code was then used to measure the intensity pattern from the centre of the drawn circle outward. This was found to be accurate to within $< 1\%$.

- In a scattering experiment all detected intensities were recorded on video tape. To test this procedure intensities were taken directly from the camera, and from video tape, and were found to be identical to within $< 1\%$. The video tape speed was found to be invariant to the position of the tape (either toward the start or end), but the recorded time was found to be 1.02 times slower than real experimental time. Therefore in all the experiments conducted a conversion factor was included in converting counter readings to real time.

Many thanks must go to Mark Haw who not only helped me conduct these tests, but provided the image integration code used in the subsequent experiment.

4.3.3 Results

A typical time evolution of scattered intensity[1] $S(Q)$ is shown in figure 4.9 for a colloid volume fraction $\phi \sim 0.1$ and polymer concentration just sufficient to induce aggregation (sample 5). The measurement was carried out after an initial homogeneous mixing of the sample i.e. the sample was shaken vigorously for a few seconds. An associated speckle pattern is shown below. To aid the procedure of estimating the peak position $Q_m a$ and height $S(Q_m a)$ the data points were fitted with a polynomial of high order (4 or more), as shown in figure 4.9. Immediately one can see a marked similarity between this behaviour and classical spinodal decomposition [42] as one finds a brightening and collapsing small angle ring. The speckle pattern associated with this sample fluctuated rapidly and the scattered ring collapsed continuously to leave peaked forward scattering. From this point onward I will refer to such behaviour as 'spinodal-like'.

As the polymer concentration is increased one observes similar behaviour until the highest polymer concentrations (sample 9) when the ring becomes frozen at a finite

---

[1] $S(Q) \equiv I(Q)$ assuming the form factor to be constant over this short region, an assumption which will be discussed later.

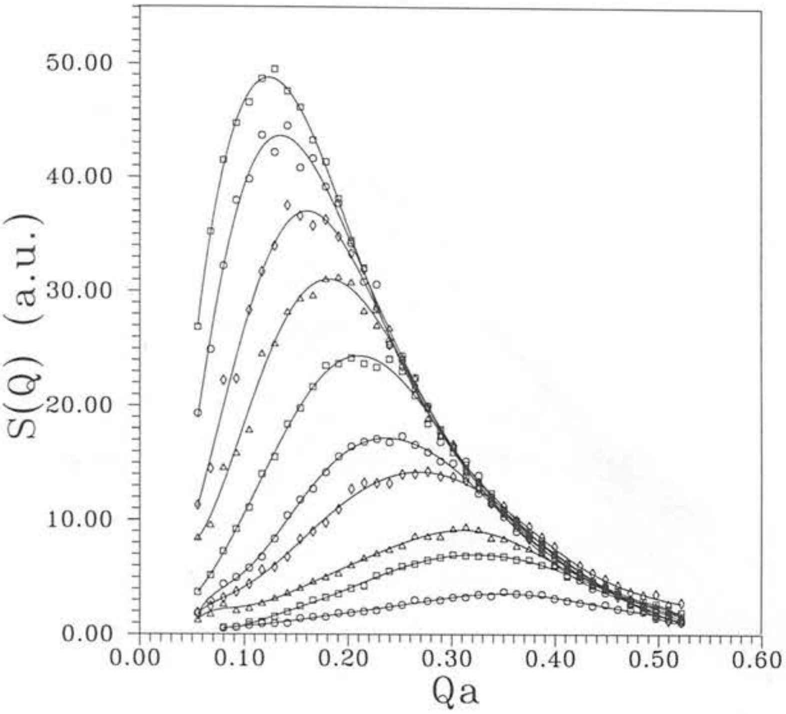

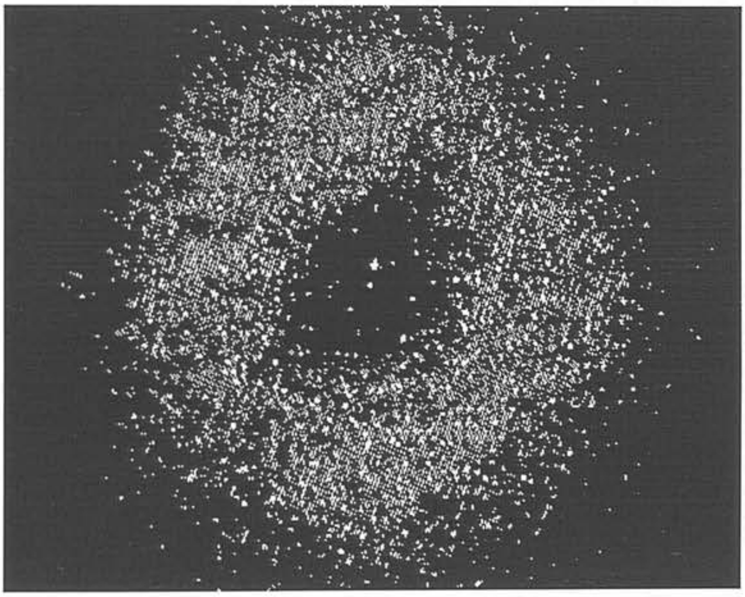

Figure 4.9. Temporal evolution of the small angle structure factors from sample 5. The curves represent times 12, 22, 27, 42, 63, 83, 103, 123, 143 and 164 seconds, respectively from bottom to top. The ring collapses continuously to yield peaked forward scattering. Below is an associated speckle pattern.

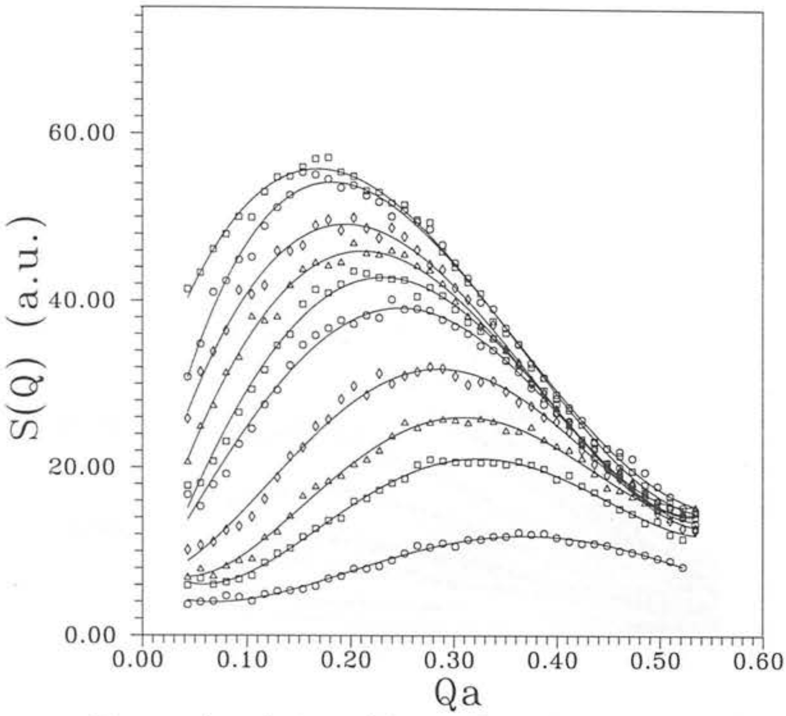

Figure 4.10. Temporal evolution of the small angle structure factors of sample 9. The curves represent times 4, 9, 14, 24, 54, 84, 164, 384, 884 and 1684 seconds, respectively from bottom to top. Note that the small angle peak becomes arrested at a finite wavevector.

wavevector, as shown in figure 4.10. The scattered speckle pattern fluctuates slowly (~ *minutes*) indicative of very slow cluster diffusion. One then observes a latency time before visible sedimentation (see figure 4.4(b)). Pre-empted by a sudden speckle fluctuation (i.e. the onset of rapid particle motion), the ring collapses rapidly, roughly coincident with the onset of visible gravitational settling. This again proceeds to peaked forward scattering. As a frozen speckle pattern would suggest an arrested large scale structure I will now refer to such behaviour as 'transient-gelation'. As this regime is the only type which shows frozen-in structure, it can be argued that this is the only true gel state.

A distinctly different phenomenon is observed at low volume fractions $\phi \sim 0.02$, the respective samples given by table 4.1. At low polymer concentrations, such as sample 1,

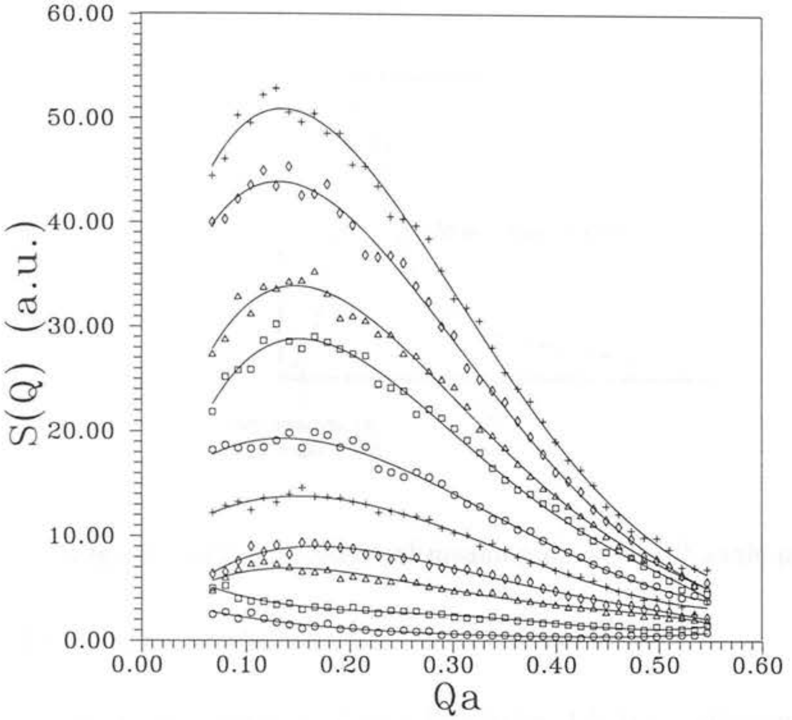

Figure 4.11. The time evolution of the small angle scattering from sample 1, representing times 17, 50, 90, 121, 156, 193, 230, 280, 330 and 388 seconds respectively from bottom to top.

there is a 'lag time' before the observation of a small angle ring (see figure 4.11). One observes a peaked forward scattering with rapidly fluctuating speckles, which forms a ring after approximately 70 seconds. Once the ring has formed it slowly collapses, while the speckle pattern fluctuates rapidly. A lag-time is a well known observation in classical nucleation [94] and such behaviour will be referred to as 'nucleation-like'. As the polymer concentration is increased one again finds a rapidly collapsing ring without a lag time (spinodal-like), leading to an arrested speckle pattern at still higher polymer concentrations (transient-gelation), although one never finds a completely frozen ring. One can conjecture that the system never gels up at this low volume fraction i.e. the absence of a frozen ring.

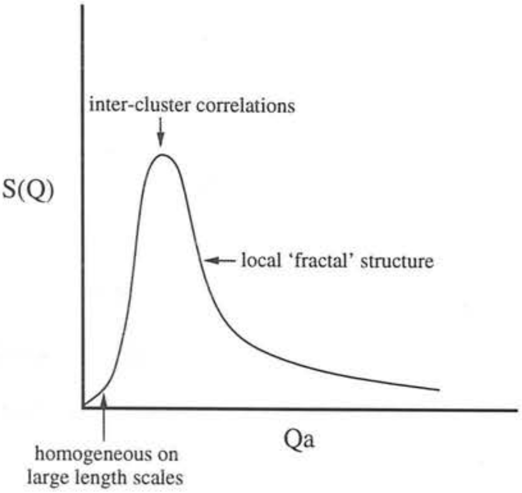

Figure 4.12. The physical meaning of the small angle peak.

4.3.4 The small angle peak

Before discussing the kinetics of cluster formation it is instructive to first discuss the shape of the small angle peak, and the physics which underlies this phenomenon. As shown in figure 4.12 the shape of the small angle structure factor can be linked to the structure of the system over a wide range of length scales.

It is well known from experiment that just to the right of the peak one observes the influence of the local 'fractal' structure within clusters [95]. The fractal [96] (or fractional) dimension d_f can be defined as relating the number of particles within a cluster, N, to the radius of gyration of that cluster, R_g,

$$N \sim \left(\frac{R_g}{a}\right)^{d_f} \tag{4.1}$$

For a dense cluster, in three dimensions, $d_f = 3$ i.e. equal to the Euclidean dimension, whereas for a linear cluster $d_f = 1$, and therefore the fractal dimension will always lie between these two extremes. As a consequence of equation (4.1) one can then write the particle density within a cluster, in a sphere of radius r, as [97],

$$C(r) \sim r^{(d-d_f)} \tag{4.2}$$

where d is the spatial dimension. This can also be regarded as the probability of finding a cluster at a distance r given one at the origin. In a scattering experiment the structure factor will simply take on the form of the Fourier transform of this correlation function i.e.,

$$S(Q) \sim Q^{-d_f} \tag{4.3}$$

Therefore to the right of the peak one can usually observe a power law regime, with an exponent of the fractal dimension.

The marked peak in the structure factor represents the effect of inter-cluster correlations. The origin of the small angle peak has been discussed in terms of both experiment [54] and simulation [43], [44], [98]. In both DLCA and spinodal decomposition simulation, it has been shown that the peak arises from the formation of depletion zones around clusters, leading to large scale correlated density fluctuations. Indeed any density fluctuation which has a radial distribution function $g(r)$, similar to that shown in figure 4.13, once Fourier transformed, will lead to the formation of a peak i.e. A large local density within a cluster, surrounded by a region where the average density is less than the average homogeneous density found far from the cluster.

At low wavevectors, $Qa \to 0$, the structure factor exhibits a marked minimum. This reflects a lack of structural correlations and homogeneous structure at the largest length scales.

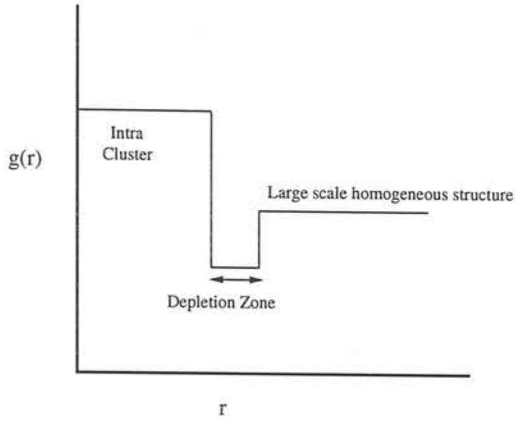

Figure 4.13. A typical radial distribution function which leads to the formation of a small angle peak.

4.3.5 Ring kinetics

In this section we examine the time dependence of the small angle scattering peak positions and intensities, firstly for a fixed volume fraction $\phi \sim 0.1$ and varying polymer concentration (figure 4.14), details of which are given in table 4.1.

The peak intensities shown in figure 4.14 are normalised relative to sample 5. To normalise the various samples relative to one another, as all the samples had slightly different index match conditions, the following procedure was adopted. Firstly the samples were centrifuged for a number of hours, a few particles were then redispersed and individual form factors measured from each sample (see section 4.6). Samples with slightly more redispersed particles scattered strongly, but as discussed in section 3.3.1 form factors are known to be invariant to the solvent refractive index at $Qa \sim 4.49$. Therefore all form factors were normalised so that they coincided at this point. The total scattered intensity was measured from the fully redispersed samples and divided by the appropriate normalised form factor. The prefactors which separated these structure factors were then multiplied to the small angle peak intensities.

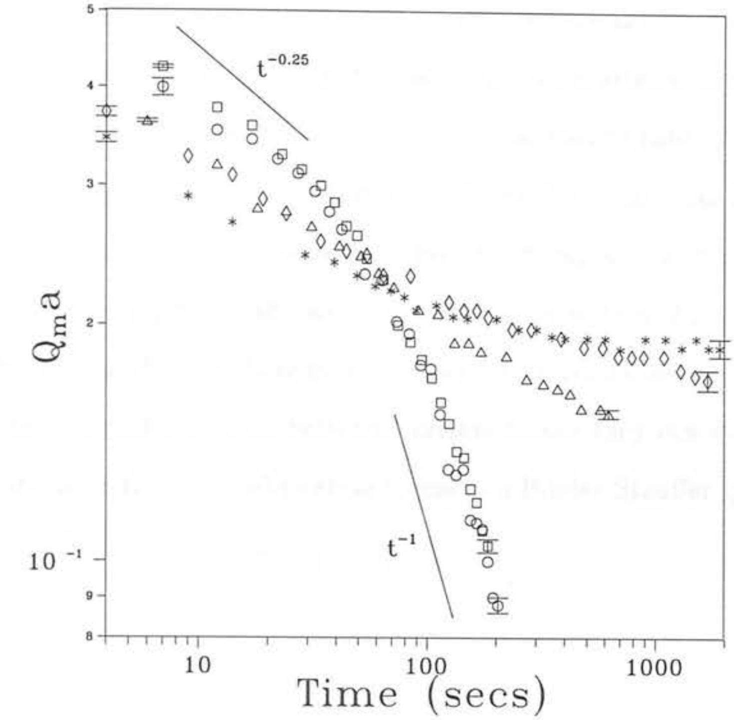

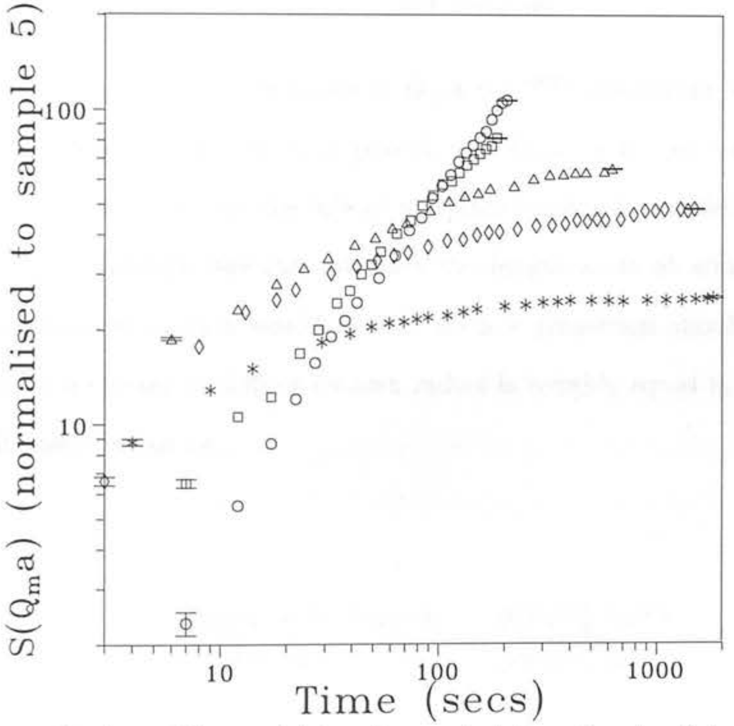

Figure 4.14. Peak position and intensity against time for $\phi \sim 0.1$. Circles ≡ sample 5, Squares ≡ sample 6, Triangles ≡ sample 7, Diamonds ≡ sample 8 and Asterisks ≡ sample 9.

A cross-over is observed in the time evolution of the peak position for the spinodal-like sample containing the least amount of polymer (sample 5). The speckle pattern associated with this sample fluctuated rapidly and the scattered ring collapsed continuously to leave peaked forward scattering. An initial growth rate, $Q_m a \sim t^{-0.25}$ crosses over to a late stage growth rate, $Q_m a \sim t^{-1.0}$. Such a cross-over has been observed previously in fluid systems undergoing spinodal decomposition, where the growth exponent crosses from $\frac{1}{3}$ to 1 [48], as was discussed in section 2.2.4. If one takes into account the effects of hydrodynamics one finds a slower initial growth rate i.e. fluid must first be squirted out from between clusters before they can coalesce. Siggia [48] showed that the inclusion of lubrication forces in a Binder-Stauffer type argument lead to a growth rate,

$$Q_m a \sim \frac{t}{ln(0.55/Q_m a)} \tag{4.4}$$

which at intermediate times scales as $Q_m a \sim t^{-0.25}$, consistent with that observed here. The observed cross-over to a growth rate $Q_m a \sim t^{-1}$ is consistent with that driven by surface tension, yet the role of a surface tension in colloid-polymer mixtures is unclear. Alternatively one can estimate the length scale at which a cross-over to a gravity-dominated motion would occur. Such a transition should occur when the time taken for a cluster to diffuse its own radius is roughly equal to the time taken to sediment its own radius i.e.,

$$\frac{Time\ taken\ to\ diffuse\ R_g}{Time\ taken\ to\ settle\ R_g} \sim \frac{(6\pi\eta R_g^3/k_BT)}{(9\eta/2R_g\ \Delta\rho\ g)} \sim 1 \tag{4.5}$$

where R_g is the radius of gyration of the clusters, $\Delta\rho$ is the difference in density between the particles and the solvent, η is the solvent viscosity and g is the acceleration due to gravity. Therefore,

$$(R_g)^4 \sim \frac{k_B T}{\Delta\rho\, g} \tag{4.6}$$

implying that one should start to see the effect of gravity at a wavevector $Qa \sim \frac{2\pi a}{R_g} \sim 0.24$ directly consistent with the observed cross-over. Therefore one can conjecture that the cross-over is purely the observation of a gravity dominated sedimentary motion.

As the interparticle potential is increased, the initial growth rate stays constant $Qa \sim t^{-0.25}$ whereas the late stage growth slows until the most concentrated case where the small angle ring has become essentially arrested at a finite wavevector (see Asterisks in figure 4.14(b)). One no longer observes a cross-over in the growth rate as the rigidity of the resulting structure prevents sedimentation i.e. the system gels up.

One possible explanation of this observed slowing down and eventual arrest of the system is that there exists a competition of time scales between the formation and rearrangement of interparticle bonds. These are characterised by two time scales, the characteristic time for bond formation τ_F and subsequent rearrangement τ_R. The early stage growth is independent of bond strength, indicative of the insensitivity of bond formation to details of the attractive potential. This is consistent with a diffusional growth regime. For a weak potential the bonds can rapidly rearrange $\left[\tau_F > \tau_R(\frac{V}{kT})\right]$. As the bonds become stronger the rearrangement time becomes extremely long $\left[\tau_R(\frac{V}{kT}) > \tau_F\right]$ and the structure becomes essentially frozen for the most rigid bonds. This slow particle motion (rearrangement), one can conjecture, weakens the structure through compacting the local structure until the system no longer percolates. The independent clusters then sediment under gravity.

In Monte Carlo simulation of phase separating systems [99] it has been shown that one finds ‘spinodal-like’ behaviour at low interparticle attractions which becomes arrested as the interparticle attraction is increased. If the particle coordinates are Fourier transformed one finds a scattered ring at low Q vectors which becomes frozen at a finite wavevector when the interparticle potential is increased sufficiently. Despite the exclusion of fluid flow and gravitational effects in the simulation the similarity to that of figure 4.14 is striking.

Similar slow growth and eventual arrest of the structure with an increasing quench depth has been seen in binary polymer mixtures undergoing spinodal decomposition [100] - [105] attributed to a 'pinning' of the underlying structure and a 'dynamical percolation to cluster transition' i.e. a system-spanning structure degenerates into dense clusters of droplets, driven by the desire to minimise the interfacial free energy, as discussed in section 2.2.4. Although surface tension is not expected to play a role, the possibility of a percolation to cluster transition in the colloid-polymer non-equilibrium states, which could be responsible for the gravitational collapse, will be discussed later.

As the colloid volume fraction is increased, one observes similar behaviour to that seen at $\phi \sim 0.1$ but the polymer concentration required to induce an aggregated state with an arrested structure reduces dramatically. At $\phi \sim 0.2$, for the three samples described in table 4.1, one observes the temporal evolution of the peak position and peak intensity shown in figure 4.15. Again one observes a cross-over in the growth rate at low polymer concentrations, approximately $Qa \sim t^{-0.25}$ to $Qa \sim t^{-1}$, leading to a frozen ring at high polymer concentrations. Indeed the phenomenology is similar to that observed at $\phi \sim 0.1$.

If the volume fraction is increased further to $\phi \sim 0.4$ one no longer observes a region which follows classical spinodal decomposition. At this volume fraction one observes a frozen speckle pattern, no matter the polymer concentration. For even small amounts of polymer (see sample 14 or 15 in table 4.1) the gel can remain in an arrested state for days, without the speckle pattern evolving. The latency time before visible sedimentation increases with polymer concentration and for the most concentrated lasts for many days (see figure 4.5). If a sample is prepared with just

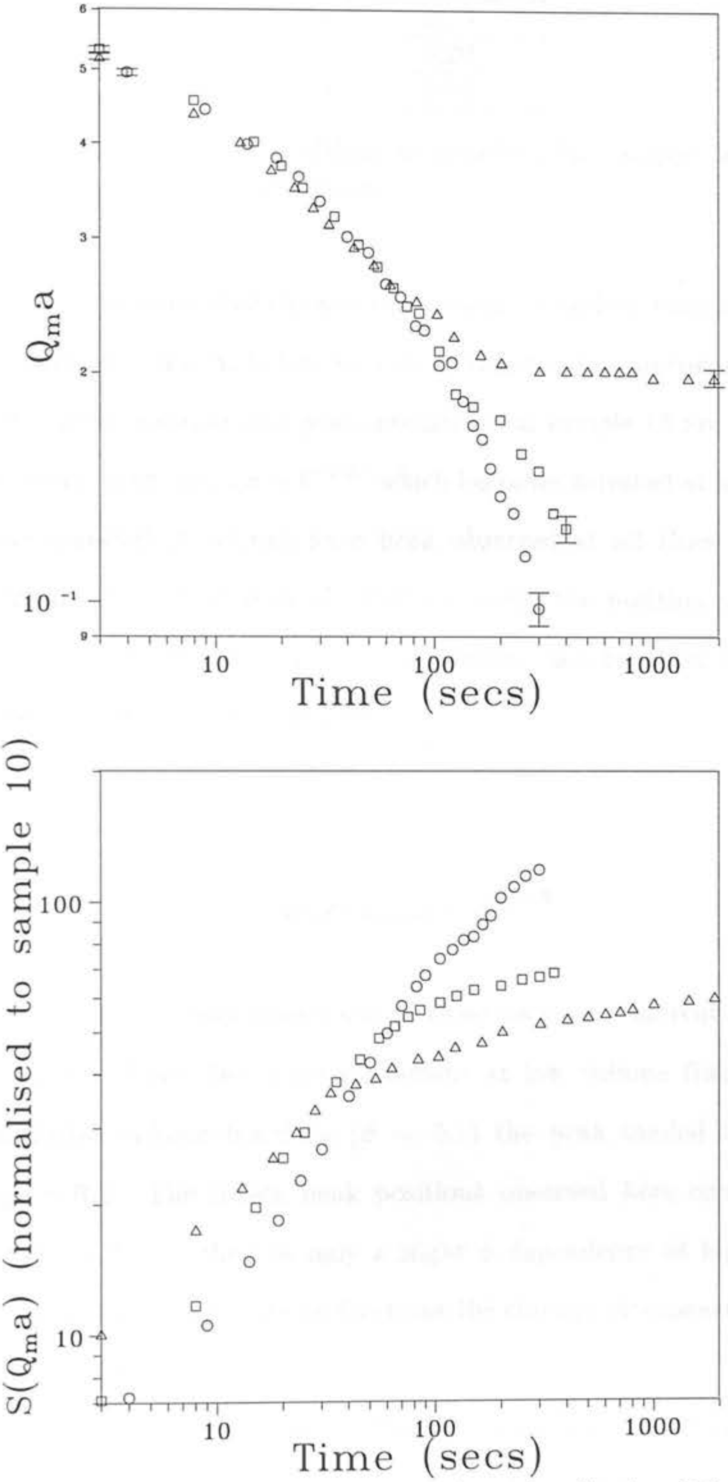

Figure 4.15. Peak position and intensity against time for $\phi \sim 0.2$. Circles ≡ sample 10, Squares ≡ sample 11 and Triangles ≡ sample 12.

ϕ	$(Q_m a)_{gelation}$
0.1	0.19
0.2	0.20
0.4	0.24

Table 4.2. Small angle peak positions at gelation, for samples with just sufficient polymer to induce an arrested structure.

sufficient polymer to cross over the non-equilibrium boundary then the speckle pattern does evolve, although slowly, before becoming arrested for approximately one day. In figure 4.16 the peak position and peak intensities for sample 13 are shown. Again one observes an initial growth $Q_m a \sim t^{-0.25}$ which becomes arrested at a finite wavevector.

Therefore arrested structures have been observed at all three volume fractions, $\phi \sim 0.1, 0.2$ and 0.4. Bibette et al. [54] measured the position of the frozen ring, formed by light scattered from emulsion aggregates, as a function of volume fraction, and compared it to the theoretical form,

$$(Q_m a)_{gelation} \sim \phi^{(d_f - 3)} \tag{4.7}$$

The above equation arises from a simple close packing of individual clusters of fractal dimension d_f. They find good agreement at low volume fractions ($\phi \leq 0.01$), whereas at higher volume fractions ($\phi \sim 0.1$) the peak tended toward a constant $(Q_m a)_{gelation} \sim 0.2$. The frozen peak positions observed here compare well to this value (see table 4.2) i.e. there is only a slight ϕ dependence at high density. It can be argued that at these high volume fractions the clusters interpenetrate and equation (4.7) no longer holds.

As discussed, at the lowest volume fraction studied $\phi \sim 0.02$ and at low polymer concentrations (sample 1) one finds a lag-time before the formation of a small angle ring i.e. a finite time before a correlation between clusters is observed. Accordingly

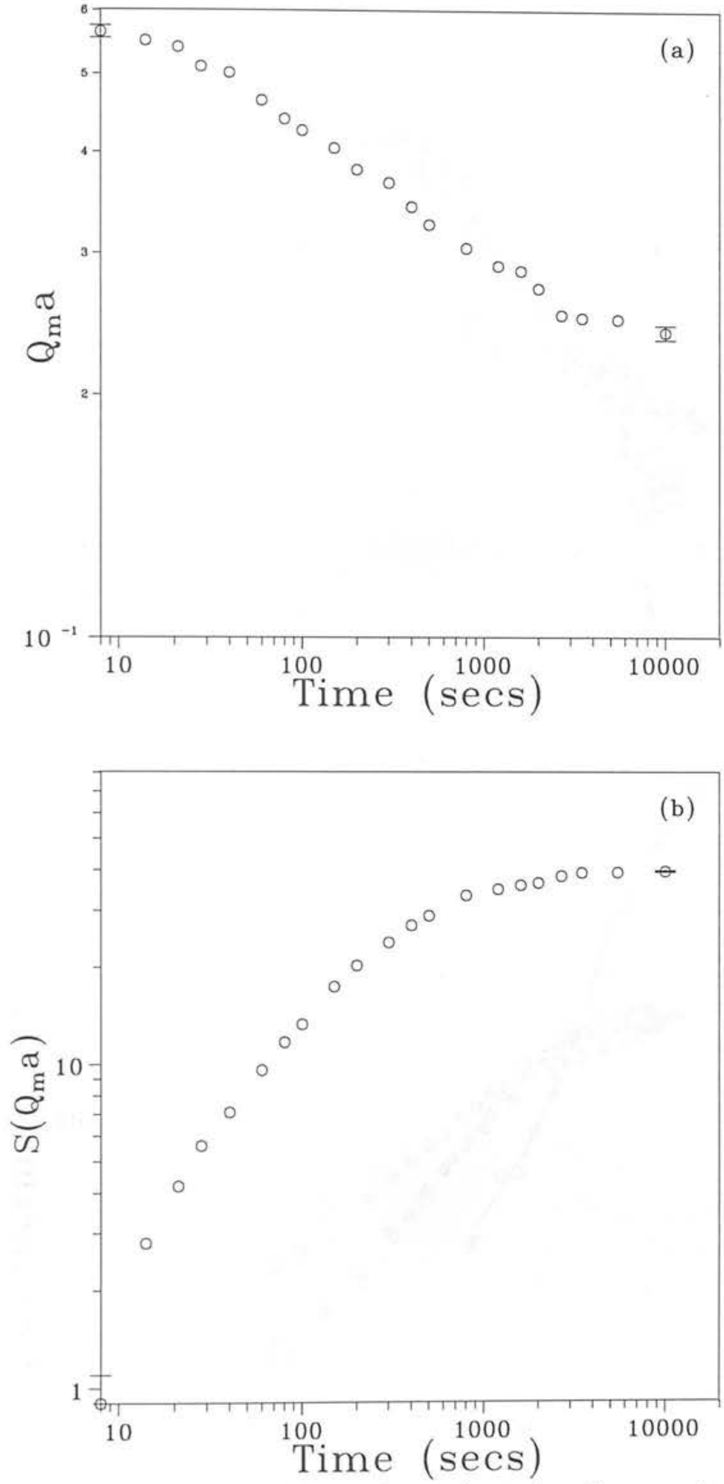

Figure 4.16. Peak position and intensity against time for sample 13, $\phi \sim 0.4$. The data is truncated at the point of the ring freezing. The ring then stays constant for approximately 1 day.

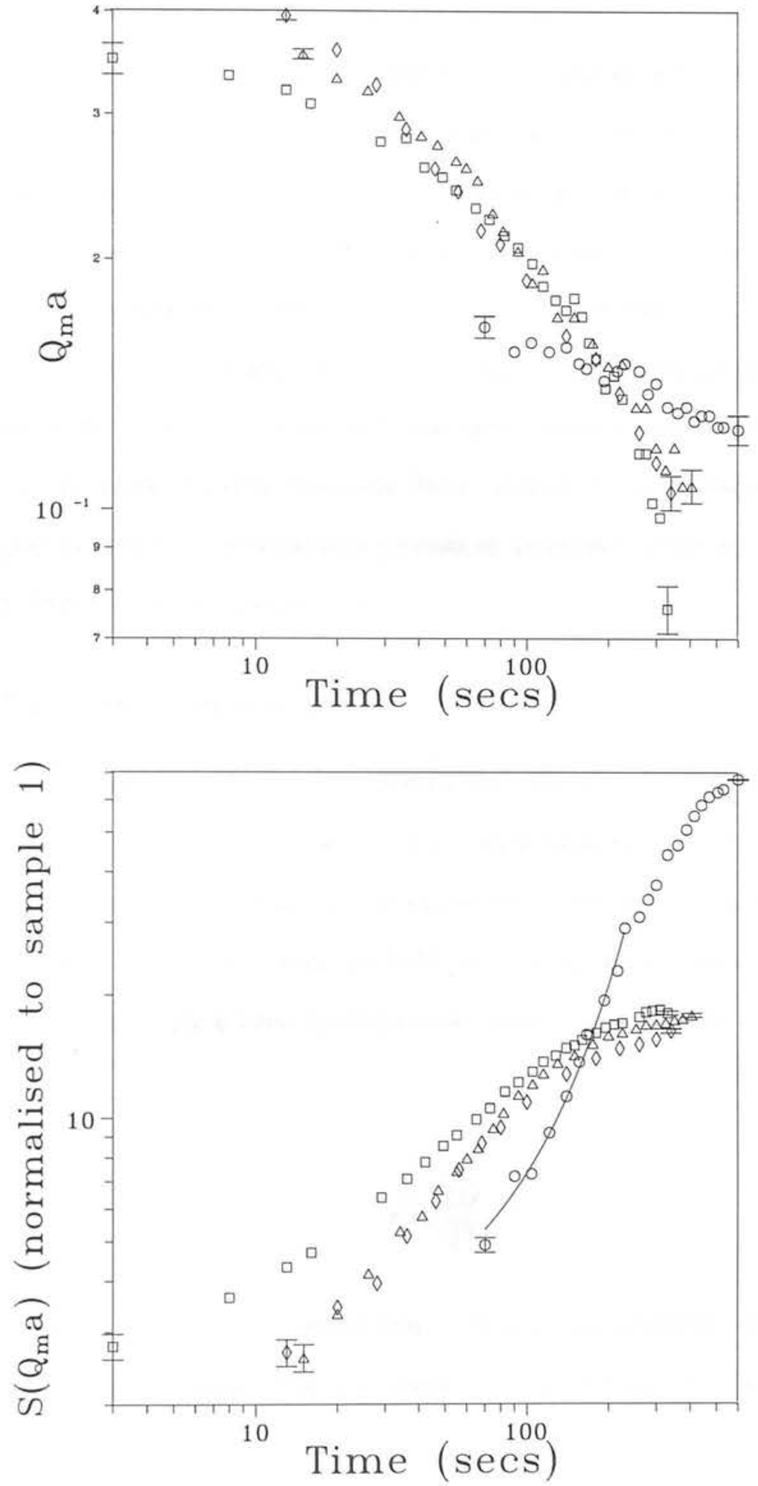

Figure 4.17. Peak position and intensity against time for $\phi \sim 0.02$. Circles ≡ sample 1, Squares ≡ sample 2, Triangles ≡ sample 3 and Diamonds ≡ sample 4. Note that the intensity of sample 1 at early times follows an exponential growth (solid line in lower figure) consistent with linear (Cahn) theory.

this behaviour was called nucleation-like. Once the ring has formed it collapses slowly while the peak intensity grows exponentially at early times, as shown in figure 4.17. A stationary ring with rapidly growing intensity is consistent with linear (Cahn) theory (equation (2.31)). One can use this early time regime to measure the characteristic diffusion coefficient, $D \sim 0.60(a)^2 s^{-1}$, which essentially represents the diffusion coefficient of the correlation length ξ at time zero. Therefore this sample shows classic linear (Cahn) type spinodal kinetics, yet as will be discussed later, visual observation alongside the existence of a 'lag time' would suggest a nucleation type mechanism. As the polymer concentration is increased one again finds a cross-over in the temporal evolution of the peak position (spinodal-like), leading to an arrested speckle pattern at still higher polymer concentrations (transient-gelation), although one never finds a completely frozen ring (see figure 4.17).

4.3.6 'Universal' behaviour

Recently Snyder and Meakin [106] suggested that the kinetics of phase separation are insensitive to the details of the system. They superimpose data from a diverse range of systems, all undergoing spinodal decomposition, ranging from metallic alloys to polymer blends. The data is seen to hold to a good agreement once the time and length scales involved have been appropriately scaled. They define τ the scaled time,

$$\tau = \frac{tD}{\xi^2} \tag{4.8}$$

where t is the (real) experimental time. D is a characteristic diffusion coefficient and ξ is a correlation length both appropriate to the system at time $t = 0$. Similarly they define a scaled wavevector, q_m

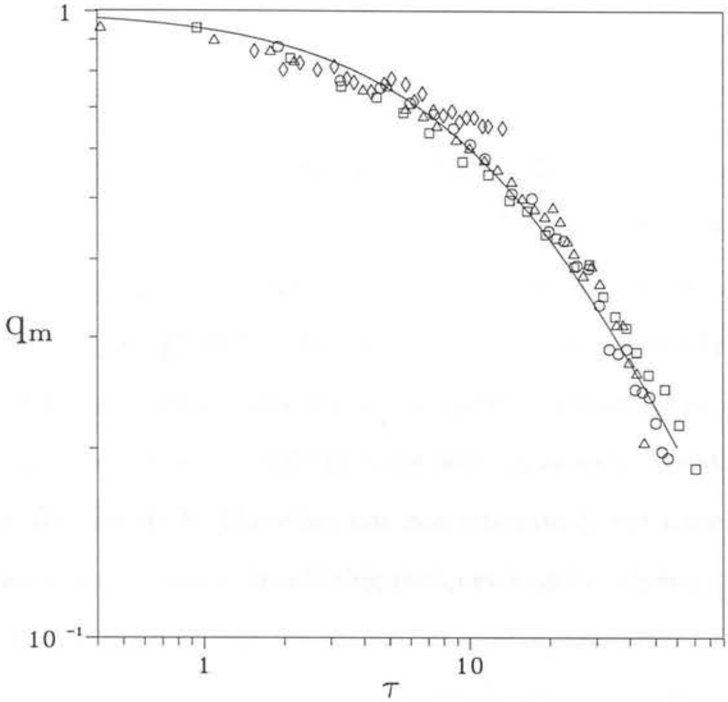

Figure 4.18. Samples 1 (diamonds), 2 (triangles), 5 (circles), and 10 (squares) which have been scaled to the 'universal' fitting form for correlation lengths $\xi \sim 5.2a, 2.7a, 2.2a$ and $1.9a$ and diffusion coefficients $0.60(a)^2s^{-1}$, $0.85(a)^2s^{-1}$, $1.32(a)^2s^{-1}$ and $1.01(a)^2s^{-1}$ respectively.

$$q_m = (Q_m a)\xi \tag{4.9}$$

Scaled quantities such as these have also been used in the work of Langer et al. [39] and Goldburg et al. [50]. Snyder and Meakin suggest that once data has been scaled in such a way, it should all follow an empirical 'universal' scaling function,

$$q_m \sim \tau^{-\chi(\tau)} \tag{4.10}$$

where,

$$\chi = \frac{ln(1+b\tau)}{ln(\tau)} \tag{4.11}$$

b is an arbitrary constant (of the order of 0.05). In principle both D and ξ can be measured experimentally. ξ is approximately $\left[\frac{1}{Q_m a(t=0)}\right]$ and as such can be determined by extrapolating the peak position data back to time zero. D can also be determined from the peak intensity growth in the very short-time linear (Cahn) regime, as discussed in section 2.2.3. Our system phase separates rapidly and there is no region in which one observes a stationary, exponentially growing peak on an experimentally accessible time scale, except for sample 1. Therefore one can estimate ξ, but cannot estimate D. On the other hand one can use D as a fitting parameter and as shown in figure 4.18 a good agreement is observed between the 'universal' scaling behaviour and the spinodal-like samples 2, 5 and 10. Therefore the data presented here is consistent with other systems which undergo spinodal decomposition. Sample 1, the only case where D is measured from the early stage kinetics, rather than fitted, shows a good agreement at early times, although at later times the data tends to diverge from the predicted behaviour. Whether these samples show a true 'universal' behaviour is somewhat dubious, as in general the diffusion coefficients used to scale the data are arbitrary fitting functions and are not measured experimentally. On the other hand the diffusion coefficients used to scale these curves are sensible (see chapter 5), and it appears reasonable that the initial correlation length should decrease with increasing volume fraction. For samples which show an arrested structure (transient-gelation) the initial growth follows the 'universal' scaling, but diverge in the late stage as the system gels.

4.3.7 Fractal geometry

Using the results in the previous section one can examine the 'fractal' nature of the structures formed. Here I utilise the phenomenological time-independent scaling relation, first used to analyse spinodal decomposition, originally suggested by Marro et al. [107],

$$[Q_m a(t)]^d S(x,t) = F(x) \tag{4.12}$$

where $Q_m a$ represents the position of the scattered peak, $x = \left(\frac{Q}{Q_m}\right)$ is the scaled wavevector, $S(x,t)$ the scaled structure factor and d the spatial dimension. $F(x)$ is a time-independent scaling function. If a system shows scaling behaviour then this implies a self-similarity to the structure as it grows i.e. The structure at early times, once magnified, is statistically equivalent to the structure at later times. It has been shown that this relation holds for a spatial dimension $d = 3$ for dense (spinodal) clusters [42]. For ramified structures the spatial dimension d can be replaced by the fractal dimension d_f [55] i.e. once equation (4.12) has been applied to the measured small angle structure factors, one finds that they superimpose for a certain exponent d (or d_f).

By repeating the scaling procedure for a number of different exponents, one can then estimate a fractal dimension which superimpose the measured structure factors over the whole Q range and over the longest possible time. In this set of experiments the scaling exponent, obtained by this method, is generally found to be robust to within ± 0.2. One could also plot the peak intensity against the peak position which should have a power law regime over which one can measure a fractal dimension, as equation (4.12) can be written,

$$S(Q_m a) \sim (Q_m a)^{-d} \tag{4.13}$$

Firstly this method is prone to error as the region over which one fits the power law is usually small and secondly this method only tests the scaling behaviour at the peak rather than throughout the whole Q range. Another alternative is to simply fit the right of the peak to a power law with an exponent of the fractal dimension. In the experiment presented here, only a small high-Q region is available (less than a decade), and as such the results obtained by fitting to a power law are subject to large errors. Interestingly it has been predicted that at high densities the fractal region will be extremely limited [43], [44] as the system will be too dense to allow the growth of large ramified structures. In terms of light scattering the interparticle peak (see section 4.6) interferes with the power law regime and leaves only a very small region over which to fit a fractal dimension. Consequently it has been suggested that the full scaling relation is the *only* method of obtaining a fractal dimension at high densities [108].

If the scaling analysis is carried out for the spinodal-like sample at $\phi \sim 0.1$, sample 5, then the scattered peaks are seen to collapse onto one another for a spatial dimension of $d = 3 \pm 0.2$, to within $\pm 5\%$, consistent with classical spinodal decomposition. What must be stressed is that the scaling only holds for *early* to *intermediate* times ($30 < t < 70$ secs). The scaled data compares well with the Furukawa scaling for spinodal decomposition, as shown in figure 4.19 [109]. The Furukawa scaling prediction is purely a phenomenological relation, and results from comparing the scaled structure factors of numerous atomic systems undergoing spinodal decomposition. The Furukawa scaling relation can be written,

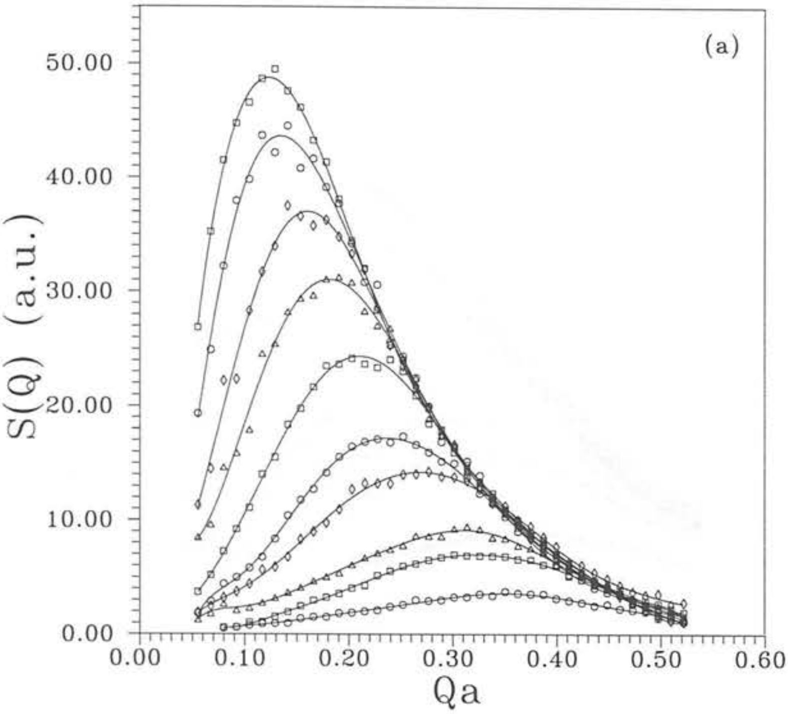

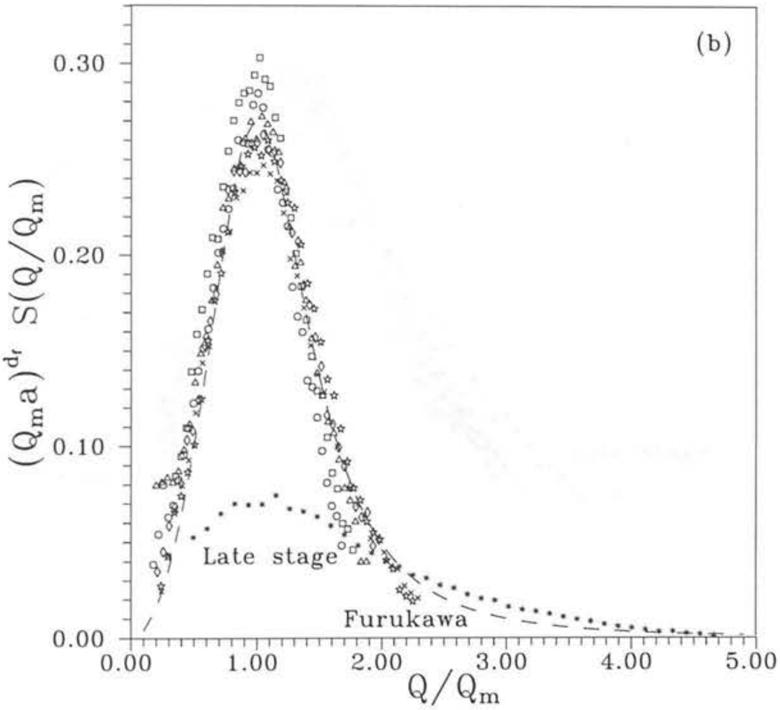

Figure 4.19. (a) Temporal evolution of the small angle structure factors of sample 5. The curves represent times 12, 22, 27, 42, 63, 83, 103, 123, 143 and 164 seconds, respectively from bottom to top. (b) Scaling behaviour of sample 5 for d=3, curves representing times 27, 32, 37, 42, 53 and 63 seconds. The late stage curve corresponds to 164 seconds and the dashed line represents the Furukawa prediction.

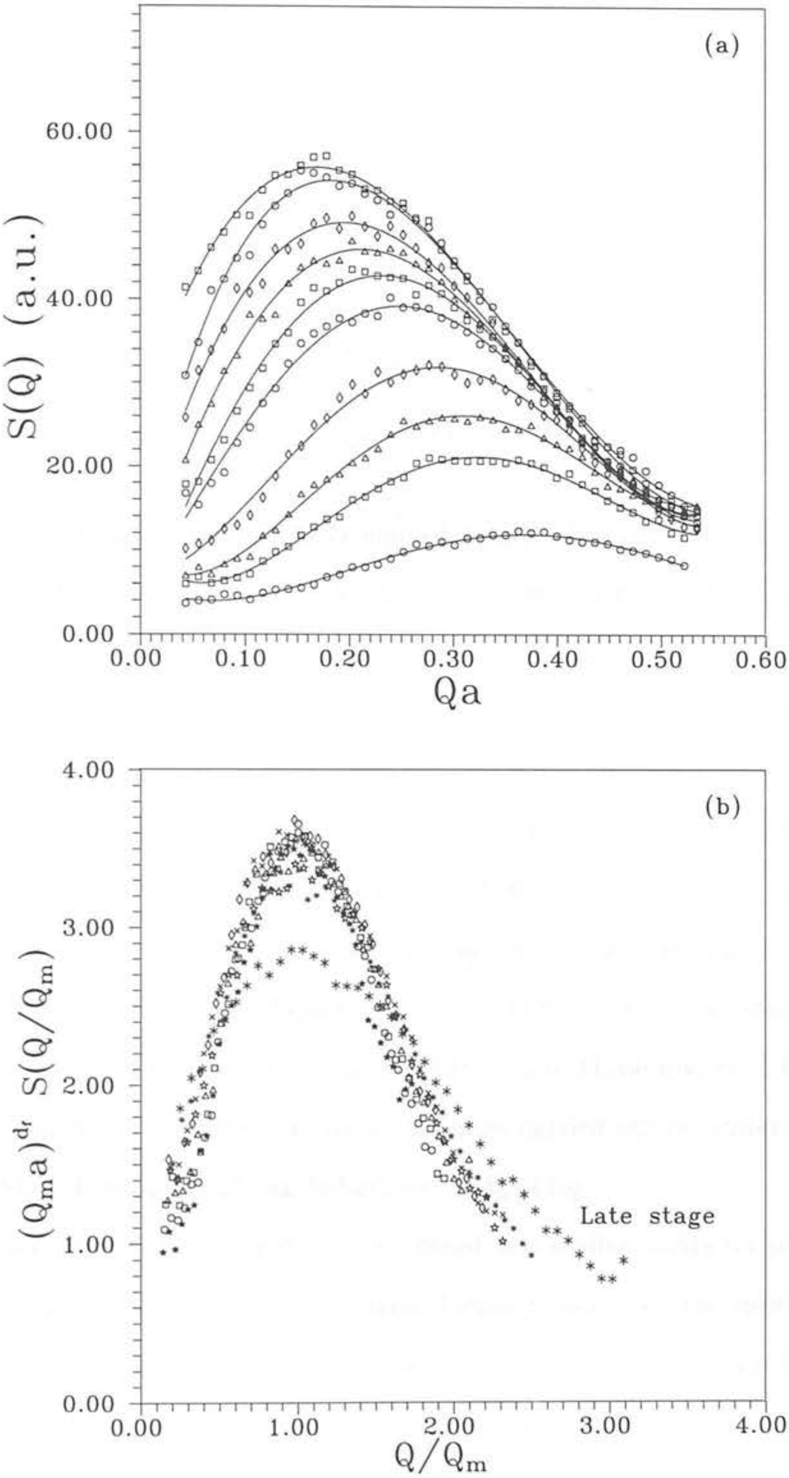

Figure 4.20. (a) Temporal evolution of the small angle structure factors of sample 9. The curves represent times 4, 9, 14, 24, 54, 84, 164, 384, 884 and 1684 seconds, respectively from bottom to top. (b) Scaling behaviour of sample 9 for d_f=1.7, curves representing 14, 19, 24, 34, 44, 54, 64, 74, 84 seconds. The late stage curve corresponds to 1084 seconds.

$$F(x) = \frac{3x^2}{[2 + x^6]} \tag{4.14}$$

in three dimensions and represents a function which has a peak at $x = 1$, and limits,

$$\lim_{x \to 0} F(x) \rightarrow x^2 \tag{4.15}$$

$$\lim_{x \to \infty} F(x) \rightarrow x^{-4} \tag{4.16}$$

i.e. in the high-Q regime, over short length scales, one observes Porod scattering from smooth structural interfaces. There is a region to the right of the main peak $1.1 \lesssim x \lesssim 2$ where $F(x) \sim x^{-3}$ i.e. $F(x) \sim x^{-d}$. This function strictly applies to a density $\phi \sim 0.1$ and is known to become unreliable for $\phi > 0.18$. Therefore the data presented here is consistent with other systems which undergo spinodal decomposition.

Spinodal decomposition in colloidal systems has been discussed extensively [110] - [112]. A sterically stabilised suspension which is rapidly quenched, so that the stabilising hairs on the colloidal particles collapse, undergoes spinodal decomposition due to the short-range van der Waals attraction [113]. In such experiments the authors observe analogous classical spinodal-like kinetics to those observed here, with similar scaling behaviour. Experiments have also been carried out on water-in-oil microemulsions which show spinodal-like behaviour [114], [115].

As the interparticle potential is increased this scaling holds for progressively lower fractal dimensions and for progressively longer times. For the most concentrated of the samples, sample 9 (classed as transient-gelation), the scattering peaks scale with a fractal dimension $d_f = 1.7 \pm 0.2$ and scaling holds for almost all intermediate to late times ($15 < t \lesssim 800$ secs) as shown in figure 4.20. The fractal dimension coincides with the accepted value for DLCA simulation in three dimensions [116].

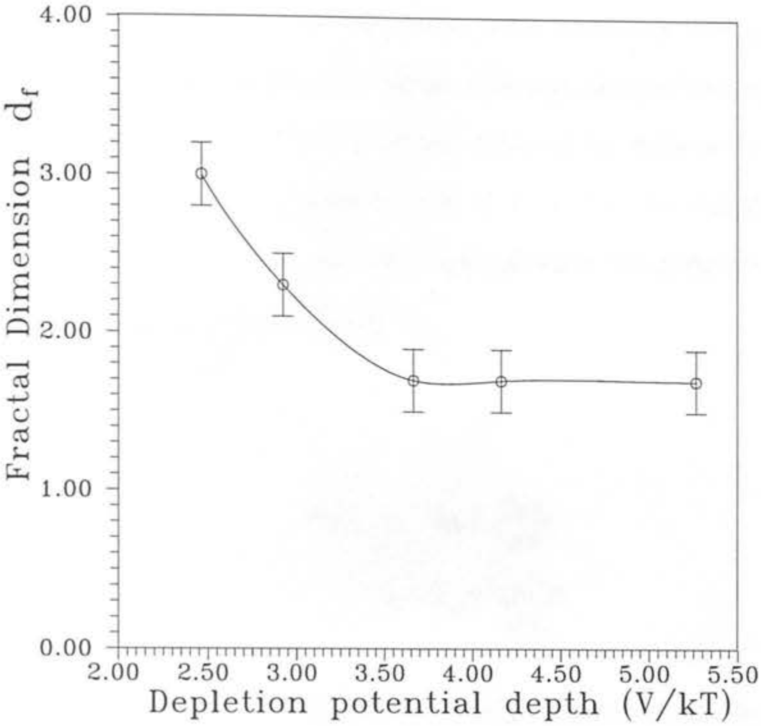

Figure 4.21. Fractal dimension against potential depth, for samples 5 to 9.

Ramified structures, similar to those found in the transient-gelation regime, were observed in salt-induced polystyrene aggregates, studied by Carpineti et al. [55], [56]. Analogous two-dimensional experiments have been conducted by Robinson and Earnshaw [117] - [119]. In both these studies the authors find aggregation kinetics and structure similar to DLCA simulation. The significant difference between these systems and depletion-induced aggregates is the irreversible nature of the inter-particle bonds. Therefore one always finds DLCA-type aggregates as bond-breaking and bond-rotation are suppressed.

Studies have recently been conducted on flocculated silica dispersions [120], [121], induced by lowering the temperature of the suspension and introducing a short-range van der Waals attraction. The authors do not find spinodal-like behaviour, rather a gel-line which arrests the structure before the system can phase separate. They find ramified aggregates consistent with those seen in the non-equilibrium transient-gelation regime, yet surprisingly they find a peaked forward scattering, rather than a small angle ring. They conjecture that the gel-line arises from nucleation and growth of ramified clusters in the fluid-solid region of the phase diagram, short of the spinodal line.

Figure 4.21 shows the fractal dimensions obtained by dynamic scaling against depletion potential depth, for samples 5 to 9, at $\phi \sim 0.1$. To calculate the depletion potential depth for each sample one must first calculate the polymer osmotic pressure in equation (1.1), which can be written as,

$$\begin{aligned} \Pi_{pol} &= k_B T \frac{\phi_{pol}}{\frac{4}{3}\pi\delta^3} && (4.17) \\ &= k_B T \frac{C_p N_A}{\alpha M_w} && (4.18) \end{aligned}$$

where ϕ_{pol} represents the volume fraction of polymer coils in the free volume, N_A is Avagadro's Number, M_w is the polymer molecular weight and α the free volume parameter as defined by equation (2.36).

As shown in figure 4.21 the fractal dimension decreases with increasing interparticle potential until it saturates at $d_f \sim 1.7$ for $\left(\frac{V_{dep}}{k_B T}\right) \sim 4$ i.e. the structure becomes increasingly ramified. In fact, once the scattered speckle pattern has become arrested and one enters the transient-gelation regime, one immediately finds the accepted DLCA fractal dimension. The variation of fractal dimension with potential depth is consistent with previous aggregation experiments [122],[123] and simulation [124] which takes into account interparticle bond breaking during the aggregation process. Another model which has been studied is aggregation with bonds which can rotate [125] rather than just break and re-bond. This simulation finds a fractal dimension which goes *up* with interparticle potential depth i.e. structure becomes increasingly dense. Therefore figure 4.21 suggests that bond *breaking* rather than bond *rotation* must be the dominant process, as the non-equlibrium structure forms.

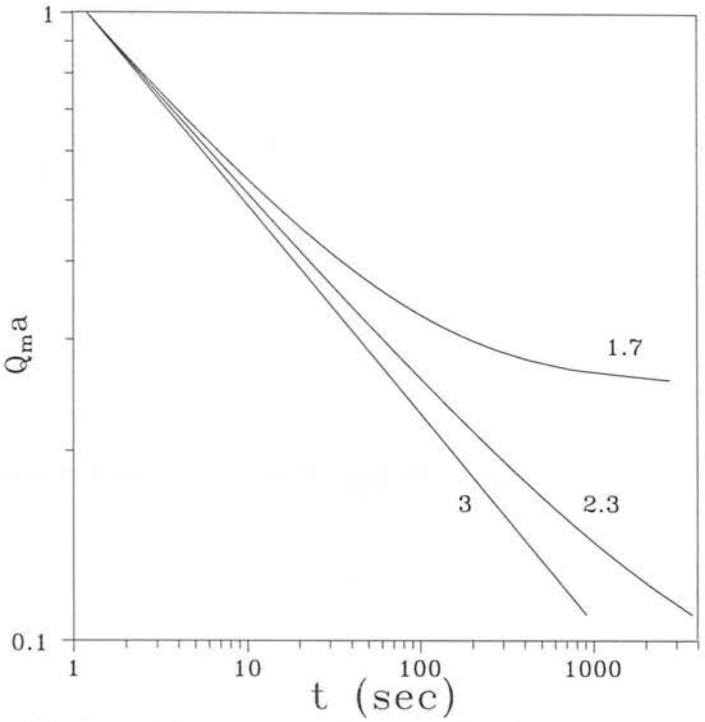

Figure 4.22. Peak position against time calculated using equation (4.22) for a decreasing fractal dimension.

Assuming the fractal dimension varies as that shown in figure 4.21, one can attempt to predict the previously presented ring kinetics, in figure 4.14, using a very simple model. One can write the volume fraction of clusters $\phi_{clusters}$ as,

$$\phi_{clusters} \sim \phi \left(\frac{R_g}{a} \right)^{3-d_f} \tag{4.19}$$

where ϕ is the colloid volume fraction, R_g the radius of gyration of clusters and d_f the fractal dimension. The clusters self diffusion coefficient slows down as the cluster volume fraction increases according to the expression [53],

$$D_{clusters} \sim D_0(1 - 1.7\phi_{clusters}) \tag{4.20}$$

The time taken for a cluster to diffuse its own radius is

$$t \sim \frac{(R_g)^2}{D_{clusters}} \tag{4.21}$$

Combining equations (4.19), (4.20) and (4.21) one finds,

$$t \sim \frac{(R_g)^3}{\left[1 - 1.7\phi\left(\frac{R_g}{a}\right)^{3-d_f}\right]} \tag{4.22}$$

Figure 4.22 shows this function plotted for a volume fraction $\phi = 0.1$ and a varying fractal dimension. The observed behaviour is very similar to that observed in figure 4.14, as one finds an identical initial growth rate and the onset of structural arrest as the fractal dimension decreases. This expression does not take into account full hydrodynamic flow or gravity-dominated motion and therefore a quantitative comparison is lacking.

One can now apply the dynamic scaling procedure to the other regions of the non-equilibrium phase. At $\phi \sim 0.2$ the structure factors from the sample which shows the spinodal-like behaviour (sample 10) scale well to a fractal dimension of 3 in the intermediate stages, and fits the Furukawa scaling prediction, as shown in figure 4.23. Although this volume fraction is just outwith the reliable range of the Furukawa scaling, one still observes a good agreement. Again as one increases the depth of the depletion potential (sample 12), the speckle pattern becomes arrested and the structure factors

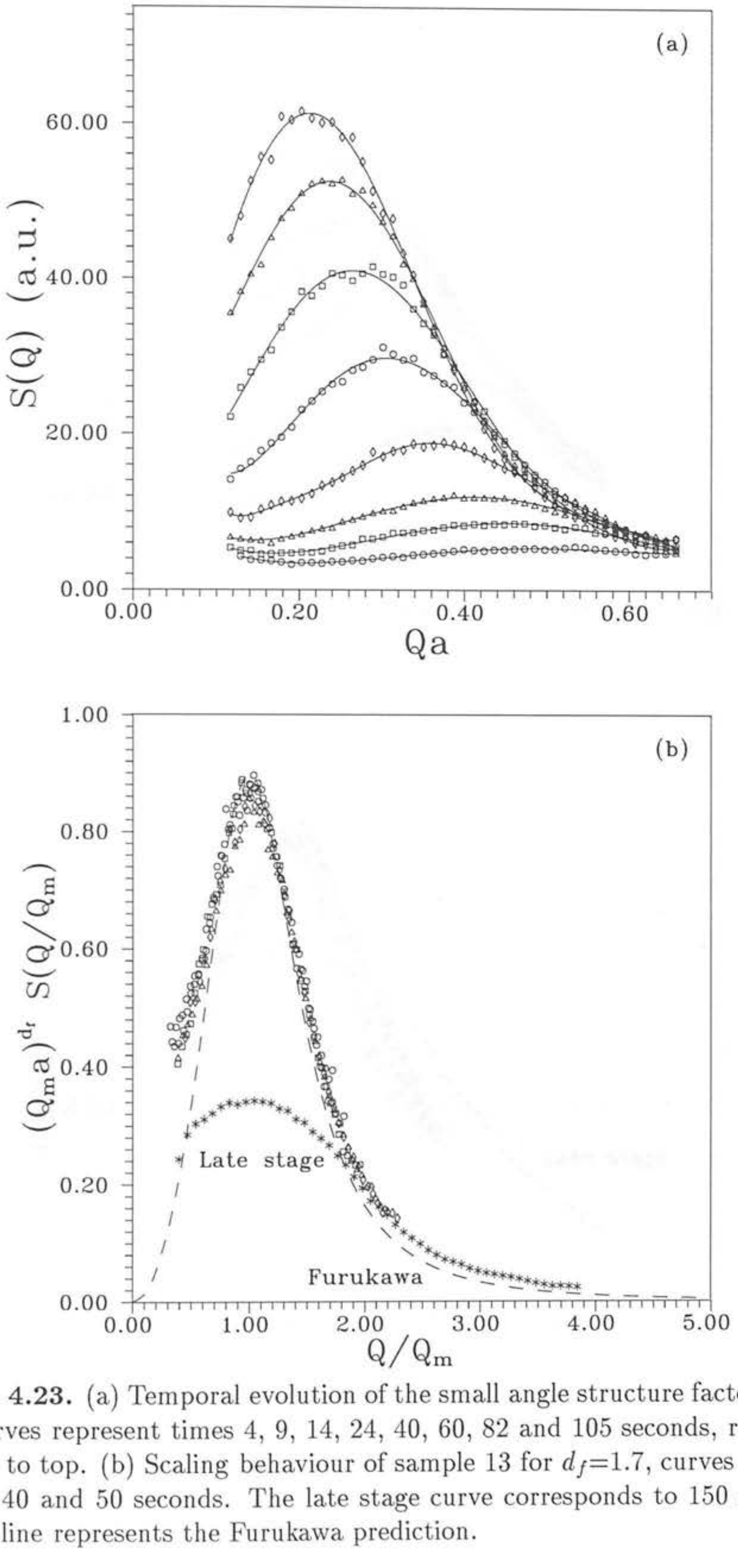

Figure 4.23. (a) Temporal evolution of the small angle structure factors of sample 10. The curves represent times 4, 9, 14, 24, 40, 60, 82 and 105 seconds, respectively from bottom to top. (b) Scaling behaviour of sample 13 for d_f=1.7, curves representing 19, 24, 30, 40 and 50 seconds. The late stage curve corresponds to 150 seconds and the dashed line represents the Furukawa prediction.

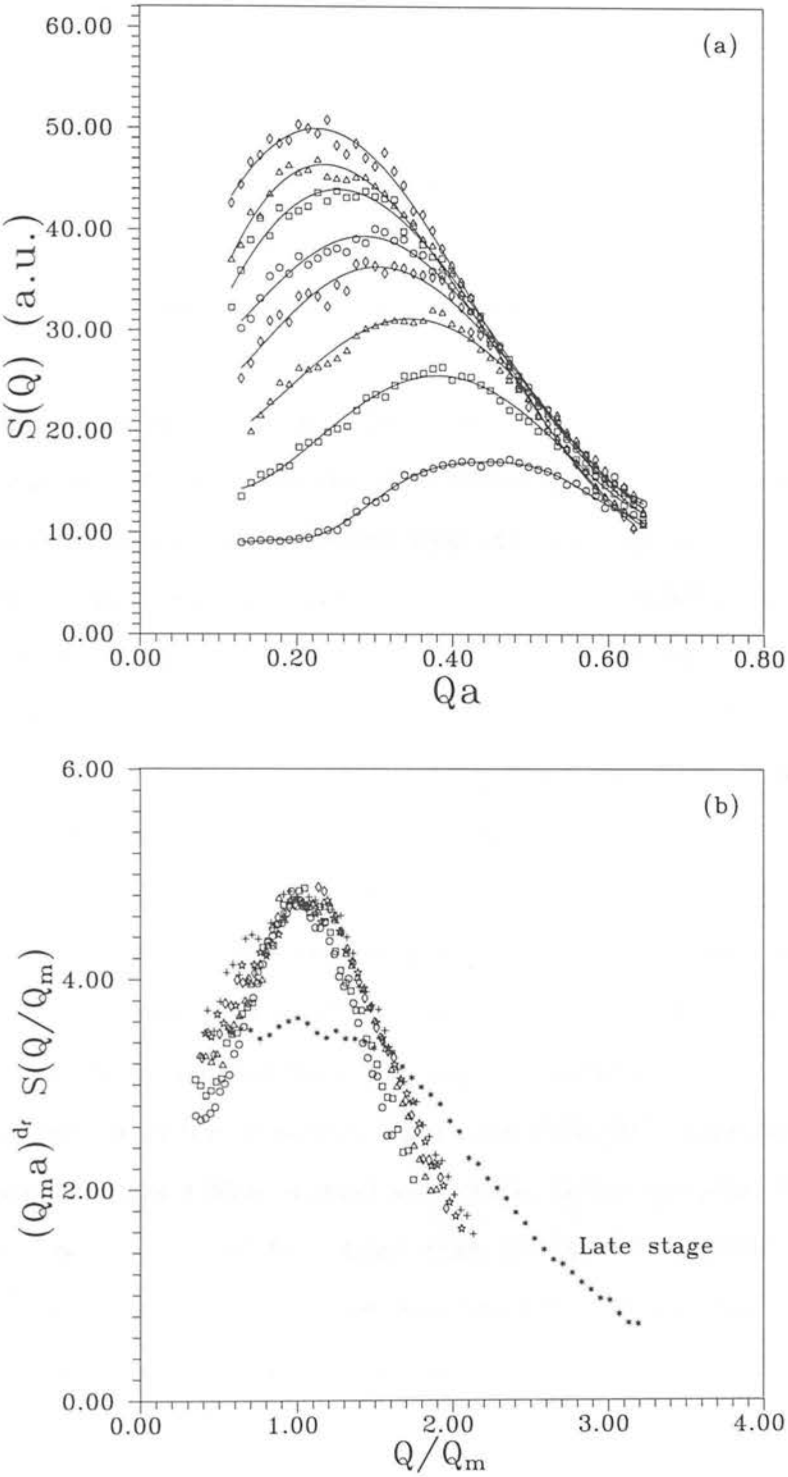

Figure 4.24. (a) Temporal evolution of the small angle structure factors of sample 12. The curves represent times 8, 18, 28, 43, 63, 103, 163 and 303 seconds, respectively from bottom to top. (b) sample 12, for d_f=1.7, curves representing 13, 18, 23, 28, 33 and 43 seconds. The late stage curve corresponds to 1003 seconds.

scale for the accepted DLCA fractal dimension $d_f \sim 1.7$ (see figure 4.24), over intermediate times i.e. once again the structure becomes increasingly ramified with additional polymer.

At $\phi \sim 0.4$ with just sufficient polymer to cross the non-equilibrium boundary (sample 13) one finds that the structure factors scale for a fractal dimension of $d_f \sim 1.7$ (see figure 4.25) over a large time scale (from mid to late stage). It is somewhat surprising that one can still obtain the accepted DLCA fractal dimension from a system at such high density.

As samples 14 and 15 did not evolve over an experimentally accessible time scale it was impossible to carry out the usual structure factor scaling analysis. Therefore the fractal dimension was determined from the power law region to the right of the peak. At such high densities this method becomes questionable [108] although without an evolving speckle pattern no other method appears suitable. Data was taken over a wide range of wavevectors in the same apparatus, by simply moving the sample relative to the screen. As the speckle pattern was time-independent, over the duration of the experiment, the data sets could be simply superimposed. This set of data was also used to examine the role of the form factor in all the small angle scattering experiments[2]. The form factors for all these samples were measured in the large angle apparatus (see figure 4.44) and were then fitted to theoretical form factors. The small angle form factor was then extrapolated back from high wavevectors.

The structure factors of samples 13, 14 and 15 in their respective terminal states, are shown in figures 4.26(a), 4.26(b) and 4.27(a), before and after the measured form factor has been accounted for. Again these structure factors have been normalised relative to one another, as discussed in section 4.3.5, and are shown in figure 4.27(b). As can be seen, once the form factors have been accounted for the structure factors remain largely unaffected until very large wavevectors, $Qa > 0.8$. As such, the form

---

[2] As the form factor is only dependent upon sample composition, and therefore time-independent, the following discussion does not affect the previous scaling behaviour.

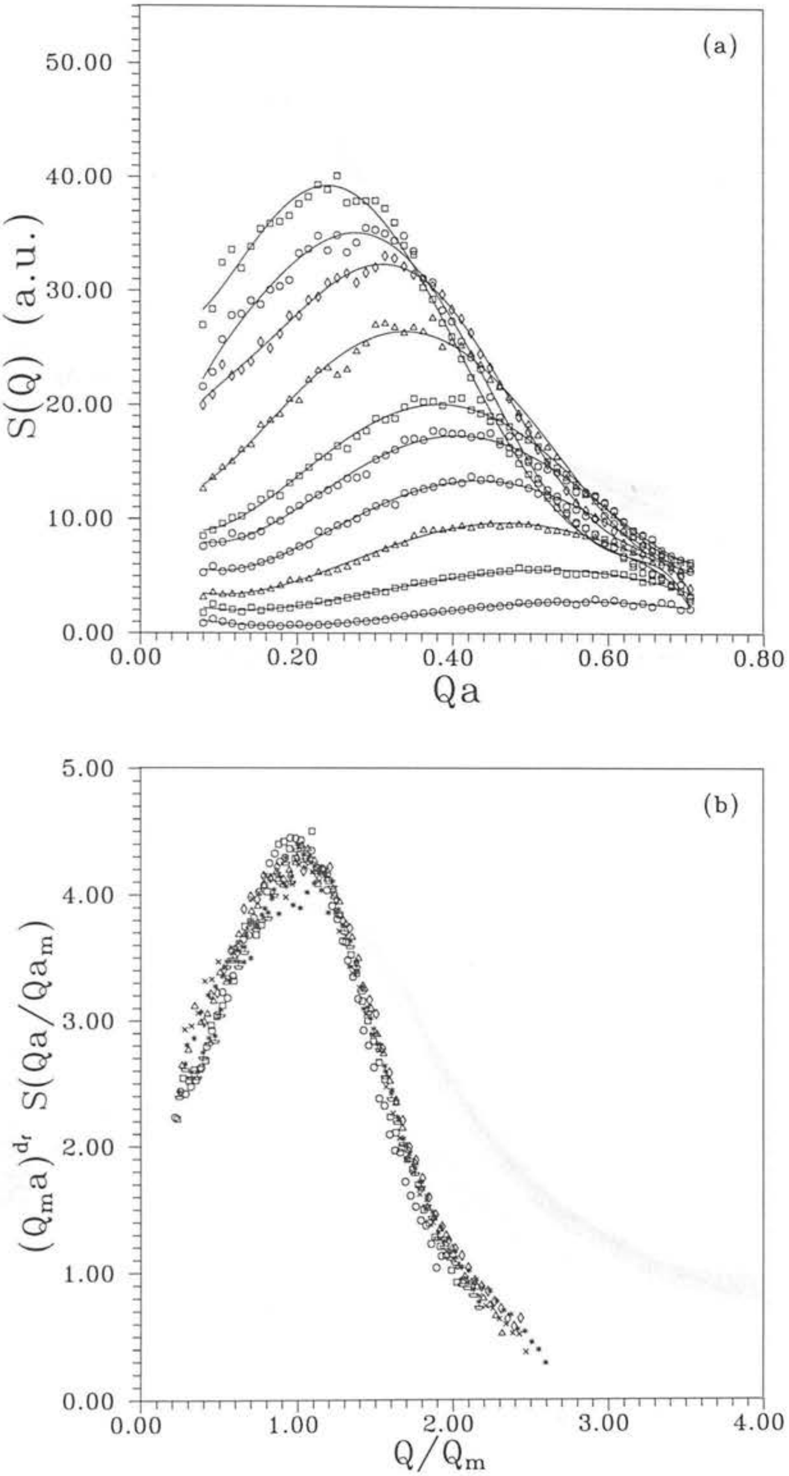

Figure 4.25. (a) Temporal evolution of the small angle structure factors of sample 13. The curves represent times 14, 28, 60, 100, 150, 200, 400, 800, 1600 and 3475 seconds, respectively from bottom to top. (b) Scaling behaviour of sample 13 for d_f=1.7, curves representing 300, 400, 500, 800, 1200, 1600 and 2000 seconds.

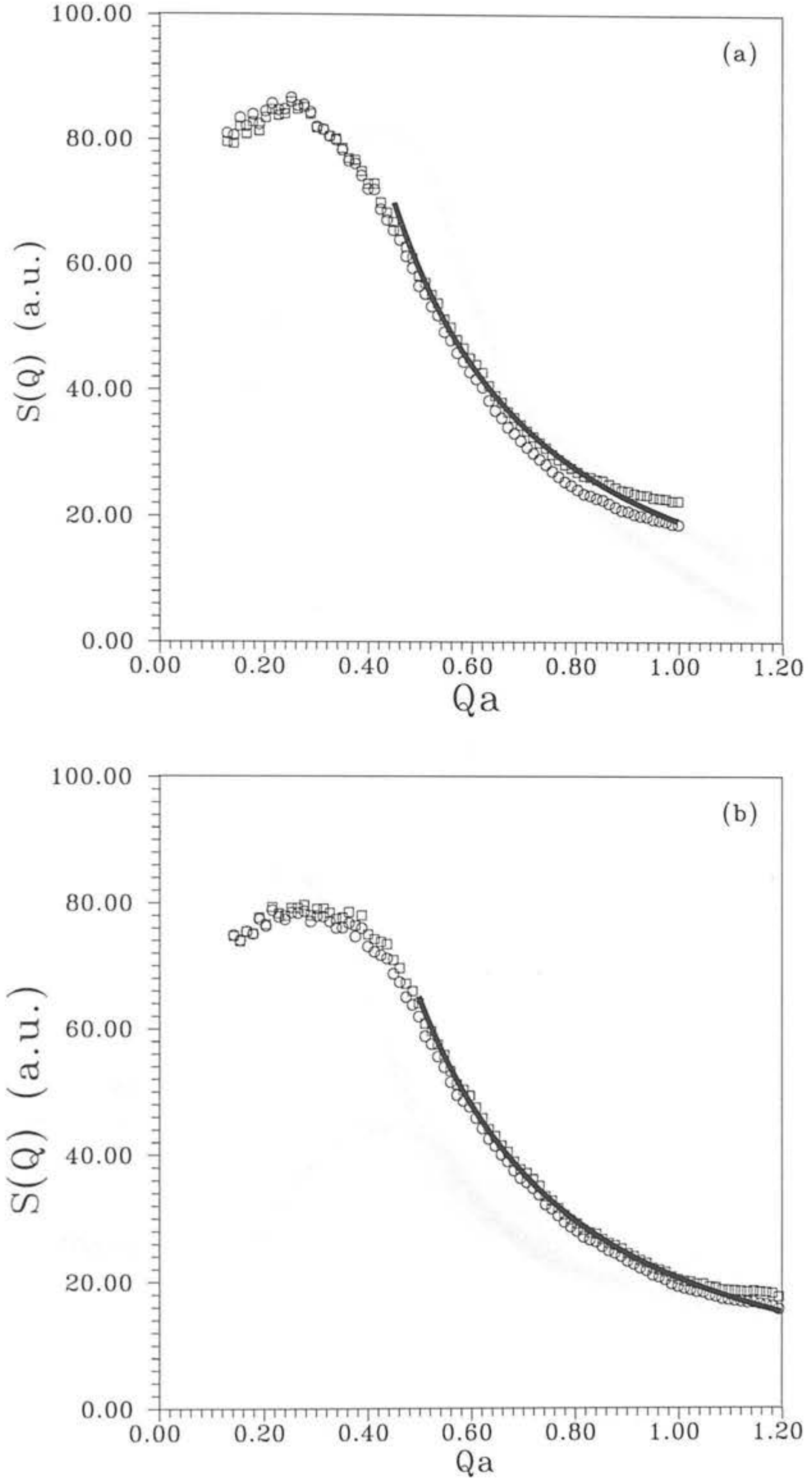

Figure 4.26. The static small angle peak for samples 13 (a) and 14 (b), $\phi \sim 0.4$. The lower curves represent the total scattered intensity and the upper the true structure factor, normalised such that the peak intensities coincide.

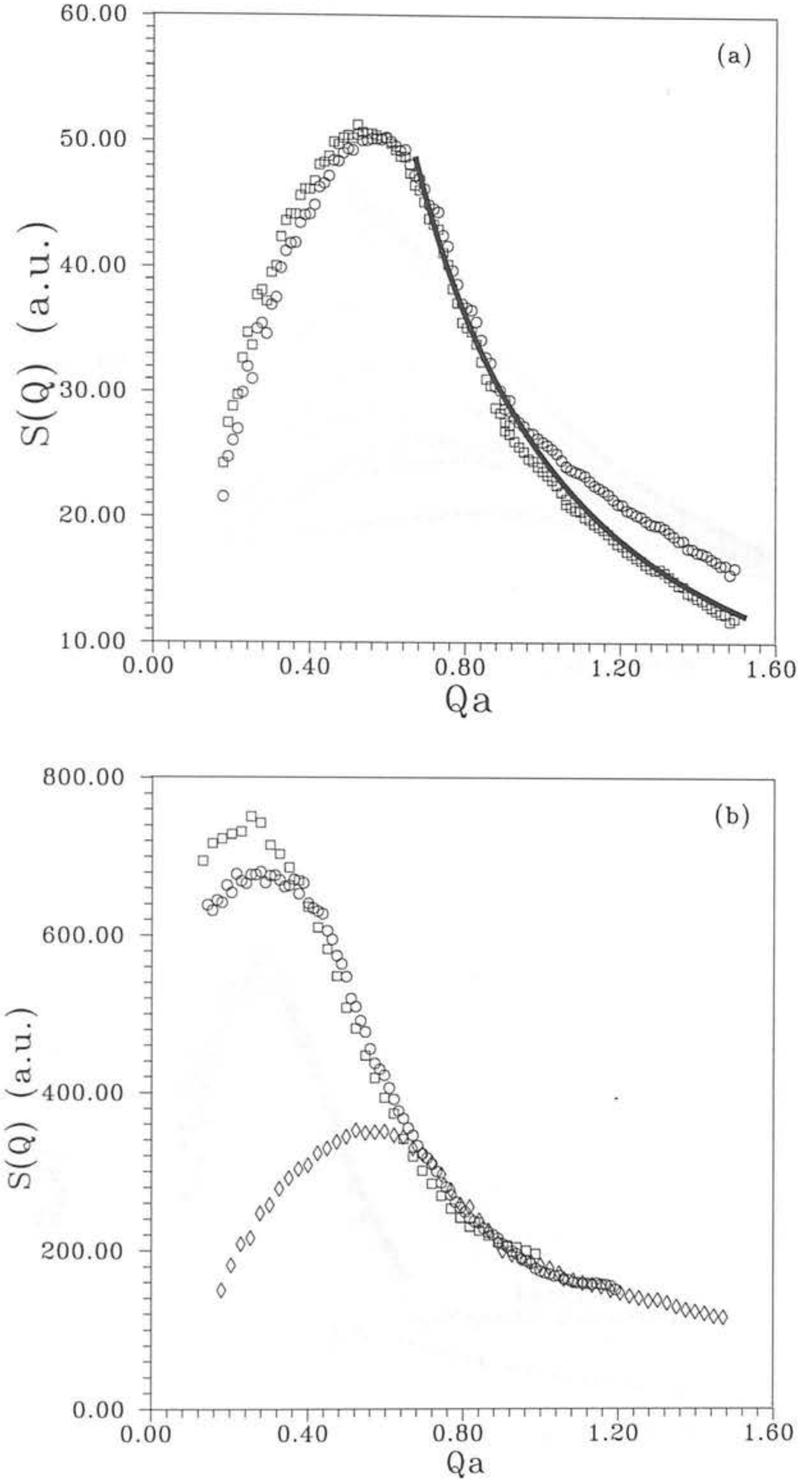

Figure 4.27. (a) The static small angle peak for sample 15, $\phi \sim 0.4$. The lower curve represents the total scattered intensity and the upper the true structure factor, normalised such that the peak intensities coincide. (b) The measured structure factors normalised relative to sample 13.

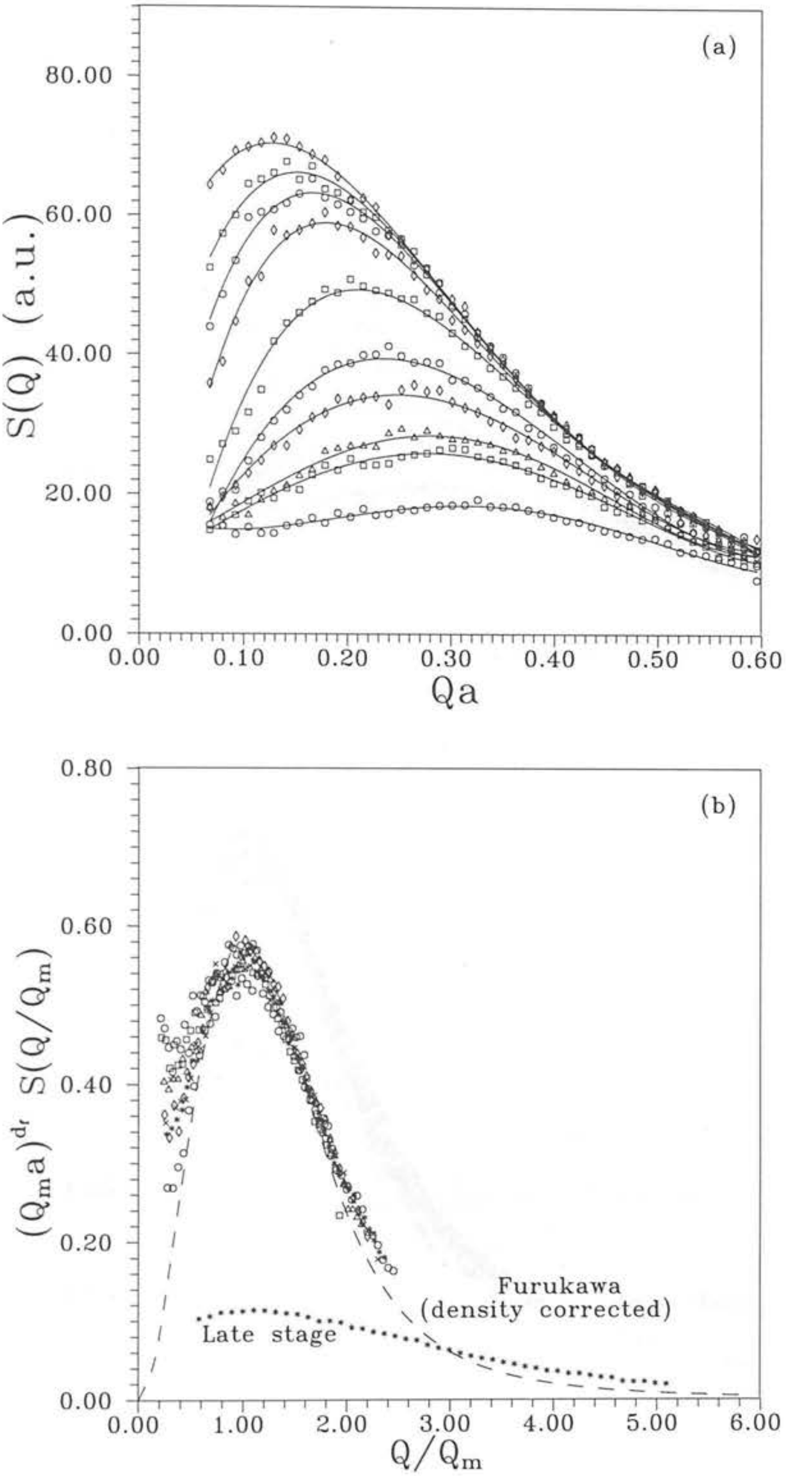

Figure 4.28. (a) Temporal evolution of the small angle structure factors of sample 2. The curves represent times 16, 29, 36, 49, 65, 93, 140, 170, 195 and 260 seconds, respectively from bottom to top. (b) Scaling behaviour of sample 2 for d_f=1.7, curves representing 13, 16, 29, 36, 42, 49 and 55 seconds. The late stage curve corresponds to 260 seconds and the dashed line represents the (density corrected) Furukawa prediction.

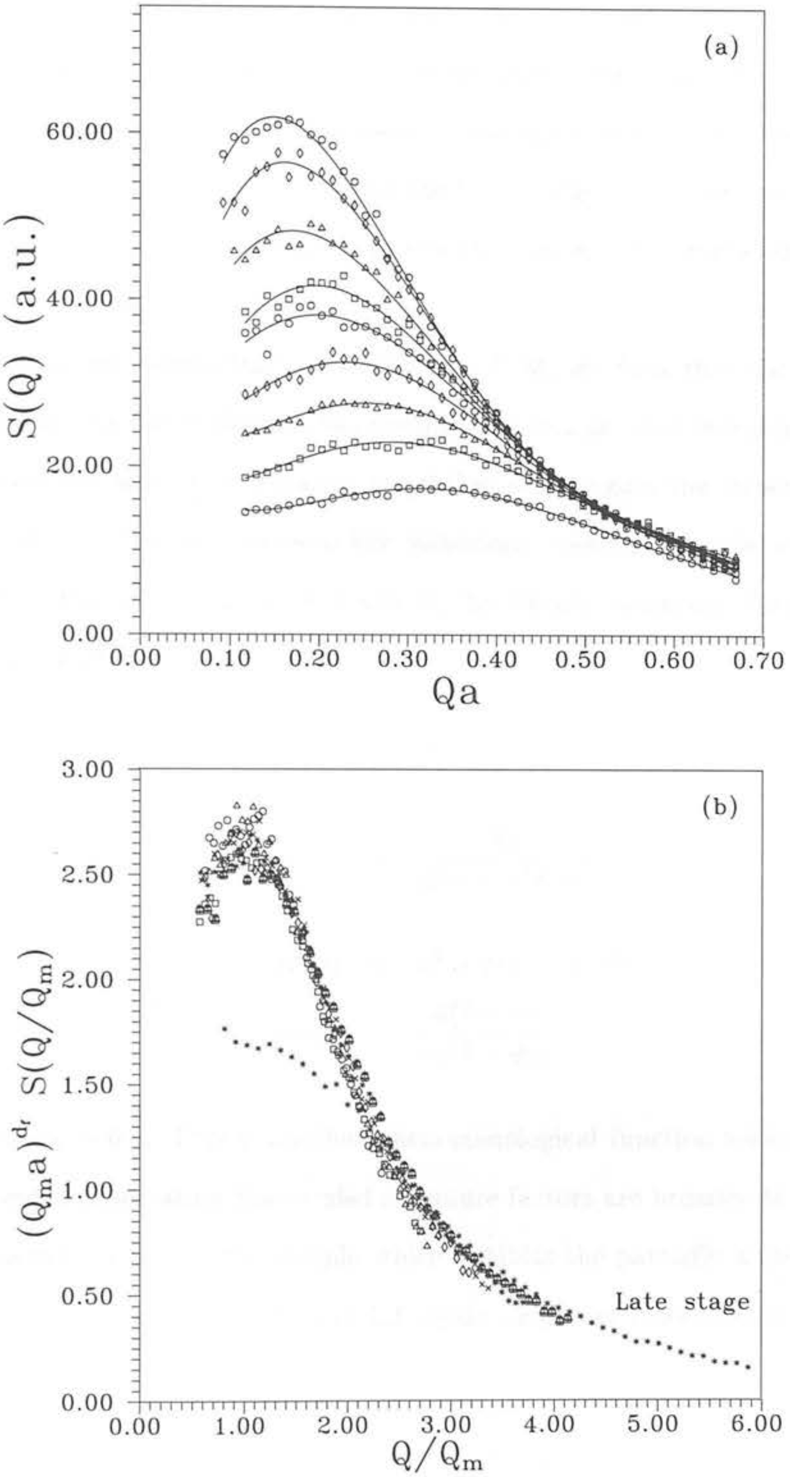

Figure 4.29. (a) Temporal evolution of the small angle structure factors of sample 4. The curves represent times 28, 36, 46, 56, 68, 80, 100, 140 and 180 seconds, respectively from bottom to top. (b) The scaling behaviour of sample 4 for d_f=1.7, curves representing 28, 36, 46, 56, 68, 80 and 100 seconds. The late stage curve corresponds to 340 seconds.

factors of the previously studied samples ($0 < Qa < 0.6$) would only play a minor, negligible, role in the data analysis. Interestingly the 'true' structure factors show a limited power law regime as shown by the deviation from a power law of exponent 1.7 (the thick black line in each of the figures). Consequently the fractal dimension of these samples is approximately $d_f \sim 1.7$, but the fractal regime is extremely small, especially for sample 15. Therefore at high densities the concept of a fractal structure becomes somewhat clouded.

At the lowest volume fraction studied $\phi \sim 0.02$, one finds that the structure factors from sample 1 (in the nucleation-like regime) do not scale until very late stage where one finds a tenuous scaling to a fractal dimension of 3. Again the structure factors from the sample which shows spinodal-like behaviour (sample 2) scale, over intermediate times, to a fractal dimension of 3 and fit the density corrected Furukawa prediction [42] (figure 4.28) which is given by,

$$F(x) = \frac{3x^2}{[2m + x^2 K(x)]} \tag{4.23}$$

$$K(x) = x^4 + 2(1 - m(\phi)) \tag{4.24}$$

$$m(\phi) = \frac{\phi(1-\phi)}{\phi_0(1-\phi_0)} \tag{4.25}$$

where $\phi_0 \sim 0.1$. This is another phenomenological function which arises from the experimental observation that scaled structure factors are broader at lower densities[3]. The structure factors of the sample which exhibits the partially arrested speckle pattern scale to a fractal dimension of 1.7, again only over intermediate time scales (see figure 4.29).

---

[3] Note that equation (4.23) reduces to (4.14) when $\phi = \phi_0$.

4.3.8 Summary

Therefore by way of summary we can define different regions of behaviour, within the non-equilibrium region, which show similar kinetics and structure[4]. These regions are as follows;

- Region 1. 'Nucleation-like': Characterised by a 'lag time' before the formation of a small angle ring at a low wavevector. The ring position decays slowly while the peak intensity grows rapidly. The early stage kinetics follow linear (Cahn) predictions. There is no definite scaling exponent, but the structure factors perhaps show a tenuous scaling to $d \sim 3$ at late stage. The speckle pattern fluctuates rapidly throughout the collapse.
- Region 2. 'Spinodal-like': Characterised by a cross-over in the cluster growth rate, $Qa \sim t^{-0.25}$ to $Qa \sim t^{-1}$. The structure factors scale in the intermediate time stage to a fractal dimension of $d_f \sim 3$ at low polymer concentrations (following the Furukawa prediction for spinodal decomposition) or $1.7 < d_f < 3$ at higher polymer concentrations. The speckle fluctuates rapidly, as the ring collapses continuously.
- Region 3. 'Transient-gelation': Characterised by a peak position which first decays as $Qa \sim t^{-0.25}$ and either decays continuously as a single power law or becomes fully arrested at a finite wavevector. Throughout the experiment the speckle fluctuates very slowly indicative of slow particle dynamics. The structure factors scale in the middle to late stage with a fractal dimension of 1.7 coincident with the accepted DLCA fractal dimension. The ring then fills in rapidly, roughly coincident with the onset of gravitational settling.

---

[4] Actually these regions were originally defined simply by the appearance of the respective speckle patterns.

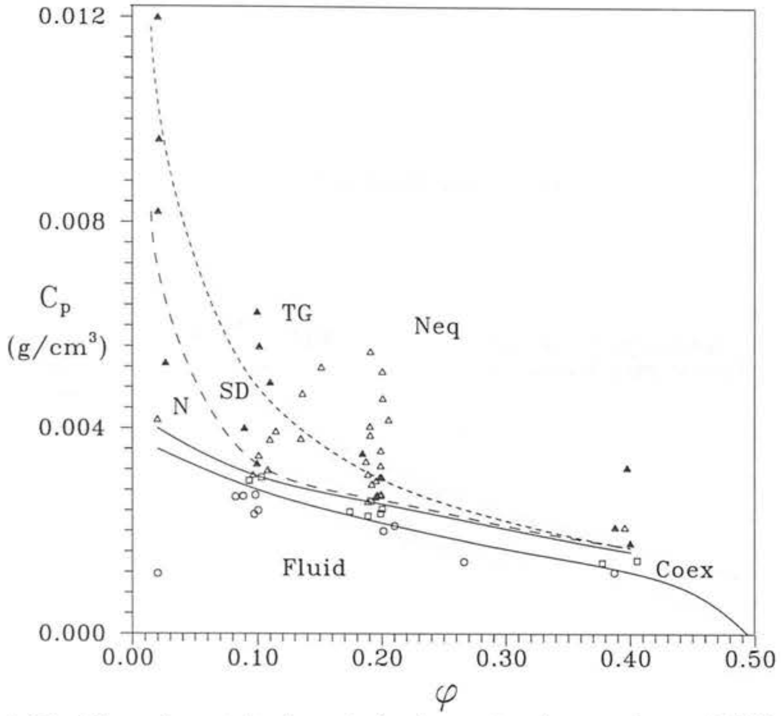

Figure 4.30. Experimental phase behaviour showing regions of different kinetics and structure. N ≡ Nucleation-like, S ≡ Spinodal-like and TG ≡ Transient-Gelation. The filled-in symbols indicate those studied by small angle scattering.

Therefore after defining these three independent regions, 'nucleation-like', 'spinodal-like' and 'transient-gelation', one can superimpose these different kinetic regimes onto the experimental phase diagram, as shown in figure 4.30. It is somewhat unusual to represent data this way, as it overlays non-equilibrium behaviour onto an equilibrium phase diagram. The dashed lines define definite boundaries between regions of different kinetic behaviour, although one would expect gradual transitions between these regimes. What is immediately striking is the similarity between the kinetic regimes in the non-equilibrium phase and the theoretical metastable gas-liquid region shown in figure 2.11, where one observes similar regions of nucleation and spinodal decomposition. It can now be conjectured that the non-equilibrium phase should be identified with the metastable gas-liquid binodal.

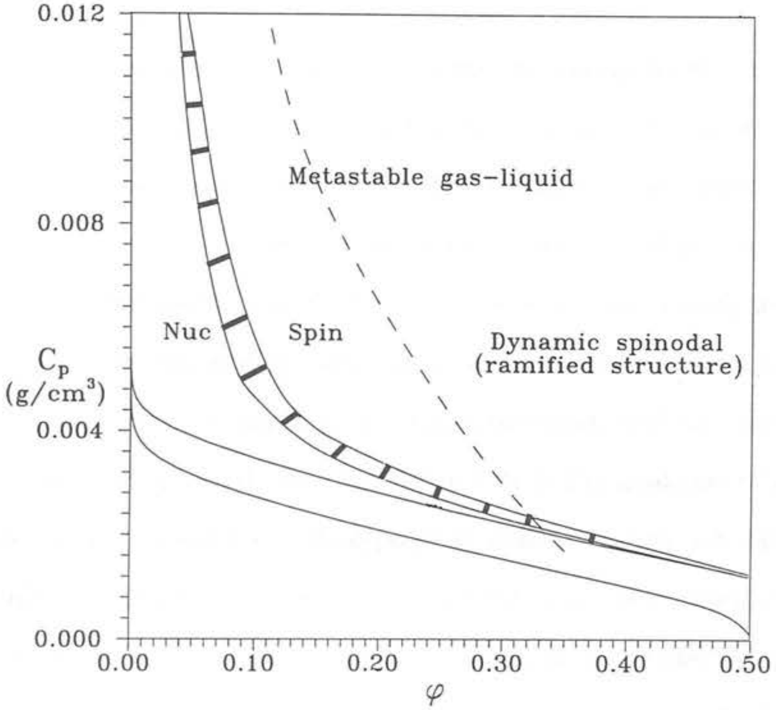

Figure 4.31. The simulations of Hayward et al. [69] mapped onto the theoretical colloid-polymer phase diagram, for a size ratio $\xi \sim 0.09$ i.e. to account for a swollen polymer. The hatched area represents the gradual transition from nucleation to spinodal decomposition.

In the fluid-crystal coexistence region one expects to observe nucleation and growth of crystals i.e. ordered clusters larger than a critical size will grow, ordered structures less than a critical size decay (e.g. see figure 2.2). If thermal fluctuations produce a dense disordered structure it will also subsequently decay. Once into the non-equilibrium region thermal fluctuations form structures governed by the local double minimum in the fluid free energy (see figure 2.12) and therefore any dense amorphous clusters grow unhindered. Therefore one can suggest that non-equilibrium aggregation is induced as the metastable gas-liquid binodal is crossed.

Therefore above the non-equilibrium boundary we expect the behaviour to follow the phase kinetics of simple fluids described in chapter 2. However it is now common knowledge that a sharp transition between nucleation and spinodal decomposition only makes sense for systems with long range forces [98]. In colloid-polymer mixtures, where only short-ranged forces exist, one expects a gradual transition from nucleation to spinodal decomposition. In such systems the free energy barrier to nucleation lowers to below k_BT as one goes far from the binodal, yet never becomes precisely zero. As such the critical cluster size reduces until it becomes comparable to the correlation length of typical thermal fluctuations. This transition regime cannot be calculated theoretically, as one requires the introduction of large scale density fluctuations, which therefore have been modeled by Kawasaki spin-exchange-type dynamic simulation [68]. Typically the transition is found to occur approximately half way between the binodal and the mean-field spinodal. As such figure 4.31 is the analogue of these simulations but applied to the theoretical colloid-polymer phase diagram (c.f. figure 2.11).

In similar studies [69], [126] a transient time-dependent percolation line is found within the binodal i.e. a system which is non-percolating at short times, percolates for a finite time as the structure grows and then disintegrates into discrete clusters. This phenomenon is known as the 'dynamic spinodal'. It is argued that at the dynamic spinodal one finds ramified, fractal, clusters and as above, one can map a dynamic spinodal onto our phase diagram.

The similarity between the different kinetic regimes in the non-equilibrium phase and that obtained by analogy to simulation is encouraging. These predictions account for the observed 'nucleation-like' behaviour, which shows characteristics of both nucleation and spinodal type kinetics i.e. sample 1 must represent a system in the transitional regime. The simulations also predict a region over which one should observe classical spinodal-like kinetics. These simulations also account for the persistence of frozen, ramified, clusters deep within the binodal and in effect the predicted kinetics are identical to the ones observed here. This not only includes the growth mechanism and structure of the clusters, but also predicts that the structure should disintegrate after a finite time. The collapse of the structure will be examined in detail later.

If these interpretations are correct then these non-equilibrium states are simply transient states, on the road to phase separation into a dense crystal and a dilute fluid. If a sample is left for a number of months one finds that the dense sediment does slowly crystallise. There is no evidence for the coexisting fluid phase, yet one expects the fluid state to be extremely dilute. Either it is too dilute to detect or the fluid becomes trapped within the dense sediment.

Prompted by this work a study of the gas-liquid phase separation has been conducted. This study was carried out on the same model system, but with a larger size ratio ($\xi \sim 0.37$ and $\xi \sim 0.54$) [127]. Within this region one finds spinodal-like behaviour as one crosses the binodal, which rapidly becomes arrested with additional polymer. Although the system never becomes fully arrested, the small angle ring collapses as a single power law and scales to a fractal dimension of 1.7. These results are only preliminary, yet the observation of similar kinetic behaviour to that of the non-equilibrium region is consistent with the conjecture that the non-equilibrium behaviour is caused by the presence of a *metastable* gas-liquid phase.

4.3.9 Small angle scattering from sediments

The nature of the ramified sediments, formed hours after the non-equilibrium states have collapsed, has also been probed by small angle light scattering (i.e. the second stage of figure 4.2). One finds a peaked forward scattering from all the sediments studied, consistent with the so called Fisher-Burford formula[5] [128] which can be written,

$$S(Q) = \frac{S(Q=0)}{[1 + 2(R_g Q)^2/3d_f]^{d_f/2}} \tag{4.26}$$

The resulting speckle pattern is completely static and shows a power law region at high wavevectors of exponent d_f. The small angle scattering from the metastable

---

[5] Although at such high densities $\phi_{sed} \geq 0.3$ it is unclear as to the validity of this expression.

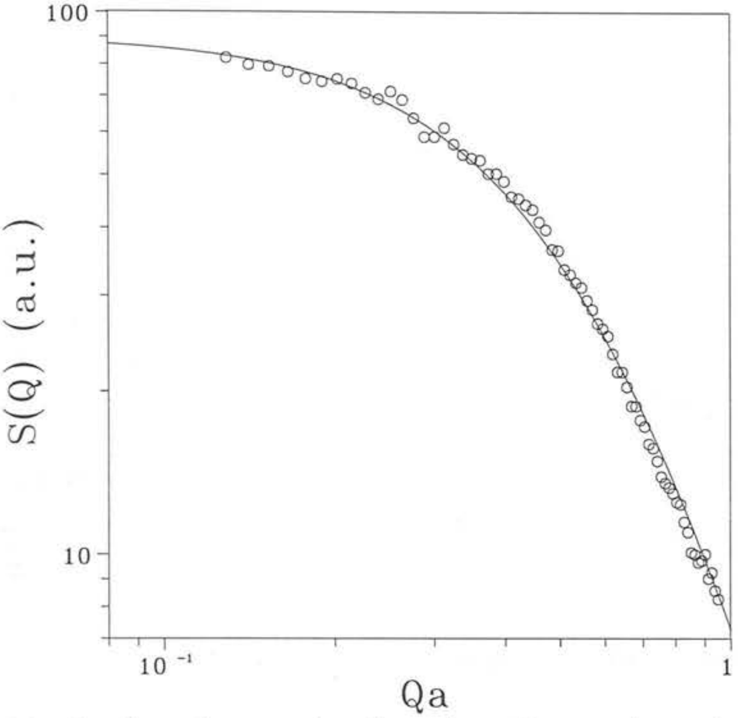

Figure 4.32. Small angle scattering from the sediment of sample 4. The solid line represents the Fisher-Burford formula with $R_g = 2.5$ and $d_f = 2.1$.

sediments of samples 4, 7, 12 and 13 (all samples which correspond to the transient gelation regime) have been measured and as a typical example figure 4.32 shows that from sample 4, fitted to the Fisher-Burford formula. The resulting fractal dimensions are shown in figure 4.33 as a function of sample volume fraction.

One can theoretically predict the resulting sediment fractal dimension after some initial assumptions. For the initial structure before sedimentation, assuming a system spanning structure, equation (4.19) can be written $\phi_{clusters} \sim 1$ or,

$$\left(\frac{R_{g1}}{a}\right)^{3-d_{f1}} \sim \frac{1}{\phi} \tag{4.27}$$

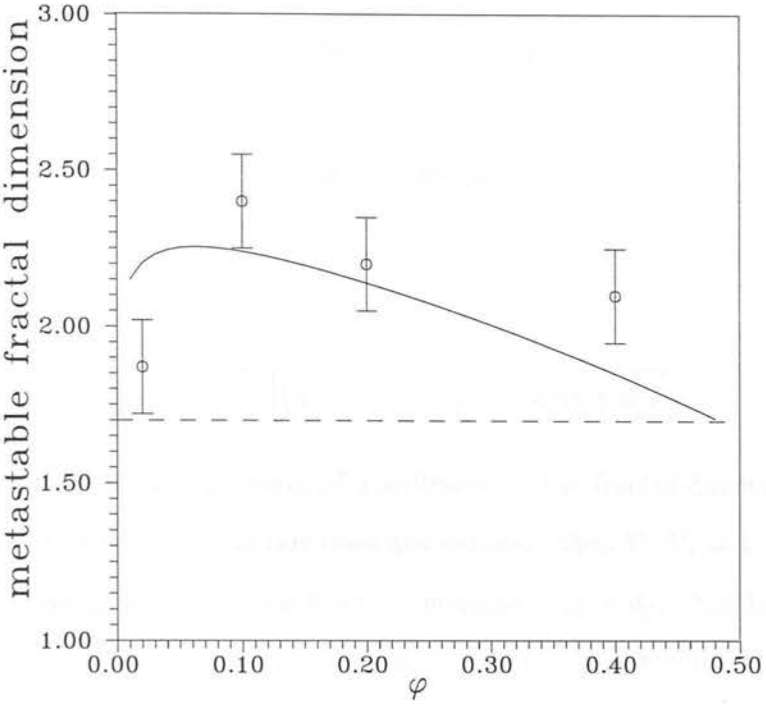

Figure 4.33. Fractal dimension of the metastable sediment against colloid volume fraction. The solid line represents that calculated from equation (4.30) using $d_{f1} = 1.7$.

where R_{g1} and d_{f1} represent the radius of gyration and fractal dimension of the initial state. For the subsequent sediment assuming all the particles are contained within the sediment,

$$\left(\frac{R_{g2}}{a}\right)^{3-d_{f2}} \sim \frac{V_2}{V_1 \phi} \tag{4.28}$$

where V_2 is the volume of the sediment and V_1 the volume of the original structure. Assuming the clusters shrink as the structure compacts, so that the total number of particles within the clusters are conserved one can write,

$$N \sim \left(\frac{R_{g1}}{a}\right)^{3-d_{f1}} \sim \left(\frac{R_{g2}}{a}\right)^{3-d_{f2}} \tag{4.29}$$

Combining the above three equations one finds,

$$d_{f2} \sim \frac{3d_{f1}}{\left[\left(1-\frac{ln(V_2/V_1)}{ln(\phi)}\right)(3-d_{f1})+d_{f1}\right]} \tag{4.30}$$

relating the fractal dimension of a sediment to the fractal dimension of its initial structure. If the original structure does not sediment then $V_2/V_1 = 1$ and therefore the resulting structure has the same fractal dimension, $d_{f2} = d_{f1}$. Similarly if the fractal dimension of the original structure equals 3 one finds that the resulting sediment has a fractal dimension of 3, independent of its volume i.e. the compacted structure never exceeds the physical limit, that of the Euclidean dimension. Using the linear relation between V_2/V_1 and ϕ shown in figure 4.3, and an initial fractal dimension $d_{f1} = 1.7$, one obtains the solid line shown in figure 4.33. Good quantitative agreement is found at high volume fractions $\phi > 0.02$. At the lowest volume fractions the theory fails badly, as the original structure does not percolate (i.e. the observation of a non-frozen ring) and accordingly equation (4.27) no longer holds.

4.3.10 Small angle scattering in the equilibrium regions

To compare the behaviour observed in the non-equilibrium region with other regions of the phase diagram three samples were prepared of composition given by table 4.3.

The single phase fluid samples, 16 and 17, both showed peaked forward scattering, without ring formation. As these samples correspond to equilibrium phases under an attractive potential, these can both be compared to equilibrium structure factors. Firstly these were fitted to the square well fluid (see section 3.4.3), in the mean spherical

	ϕ	C_P	Phase
16	0.098	2.32e-3	Fluid
17	0.099	2.70e-3	Fluid
18	0.103	3.05e-3	Coexistence

Table 4.3. Fluid and coexistence samples all of volume fraction $\phi \sim 0.1$.

approximation, with a potential range equal to the depletion potential range, i.e. equal $(\frac{\delta}{a})$, and variable depth. In figure 4.34 the small angle scattering from sample 16 and 17 are shown, fitted to square well depths $-2.45k_BT$ and $-2.55k_BT$ respectively. These compare well to the actual depletion potential depths, as calculated from equation (1.1), of $-2.16k_BT$ and $-2.42k_BT$. The low angle structure factors also fit predictions of the Baxter AHS model as discussed in section 3.4.2. These show good fits for stickiness parameters $\tau_B \sim 0.135$ and $\tau_B \sim 0.110$ respectively.

The coincidence of both these theoretical structure factors lie in their second virial coefficients. The second virial coefficient of the colloidal particles B_2, as defined in section 2.5.3, can be written,

$$\begin{aligned} B_2 &\equiv -\frac{1}{2}\int f(\mathbf{r})\, d^3r && (4.31) \\ &= -\frac{1}{2}\int \left(exp\left[-\frac{\epsilon}{k_BT}\right] - 1\right) d^3r && (4.32) \end{aligned}$$

where $f(\mathbf{r})$ is known as a Mayer function [77]. The static structure factor may be written as, see appendix C,

$$\begin{aligned} S(Q) &\equiv 1 + \rho \int (g(r) - 1)e^{i\mathbf{Q}.\mathbf{r}}\, d^3r && (4.33) \\ &= 1 + \rho \left[\int (g(r) - 1)\, d^3r + i\int (g(r) - 1)\mathbf{Q}.\mathbf{r}\, d^3r + ...\right] && (4.34) \end{aligned}$$

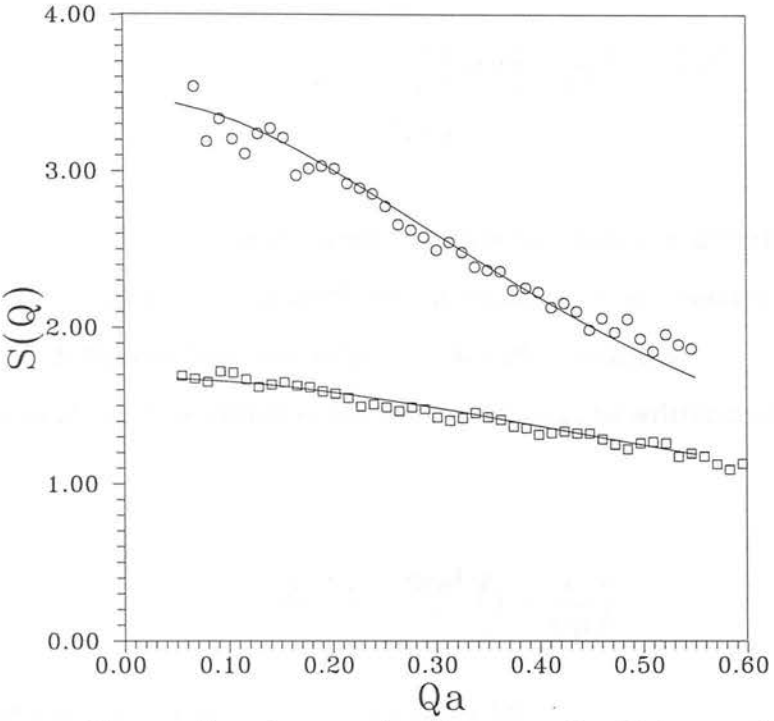

Figure 4.34. The small angle scattering from samples 16 (squares) and 17 (circles), compared with square well predictions with parameters given in the text.

by expanding the exponential factor. Therefore in the low Q limt,

$$S(Q \to 0) \sim 1 + \rho \int (g(r) - 1)\; d^3r \tag{4.35}$$

For a dilute system it is well known that [67],

$$g(r) \sim exp\left[-\frac{\epsilon}{k_BT}\right] + O(\epsilon) \tag{4.36}$$

Therefore,

$$S(Q \rightarrow 0) \sim 1 + \rho \int \left(exp\left[-\frac{\epsilon}{k_B T} \right] - 1 \right) d^3 r \tag{4.37}$$

$$\sim 1 - 2\rho B_2 \tag{4.38}$$

Therefore in the small angle limit the structure factor is governed solely by the second virial coefficient of the particles. As equation (4.36) assumes a dilute system, one expects deviations from this behaviour at higher densities.

The second virial coefficient of the AHS system can be written as (see appendix D),

$$B_{2,AHS} = \frac{2\pi a^2}{3} \left(1 - \frac{1}{4\tau_B} \right) \tag{4.39}$$

and that for the square well (see appendix D),

$$B_{2,SW} = \frac{2\pi a^2}{3} \left[1 - \left(exp\left[-\frac{\epsilon}{k_B T} \right] - 1 \right) \left(2\left(\frac{\delta}{a} \right) + \left(\frac{\delta}{a} \right)^2 \right) \right] \tag{4.40}$$

When either of these are compared to the hard sphere virial coefficient $\left(\frac{2\pi a^2}{3} \right)$ (see appendix D) it is evident that they both represent a reduced second virial coefficient and therefore a less repulsive potential. In fact when the second term in either of these becomes sufficiently large both second virial coefficients become negative, indicative of an effective attraction between the colloidal particles. If these two second virial coefficients are equated, i.e. to give similar small angle scattering, one finds,

$$\tau_B = \frac{1}{4\left[exp\left[-\frac{\epsilon}{k_B T} \right] - 1 \right] \left[2\left(\frac{\delta}{a} \right) + \left(\frac{\delta}{a} \right)^2 \right]} \tag{4.41}$$

Therefore, for say sample 17, which fits a square well structure factor for a range $\frac{\delta}{a} \sim 0.08$ and depth $\epsilon \sim -2.55k_BT$ we expect it to fit an AHS model for a stickiness parameter $\tau_B \sim 0.127$. The slight disparity between this value and that obtained by fitting, $\tau_B \sim 0.110$, arises from the non-dilute nature of the sample and the approximation of equation (4.34).

Within the fluid-crystal coexistence region one simply observes a peaked forward scattering until the non-equilibrium line is approached e.g. sample 18. Then a ring is observed in the small angle scattering, which shows a cross-over in the peak position against time, while the intensity grows slowly. This proceeds to peaked forward scattering, well before the observation of any iridescence within the sample. The structure factors fail to scale with any fractal dimension and therefore this represents a different growth mechanism to that of the non-equilibrium region and as yet is poorly understood. This is outwith the scope of this work and will not be discussed further. It must be stressed that the ring observed here is not that seen in the work of Schatzel et al. [71], who observed a small angle ring arising from inter-crystallite correlations, in the absence of added polymer. The small angle ring observed here arises long before any iridescence is observed and must represent scattering from an initial transient network before nuclei have formed.

4.4 Video-enhanced microscopy

It is not enough to simply measure the light scattered from a colloidal suspension to uniquely determine its structure. To examine the direct structure, and not that in reciprocal space, one can utilise microscopy. As light is diffracted through a sample one obtains an interference pattern which is simply the Fourier transform of the direct structure. One needs to insert a lens to Fourier transform this pattern, back into a real image. Although this procedure removes the theoretical complications, implicit in determining the average structure by light scattering, microscopy can often be dominated by local defects which can confuse interpretation.

In the discussion presented here I assume a simple microscope design consisting of a light source, a 'condenser' lens to concentrate the light onto the sample, the sample itself (assumed thin), followed by an 'objective' lens which collects the light and forms the primary image. Obviously in practice one uses more complex techniques to improve the resolution of the image and contrast between the sample and the background. For a good introduction to optical microscopy see [129].

4.4.1 Experimental techniques

For this study I utilise two techniques; those of phase contrast microscopy and differential interference contrast (DIC) microscopy. For an excellent detailed discussion of both these techniques see [130]. In phase contrast microscopy an extra path difference is added to the light not scattered from the sample. In doing so invisible optical path differences in the object can be transferred into visible differences of light intensity in the image. In DIC the sample is illuminated by linearly polarised light which is split into two beams by a prism, leading to a slightly different optical path length between the two beams. Once traversing the sample the beams recombine, at which point they interfere and pass through another polaroid. The phase change introduced by the sample then produces an interference pattern which contains both phase and amplitude information. The resulting image, which looks like a relief map, actually represents the gradients of phase differences across the sample, unavailable by most other optical techniques. DIC is actually capable of producing a higher contrast between sample and background than phase contrast, although the alignment procedure of both beam splitters is extremely time consuming.

For either of these techniques, the resulting images were constantly monitored using a CCD camera which was linked to a PC equipped with an 8 bit frame grabber (256 grey scales). The subsequent images could then be enhanced using computer algorithms, a technique known as video enhanced microscopy.

4.4.2 Resolution

As light is diffracted through a sample an interference pattern is formed in the back focal plane of the objective lens. For example, consider diffraction through a circular aperture. One obtains the well known Airy disk diffraction pattern with intense rings of light representing the first, second, third etc. maxima. Now consider diffraction through two such apertures so that the interference patterns now overlap somewhat. Obviously there comes a point where one can no longer determine whether this pattern has arisen from two apertures or only one, when they overlap completely. The Rayleigh criterion [131] for resolving two such diffraction patterns is somewhat arbitrary[6]: Resolution occurs when the first dark ring of one pattern coincides with the central maximum of the other. This minimum separation can be written,

$$d = \frac{0.61\lambda}{nsin(\alpha)} \tag{4.42}$$

where λ is the wavelength of incident light, n is the refractive index of the medium between the sample and the objective lens and α is the so-called half-angle of acceptance of the lens, i.e. the maximum scattering angle from the sample which will still strike the objective lens[7]. In a microscope a condenser lens is used so that a solid cone of light is admitted to the sample. Now the resolving power may be written,

$$d = \frac{1.22\lambda}{[nsin(\alpha)]_{obj} + [nsin(\alpha)]_{cond}} \tag{4.43}$$

---

[6] In the words of Rayleigh: 'This rule is convenient on account of its simplicity and it is sufficiently accurate in view of the necessary uncertainty as to what exactly is meant by resolution'.

[7] The term $nsin(\alpha)$ is often referred to as the numerical aperture (NA)

where *obj* and *cond* represent objective and condenser respectively. Using typical values $[nsin(\alpha)]_{obj} = [nsin(\alpha)]_{cond} \sim 1.3$, $\lambda \sim 0.5\mu m$ we find that $d \sim 0.24\mu m$. The resolution can be improved further using 'oil immersion techniques' where one inserts a thin film of oil, of a high refractive index, between the sample and the objective lens i.e. increasing the half-angle of acceptance.

In the previous scattering experiments the particles used had a radius $a \sim 238nm$, and therefore these particles are just above the resolution limit. As large clusters, of many tens of particles, are being formed in these samples the following phase contrast experiments examined only the large scale structure. In practice contrast between sample and background, rather than resolution, would present the largest problems. For the DIC studies larger particles were used, $a \sim 500nm$, so that individual particles could be resolved.

4.4.3 Phase contrast results

All the results presented in this section were obtained using a standard Olympus BX-50 microscope, operating in the phase contrast mode. Images were taken using a typical magnification of ×200. The samples were homogeneously mixed and a drop removed and placed onto a microscope slide. A cover slip was then placed on top and vigorously agitated to break up any remaining aggregates. As the observed images lacked a strong contrast a computer algorithm was written to take the initial grey scale image (256 pixel values) and convert it into a simple binary image (black and white) about some mean pixel value. As most images were subject to an intensity gradient across the sample, the code was refined to threshold about course-grained mean values in the image. The image was divided into cells and average pixel values were calculated for each. The cells were then thresholded about a value relative to the average pixel value in each cell.

Firstly sample 5 was examined and the resulting images are shown in figure 4.35. As can be seen a significant coarsening of the structure is observed, from initially separate clusters to a single system spanning cluster in the final image. The small angle scattering measurements suggest that one should observe a dense, compact, structure ($d_f \sim 3$) and the growth should follow the accepted behaviour associated with classical spinodal decomposition. If one compares this structure with that of a molecular system undergoing spinodal decomposition, e.g. from reference [132], one observes a marked similarity.

Once the system has percolated it is seen to slowly disintegrate about thin necks in the structure into discrete clusters. Immediately a macroscopic flow is observed which breaks up the remaining structure. A possible interpretation is that the system, once percolating, actually supports the coverslip on the slide, as the slide to coverslip separation is only $\sim 25\mu m$. For example the clusters shown in figure 4.35 are up to approximately $\sim 18\mu m$ in size. Once the structure starts to disintegrate the coverslip is no longer supported, collapses and induces a large scale flow. To avoid this problem one can remove the effect of gravity, results of which will be presented later.

From the light scattering data one expects the structure of the clusters to become ramified as the depletion potential is increased. As shown in figure 4.36 sample 9 indeed shows the formation of tenuous, ramified structures consistent with the transient-gelation regime discussed previously. Although the structure is not resolved in fine detail, there is certainly a significant difference between the clusters observed here and that of sample 5 (figure 4.35). Also little structural change is observed as time progresses, consistent with the observation of a frozen ring in the small angle light scattering. Again, after a certain time, a large scale macroscopic flow destroys the structure.

For the third regime, the nucleation-like behaviour of sample 1, one observes small clusters which form after a finite time (see figure 4.37) i.e. consistent with the observation of a 'lag time' before the formation of a small angle ring. One can estimate the critical cluster size to be approximately 5 particle radii. Although the light scattering showed very early time spinodal-like kinetics, the microscopy is reminiscent of classical

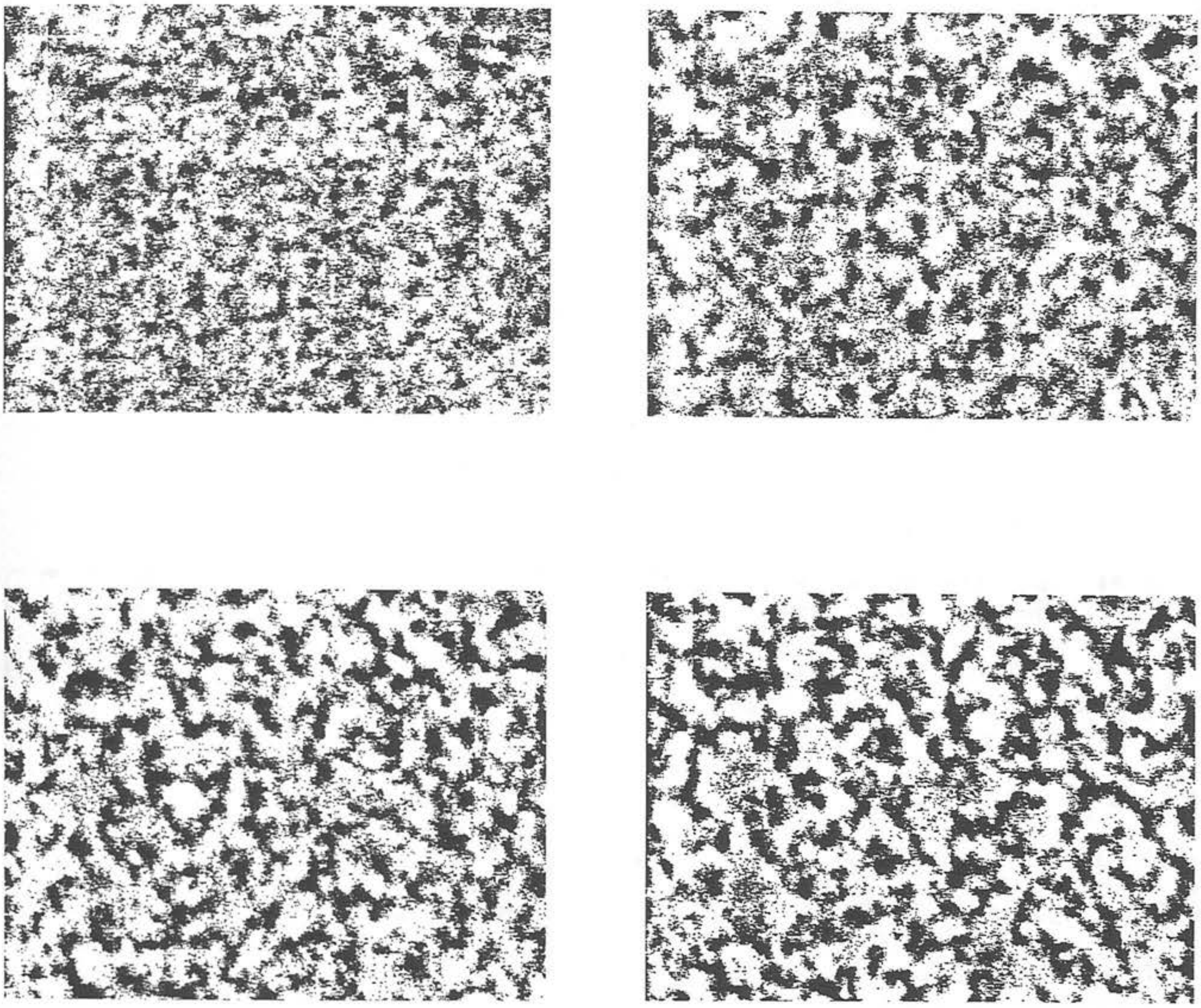

Figure 4.35. Sample 5, showing confirmation of the spinodal-like behaviour measured by light scattering. The images were taken at times 2, 35, 70, and 200 seconds respectively from left to right in both cases. The horizontal scale is approximately $129\mu m$ and the vertical approximately $94\mu m$ N.B. The particle radius $a \sim 0.24\mu m$.

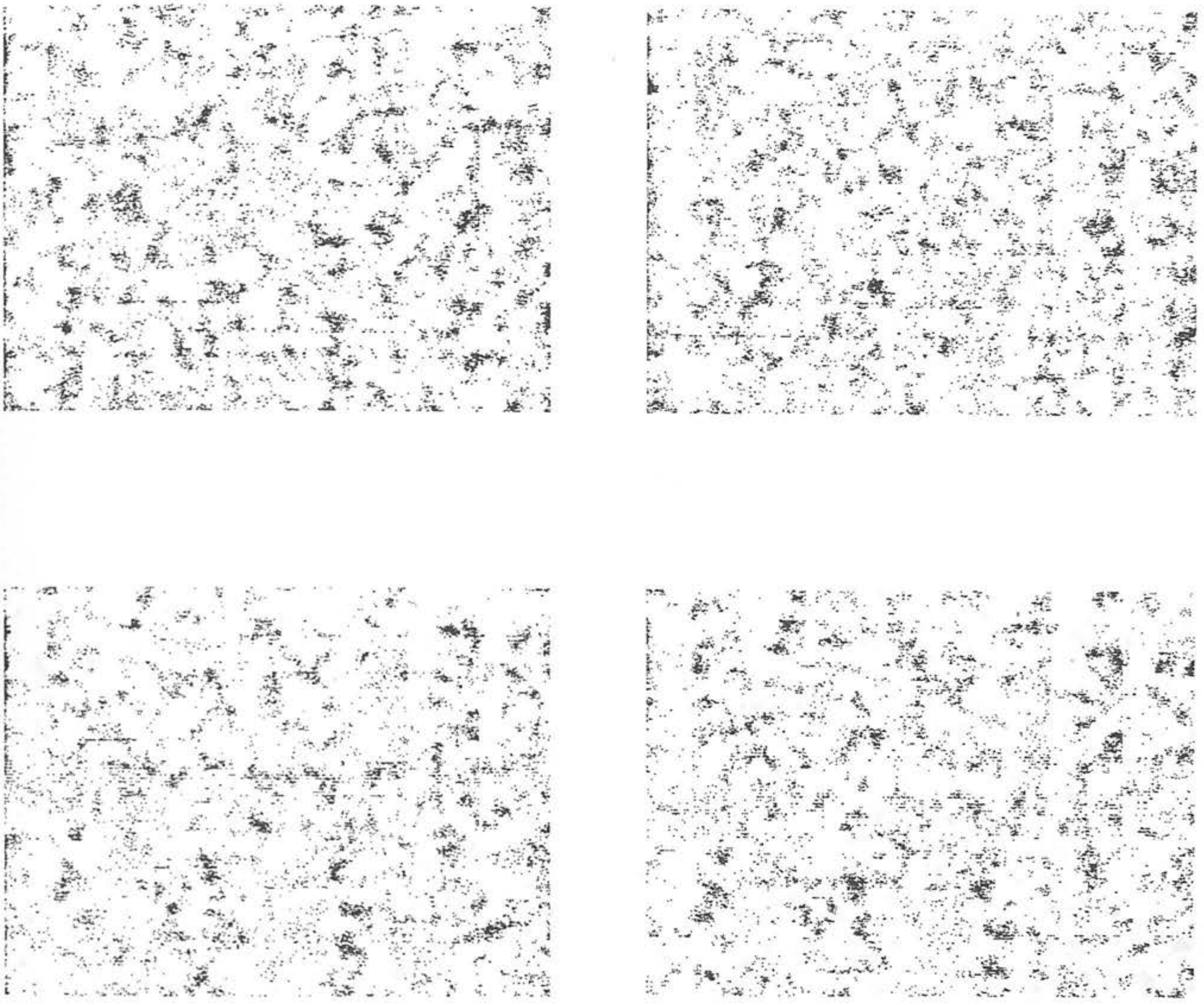

Figure 4.36. Sample 9, showing confirmation of the ramified structure measured by light scattering. The images were taken at times 2, 35, 95, and 200 seconds respectively from left to right in both cases. Note the lack of substantial structural change. The horizontal scale is approximately $129\mu m$ and the vertical approximately $94\mu m$ N.B. The particle radius $a \sim 0.24\mu m$.

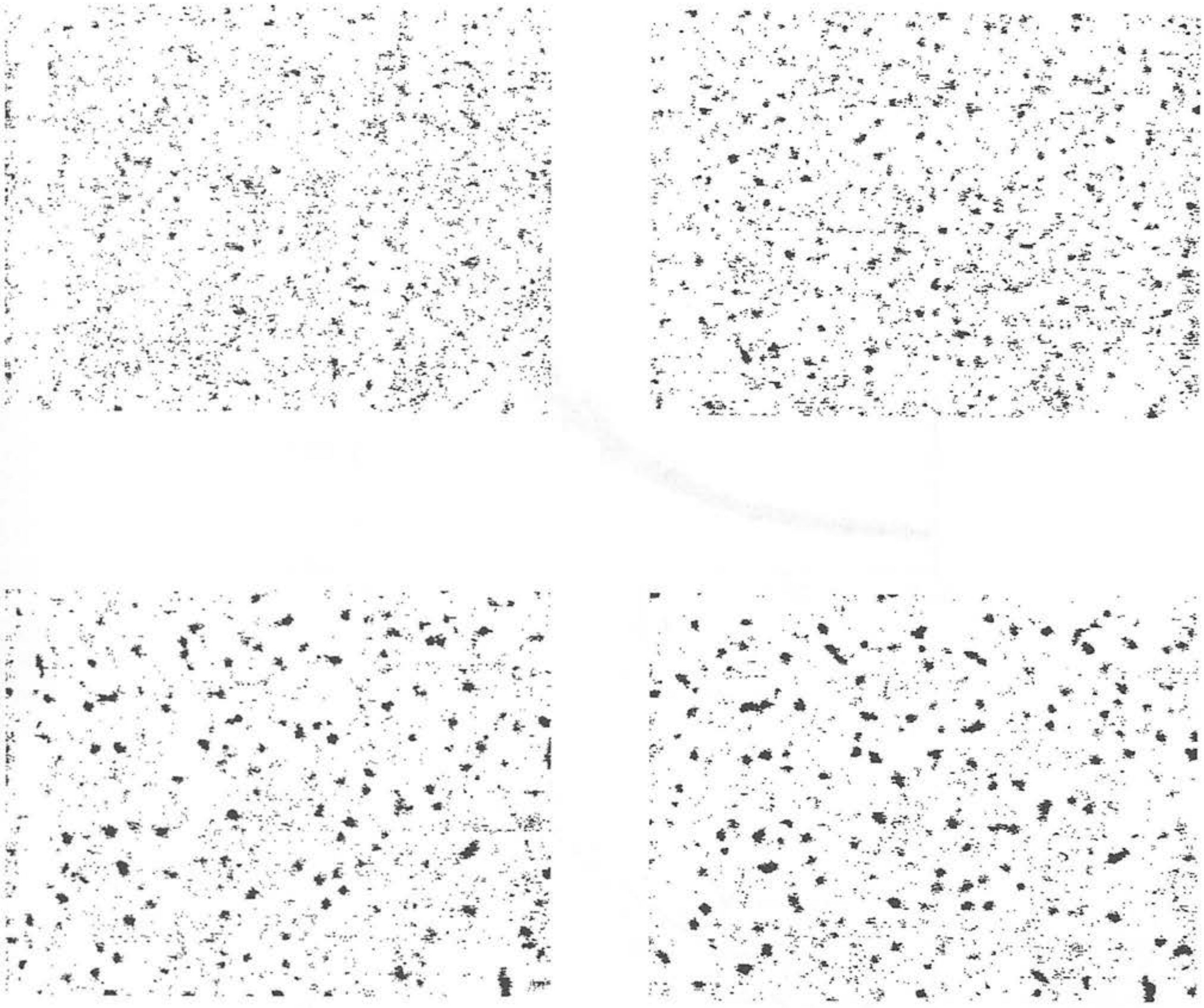

Figure 4.37. Sample 1, showing confirmation of the 'lag time' before enough clusters form to give structural correlations in light scattering. The images were taken at times 3, 37, 82, and 213 seconds respectively from left to right in both cases. The horizontal scale is approximately $129\mu m$ and the vertical approximately $94\mu m$ N.B. The particle radius $a \sim 0.24\mu m$.

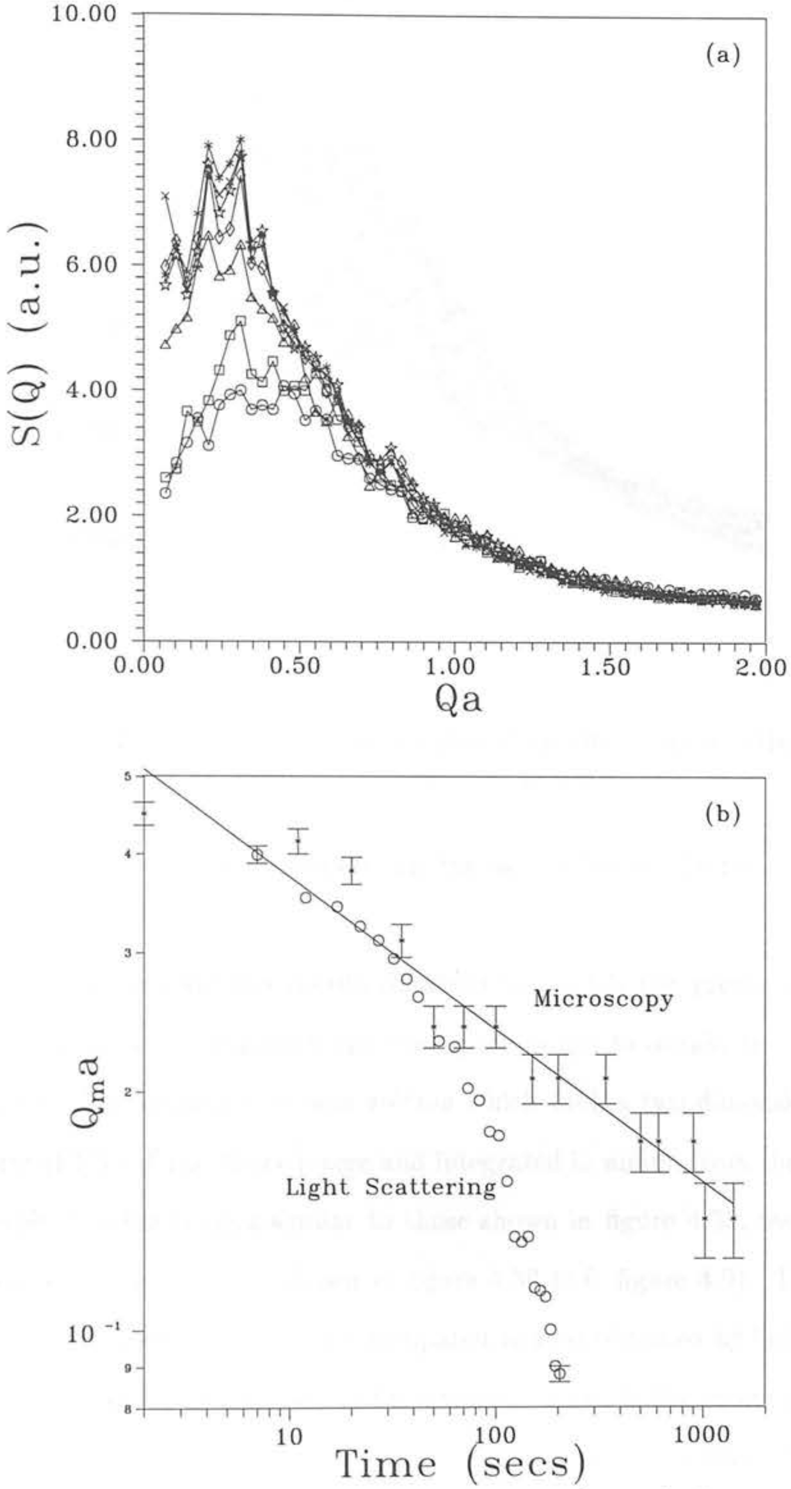

Figure 4.38. (a) FFTs from microscope images of sample 5, representing times 2, 20, 35, 150, 200, 500 and 900 seconds respectively from bottom to top (b) The peak position against time from microscopy and light scattering.

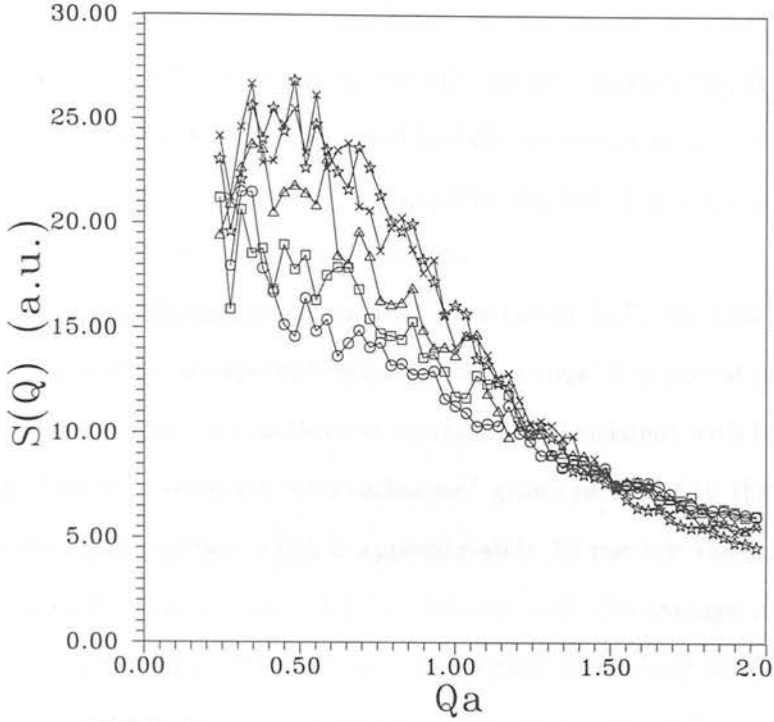

Figure 4.39. FFT's from microscope images of sample 1, representing times 3, 23, 82, 123, and 213 seconds respectively from bottom to top.

nucleation and growth, confirmation that the sample lies within the transitional regime of figure 4.31.

To directly compare the results obtained here with the previous light scattering data, one can Fourier transform the real space image to obtain the equivalent structure factor[8]. Therefore a code was written which took a two dimensional fast Fourier transform (FFT) of the direct image and integrated in annuli from the centre outward. For sample 5, using images similar to those shown in figure 4.35, we obtain a brightening and collapsing ring as shown in figure 4.38 (c.f. figure 4.9). The peak position against time is shown below. When compared to that obtained by light scattering, one observes the kinetics in this case to be extremely slow. If the structure percolates between the microscope slide and cover slip the structure will become effectively arrested

---

[8] Note that the structure factors represent scattering from a two-dimensional section of the structure, rather than a three-dimensional volume element in the light scattering experiments.

by these enforced boundaries. This conjecture is upheld by the observation of equal initial growth rates in either case i.e. before the system has percolated and experienced the effect of the walls. In fact in all the microscope experiments, the kinetics were observed to be slower than those observed by light scattering ($25\mu m$ width compared with a $1cm$ cell thickness). Therefore one expects the cell dimension to play a significant role in determining the subsequent kinetics.

Fourier transforming images such as those shown in figure 4.36 leads to the formation of a frozen ring, as expected. Similarly a 'lag time' is observed before the formation of a ring from images such as those in figure 4.37. Consistent with light scattering data the ring stays at a constant wavevector and grows in intensity (figure 4.39). The inverse of the peak position ($\frac{2\pi}{Q_m}$) is approximately 15 particle radii and corresponds to a distance of 6.5 mm in figure 4.37, consistent with the average inter-cluster separation. This would suggest that the small angle peak arises from inter-cluster rather than intra-cluster correlations, consistent with previous studies [54].

4.4.4 DIC results

A similar study was also conducted using a DIC microscope at Unilever research, Port Sunlight Laboratory. The setup consisted of a standard Olympus BH2-BHS microscope fitted with DIC optics and a motorised translation stage, interfaced to a Kontron IBAS image processing system. The stepper motor controlling the translation stage was calibrated using a sample of known thickness. Sequential optically sectioned images could then be gathered automatically throughout the sample.

A sample was prepared with a particle radius $a \sim 500nm$ ($\xi \sim 0.04$), polydispersity $\sigma \sim 0.05$, volume fraction $\phi \sim 0.2$ and just sufficient polymer to induce aggregation. Firstly single images were taken of which a typical example is shown in figure 4.40, for a magnification of ×100. Again one observes dense clusters, which look similar to those observed in atomic systems undergoing spinodal decomposition. Using the translation stage one can then capture a series of images which could then be rendered using

Figure 4.40. A single DIC image of a spinodal-like sample.

'Odyssey' movie presentation software (originally intended for confocal microscopy). Although the resolution of the rendered image could be improved using oil immersion, it was found that the oil coupled the lens to the stage, inducing flow in the sample as the stage was translated. A subsequent three-dimensional image can then be reconstructed and a hard copy produced (see figure 4.41). This technique, although in its infancy, provides full three-dimensional information rather than a two-dimensional slice through a sample.

Again one observes dense spinodal-like structures which can be roughly quantified by the local volume fraction of particles, ϕ_L. By simply counting the number of particles within known three dimensional volume elements as the focal plane of the microscope

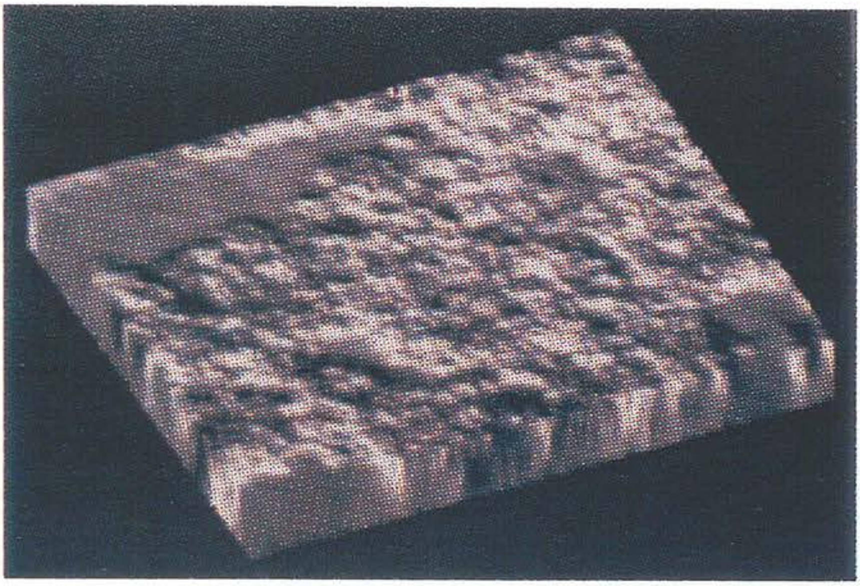

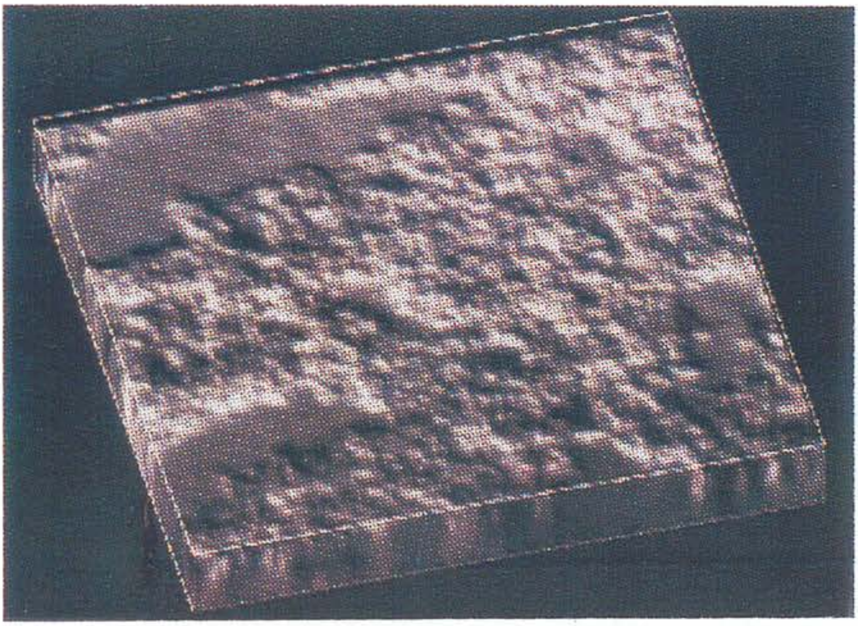

Figure 4.41. Rendered DIC images, from a spinodal-like sample.

is scanned through the sample, one can estimate ϕ_L. In practice one would require a very large number of elements to obtain the true ensemble average. From averaging ten representative volume elements one finds a local volume fraction $\phi_L \sim 0.53 \pm 0.05$, indicative of an extremely dense amorphous structure (c.f. close packing $\phi_L = 0.64$).

4.5 Observations on larger length scales

To directly observe the non-equilibrium samples, in situ, on a somewhat larger, intermediate, length scale one can use a CCD camera with a high powered lens. Rather than resolving individual clusters one obtains a 'textured' image, indicative of large scale density fluctuations. In doing so, one can directly observe macroscopic flow between clusters. Therefore sample 12 was examined to compare the real space kinetics on intermediate length scales with those observed by small angle light scattering. Both experiments were carried out on the same sample in a $1cm \times 1cm$ cross section cell.

4.5.1 The structure formation

After the sample is homogeneously mixed one observes a large scale flow as the small angle ring forms and collapses. The flow ceases as the small angle ring freezes. Subsequently the structure remains arrested, although during this regime the speckle pattern fluctuates very slowly (of the order of 100 seconds). Obviously such slow diffusion cannot be resolved by direct imaging on this large length scale. Approximately after a thousand seconds small scale vortices are observed, which induce a slow fluctuation in the scattered speckle pattern. The fluctuations increase over time until the speckles fluctuate rapidly and the ring collapses completely. A slowly diffusing large scale flow is observed, coincident with the collapse of the ring, marking the onset of gravitational settling. These observations are summarised in figure 4.42.

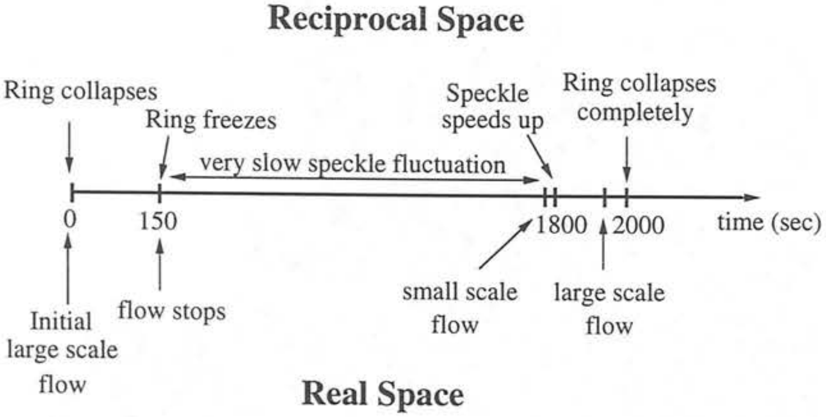

Figure 4.42. Comparing real and reciprocal space kinetics.

4.5.2 The structural collapse

An interesting observation is that the onset of the small scale vortices observed above, marking the collapse of the gel structure, occur first at the *top* of the sample. The vortices are first seen to occur at the juncture between the meniscus and the wall of the sample. The flow then propagates downward throughout the sample. Similarly if one looks at the scattered speckle pattern from the top and bottom of the sample, the ring collapses at the top before that at the bottom[9]. A logical conjecture is that the collapse is driven by the presence of the meniscus. To test this hypothesis sample 9 was inserted into a smaller cell which was filled completely and turned upside down. Now the top of the sample no longer had a meniscus and simply met a flat wall. Again the collapse was seen to start at the top, this time uniformly across the sample. As yet it is unclear why the collapse first occurs at the top of the sample.

The structural collapse could also be attributed to gravity (although the collapse would then start at the bottom of the sample), so the fully filled sample (9) was slowly tumbled, with a period of approximately one minute, so that on average the effect of

---

[9] It must be stressed that all the previous small angle scattering experiments were taken from the middle of the sample, and therefore can be compared directly to one another.

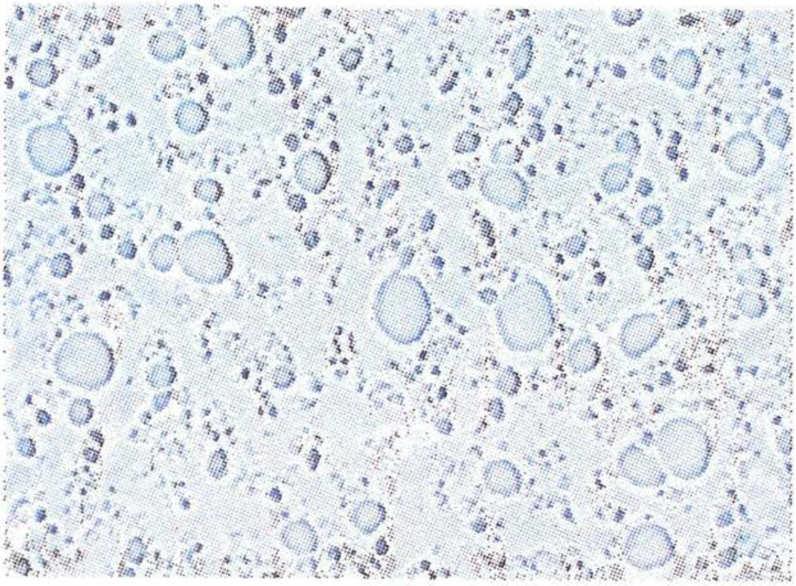

Figure 4.43. Dense clusters formed by removing the effect of gravity. The horizontal and the vertical scales are $1030\mu m$ and $800\mu m$ respectively. The particle radius is $a \sim 0.238\mu m$ and therefore the diameter of a typical cluster is approximately 160 particle diameters.

gravity would be removed. The rotational period was selected to be intermediate to the initial ring formation time and that of the structural collapse. After a number of hours of tumbling a drop was removed from the sample and inserted into the phase contrast microscope. The resulting image is shown in figure 4.43. Strikingly the initially percolating structure (figure 4.36) has disintegrated into large, polydisperse clusters with a typical diameter of approximately 160 individual particle diameters. This appears to be a true phase separation into dense droplets of one phase and perhaps a dilute phase of another. These clusters appear very similar to those observed by Hashimoto et al. [104] in a binary polymer mixture undergoing spinodal decomposition, the so-called 'percolation to cluster' transition. As discussed they attribute this transition to the structure minimising its surface tension, although the role of a surface tension in colloid-polymer mixtures is somewhat unclear. The disintegration of the gel into discrete clusters could be caused by the osmotic pressure difference between the (colloid poor) polymer solution and the initially percolated (colloid rich) structure i.e. simply a depletion effect. The net force on the structure would tend to pinch the structure at weak points ('necks') and drive particles into the bulk ('bulges'). Once the structure has disengaged the pressure of the polymer solution would tend to form spherical clusters or droplets. Alternatively slow particle rearrangement driven by Brownian motion would tend to compact the structure on a local length scale until the system no longer percolates and dense discrete clusters are formed. This mechanism is consistent with that observed in Ising-like simulation [69], [126] i.e. the so-called 'dynamic spinodal'.

4.6 Large angle scattering

Now that the large scale structure has been fully determined it would appear appropriate to briefly study the small scale structure. To carry out such measurements a typical conventional light scattering apparatus was used, which is shown schematically in figure 4.44.

4.6.1 Experimental setup

The system comprises a Kr^+-ion laser, with an expanded beam, passing through a cylindrical liquid bath, of refractive index approximately equal to the sample studied (i.e. $n \sim 1.49$). An expanded beam is utilised, when studying non-equilibrium samples, to provide a large scattering volume, which averages the scattering over a large number of typical particle configurations i.e. providing an ensemble average over a number of speckles. The sample, a cell of cross section $1cm \times 1cm$, is then positioned in the centre of the liquid bath. In such an arrangement there will be little, to no, refraction effects as the light enters and exits the sample cell. Once the light exits the liquid bath, at an angle θ, the bath acts as a lens and focuses the light onto a slit in front of a photomultiplier tube (PMT). Often included inbetween the slit and the PMT is a diffuser which 'averages' the light which then reaches the detector. An averaged PMT input reduces the effect of speckle noise in the output signal. The detector is attached

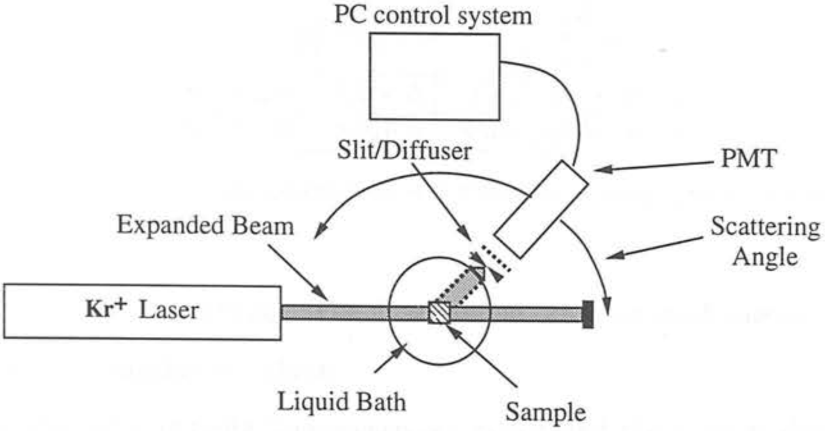

Figure 4.44. Experimental setup for large angle conventional light scattering from non-equilibrium samples. For fully ergodic samples i.e. those without frozen-in density fluctuations, the broad beam is replaced by a narrow, focused beam.

to a computer controlled turntable, which is accurate to $\pm 0.1^0$.

Such a setup is ideal for studying colloidal suspensions with frozen-in density fluctuations. If one examines fully ergodic samples or requires a form factor measurement then a narrow, focused beam is used without a diffuser to isolate only a few coherence areas (speckles).

4.6.2 Results

Conventional light scattering is frequently used to examine the structure of colloidal fluids on short length scales (i.e. large Q vectors). To determine the short range structure of the non-equilibrium phase, and its relation to the other phases, three samples were prepared as described in table 4.4.

The first sample, 19, was a suspension of volume fraction $\phi \sim 0.2$ with no added polymer. This sample would provide a good reference base and in turn test the hard sphere behaviour of the dispersion. The second sample, 20, contained sufficient polymer to induce phase separation, again at a volume fraction $\phi \sim 0.2$. Sample 20 phase separated into coexisting colloidal fluid and colloidal crystal within approximately four

	ϕ	C_P	*Phase*
19	0.182	0	Fluid
20	0.202	3.06e-3	Fluid-Crystal
21	0.198	3.91e-3	Non-equilibrium

Table 4.4. Samples of volume fraction $\phi \sim 0.2$ and increasing polymer concentration.

hours after homogeneous mixing. The final sample, 21, contained enough polymer to cross into the non-equilibrium phase.

The samples were initially homogeneously mixed and the angular dependence of the total scattered intensity was measured almost immediately i.e. well before the collapse of the non-equilibrium structure and before visible iridescence was observed in the fluid-crystal sample. They were then centrifuged over a number of hours until a dense sediment had formed. A few particles were gently redispersed and form factor measurements were made in identical experimental conditions. As samples 20 and 21 contained large concentrations of polymer, care had to be taken not to redisperse too many colloidal particles as aggregation could easily occur. The formation of any small clusters was observed as a small, but pronounced, peak in the measured form factor at $Qa \sim 3.9$ (see equation(4.44)). As such the measured form factor was rejected.

4.6.3 Discussion

The measured structure factors are shown in figure 4.45, approximately normalised so that $S(Qa \to \infty) \sim 1$. As can be seen the sample without polymer, 19, matches the Percus-Yevick approximation of a monodisperse hard-sphere fluid of equal volume fraction, to within ±3% (see section 3.4.1). Strikingly the main peak in the structure factor moves to larger wavevectors as the depletion potential depth is increased i.e. the interparticle separation decreases due to the onset of particle clustering. One also finds that the structure factor peaks concomitantly increase, as the preferred interparticle spacing becomes strongly correlated.

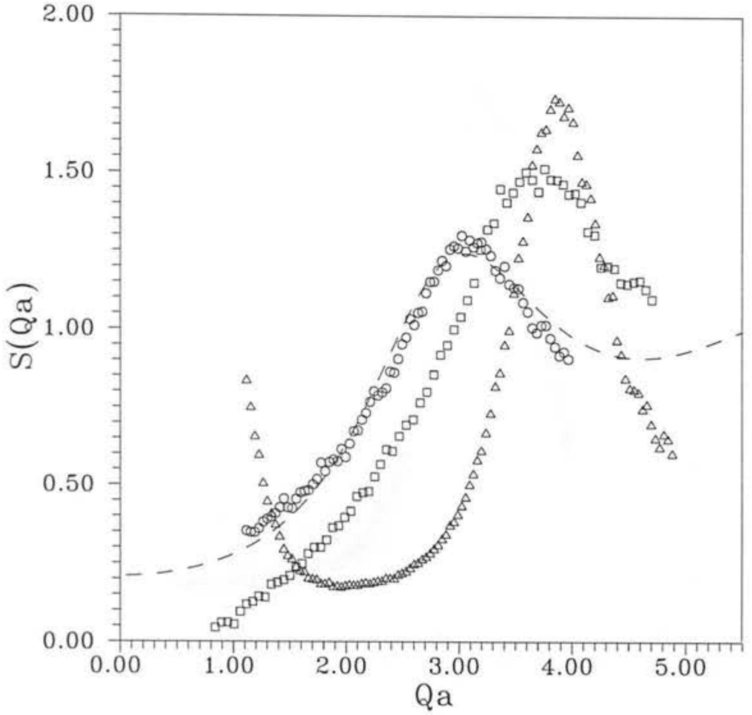

Figure 4.45. Structure factors of samples with colloid volume fraction $\phi \sim 0.2$ and increasing polymer concentration, Circles ≡ 19, Squares ≡ 20 and Triangles ≡ 21.

One can calculate the structure factor of a pair of particles in contact (referred to as a *doublet*), which can be written (see appendix E)[133],

$$S(Q) = \left[\frac{sin(2Qa)}{2Qa}\right] + 1 \tag{4.44}$$

The doublet structure factor has a peak at $Qa \sim 3.9$, coincident with the peak in the non-equilibrium structure factor. Therefore one can regard the non-equilibrium state as an ensemble of particles in contact i.e. as expected, an aggregate.

A similar variation of interparticle peak position with interaction strength has been seen in colloidal suspensions with a decreasing quality of solvent [134]. In such studies the structure factors can be compared directly to the AHS model. As PY structure

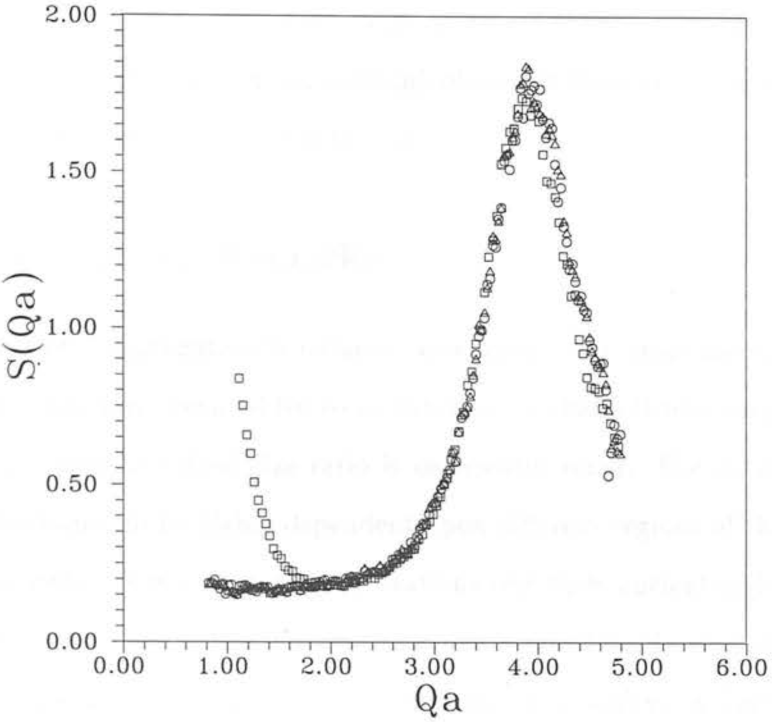

Figure 4.46. Structure factors of non-equilibrium samples of different composition, Squares ≡ 21, Circles ≡ 22 and Triangles ≡ 23.

factors only apply to systems in equilibrium, the non-equilibrium state cannot be compared directly to such models, yet it is interesting to note that the first peak in the AHS fluid, in the low τ_B, $\phi = 0.2$ limit, lies at $Qa \sim 3.9$ (see figure 3.7).

One finds that the interparticle peak in the structure factor is independent of which non-equilibrium region is studied. For example figure 4.46 shows three non-equilibrium structure factors of composition given by tables 4.4 and 4.5. These samples are all of volume fraction $\phi \sim 0.2$ but have varying amounts of polymer, so that they cover

	ϕ	C_P
22	0.204	2.89e-3
23	0.212	3.35e-3

Table 4.5. Non-equilibrium samples of volume fraction $\phi \sim 0.2$ and different polymer concentration.

the spinodal-like (22) and transient-gelation regimes (21, 23). The interparticle peaks coincide to within 2% i.e. the short range structure is somewhat insensitive to the details of the interparticle potential, although obviously there is a composition dependent enhanced small angle scattering ($Qa < 1$).

4.7 Concluding Remarks

Non-equilibrium aggregation is induced once sufficiently large amounts of a non adsorbing polymer have been added to an otherwise stable colloidal suspension, provided that the polymer to colloid size ratio is sufficiently small. The resulting aggregation kinetics are found to be highly dependent upon different regions of the phase diagram.

At low colloid and polymer concentrations one finds nucleation-like behaviour. A 'lag-time' is observed before the formation of a small angle ring of scattered light, which remains at a fixed wavevector and grows in intensity. A finite time before an inter-cluster correlation is observed is a well known phenomenon in nucleation experiments. Consistent with this observation, microscopy shows the formation of dense discrete clusters which form only after an initial period. These independent clusters then sediment under gravity to form a metastable sediment.

At intermediate colloid concentrations and just sufficient polymer to induce aggregation one finds behaviour reminiscent of classical spinodal decomposition i.e. the formation of a dense interconnected system-spanning structure. Accordingly one finds a continuously collapsing and brightening small angle ring, indicative of a characteristic length scale which grows rapidly over time. The measured structure factors scale to a fractal dimension of 3 and coincide with the Furukawa prediction for classical spinodal decomposition. The time evolution of the small angle ring suggests an initial diffusion-driven growth, which switches to a gravity dominated motion once the clusters have grown sufficiently large. Once gravity has taken effect the structure collapses to form a metastable sediment.

Upon the addition of still further polymer or upon an increase in the colloid volume fraction, the aggregation is seen to follow a DLCA-type mechanism to form a system-spanning gel structure. At small angles one initially observes a collapsing ring of scattered light, which becomes frozen at a finite wavevector. This can be attributed to an initial diffusion-driven growth, which rapidly leads to the formation of an arrested system spanning network with a structural rigidity which prevents gravitational settling. The small angle structure factors from such a sample scale to a fractal dimension of 1.7 consistent with a DLCA-type mechanism. After a finite time the arrested small angle ring collapses rapidly, roughly coincident with the onset of visible sedimentation. This can be attributed to a slow particle rearrangement, driven by Brownian motion, which tends to compact the structure on a small local length scale, leading to the formation of discrete clusters which settle under gravity. On a larger intermediate length scale the onset of sedimentation is characterised by vortices observed at the top of the structure. The flow then propagates downward through the sample, disrupting the system-spanning network and inducing the structural collapse. As yet it is unclear what drives this process. Once the collapse is underway back flow of the solvent destroys the remaining structure and proceeds until a ramified metastable sediment is formed. This collapse is suppressed in the absence of gravity and the system phase separates into dense independent droplets due to the slow particle rearrangement.

The short-range structure of these transient states is found to be insensitive to the large scale structure. The particles are found to be in contact with one another in all the different kinetic regimes and therefore, as expected, these represent aggregated states.

The onset of aggregation, i.e. the non-equilibrium line, is found to be consistent with the theoretical metastable gas-liquid boundary. Once analogies have been made between the colloid-polymer system and Ising-like simulation, of phase separating systems with a short-ranged potential, the different kinetic regimes within the non-equilibrium region can be explained. Not only are the predicted kinetic regimes quantitatively similar to those observed, but one also expects the structure to percolate for only a finite time i.e. the observed structural collapse.

Although an extensive study of the kinetics of the non-equilibrium phase has been presented, as yet diffusion within these samples has been largely ignored i.e. the study of particle dynamics (how structures diffuse) rather than the study of kinetics (how individual 'snap-shots' of the structure evolves). In the next chapter I present a detailed dynamic light scattering study of the non-equilibrium phase.

Chapter 5

Dynamic structure of the non-equilibrium phase

5.1 Introduction

Through the study of temporal speckle fluctuations one can obtain a direct measure of the dynamic properties of a colloidal suspension, a technique known as dynamic light scattering (DLS) (see chapter 3). In this chapter I present results of a DLS study of the non-equilibrium aggregates. Comparison is also made with the static results obtained in the previous chapter. The dynamics of concentrated colloidal suspensions have been studied in detail [53], [135], yet the dynamics of colloidal aggregates and particle gels have remained relatively uninvestigated, as have the dynamics of colloid-polymer mixtures.

5.2 Experimental setup

To conduct these experiments a conventional DLS apparatus was used as shown schematically in figure 5.1. The system comprises an Ar^+ laser ($\lambda = 514.5nm$), with a focused beam, passing through a cylindrical water bath which was regularly filtered to remove

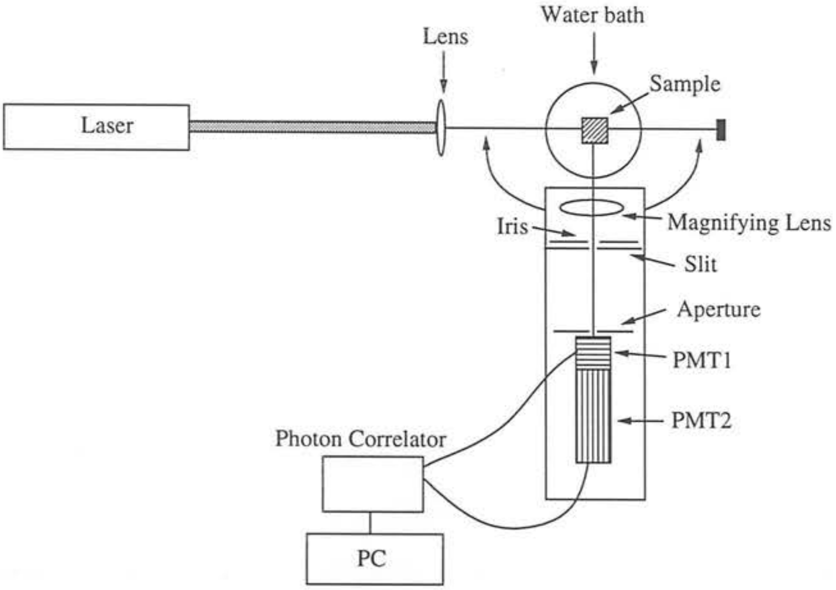

Figure 5.1. Experimental setup for dynamic light scattering.

dust. The sample is contained in a cell of cross section $1cm \times 1cm$, and is positioned in the centre of the water bath. In this setup refraction at the cell-water interface must always be taken into account when calculating the resulting scattering vector. The light scattered at an angle θ is focused onto a slit, which passes to an aperture in front of the PMTs, normally adjusted to the size of a single coherence area (speckle). The light then enters a beam splitter and into two separate PMTs, positioned perpendicular to one another. The two signals form the input to a Photon correlator (ALV-5000) controlled by a PC. The PMTs can be rotated on a goniometer to study different Q vectors and therefore the dynamics of the suspension on different length scales. Finally the whole system is floated on a steel table to remove the effect of vibrations.

Such a setup is ideal for studying ergodic samples. If one studies non-ergodic samples, i.e. samples with density fluctuations which relax on a time scale far greater than that of the experiment, then a different setup must be utilised in order to obtain a fully ensemble averaged field correlation function. In this study the improved manual case was used (as defined in section 3.5.3) so that ten different speckles were measured simultaneously. To do so one first inserts an ergodic sample into the apparatus and the optics adjusted until the intensity correlation function has an intercept of 2 i.e. approximately one coherence area is measured (see section 3.5). The initial focusing lens is removed and the aperture opened until the intercept drops to approximately 1.1 i.e. the coherence is decreased by a factor of ten, and one can then assume that approximately ten independent Fourier components are measured at once. In doing so one can introduce stray light so care must be taken to shield the PMTs. A number of measurements can then be taken of the non-ergodic sample and the results combined to obtain a full ensemble average. In practice one must take an increasing number of measurements until iteratively one obtains reproducible correlation functions.

The output signals from the PMTs were *cross*-correlated throughout to remove the effect of after-pulsing. After-pulsing is observed if residual gas atoms are present in a PMT, which occurs if the vacuum leaks over time. If the primary electron has sufficient energy to ionize a residual gas atom then the ion becomes highly attracted to the primary photo-plate. The ion strikes the plate and another electron is emitted, resulting in two pulses, one primary one secondary, in the PMT signal. In conventional light scattering this has no overall effect as one extra count in several thousand is negligible, yet in DLS one finds a correlation between these two pulses. It is highly unlikely that this should occur in two PMTs at the same time (probability $\sim 10^{-6}$) and therefore by cross-correlating the signals one removes the spurious correlation. After-pulsing occurs on a very short time scale and tends to distort the initial short-time decay of the intensity correlation function.

Thermal lensing [136] was found to be a considerable problem for samples near index match, especially using the Ar^+ laser. Thermal lensing occurs when the incident laser intensity heats the sample. In doing so a temperature gradient is set up which induces convective flow and acts to expand the beam like a lens. Thermal lensing was easily identified, as the straight through beam became greatly expanded and the shape

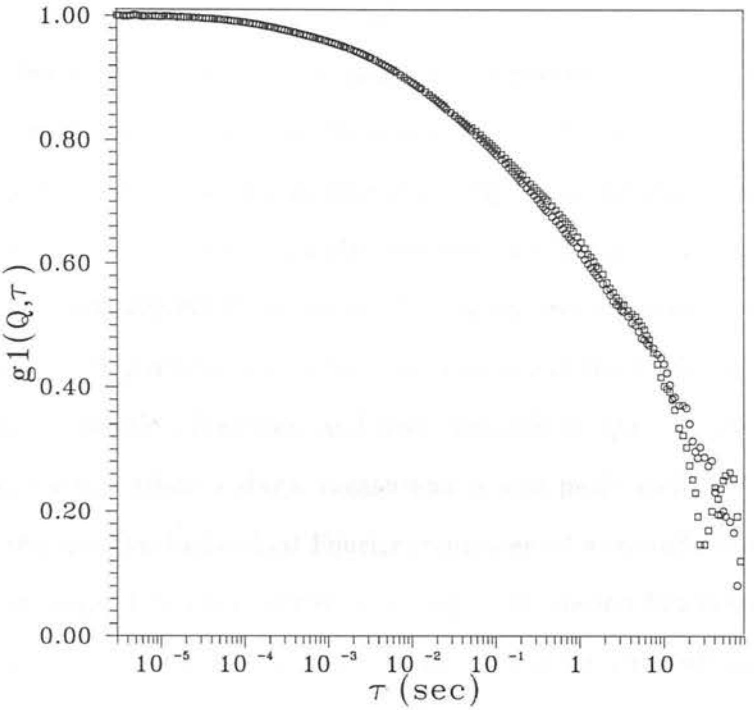

Figure 5.2. Two full ensemble averaged correlation functions, taken at $Qa \sim 6.25$ i.e. single particle motion, from a typical transient-gelation sample. Each represents a measurement over ten individual speckles.

of the intensity correlation function indicated an extremely fast short-time diffusion. To remove this problem the Ar^+ laser could be replaced by a low power He-Ne laser, $\lambda = 632.8nm$, which although appeared to remove thermal lensing, led to problems in signal detection as the sample only scattered weakly.

A detailed discussion of DLS techniques can be found in reference [136].

5.3 Temporal evolution of the single particle dynamics

Sample 9 (see the $\phi \sim 0.1$ section of table 4.1) was taken as a typical example of a sample in the transient-gelation regime of the non-equilibrium region and the single particle dynamics were measured as the structure grew, became arrested and then collapsed. Care had to be taken to avoid measurements at the minimum of the form factor, as these would only probe the effects of polydispersity [92]. Therefore the minimum was always estimated by eye before the appropriate wavevector to study was chosen. Measurements were taken using the apparatus shown in figure 5.1 at a scattering wavevector $Qa \sim 6.25$. As the main peak in the non-equilibrium structure factor occurs at $Qa \sim 3.9$ one can assume that only single particle motion is studied at such a high Q vector, and one simply measures a self diffusion. It is well known that the effect of non-ergodicity is small at high wavevectors [88], i.e. as on such short length scales the particles do not feel the presence of the frozen-in structure, and accordingly the correlation functions and first channels at $Qa \sim 6.25$ were found to be highly reproducible when a single measurement was performed with an expanded aperture, i.e. ten speckles (individual Fourier components) were sufficient to obtain the full ensemble average. Two such ensemble averaged correlation functions are shown in figure 5.2 for a typical transient-gelation type sample, in its arrested state.

Sample 9 was tumbled thoroughly, inserted into the apparatus and consecutive intensity correlation functions measured until visible sedimentation was observed. Each measurement was of duration 500 seconds. The resulting intensity correlation functions were then converted into normalised field correlation functions using equation (3.36), and are shown in figure 5.3 in both the linear-log and log-linear representations. For non-interacting Brownian particles the correlation function would be a single exponential (c.f. equation (3.49)) and simply a straight line in the lower figure.

Obviously the field correlation functions are far from single-exponential [18] i.e. as expected these are highly-interacting systems. In fact the correlation functions take on the form of stretched exponentials,

$$g^{(1)}(Q,\tau) \sim e^{-(\tau/\tau_c)^b} \tag{5.1}$$

where τ_c is a characteristic time and $0 < b < 1$. Such a correlation function

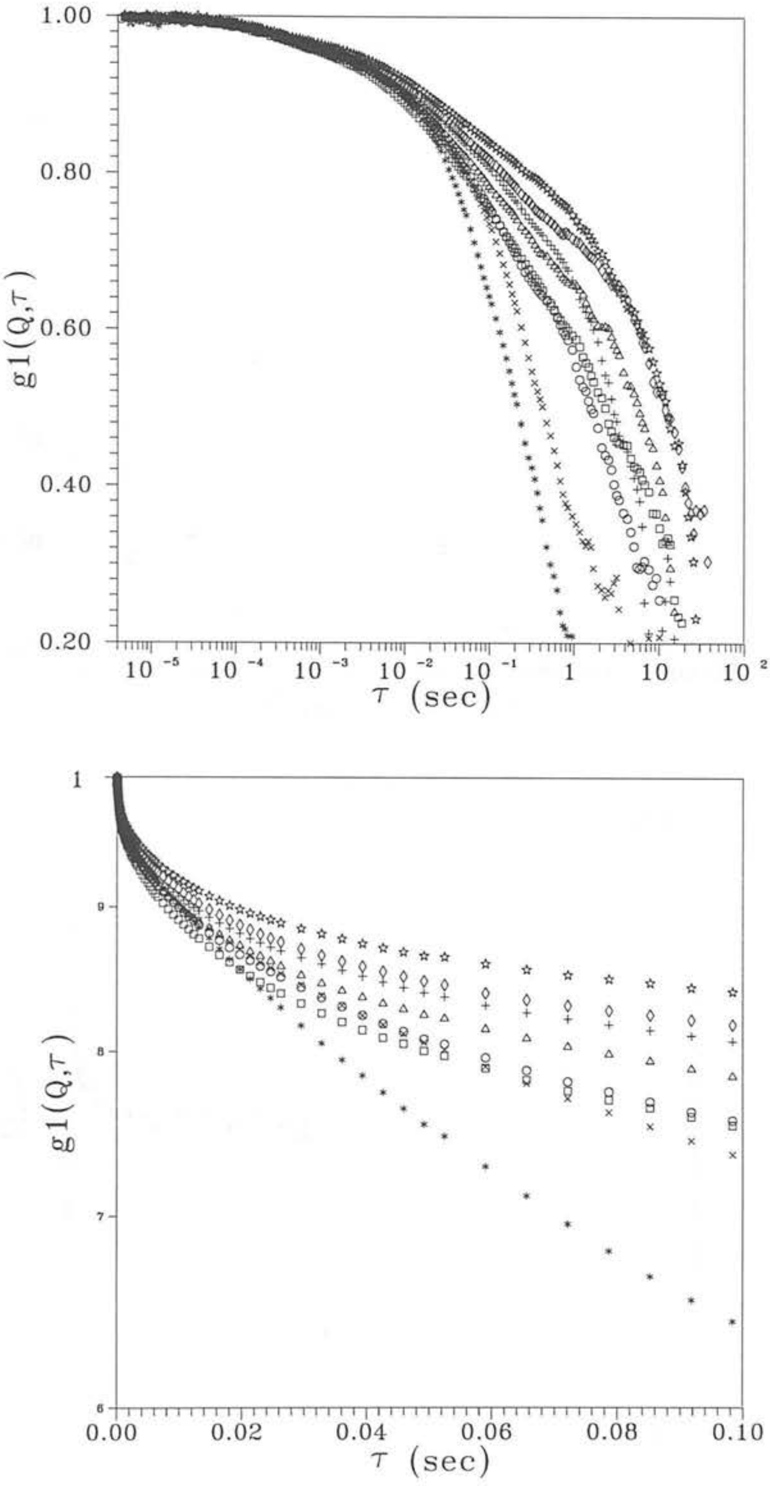

Figure 5.3. Field correlation functions as a function of delay time for sample 9. Circles ≡ the first, Squares ≡ the second, Triangles ≡ the third, Diamonds ≡ the fourth, Pentagram ≡ the fifth Crosses(+) ≡ the sixth, Crosses (×) ≡ the seventh and Asterisks ≡ the eighth 500 seconds.

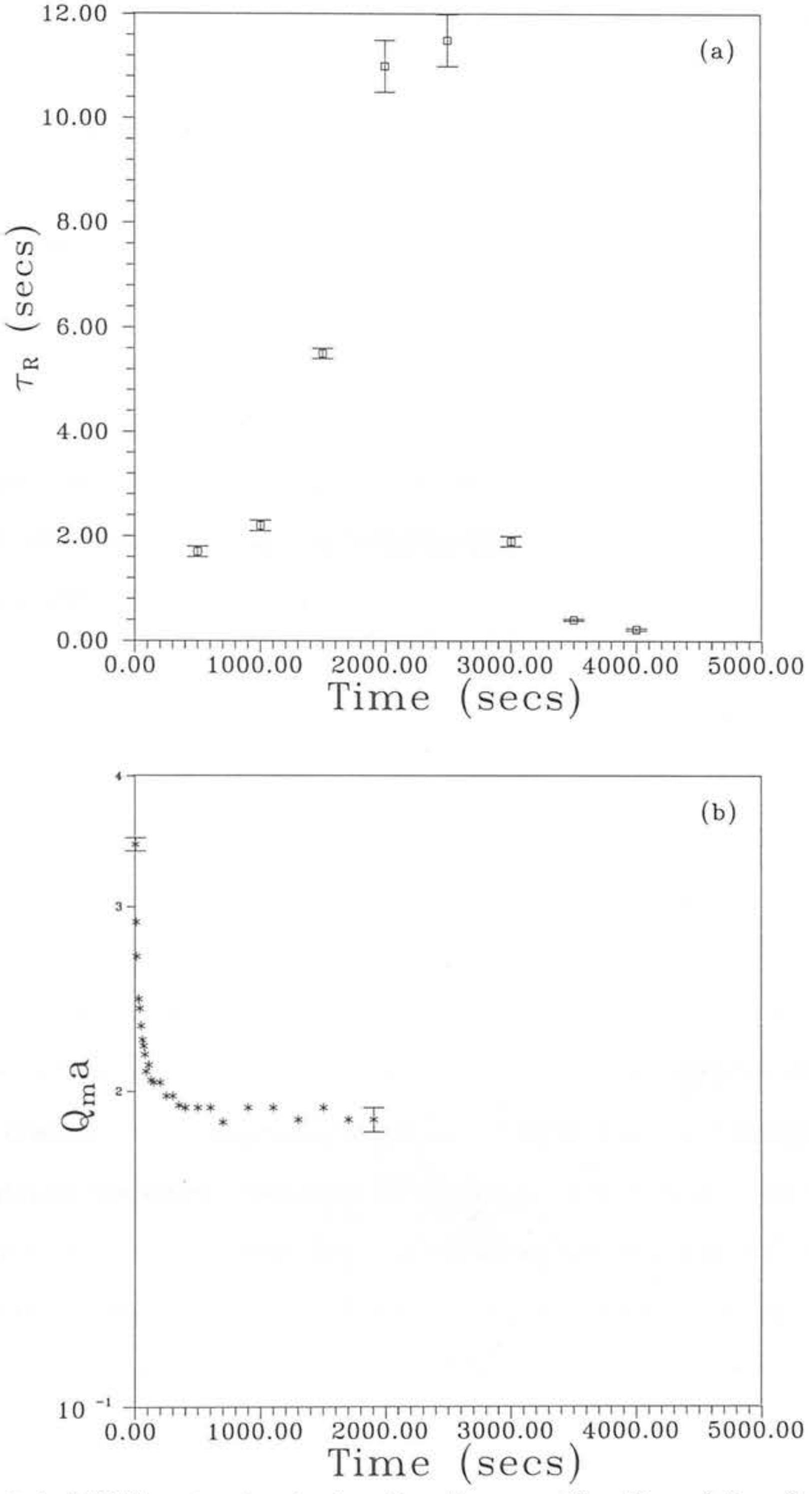

Figure 5.4. (a) The structural relaxation time as a function of time for sample 9. (b) The small angle peak position against time for sample 9.

would suggest decay processes which relax over many similar time scales, rather than a single characteristic time. The correlation functions never decay as single power laws which were observed by Martin et al. [137], [138] in silica gels. They attributed such behaviour to long range fractal structure and self similar relaxation times, although without taking non-ergodicity into account the validity of their data is questionable. Analogies can also be drawn between the non-equilibrium behaviour and the colloidal glass transition, found at high colloid volume fraction in the absence of polymer [89], [139] - [141]. In this case particle motion becomes retarded as the particles become caged-in by the presence of all the others, due to the very high volume fraction of the suspension, rather than through an attractive potential. Close to the glass transition the field correlation functions show two independent decay processes: the α decay associated with the final breakdown of particle cages and the β decay associated with the slow rearrangements of the particle cages. In the colloid-polymer non-equilibrium aggregates there appears to be no evidence for the β decay, perhaps due to the processes relaxing on similar time scales so that the α and β decays become superimposed.

Note also the large amount of statistical noise in the correlation functions at long times. To improve this data one would require extremely long runs which would then encompass the growth, arrest and collapse of the structure. Therefore there is an obvious trade-off between a long experimental time to obtain good statistics against a shorter experimental time to avoid integrating over too many different dynamic regimes.

One possible way of characterising these stretched exponential decays is to measure the structural relaxation time, i.e. the time taken for the field correlation function to decay to $\left(\frac{1}{e}\right)$ of its initial value. In the high-Q limit (yet less than $Q \rightarrow \infty$) the structural relaxation time corresponds to the time taken for a particle to diffuse a distance comparable to its own diameter. Without a long-time single-exponential decay it becomes impossible to measure a long-time diffusion coefficient, so the structural relaxation time would appear the most appropriate measure of the long-time diffusion. The structural relaxation time as a function of elapsed time is shown in figure 5.4(a).

Below is the small angle peak position plotted against the same time axis, data which was shown previously in figure 4.14.

The relaxation time shows a marked increase as the small angle ring collapses and freezes i.e. the single particle diffusion slows down as the large scale structure becomes arrested. As the small angle ring fills in completely the relaxation time suddenly decreases (after approximately 2000 seconds) and does so until visible sedimentation is observed. Although it is reassuring to observe particle motion consistent with the small angle scattering data, the comparison is limited as each correlation function represents an integration over 500 seconds and one loses time resolution i.e. the afore-mentioned trade-off. Interestingly as the small angle ring remains stationary the structural relaxation time still increases ($100 < t < 2000$), and one can conjecture that the structure is compacting over this period, as indicated by the reduction in the long time diffusion. Meanwhile the large scale structure remains unaffected as the short length-scale structure evolves. As the large length scale structure collapses, i.e. when the small angle ring fills-in, the single particle motion rapidly increases.

Even when the large scale structure is in a completely arrested state i.e. the persistence of a frozen ring, the correlation functions still decay, albeit slowly, indicative of slow single particle motion, which as above, one could conjecture acts to compactify the local small scale structure. As the depletion potential depth is only a few k_BT any small thermal fluctuations will be sufficient to break the interparticle bonds and the structure will tend to compact locally as bonds break and reform, until the structure no longer percolates and the now discrete clusters settle under gravity.

What should also be noted from figure 5.3 is the time-invariant, short-time limit of the correlation function, $0.92 \lesssim g^{(1)}(Q,\tau) < 1$. This would suggest that the very short-time motion is insensitive to the large scale structure.

5.4 Short-Time dynamics

In a typical non-equilibrium sample each particle will sit in the depletion potential surrounded by its nearest neighbours in the aggregate. In the very short-time regime the particle diffusion is simply governed by its hydrodynamic interactions with the surrounding particles. As each particle has a typical thermal energy of k_BT the short-time motion, on a slightly longer time scale, should be governed by the particles 'rattling' about some mean position, at a range given by the width of the depletion potential k_BT above its minimum. As the bonds are only a few k_BT in depth, small thermal fluctuations will then break the bond and the particle will diffuse throughout the sample. Thermal vibration of particles about their equilibrium positions is consistent with a Debye-Waller like motion (DWM) [142] in atomic systems. Such motion would be insensitive to the large scale structure, consistent with that observed in figure 5.3.

To test this hypothesis the short-time motion of a number of samples was examined. So far the polymer has been largely ignored and all theoretical interpretations have assumed a simple one-component colloidal suspension subject to a strong, short-ranged attractive potential. When the short-time motion is studied care must be taken to account for the polymer diffusion which would contribute to these short-time scales, as the polymer free diffusion is 14 times faster than that of the colloidal particles. Similarly any slight differences in solution viscosity between samples with more or less added polymer has so far been ignored.

To account for the polymer scattering the samples were first centrifuged until all the colloidal particles were contained in the sediment. Then the correlation function of the polymer solution in the supernatant was measured. Assuming that the overall correlation function is simply a linear superposition of the individual colloid and polymer correlation functions scaled by their relative intensities, one can write,

$$g^{(1)}(Q,\tau)_{colloid} \sim \left(\frac{1}{1-\chi(Q)}\right) g^{(1)}(Q,\tau)_{total} - \left(\frac{\chi(Q)}{1-\chi(Q)}\right) g^{(1)}(Q,\tau)_{polymer} \quad (5.2)$$

where $\chi(Q)$ is the ratio of polymer to colloid scattering, $\chi(Q) = I_{pol}(Q)/I_{col}(Q)$. As $\chi(Q)$ is small (of the order of 4%) and as the polymer correlation function decays quickly the overall correction will be small, yet must still be taken into account. Samples were also prepared with appropriate concentrations of polymer and a few trace colloidal particles of known size. By measuring the short-time diffusion coefficient of the colloidal particles one can infer the viscosity of the background solution η through the Stokes-Einstein equation. Surprisingly the correlation functions did not decay as single exponentials despite the dilute nature of the suspension. This phenomenon is as yet poorly understood. In each case only the short-time motion of the colloidal particles was measured to obtain a diffusion coefficient and infer the background viscosity.

Field correlation functions were measured for a number of non-equilibrium samples at $Qa \sim 6.25$, details of which are given in table 5.1. Using equation (3.55), and assuming self diffusion, mean squared (MS) displacements of the particles were calculated from each sample in its most arrested state. These are shown in figure 5.5 against a time scaled by the relative viscosities of the polymer solutions $\left(\frac{\eta_o}{\eta}\right)$. It must be stressed that the correction for the polymer scattering is negligible on this long time scale ($\tau > 1 \times 10^{-4}$ secs). As is evident one can define two regimes within the MS displacement, one short-time and one long, as the displacement tends to saturate at long times. It is somewhat arbitrary as to how one defines 'short' or 'long'. The distinction was made at the point where the diffusion coefficient had decayed to one hundredth of its initial value and by extrapolating back one can estimate a range for the short-time motion. Below in figure 5.5 is the root mean squared short-time motion for each of the samples, against the range of the depletion potential, k_BT above its minimum.

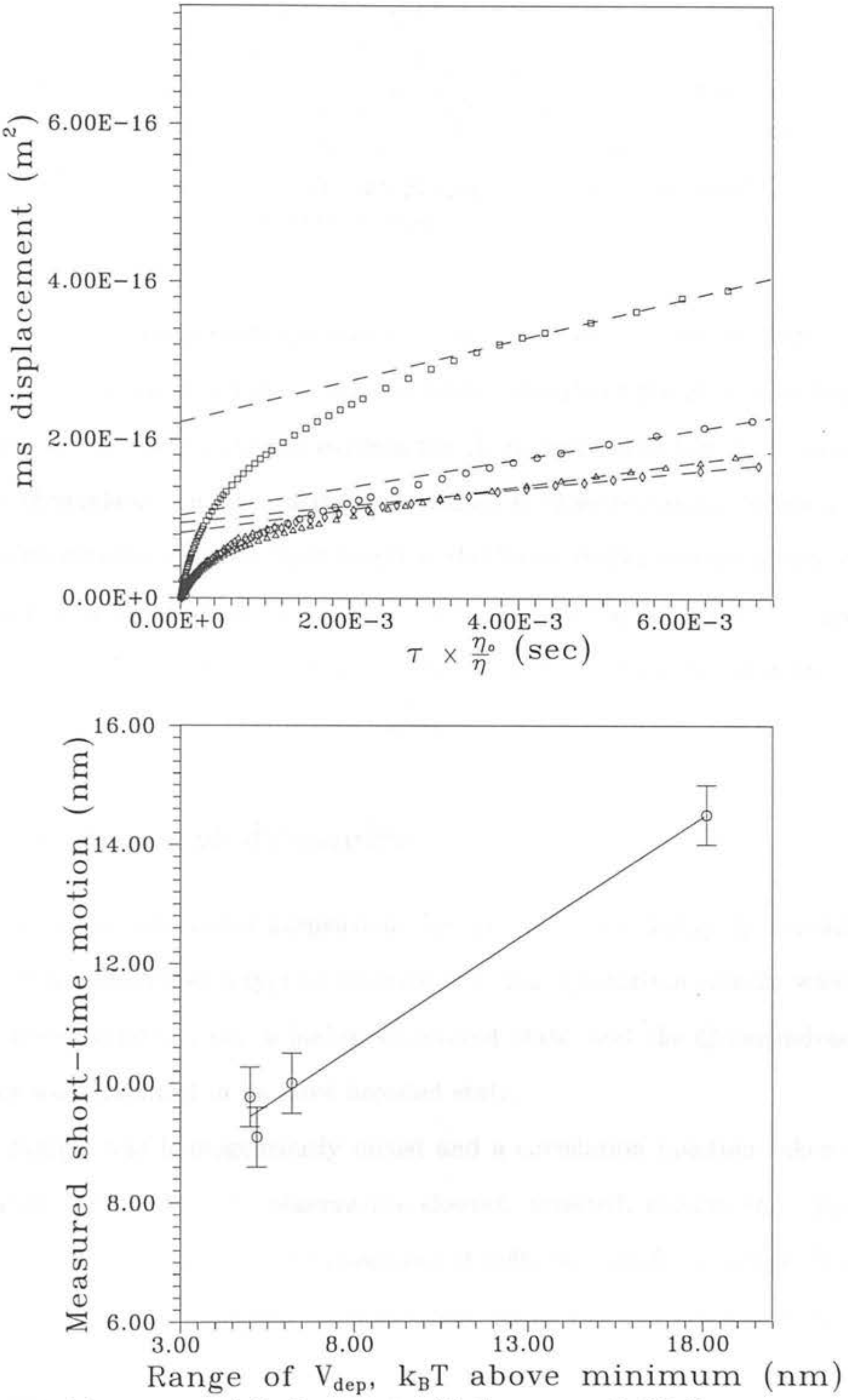

Figure 5.5. Mean squared displacements, Circles ≡ sample 25, Squares ≡ sample 26, Diamonds ≡ sample 9 and Triangles ≡ sample 24. Below is the root mean squared displacement against the predicted short-time motion.

	ϕ	C_P	ξ	predicted DWM	measured short-time motion
9	0.100	6.27e-3	~ 0.07	5.0 nm	9.7 $\pm 0.4 nm$
24	0.198	3.91e-3	~ 0.07	5.2 nm	9.1 $\pm 0.4 nm$
25	0.212	3.35e-3	~ 0.07	6.2 nm	10.0 $\pm 0.4 nm$
26	0.192	2.74e-3	~ 0.19	18.1 nm	14.5 $\pm 0.4 nm$

Table 5.1. Various non-equilibrium samples alongside their predicted DWM and measured root mean squared short-time motion.

Within error the data is certainly consistent with a short-time Debye-Waller type motion. As shown in figure 5.3 this motion persists throughout the growth and collapse of the large-scale structure. As one expects the short-range structure to remain roughly constant throughout, i.e. the particles remaining in close proximity to one another, it comes as no surprise that the short length scale Debye-Waller motion is time invariant.

Rather than simply studying the self motion, at high-Q, it would now appear appropriate to study the Q-dependence of the short-time dynamics and therefore the dynamics over a wide range of length scales.

5.5 Q-dependent dynamics

The dynamics of structured suspensions are known to be highly Q-dependent [53]. Sample 12 was chosen as a typical example of a non-equilibrium sample which underwent transient-gelation, i.e. a highly structured state, and the Q-dependence of the dynamics was examined in its most arrested state.

The sample was homogeneously mixed and a correlation function taken after approximately 500 seconds, to observe the slowest, arrested, motion (c.f. figure 4.15. Such motion is equivalent to that measured at 2000 seconds from sample 9, shown in figure 5.4(a)). With an enlarged pin hole a 500 second run was taken and ten independent Fourier components measured. At low wavevectors non-reproducible correlation

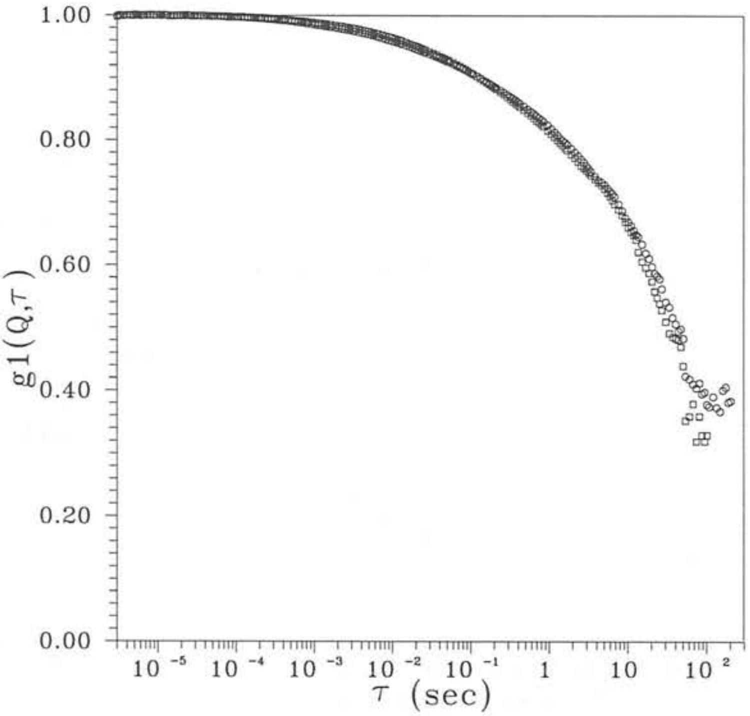

Figure 5.6. Two full ensemble averaged correlation functions from sample 12, taken at $Qa \sim 3.9$ i.e. the high-Q peak in the structure factor. Note the non-ergodic background at long times.

functions, highly fluctuating intensities and low first channels were observed i.e. fingerprints of non-ergodicity. Therefore a number of correlation functions were measured until reproducible ensemble averages were obtained. It was found that by repeating the same procedure ten times, and constructing an ensemble average encompassing 100 independent speckles, one obtained highly reproducible correlation functions. As shown in figure 5.6 the reproducibility of the ensemble averaged correlation functions was found to be excellent, until very late stage when the so called 'non-ergodic background' was found to have a statistical error of ±10%. Such an error in the long time decay of the correlation function is typical [143]. The non-ergodic background, i.e. that the correlation function does not decay to zero, is indicative of the presence of frozen-in density fluctuations. The density fluctuations on this length scale relax on a time scale far greater than that of the experiment. As sample 12 was within the transient gelation

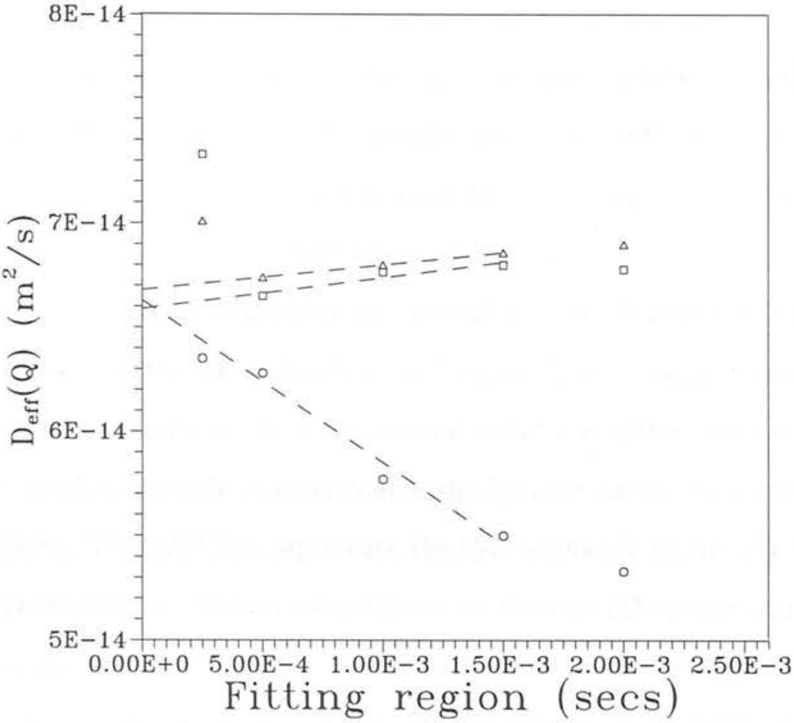

Figure 5.7. Fitting the field correlation function over smaller and smaller time regions, at $Qa = 6.7$. Circles ≡ linear, Squares ≡ quadratic and Triangles ≡ cubic.

regime, the observation of frozen-in density fluctuations is consistent with the arrested structure suggested by the small angle scattering shown in figure 4.15.

These ensemble averaged correlation functions were measured from sample 12, over a wide range of wavevectors ($2 < Qa < 7$), and the full Q-dependent short-time diffusion coefficient measured. Again at these short time scales the polymer scattering had to be accounted for and in fact the short-time diffusion coefficient was found to be rather sensitive to the polymer scattering. Also care had to be taken when measuring the short-time diffusion coefficient as the correlation functions were highly non-single exponential. The short-time decay of the correlation functions were fitted to linear, quadratic and cubic polynomials, and by fitting over shorter and shorter regions a number of diffusion coefficients were measured using equation (3.51). The diffusion coefficients obtained from each of the polynomials converged as the fitting region decreased. At the same time the statistical uncertainty grew as less data was used in the fitting procedure, which caused the data to diverge. Therefore from the behaviour over large fitting regions one can then extrapolate back to obtain an effective short-time diffusion coefficient. A typical example of the fitting procedure is shown in figure 5.7. A similar technique was used by Brown et al. [144] who studied non-exponential relaxations of polystyrene in cyclohexane.

As shown in figure 5.8(a) the short-time diffusion coefficient obtained by this method varies inversely as the static structure factor (see figure 4.45), consistent with equation (3.52). After measuring the experimental structure factor, equation (3.52) can be used to calculate the full Q-dependent hydrodynamic factor (or mobility) as shown in figure 5.8(b). The solid line represents the hydrodynamic factor of a hard-sphere fluid of volume fraction $\phi = 0.2$ calculated from the theory of Beenaker and Mazur [86], [87], using a code provided by D.J. Pine. Strikingly the measured hydrodynamic factor is far reduced, compared to that of a hard-sphere fluid. This implies that the particles interact strongly through a hydrodynamic coupling, due to their close proximity to other particles in the aggregate. The reduction in the hydrodynamic factor can be attributed to a large increase in the local volume fraction. If one compares the high-Q limit (i.e. short-time self diffusion D_s) with the theory of Beenaker and Mazur (only really valid up to $\phi \sim 0.3$) one can infer a local volume fraction of particles $\phi_L \sim 0.58$, which compares well with that obtained by microscopy in section 4.4.4. Note also the shift in the peak of the hydrodynamic factor to larger wavevectors, due to the small interparticle separation i.e. the hydrodynamic factor has a peak coincident with the peak in the static structure factor, consistent with that seen in simple hard-sphere fluids [53], [86], [87], [135].

Again to characterise the long-time decays of these correlation functions one can measure the structural relaxation time. Figure 5.9 shows the Q-dependent structural relaxation time measured from sample 12, multiplied by the square of the appropriate wavevector. To compare decays at different wavevectors one must obviously take into

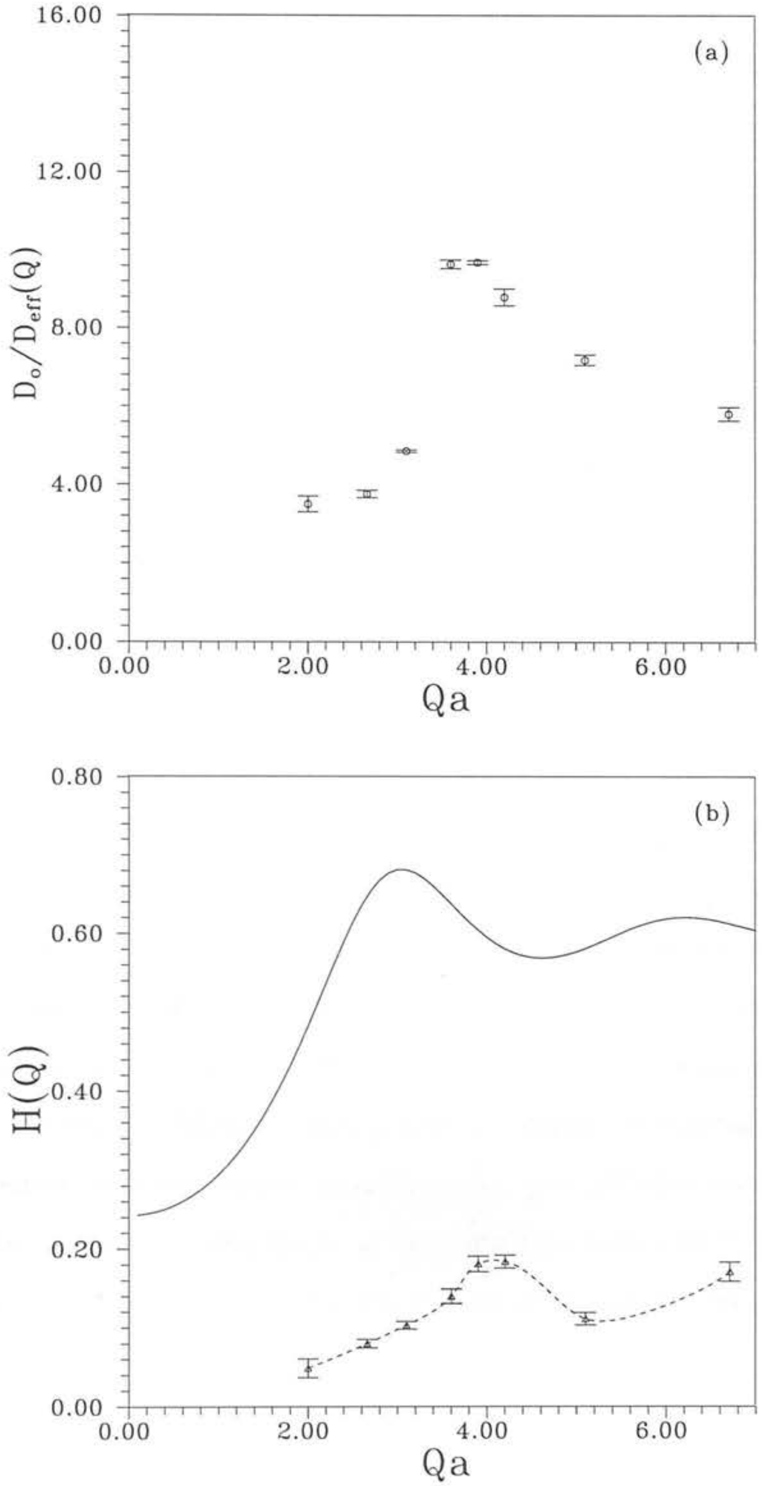

Figure 5.8. (a) The free diffusion coefficient D_0 divided by the effective short-time diffusion coefficient $D_{eff}(Q)$ for sample 12. (b) The hydrodynamic factor $H(Q)$ of sample 12. The solid line represents the theory of Beenaker and Mazur for a volume fraction $\phi = 0.2$, calculated using a code provided by D.J. Pine.

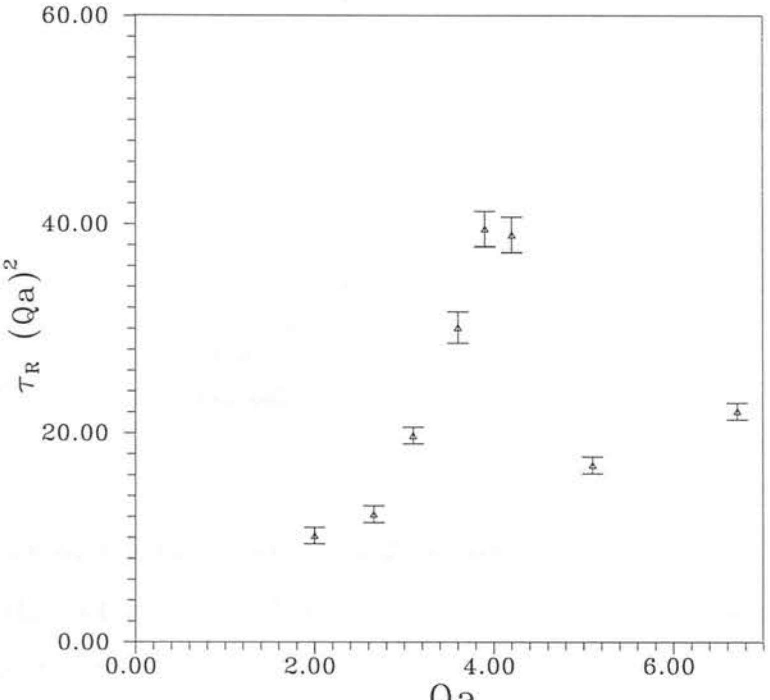

Figure 5.9. The Q-dependent structural relaxation time of sample 12.

account the Q^2-dependence of the diffusion coefficient (c.f. equation (3.51)). The structural relaxation time, in accord with the short-time dynamics presented above, varies inversely as the static structure factor. In hard-sphere suspensions it is known that the long-time diffusion coefficient varies inversely as the static structure factor [135]. In this case a long-time diffusion coefficient can be measured as the long-time decay of the field correlation function follows a single exponential. Although in the case presented here one cannot measure a long time diffusion coefficient, due to the highly stretched exponential nature of the correlation functions, it is reassuring that a property of the long-time diffusion, the structural relaxation time, varies in a similar manner.

5.6 Long-time dynamics

	ϕ	C_p	*Phase*
a	0.182	0	Fluid
b	0.202	2.18e-3	Fluid
c	0.203	2.46e-3	Fluid
d	0.203	2.70e-3	Fluid
e	0.200	2.80e-3	Fluid
f	0.202	3.06e-3	Fluid-Crystal
g	0.203	3.24e-3	Non-equilibrium
h	0.201	3.46e-3	Non-equilibrium
i	0.202	3.66e-3	Non-equilibrium
j	0.202	3.88e-3	Non-equilibrium

Table 5.2. Samples all of volume fraction $\phi \sim 0.2$ and increasing in polymer concentration.

It was shown that a sample within the transient-gelation regime of the non-equilibrium region exhibits frozen-in density fluctuations at very long time scales. To examine the long-time dynamics, and its dependence upon different regions of the phase diagram, a number of different samples were prepared of volume fraction $\phi \sim 0.2$ and varying in polymer concentration, given by table 5.2. These ranged from single phase fluids (samples a to e), to a fluid-crystal coexistence sample (sample f) and four different non-equilibrium samples (samples g to j). The non-equilibrium samples spanned the spinodal-like (sample g) and transient-gelation regimes (samples h to j). Full ensemble averaged measurements were only necessary for the non-equilibrium samples, as the other samples showed highly reproducible correlation functions i.e. these represented fully ergodic systems. Three measurements were carried out at wavevectors $Qa = 2.5$, $Qa = 3.3$ and $Qa = 5.5$ i.e. one well below, one near, and one well above the main high-Q peak in the structure factor. To compare the non-equilibrium samples directly, they were all homogeneously mixed and correlation functions taken 500 seconds later, each of duration 500 seconds. The resulting normalised, ensemble averaged, field correlation functions are shown in figures 5.10(a), 5.10(b) and 5.11. It was latterly found that the short-time decays of the correlation functions contained the effects of after-pulsing as only one PMT was used in this study. Accordingly the data at very short-times is

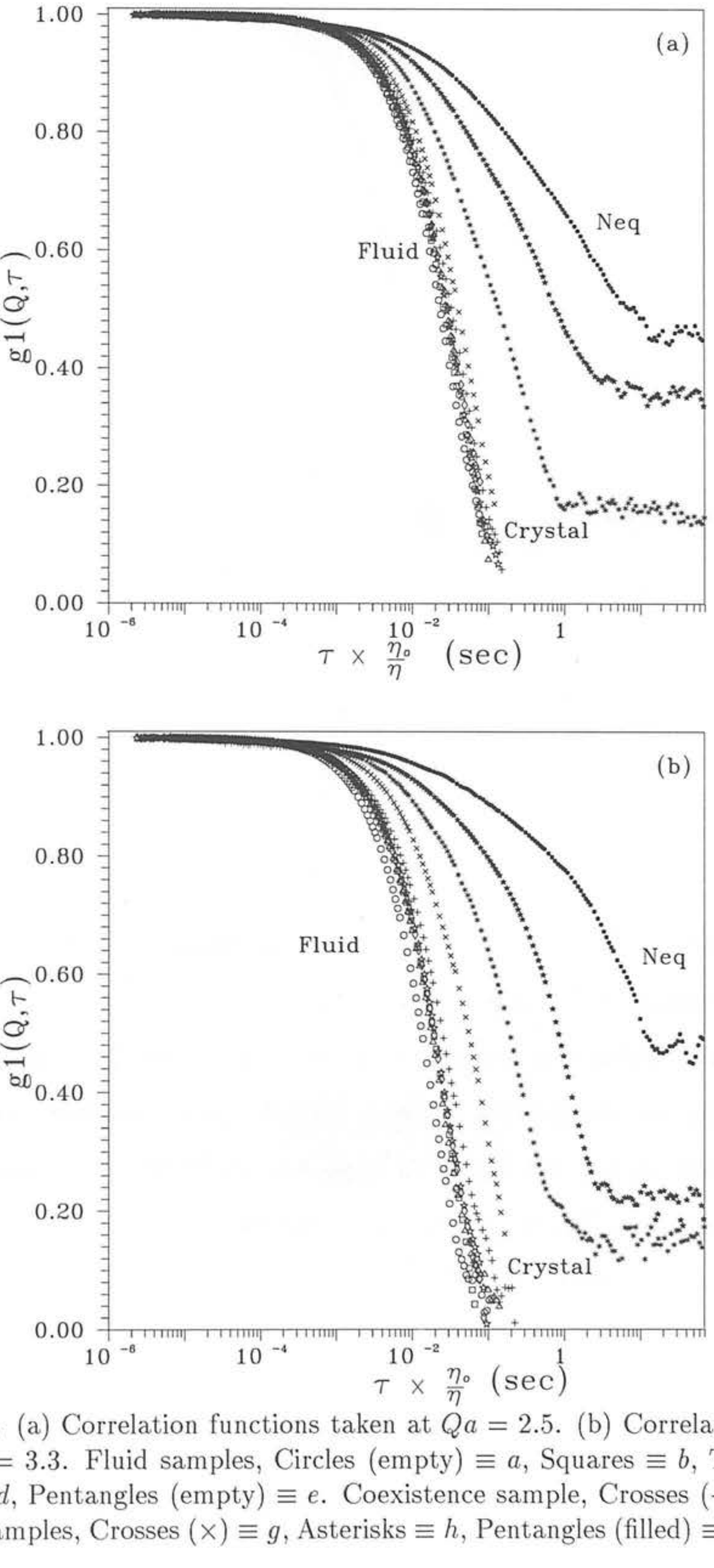

Figure 5.10. (a) Correlation functions taken at $Qa = 2.5$. (b) Correlation functions taken at $Qa = 3.3$. Fluid samples, Circles (empty) $\equiv a$, Squares $\equiv b$, Triangles $\equiv c$, Diamonds $\equiv d$, Pentangles (empty) $\equiv e$. Coexistence sample, Crosses (+) $\equiv f$. Non-equilibrium samples, Crosses (×) $\equiv g$, Asterisks $\equiv h$, Pentangles (filled) $\equiv i$ and Circles (filled) $\equiv j$.

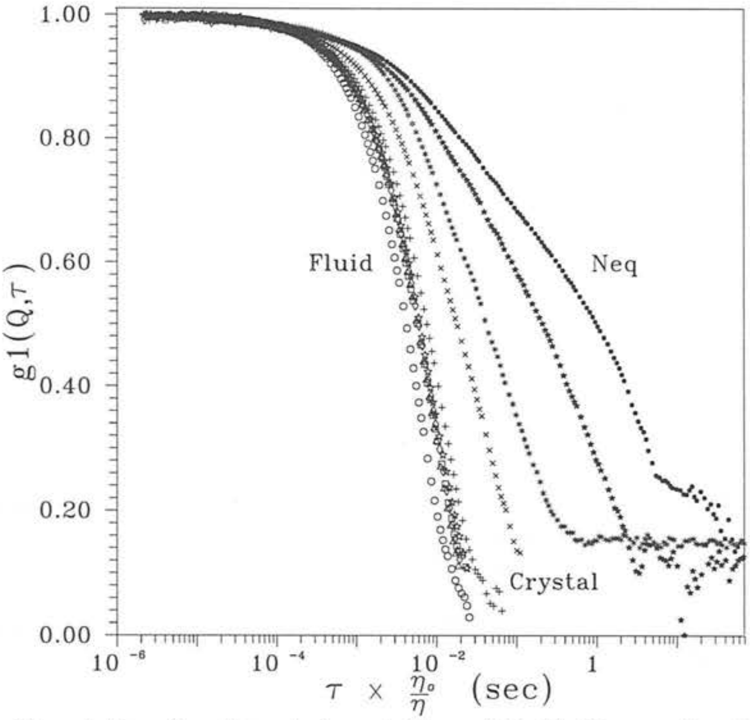

Figure 5.11. Correlation functions taken at $Qa = 5.5$. Fluid samples, Circles (empty) $\equiv a$, Squares $\equiv b$, Triangles $\equiv c$, Diamonds $\equiv d$, Pentangles (empty) $\equiv e$. Coexistence sample, Crosses (+) $\equiv f$. Non-equilibrium samples, Crosses (×) $\equiv g$, Asterisks $\equiv h$, Pentangles (filled) $\equiv i$ and Circles (filled) $\equiv j$.

unreliable and will not be discussed further.

The hard-sphere fluid (sample a) shows a fast, single exponential decay at all three wavevectors. As the polymer concentration is increased little happens to the field correlation function, so long as the increase in background viscosity is accounted for. The correlation functions all deviate from single exponential decays and have similar relaxation times. Once the phase boundary is crossed the sample which ultimately crystallises shows a marked decrease in the particle dynamics, and again a deviation from single-exponentiality. Once into the non-equilibrium region the dynamics become progressively arrested, as the polymer concentration is increased. Again one recovers the highly non-exponential decays observed previously. At high wavevectors the non-ergodic background is small. At lower wavevectors a large non-ergodicity is observed

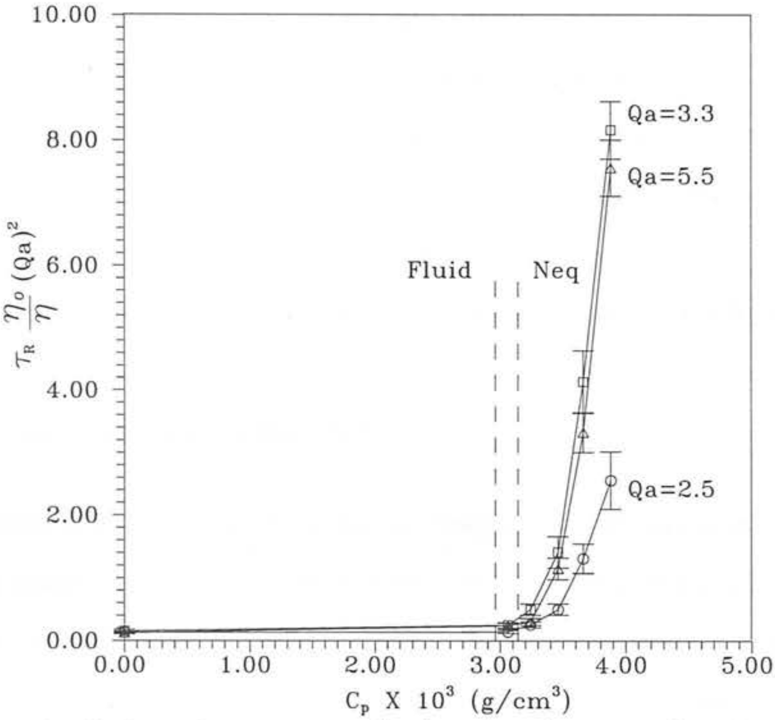

Figure 5.12. Q-dependent structural relaxation time as a function of polymer concentration.

for all but the spinodal-like sample (sample g), although it must be stressed that the non-ergodic background measured by this method is only accurate to within ±10%. Consistent with the arrested large scale structure in the transient-gelation regime, the non-ergodic backgrounds suggest non-decaying density fluctuations, although in contrast to the colloidal glass transition, crystallisation becomes suppressed before the persistence of these frozen-in density fluctuations i.e. within the spinodal-like regime.

To characterise these highly non-exponential decays, one can again measure the structural relaxation time. In figure 5.12 the structural relaxation time is shown as a function of polymer concentration, normalised by the relative background viscosities and multiplied by the square of the appropriate wavevector. As is evident from figure 5.12 little happens to the relaxation time until one enters the non-equilibrium region, upon which the relaxation time diverges rapidly. In fact the relaxation time divergence is consistent with a power law, yet as this is fitted over such a small region the relevance is somewhat dubious. Concomitantly the relaxation time and therefore the dynamics of the system become progressively more Q-dependent i.e. the system tends to become highly structured as the state becomes arrested. The spinodal-like sample (sample g) has very little Q-dependence to its relaxation times, consistent with the lack of frozen-in structure and accordingly the absence of a non-ergodic background.

5.7 Concluding remarks

In this chapter I discussed the dynamic structure of the non-equilibrium phase. Although a number of interesting phenomena have been observed a fundamental trade-off limits the information which can be gleaned from such a dynamic measurement: a long experimental time is required for good statistics, whereas a short experimental time improves the time resolution of the measurement as the structure evolves continuously.

Despite this limitation the dynamics have been examined for a number of samples. The single particle dynamics of a typical sample which undergoes transient-gelation has been measured, and the time-dependence of the dynamics is found to be consistent with the previously presented small angle data. Interestingly the short-time motion is found to be invariant to the large scale structure, throughout the systems evolution and appears to be consistent with a Debye-Waller like motion. The Q-dependent effective diffusion coefficient associated with this short-time motion has been measured and is found to vary inversely as the static structure factor as does the structural relaxation time, consistent with other colloidal systems. Finally a number of samples were studied at a single volume fraction and increasing in polymer concentration. The structural relaxation time was seen to diverge as the non-equilibrium boundary was crossed. It was also found that samples which underwent transient-gelation showed the persistence of frozen-in density fluctuations at long times, whereas spinodal-like samples did not.

Such arrested structure is consistent with that suggested by small angle scattering. Although a significant error exists in the non-ergodic background obtained by this method, it still appears to be the most appropriate for studying weakly flocculated structures (see section 3.5.3).

Little theoretical work has yet been presented on the dynamics of highly interacting systems. As such these systems represent complex many-body problems and in my opinion computer simulation is the most likely route to render these problems soluble. For example lattice Boltzmann simulation of the dynamics of hard-sphere systems has recently been presented, which matches experiment over a wide range of density [135]. This type of simulation could now be extended to model the colloid-polymer system and in particular study the highly non-exponential relaxations observed in the non-equilibrium aggregates.

Chapter 6

Conclusion

'The many men, so beautiful
And they all dead did lie:
And a thousand, thousand slimy things
Lived on; and so did I'

- **Rime of the Ancient Mariner**, Samuel Taylor Coleridge (1797).

6.1 Thesis summary

A detailed study of non-equilibrium aggregation in a model colloid-polymer mixture has been presented. Although aggregation has been observed frequently in colloid-polymer mixtures both the static and dynamic structure of these aggregates, and accordingly the aggregation kinetics, have remained uninvestigated. In this study it was shown that the non-equilibrium region in the phase diagram can be split into three distinctly different kinetic regimes. At low colloid and polymer concentrations one finds behaviour reminiscent of classical nucleation and growth, characterised by a stationary ring of scattered light which forms at small angles only after a finite time. At higher colloid and polymer concentrations one observes behaviour analogous to classical spinodal decomposition as one finds a continuously brightening and collapsing small angle ring.

The static structure of these states is found to be consistent with atomic systems which undergo spinodal decomposition. The dynamics suggest that the particles are relatively free to diffuse throughout the aggregation process, consistent with the observation of a continuously evolving speckle pattern. At still higher colloid or polymer concentrations one finds that the depletion potential becomes sufficiently large to cause the system to gel. In this case one finds a ring which initially collapses but becomes arrested at a finite wavevector. The early stage growth is found to follow a DLCA-type mechanism. Accordingly one finds retarded particle dynamics and the persistence of frozen-in density fluctuations. After a finite time the ring suddenly collapses roughly coincident with visible gravitational settling, attributed to a slow particle rearrangement. In the absence of gravity this slow Brownian-driven rearrangement leads to the formation of dense discrete droplets.

As yet the origin of non-equilibrium aggregation has received little attention. It was suggested that the non-equilibrium behaviour observed here is induced by the presence of an incipient metastable gas-liquid phase boundary, calculated using a recent mean-field theory. The distinctly different kinetic regimes observed in the non-equilibrium region can be explained once analogies have been drawn between the colloid-polymer system and recent Ising-like simulation.

6.2 Comparison with the study of Allain et al.

Here I draw analogies between this work and a very recent study of aggregation phenomena, which in particular studies the effect of gravity on aggregation kinetics. Aggregation almost always occurs under the influence of gravity, but the effect of gravity has received little attention. A study which does examine the effects of both aggregation and sedimentation is that of Allain et al. [93], [145], who investigate the formation of calcium carbonate aggregates formed under a van der Waals attraction. As bond

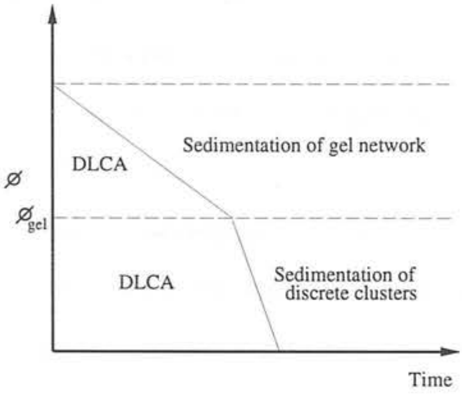

Figure 6.1. The different effects of gravity on the late stages of colloidal aggregation.

breaking and bond rotation are always suppressed, due to the very strong interparticle bonds, they always observe behaviour analogous to DLCA i.e. equivalent to the transient-gelation regime observed here. In contrast to our study their system is poorly characterised with a large polydispersity, hindering detailed comparison with the work presented here. They identify two different kinetic regimes to the aggregation process when the system is subject to the influence of gravity:

- The early stage kinetics are dominated by diffusion i.e. a DLCA-type mechanism.
- The late stage kinetics are primarily governed by gravitational effects.

The late stage growth, i.e. once the clusters have grown sufficiently large to be affected by gravity, is found to be strongly dependent upon the initial colloid volume fraction. If ϕ is sufficiently small, $\phi < \phi_{gel}$, they observe the formation of discrete clusters which rapidly sediment *before* the formation of a system-spanning gel. If ϕ is sufficiently large, $\phi > \phi_{gel}$, a percolating structure forms and after an initial latency time the whole network sediments. This behaviour is summarised in figure 6.1.

Analogous behaviour has been observed here. At low volume fractions of colloid and large polymer concentrations, e.g. sample 4 at $\phi \sim 0.02$, one observes early stage DLCA kinetics. Despite a partially retarded speckle pattern the small angle ring never becomes completely arrested. It was conjectured that the effect of gravity was sufficiently large to prevent gelation so that only discrete clusters were formed which sedimented before the system could percolate. Consistent with this hypothesis there appears to be little latency time before visible sedimentation.

As the volume fraction was increased, yet still with a sufficiently large polymer concentration, e.g. sample 9 at $\phi \sim 0.1$, the early stage kinetics again follow a DLCA-type mechanism, to yield a system-spanning gel. The gel slowly breaks up due to the effect of Brownian motion, which tends to break interparticle bonds and compactify the local short-range structure. Discrete clusters are formed under this slow rearrangement, which rapidly sediment under gravity. Consistent with this hypothesis the gel was observed to break up into independent amorphous clusters once the effect of gravity had been removed. If the collapse was purely gravity driven then the collapse of the structure would be initiated at the bottom of the sample and a small angle ring would persist at the top, contrary to what is observed. Consistent with our study they find that the gel latency time increases and sediment velocity decreases with increasing colloid volume fraction (see figures 4.4 and 4.5).

Allain et al. estimate the critical volume fraction required to form a system-spanning gel, ϕ_{gel}, which can be written,

$$\phi_{gel} \sim \left(\frac{4\pi \, \Delta\rho \, g a^4}{3 k_B T} \right)^{(3-d_f)/(1+d_f)} \tag{6.1}$$

This equation arises from equating the Brownian and gravitational time scales for a ramified cluster to diffuse a distance comparable to its own diameter. If one assumes that a fractal dimension of 1.7 is necessary for a fully frozen gel structure, one finds $\phi_{gel} \sim 0.10$ in the system studied in this thesis, consistent with the lack of a completely frozen ring or latency time at $\phi \sim 0.02$, no matter the polymer concentration. In the same model system, but with a larger particle radius ($a \sim 300nm$), very recent observations suggest that the structure fails to gel at any colloid or polymer concentration until $\phi \gtrsim 0.2$, consistent with equation (6.1) which suggests $\phi_{gel} \sim 0.18$ [146].

The study of Allain et al. was only restricted to a deep interparticle attraction and therefore they failed to observe the rich variety of aggregation kinetics observed here i.e. neither nucleation-like or spinodal-like behaviour which were observed at low interparticle attractions. Without light scattering data they also did not determine the exact nature of the structures formed; neither did they link their observed phenomena to the underlying equilibrium phase behaviour. In our study it was argued that non-equilibrium aggregation is induced by the presence of an incipient metastable gas-liquid boundary. Once analogies have been made to Ising-like simulation all the different kinetic regimes can be explained.

6.3 Possible future work

In contrast to the work of Allain et al. the colloid-polymer system represents a binary mixture and throughout this work the role of the polymer molecules has been largely ignored. In all theoretical treatments the system has been regarded as a single one-component colloidal fluid, subject to a deep, short-ranged interparticle attraction which becomes sufficiently large to induce non-equilibrium aggregation. In future studies the role of the polymer should be examined in more detail. Ideally one would have a colloidal suspension which could be exactly index-matched, so that only the polymer molecules scattered light. Alternatively one could fluorescently tag the polymer molecules, which could be studied using fluorescence techniques such as confocal microscopy or fluorescence recovery after photobleaching.

Rather than simply studying aggregation kinetics the fundamental relation between atomic and colloidal phase kinetics requires more investigation, and the model colloid-polymer system provides an ideal opportunity to do so. One can now readily examine very early stage phase separation kinetics, due to the very slow diffusion rates in colloid-polymer systems, and their dependence upon gravity, effects which cannot be studied in atomic systems. One can also examine the very short scale structure throughout the phase separation process. There are a number of different regions of the phase diagram which could be studied, through the use of small angle scattering techniques in particular. These include the gas-liquid phase, gas-crystal phase and three phase regions of the phase diagram, found in a colloid-polymer mixture with a sufficiently large size ratio. If the predicted solid-solid phase transition is observed, in a colloid-polymer mixture with a sufficiently small size ratio, then one would expect to find an enhanced small angle scattering which could be used to study kinetics. Also the kinetics of the crystal-fluid phase separation, observed for all size ratios less than 0.33, could be studied in more detail.

Finally in a recent computer simulation it was shown that C_{60} may not have a stable liquid phase, as the inter-molecular potential is too short-ranged. Hagen et al. [62] mapped out a metastable gas-liquid boundary which showed a marked similarity to the non-equilibrium region observed in colloid-polymer mixtures. Whether there is a stable liquid phase remains a contentious issue. Would one observe similar kinetic regimes within a metastable gas-liquid phase of C_{60}, similar to those seen in colloid-polymer mixtures? Would one even observe a C_{60} gel state? As yet these questions remain open.

Appendix A

Scattered electric field from a sphere

Equation (3.4) can be written,

$$b(Q) = 4\pi \int_0^a dr \; r^2 (n - n_0) \frac{sin(Qr)}{Qr} \tag{A.1}$$

assuming a spherical particle of radius a. Ignoring the phase factor in the resulting electric field (which will make no contribution to the form factor),

$$\begin{aligned} E(Q) &= \frac{4\pi a^2}{(Qa)^2}(n - n_0) \int_0^a Qrsin(Qr) \; dr && \text{(A.2)} \\ &= \frac{4\pi a^3}{(Qa)^3}(n - n_0)(sin(Qa) - (Qa)cos(Qa)) && \text{(A.3)} \\ &= V_{sphere} \frac{3}{(Qa)^3}(n - n_0)(sin(Qa) - (Qa)cos(Qa)) && \text{(A.4)} \end{aligned}$$

where $V_{sphere} = \frac{4}{3}\pi a^3$ is the volume of the sphere.

Appendix B

Scattered electric field from a shell

Consider a shell of inner radius a, outer radius $a + \Delta$ and refractive index n_s. Using the result derived in Appendix A, equation (A.3) can be written,

$$\begin{aligned} E(Q) &= \frac{4\pi a^3}{(Qa)^3}(n_s - n_0)\ |sin(Qr) - (Qr)cos(Qr)|_a^{a+\Delta} && \text{(B.1)} \\ &= \frac{4\pi a^3}{(Qa)^3}(n_s - n_0)(sin(Qa)cos(Q\Delta) + cos(Qa)sin(Q\Delta) \\ &\quad - [Qa + Q\Delta]\,[cos(Qa)cos(Q\Delta) - sin(Qa)sin(Q\Delta)] \\ &\quad -sin(Qa) + (Qa)cos(Qa)) && \text{(B.2)} \end{aligned}$$

Assuming a thin shell $\Delta << a$ this can be written,

$$\begin{aligned} E(Q) &\sim \frac{4\pi a^3}{(Qa)^3}(n_s - n_0)\left((Q^2 a\Delta)sin(Qa) - (Q\Delta)^2 sin(Qa)\right) && \text{(B.3)} \\ &\sim 4\pi a^2\Delta(n_s - n_0)\frac{sin(Qa)}{Qa} && \text{(B.4)} \end{aligned}$$

$$= \quad V_{shell}(n_s - n_0)\frac{sin(Qa)}{Qa} \tag{B.5}$$

where $V_{shell} = 4\pi a^2 \Delta$ is the volume of the shell.

Appendix C

The relation between $S(Q)$ and $g(r)$

Equation (3.10) can be written,

$$
\begin{aligned}
S(Q) &= \frac{1}{N}\sum_{i=1}^{N}\sum_{j=1}^{N}\langle e^{(i\mathbf{Q}.(\mathbf{r}_i-\mathbf{r}_j))}\rangle && \text{(C.1)}\\
&= 1+\frac{1}{N}\langle\sum_{i\neq j}^{N}\sum_{j\neq i}^{N} e^{(i\mathbf{Q}.(\mathbf{r}_i-\mathbf{r}_j))}\rangle && \text{(C.2)}
\end{aligned}
$$

separating the $i=j$ and $i\neq j$ terms. Introducing the Dirac delta function $\delta(\mathbf{r})$,

$$
\begin{aligned}
S(Q) &= 1+\frac{1}{N}\langle\sum_{i\neq j}^{N}\sum_{j\neq i}^{N}\int\int e^{(i\mathbf{Q}.(\mathbf{r}-\mathbf{r}'))}\delta(\mathbf{r}-\mathbf{r}_i)\delta(\mathbf{r}'-\mathbf{r}_j)\rangle\, d\mathbf{r}d\mathbf{r}' && \text{(C.3)}\\
&= 1+\frac{1}{N}\int\int e^{(i\mathbf{Q}.(\mathbf{r}-\mathbf{r}'))}.\langle\sum_{i\neq j}^{N}\sum_{j\neq i}^{N}\delta(\mathbf{r}-\mathbf{r}_i)\delta(\mathbf{r}'-\mathbf{r}_j)\rangle\, d\mathbf{r}d\mathbf{r}' && \text{(C.4)}\\
&= 1+\frac{1}{N}\int\int e^{(i\mathbf{Q}.(\mathbf{r}-\mathbf{r}'))}\rho^{(2)}(\mathbf{r},\mathbf{r}')\, d\mathbf{r}d\mathbf{r}' && \text{(C.5)}
\end{aligned}
$$

The function $\rho^{(2)}(\mathbf{r},\mathbf{r}')$ is known as the two-particle distribution function and is related to the pair correlation $g(r)$,

$$g(r) \equiv \frac{\rho^{(2)}(\mathbf{r})}{\rho^2} \qquad \text{(C.6)}$$

where ρ is the homogeneous density. Therefore,

$$S(Q) = 1 + \rho \int e^{i\mathbf{Q}.\mathbf{r}} g(r)\, d\mathbf{r} \qquad \text{(C.7)}$$

by integrating out the dummy variable $\mathbf{r}'$.

In a very dilute gas $g(r) = 1$ due to a lack of pair correlations (i.e. $\rho^{(2)}(\mathbf{r}) = \rho^2$) and the structure factor is simply a delta function which can be regarded as a contribution to the forward scattering. It is common practice to ignore this contribution and rewrite equation (C.7) as,

$$S(Q) = 1 + \rho \int e^{i\mathbf{Q}.\mathbf{r}} (g(r) - 1)\, d\mathbf{r} \qquad \text{(C.8)}$$

Appendix D

Second Virial coefficients

The second virial coefficient is defined as,

$$
\begin{aligned}
B_2 &\equiv -\frac{1}{2}\int f(\mathbf{r})d^3r && \text{(D.1)}\\
&= -\frac{1}{2}\int\left(exp\left[-\frac{\epsilon}{k_BT}\right]-1\right)d^3r && \text{(D.2)}
\end{aligned}
$$

Therefore for a hard sphere fluid,

$$
\begin{aligned}
B_{2,HS} &= -\frac{1}{2}\int_{r=0}^{a}\left(exp\left[-\frac{\epsilon=\infty}{k_BT}\right]-1\right)d^3r\\
&\quad -\frac{1}{2}\int_{r=a}^{\infty}\left(exp\left[-\frac{\epsilon=0}{k_BT}\right]-1\right)d^3r && \text{(D.3)}\\
&= \frac{1}{2}\int_{r=0}^{a}d^3r && \text{(D.4)}\\
&= \frac{2\pi a^2}{3} && \text{(D.5)}
\end{aligned}
$$

In the case of the AHS model,

$$\begin{aligned} B_{2,AHS} &= -\frac{1}{2}\int_{r=0}^{a}\left(exp\left[-\frac{\epsilon=\infty}{k_BT}\right]-1\right)d^3r \\ &\quad -\frac{1}{2}\int_{r=a}^{a+\delta}\left(\frac{(a+\delta)}{12\tau_B\delta}-1\right)d^3r \\ &\quad -\frac{1}{2}\int_{r=(a+\delta)}^{\infty}\left(exp\left[-\frac{\epsilon=0}{k_BT}\right]-1\right)d^3r \qquad (D.6) \\ &= \frac{1}{2}\int_{r=0}^{a}d^3r-\frac{1}{2}\int_{r=a}^{a+\delta}\frac{(a+\delta)}{12\tau_B\delta}d^3r+\frac{1}{2}\int_{r=a}^{a+\delta}d^3r \qquad (D.7) \\ &= \frac{2\pi a^2}{3}\left(1-\frac{1}{4\tau_B}\right) \qquad (D.8) \end{aligned}$$

in the limit $\delta \to 0$.

For the SW fluid,

$$\begin{aligned} B_{2,SW} &= -\frac{1}{2}\int_{r=0}^{a}\left(exp\left[-\frac{\epsilon=\infty}{k_BT}\right]-1\right)d^3r \\ &\quad -\frac{1}{2}\int_{r=a}^{a+\delta}\left(exp\left[-\frac{\epsilon}{k_BT}\right]-1\right)d^3r \\ &\quad -\frac{1}{2}\int_{r=(a+\delta)}^{\infty}\left(exp\left[-\frac{\epsilon=0}{k_BT}\right]-1\right)d^3r \qquad (D.9) \\ &= \frac{1}{2}\int_{r=0}^{a}d^3r-\frac{1}{2}exp\left[-\frac{\epsilon}{k_BT}\right]\int_{r=a}^{a+\delta}d^3r+\frac{1}{2}\int_{r=a}^{a+\delta}d^3r \qquad (D.10) \\ &= \frac{2\pi a^2}{3}-\left(exp\left[-\frac{\epsilon}{k_BT}\right]-1\right).\frac{2\pi}{3}\left((a+\delta)^2-a^2\right) \qquad (D.11) \\ &= \frac{2\pi a^2}{3}\left[1-\left(exp\left[-\frac{\epsilon}{k_BT}\right]-1\right)\left(2\left(\frac{\delta}{a}\right)+\left(\frac{\delta}{a}\right)^2\right)\right] \qquad (D.12) \end{aligned}$$

Appendix E

Structure factor of a doublet

$$
\begin{aligned}
S(Q) &= \frac{1}{N}\sum_{i=1}^{N}\sum_{j=1}^{N} e^{i\mathbf{Q}.(\mathbf{r_i}-\mathbf{r_j})} && \text{(E.1)}\\
&= \frac{1}{N}\sum_{i=1}^{N} e^{i\mathbf{Q}.\mathbf{r_i}} \sum_{i=1}^{N} e^{-i\mathbf{Q}.\mathbf{r_i}} && \text{(E.2)}\\
&= \frac{1}{N}|\sum_{i=1}^{N} e^{i\mathbf{Q}.\mathbf{r_i}}|^2 && \text{(E.3)}
\end{aligned}
$$

as the two sums $\sum_i, \sum_j$ are independent. In the case shown in figure E.1, for two particles of radius a, centred at a and $-a$, this can be written,

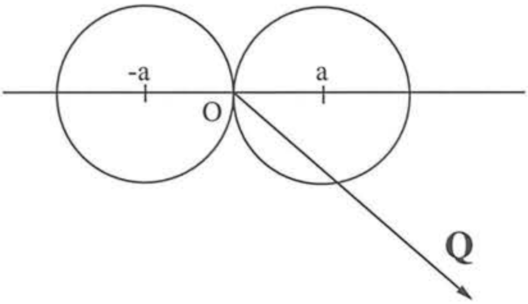

Figure E.1. Scattering geometry.

$$\frac{1}{N}|\sum_{i=1}^{N} e^{i\mathbf{Q}.\mathbf{r_i}}|^2 \;=\; 2\,cos^2\left((Qa)cos(\theta)\right) \tag{E.4}$$

Averaging around **Q**,

$$\frac{1}{N}\langle|\sum_{i=1}^{N} e^{i\mathbf{Q}.\mathbf{r_i}}|^2\rangle \;=\; \frac{1}{4\pi}\int\int 2\,sin(\theta)\;cos^2((Qa)cos(\theta))\;d\theta d\phi \tag{E.5}$$

$$= \left[\frac{sin(2Qa)}{2Qa}\right] + 1 \tag{E.6}$$

Bibliography

[1] **C.R. Vester.** *Kolloid-Z*, **84**, 63 (1938).

[2] **A. Vrij.** *Pure and app. chem.*, **48**, 471 (1976).

[3] **S. Asakura and F. Oosawa.** *J. Chem. Phys.*, **22**, 1255 (1954).

[4] **S. Asakura and F. Oosawa.** *J. Polym. Sci.*, **33**, 183 (1958).

[5] **E. Dickinson.** *Chem. and Ind.*, 595 (1990).

[6] **J. Israelachvili.** *Intermolecular and surface forces*, 2nd Edition, Academic, London (1991).

[7] **E.J.W. Verwey and J.T.G. Overbeek.** *Theory of the stability of Lyophobic Colloids*, Elsevier, Amsterdam (1948).

[8] **D.H. Napper.** *Polymeric stabilization of Colloidal Particles*, Academic, London (1983).

[9] **C. Cowell, F.K.R. Li-In-On and B. Vincent.** *J. Chem. Soc. Faraday Trans.*, **74**, 337 (1978).

[10] **B. Vincent, P.F. Luckham and F.A. Waite.** *J. Coll. Int. Sci.*, **73**, 508 (1980).

[11] **J. Clarke and B.Vincent.** *J. Coll. Int. Sci.*, **82**, 208 (1981).

[12] **P.R. Sperry.** *J. Coll. and Int. Sci.*, **87**, 375 (1982).

[13] **P.R. Sperry.** *J. Coll. and Int. Sci.*, **99**, 97 (1984).

[14] **B. Vincent, J. Clarke and K.G. Barnett.** *Colloids Surfaces*, **17**, 51 (1986).

[15] **C. Smits, J.S. van Duijneveldt, J.K.G. Dhont, H.N.W. Lekkerkerker and W.J. Briels.** *Phase transitions*, **21**, 157 (1990).

[16] **W.C.K. Poon, J.S. Selfe, M.B. Robertson, S.M. Ilett, A.D. Pirie and P.N. Pusey.** *J. Phys. II France*, **3**, 1075 (1993).

[17] **P.N. Pusey, W.C.K. Poon, S.M. Ilett and P. Bartlett.** *J. Phys. Condens. Matter*, **6**, A29 (1994).

[18] **P.N. Pusey, A.D. Pirie and W.C.K. Poon.** *Physica A*, **201**, 322 (1993).

[19] **P.D. Patel and W.B. Russel.** *J. Coll. and Int. Sci.*, **131**, 192 (1989).

[20] **F. Leal Calderon, J. Bibette, J. Biais.** *Europhys. Lett.*, **23**, 653 (1993).

[21] **S.M. Ilett, A. Orrock, W.C.K. Poon and P.N. Pusey.** *Phys. Rev. E*, **51**, 1344 (1995).

[22] **M.P. Aronson.** *Langmuir*, **5**, 494 (1989).

[23] **J. Bibette, D. Roux and B. Pouliguy.** *J. Phys. II France*, **2**, 401 (1992).

[24] **R. Piazza and G. Di Pietro.** *Europhys. Lett.*, **28**, 445 (1994).

[25] **S. Sanyal, N. Easwer, S. Rawaswamy and A.K. Sood.** *Europhys. Lett.*, **18**, 107 (1992).

[26] **J.S. van Duijneveldt, A.W. Heinen and H.N.W. Lekkerkerker.** *Europhys. Lett.*, **21**, 369 (1993).

[27] **P.D. Kaplan, J.L. Rouke, A.G. Yodh and D.J. Pine.** *Phys. Rev. Lett.*, **72**, 582 (1994).

[28] **H. de Hek and A. Vrij.** *J. Coll. and Int. Sci.*, **84**, 409 (1981).

[29] **B. Vincent, J. Edwards, S. Emmett and A. Jones.** *Colloids Surf.*, **18**, 261 (1986).

[30] **A. Jones and B. Vincent.** *Colloids Surf.*, **42**, 113 (1989).

[31] **B. Vincent.** *Colloids Surf.*, **50**, 241 (1990).

[32] **H. de Hek and A. Vrij.** *J. Coll. and Int. Sci.*, **88**, 258 (1982).

[33] **P. Tong, T.A. Witten, J.S. Huang, L.J. Fetters.** *J. Phys. France*, **51**, 2813 (1990).

[34] **W.C.K. Poon and P.N. Pusey.** *in: Observation, Prediction and Simulation of Phase transitions in Complex Fluids*, M. Baus, L.F. Rull and J-P Ryckaert (editors), Kluwer, Dordrecht, (1995).

[35] **M. Planck.** *Treatise on Thermodynamics*, translated by A. Ogg, Dover, New York (1945).

[36] **J.W. Cahn.** *Trans. Metall. Soc. AIME*, **242**, 166 (1968).

[37] **J. Frenkel.** *Kinetic Theory of Liquids*, Dover, New York (1990).

[38] **A.C. Zettlemoyer.** *Nucleation*, M.Decker, New York (1969).

[39] **J.S. Langer, M Bar-on and H.D. Miller.** *Phys. Rev. A.*, **11**, 1417 (1975).

[40] **C. Billotet and K. Binder.** *Z. Phys. B*, **32**, 195 (1979).

[41] **T. Hashimoto.** *in: Current topics in Polymer Science Vol II*, R.M. Ottenbrite, L.A. Utracki and S. Inoue Eds., Hanser, New York (1987).

[42] **H. Furukawa**. *Adv. Phys.*, **34**, 703 (1985).

[43] **M.D.Haw, W.C.K. Poon and P.N. Pusey**. *Physica A*, **208**, 1 (1994).

[44] **M.D. Haw, M. Sievwright, W.C.K. Poon and P.N. Pusey**. *to appear in Physica A.*

[45] **K. Binder and D. Stauffer**. *Phys. Rev. Lett.*, **33**, 1006 (1974).

[46] **I.M. Lifshitz and V.V. Sloyozov**. *J. Phys. Chem. Solids*, **19**, 35 (1961).

[47] **K. Kawasaki and T. Ohta**. *Prog. Theor. Phys.*, **59**, 362 (1978).

[48] **E.D. Siggia**. *Phys. Rev. A*, **20**, 595 (1979).

[49] **N.C. Wong and C.M. Knobler**. *J. Chem. Phys.*, **69**, 725 (1978).

[50] **Y.C. Chou and W.I.Goldburg**. *Phys. Rev. A.*, **20**, 2105 (1979).

[51] **J.G. Kirkwood and F.P. Buff**. *J. Chem. Phys.*, **19**, 774 (1951).

[52] **W. van Megen and I. Snook**. *Adv. Coll. Int. Sci.*, **21**, 119 (1984).

[53] **P.N. Pusey**. *in: Liquids, freezing and the glass transition*, J.P. Hansen,D Leveque and J. Zinn-Justin (editors), North-Holland, Amsterdam,763 (1991).

[54] **J. Bibette, T.G. Mason, H. Gang and D.A. Weitz**. *Phys. Rev. Lett.*, **69**, 981 (1992).

[55] **M. Carpineti and M. Giglio**. *Phys. Rev. Lett.*, **68**, 3327 (1992).

[56] **M. Carpineti and M. Giglio**. *Phys. Rev. Lett.*, **70**, 3828 (1993).

[57] **H.N.W. Lekkerkerker, W.C.K. Poon, P.N. Pusey, A. Stroobants and P.B. Warren**. *Europhys. Lett.*, **20**, 559 (1992).

[58] **P. Bartlett**. *J. Phys. Condens. Matter*, **2**, 4979 (1990).

[59] **H.N.W. Lekkerkerker.** *Colloid Surf.*, **51**, 419 (1990).

[60] **C.F. Tejero, A. Daanoun, H.N.W. Lekkerkerker and M. Baus.** *Phys. Rev. Lett*, **73**, 752 (1994).

[61] **A. Cheng, M.L. Klein and C. Caccamo.** *Phys. Rev. Lett.*, **71**, 1200 (1993).

[62] **H.H.J. Hagen, E.J. Meijer, G.C.A.M. Mooij, D. Frenkel and H.N.W. Lekkerkerker.** *Nature*, **365**, 425 (1993).

[63] **P. Bolhuis and D. Frenkel.** *Phys. Rev. Lett*, **72**, 2211 (1994).

[64] **C.F. Tejero, A. Daanoun, H.N.W. Lekkerkerker and M. Baus.** *Phys. Rev. E*, **51**, 558 (1995).

[65] **P.N. Pusey and W. van Megen.** *Nature*, **320**, 340 (1986).

[66] **J. Brandrup and E.H. Immergut.** *Polymer Handbook*, Wiley-Interscience, New York (1989).

[67] **W.B.Russel, D.A. Saville and W.R. Schowalter.** *Colloidal Dispersions*, Cambridge University Press, Cambridge.

[68] **K. Binder, C. Billotet and P. Mirold.** *Z. Physik B.*, **30**, 183 (1978).

[69] **S. Hayward, D.W. Heermann and K. Binder.** *J. Stat. Phys.*, **49**, 1053 (1987).

[70] **P.B. Warren, S.M. Ilett and W.C.K. Poon.** *submitted to Phys. Rev. E.*

[71] **K. Schatzel and B.J. Ackerson.** *Phys. Rev. Lett.*, **86**, 337 (1992).

[72] **B.J. Berne and R. Pecora.** *Dynamic Light Scattering*, Wiley-Interscience, New York (1976).

[73] **P.N. Pusey and R.J.A. Tough.** *in: Dynamic Light Scattering*, R. Pecora (editor), Plenum, New York (1985).

[74] **P.G. de Gennes.** *Physica*, **25**, 825 (1959).

[75] **V. Bloomfield.** *in: Dynamic Light Scattering*, R. Pecora (editor), Plenum, New York (1985).

[76] **J.P. Boon and S. Yip.** *Molecular Hydrodynamics*, McGraw-Hill, New York (1980).

[77] **J.P. Hansen and I.R. McDonald.** *Theory of simple liquids*, Academic Press, London (1986).

[78] **L. Verlet and J.J. Weis.** *Phys. Rev.*, **139**, A1138 (1965).

[79] **R.J. Baxter.** *J. Chem. Phys.*, **49**, 2270 (1968).

[80] **J.W. Jansen, C.G. de Kruif and A. Vrij.** *J. Coll. Int. Sci.*, **114**, 471 (1986).

[81] **C.G. de Kruif, P.W. Rouw, W.J. Briels, M.H.G. Duits, A. Vrij and R.P. May.** *Langmuir*, **5**, 422 (1989).

[82] **J. Bibette, D. Roux and B. Pouligny.** *J. Phys. II France*, **2**, 401 (1992).

[83] **J.S. Huang, S.A. Safran, M.W. Kim, G.S. Grest, K.M. Kotharcky and N. Quirke.** *Phys. Rev. Lett.*, **53**, 592 (1984).

[84] **R.V. Sharma and K.C. Sharma.** *Physica*, **89A**, 213 (1977).

[85] **R. Pecora.** *Dynamic Light Scattering*, Plenum, New York, (1985).

[86] **C.W.J. Beenaker and P. Mazur.** *Physica*, **120A**, 388 (1983).

[87] **C.W.J. Beenaker and P. Mazur.** *Physica*, **126A**, 349 (1984).

[88] **P.N. Pusey and W. van Megen.** *Physica*, **157A**, 705 (1989).

[89] **W. van Megen and P.N. Pusey.** *Phys. Rev. A.*, **43**, 5429 (1991).

[90] **J-Z Xue, D.J. Pine, S.T. Milner, X-L Wu and P.M.Chaikin.** *Phys. Rev. A.*, **46**, 6550 (1992).

[91] **P. van Beurten and A. Vrij.** *J. Chem. Phys.*, **74**, 2744 (1981).

[92] **P.N. Pusey and W. van Megen.** *J. Chem. Phys.*, **80**, 3513 (1984).

[93] **C. Allain, M. Cloitre and M. Wafra.** *Phys. Rev. Lett.*, **74**, 1478 (1995).

[94] **K. Binder and D. Stauffer.** *Adv. Phys.*, **25**, 343 (1976).

[95] **J.E. Martin and A.J. Hurd.** *J. Appl. Cryst.*, **20**, 61 (1987).

[96] **B.B. Mandelbrot.** *The Fractal Geometry of Nature*, Freeman, New York (1982).

[97] **B. Cabane.** *in: Neutron, X-Ray and Light Scattering*, P. Lindner and Th. Zaub (eds), Elsevier (1991).

[98] **K. Binder.** *Rep. Prog. Phys*, **50**, 783 (1987).

[99] **S.C. Glotzer, M.F. Gyure, F. Sciortino, A. Coniglio and H.E. Stanley.** *Phys. Rev. E.*, **49**, 247 (1994).

[100] **T. Hashimoto, M. Itakura and H. Hasegawa.** *J. Chem. Phys.*, **85**, 6118 (1986).

[101] **T. Hashimoto, M. Itakura and N. Shimidzu.** *J. Chem. Phys.*, **85**, 6773 (1986).

[102] **T. Izumitani, M. Takenaka and T. Hashimoto.** *J. Chem. Phys.*, **92**, 3213 (1990).

[103] **M. Takenaka, T. Izumitani and T. Hashimoto.** *J. Chem. Phys.*, **92**, 4566 (1990).

[104] **T. Hashimoto, M. Takenaka and T. Izumitani.** *J. Chem. Phys.*, **97**, 679 (1992).

[105] **M. Takenaka, T. Izumitani and T. Hashimoto.** *J. Chem. Phys.*, **98**, 3528 (1993).

[106] **H.L. Snyder and P. Meakin.** *J. Chem. Phys.*, **79**, 5588 (1983).

[107] **J. Marro, J.L. Lebowitz and M.H. Kalos.** *Phys. Rev. Lett.*, **43**, 282 (1979).

[108] **B.D. Bulter, H.J.M. Hanley, D. Hansen and D.J. Evans.** *Phys. Rev. Lett.*, **74**, 4468 (1995).

[109] **H. Furukawa.** *Physica A*, **123**, 497 (1984).

[110] **J.K.G. Dhont, A.F.H. Duyndam and B.J. Ackerson.** *Physica A.*, **189**, 503 (1992).

[111] **J.K.G. Dhont and A.F.H. Duyndam.** *Physica A.*, **189**, 532 (1992).

[112] **J.K.G. Dhont, A.F.H. Duyndam and B.J. Ackerson.** *Langmuir*, **8**, 2907 (1992).

[113] **M.H.G.M. Penders and A. Vrij.** *Adv. Coll. and Int. Sci.*, **36**, 185 (1991).

[114] **S.H. Chen, D. Lombardo, F. Mallamace, N Micali, S. Trusso and S. Vasi.** *Prog. Colloid Polym. Sci.*, **93**, 311 (1993).

[115] **S.H. Chen, J. Rouch, F. Sciortino and P Tartaglia.** *J. Phys. Condens. Matter*, **6**, 10855 (1994).

[116] **P. Meakin.** *Physica Scripta*, **46**, 295 (1992).

[117] **D.J. Robinson and J.C. Earnshaw.** *Phys. Rev. Lett.*, **71**, 715 (1993).

[118] **J.C. Earnshaw and D.J. Robinson.** *Phys. Rev. Lett.*, **72**, 3682 (1994).

[119] **J.C. Earnshaw and D.J. Robinson.** *Physica A*, **214**, 23 (1995).

[120] **M. Chen and W.B. Russel.** *J. Coll. and Int. Sci.*, **141**, 564 (1991).

[121] **M.C. Grant and W.B. Russel.** *Phys. Rev. E.*, **47**, 2606 (1993).

[122] **J. Liu, W.Y. Shih, M. Sarikaya and I.A. Aksay.** *Phys. Rev. A*, **41**, 3206 (1990).

[123] **P.W. Zhu and D.H. Napper.** *Phys. Rev. E*, **50**, 1360 (1994).

[124] **W.Y. Shih, I.A. Aksay and R. Kikuchi.** *Phys. Rev. A.*, **36**, 5015 (1987).

[125] **E. Dickinson, C. Elvingson and S.R. Euston.** *J. Chem. Soc. Faraday Trans. 2*, **85**, 891 (1989).

[126] **G. Lironis, D.W. Heermann and K. Binder.** *J. Phys. A:Math. Gen.*, **23**, L329 (1990).

[127] **J. Stefanou.** *undergraduate project*, Edinburgh University (1995).

[128] **M.E. Fisher and R.J. Burford.** *Phys. Rev. A*, **156**, 583 (1967).

[129] **S. Bradbury.** *An introduction to the optical microscope*, Oxford University Press, (1984).

[130] **M. Pluta.** *Advanced light Microscopy*, Vol. 2, Elsevier, (1988).

[131] **E. Hecht.** *Optics*, Addison-Wesley, (1974).

[132] **J.M. Gunton, M. San Migue and P.S. Sahni.** *in: Phase Transitions and Critical Phenomena*, C. Domb and J.L. Lebowitz (editors), Vol. 8, Academic Press, London (1983) Chapter 3.

[133] **A. Guinier.** *X-ray Diffraction*, Freeman, New York (1963).

[134] **A.T.J.M. Wouterson, R.P. May and C.G. de Kruif.** *J. Coll. Int. Sci.*, **151**, 410 (1992).

[135] **P. Segre, O. Behrend and P.N. Pusey.** *submitted to Phys. Rev. E.*

[136] **N.C. Ford Jr.** *in: Dynamic Light Scattering*, R. Pecora (editor), Plenum, New York (1985).

[137] **J.E. Martin and J.P. Wilcoxon.** *Phys. Rev. Lett.*, **61**, 373 (1988).

[138] **J.E. Martin, J.P. Wilcoxon and J. Odinek.** *Phys. Rev. A*, **43**, 858 (1991).

[139] **W. van Megen and S.M. Underwood.** *Phys. Rev. E.*, **47**, 248 (1993).

[140] **W. van Megen and S.M. Underwood.** *Phys. Rev. Lett.*, **70**, 2766 (1993).

[141] **W. van Megen and S.M. Underwood.** *Phys. Rev. E.*, **49**, 4206 (1994).

[142] **C. Kittel.** *Introduction to Solid State Physics*, Wiley, New York, (1976).

[143] **K. Schatzel.** *Applied Optics*, **32**, 3880 (1993).

[144] **J.C. Brown, P.N. Pusey and R. Dietz.** *J. Chem. Phys.*, **62**, 1136 (1975).

[145] **C. Allain and M. Cloitre.** *Adv. in Coll. and Int. Sci.*, **46**, 129 (1993).

[146] **S.P. Meeker.** *private communication.*

Publications:

Work from this thesis which has either been published or submitted for publication:

'An experimental study of a model colloid-polymer mixture'
J. Phys. II France **3** 1075 (1993).

'Aggregation Dynamics in a Model Colloid-Polymer Mixture'
Analytical Proceedings **30** 493 (1993).

'Dynamics of Colloid-Polymer mixtures'
Physica A **201** 322 (1993).

'Gelation in Colloid-polymer mixtures'
To appear in Faraday Discussion 101: 'Gels'.

The DIC microscopy presented in chapter 4 has been included in:

'Developments in Wide Field Microscopy:
3D Spatial Investigations using Differential Interference Contrast
(DIC) Microscopy'
Scott Singleton *Unilever internal report* June (1994).